博士論文

Geology and geochemistry of banded iron formations: Implications for secular variations of transitional element compositions in the seawater

(縞状鉄鉱層の地質学・地球化学的研究

：海洋遷移金属元素組成の経年変化の復元)

青木翔吾

Contents page

論文の内容の要旨

論文題目

縞状鉄鉱層の地質学・地球化学的研究：
海洋遷移金属元素組成の経年変化の復元
(Geology and geochemistry of banded iron formations:
Implications for secular variations of transitional element compositions in the seawater)

氏名　　青木　翔吾

共進化モデルでは、生命は表層環境とともに進化してきたとされる。特に、生物が属する系統やその代謝の違いに関連し、遷移金属タンパク質の種類や構成割合が異なることから、地球史を通した海水の遷移金属元素濃度の変化が、生物の代謝や系統の進化・絶滅に影響を及ぼしたことが指摘されている。本博士論文では過去の海水遷移金属組成の復元を試み、海洋化学組成の変化と生物進化との関連から共進化モデルを提唱する。

本博士論文は 5 章からなる。第 1 章では、過去の海水遷移金属元素組成の経年変化と生物進化との関連を物質学的に検証するためには当時の海洋組成を推定する必要があり、各時代の海洋で堆積した化学堆積岩の化学組成から海洋組成の復元することの重要性が書かれている。特に、鉄酸化物とシリカの互層からなる縞状鉄鉱層は、先カンブリア時代の地質体にほぼ普遍的に存在するため、海洋化学組成の経年変化の復元に適しており、近年盛んに研究がされてきた。しかし、先行研究で報告された縞状鉄鉱層の分析値は、各年代・各地質体で非常に大きくばらついており、海水組成の定量的な議論のみならず定性的な推定さえ疑問視されている。一般に、鉄質堆積物の化学組成は、①共存する海水組成、②堆積速度、③妨害元素による吸着の阻害や④堆積時に混入する砕屑粒子や水酸化鉄粒子以外の化学沈殿物、に依存する。しかし、従来の研究では特に堆積時に混入する砕屑粒子や水酸化鉄粒子以外の化学沈殿物の影響が過小評価されてきた。

そこで、本博士論文研究では、縞状鉄鉱層中の砕屑粒子や水酸化鉄粒子以外の化学沈殿物に多く含まれる元素との相関関係から、縞状鉄鉱層の微量元素濃度のばらつきが主に砕屑粒子や水酸化鉄粒子以外の化学沈殿物によることを示し、特に砕屑粒子の影響を除去することで定量的に海水組成を復元する方法論、水酸化鉄以外の化学沈殿物の影響に基づいて当時の海洋遷移金属元素循環を定性的に推定する方法論を提案した。そして、

その方法を各時代の縞状鉄鉱層の地球化学的研究に適用し、定量的・定性的に遷移金属元素海洋組成変化を推定し、海洋化学組成の変化と生物進化の共進化史を読み解いた。

第 2 章では、西グリーンランド南部に存在する初期太古代(38-37 億年前)に形成された Isua 表成岩帯の縞状鉄鉱層の化学分析結果が述べられている。先行研究は、この時代の縞状鉄鉱層が非常に高い Ni 濃度および Ni/Fe 比を持つことから、太古代の海洋が Ni に富んでいたことを提唱した。本研究では、表成岩帯北東部において採取された縞状鉄鉱層の露頭試料の全岩化学組成を岩相ごとに行い、遷移金属元素濃度のばらつきの要因が砕屑性粒子の混入によるものであることを示した。Isua 表成岩帯の縞状鉄鉱層は構成鉱物の構成割合によって、それぞれ、磁鉄鉱、石英、角閃石に富むものの 3 つのタイプに分類される。角閃石に富むタイプは、高い Ca, Mg 含有量を有し、かつ、遷移金属元素や希土類元素に富む。角閃石は炭酸塩鉱物あるいは砕屑性鉱物由来とされることから、その高い遷移金属元素や希土類元素濃度も炭酸塩鉱物あるいは砕屑性鉱物の混入に起因すると考えられる。このことは、先行研究で分析された Isua 表成岩帯の縞状鉄鉱層の試料にもあてはまり、先行研究で示された高い Ni/Fe 比を持つ試料は Ca や Mg 含有量が高いので、角閃石に富む試料であったと考えられる。結果として、先行研究によって推定された太古代の海洋遷移金属濃度は過剰に見積もられていることと考えられる。

また、水酸化鉄起源とされる磁鉄鉱に富む試料も Ni、V や U 濃度と Zr 濃度に正の相関関係が存在する。このことは、磁鉄鉱に富む試料中にも海水から直接、鉄酸化物に吸着した初生的遷移元素に加えて、砕屑粒子由来のものが存在することを示す。そのため、海水組成を推定するのには、その後者の影響を取り除く必要がある。そこで正相関の切片の値を砕屑粒子の影響の無い初生的に水酸化鉄に吸着した元素であると仮定して、その濃度を求めると 18-22ppm 程度であり、従来の想定よりも 1/10 程度であることが分かった。更に、Zr 濃度と遷移金属元素濃度との相関関係は他の時代の縞状鉄鉱層にも見られ、同様の方法で計算した水酸化鉄に吸着した元素濃度を形成年代ごとにコンパイルし直した。その結果、初期太古代の縞状鉄鉱層は Ni 濃度が 4-10 倍程度高く、従来の推定と同じように初期太古代海洋は Ni 濃度が高かったことが推定される。このことから、初期太古代海洋は、Ni を必須元素として用いる、初期生命の 1 つであるメタン生成菌の繁栄には適した環境であったと推定される。しかし、従来の推定よりも早い、29 億年前には縞状鉄鉱層の Ni 濃度は減少していたことがわかった。このことから 29 億年以降の海洋は Ni に不足し、メタン生成菌の繁栄は制限されたのではないかと推定した。このことは、29 億年には既に酸素発生型光合成が出現し、地球表層環境が酸化的になっていたことを示唆するいくつかの先行研究を支持する。

第 3 章では、カナダ Saglek 岩体に存在する 39.5 億年以前に形成された Nulliak 表成岩帯の縞状鉄鉱層の化学分析を行ない、初期太古代海洋の遷移金属元素濃度推定に関して、第 2 章の Isua 表成岩帯で行なった推定の再現性を確かめた。岩相観察から、この地域の縞状鉄鉱層は、磁鉄鉱、石英と輝石から構成されていることがわかった。輝石の存在は、

この地域の縞状鉄鉱層が堆積後にグラニュライト相程度の高温変成作用を被ったことが推定される。また、全岩 Ca、Mg、Fe 濃度から、輝石は初生的にはドロマイトなどの炭酸塩鉱物として沈殿したものであると示唆される。しかし、Isua 表成岩帯の縞状鉄鉱層とは異なり、そのような Ca-Mg 炭酸塩鉱物の遷移金属元素濃度への影響は見られなかった。一方で、遷移金属元素濃度(V, Cr, Ni, Cu, U)と Zr 濃度との間には正の相関関係が見られ、分析値のばらつきが砕屑粒子の混入によって説明できることがわかった。第 2 章で行なった方法と同様に、砕屑粒子の影響のない縞状鉄鉱層の組成を推定したところ、鉄酸化物に存在する Ni の濃度は 10-30ppm となり、Isua 表成岩帯の縞状鉄鉱層と同様に、Ni 濃度はそれ以後の地質帯で形成された試料に比べて高く、初期太古代の海洋は Ni 濃度が高かったことが改めて確かめられた。

第 4 章では、古原生代(24-22 億年前)に形成された南アフリカ Transvaal 超層群 Hotazel 層の縞状鉄鉱層および Mn 堆積物の化学分析を行ない、大酸化イベント当時の海洋生命必須元素循環の推定を行なうとともに、それ以後の地質帯から出現が示唆される真核生物の進化への影響を議論した。全岩化学分析の結果、試料の全岩遷移金属(Co, Ni, Zn)濃度は Mn 濃度と正の相関をもつことが分かった。このことは、現在の酸化的な海洋環境と同様に、Mn 酸化物がこれらの海水中に溶けている遷移金属元素を吸着除去していたことを示唆する。一方で、Mn 鉱物を含まない縞状鉄鉱層試料について、微量元素濃度イメージングを行なったとところ、Zn は Fe 酸化物層に濃集しているのに対して、Co は Al 濃度の高い層やスポットに濃集していることが分かった。Al は砕屑粒子などを起源とすると考えられるので、Mn 酸化物を含まない縞状鉄鉱層中の Co は砕屑粒子由来と考えられる。全岩組成分析による Mn 濃度と遷移金属濃度との相関関係と、遷移金属元素濃度イメージングによる Zn と Co 濃度の分布の違いから、酸化的な海洋環境で、Zn は比較的海水に溶けていたのに対して、Co は Mn 酸化物によって 2 価から溶解度の低い 3 価に酸化され、Mn 酸化物中に固定されたことで海洋 Co 濃度は低かったことが、定性的に推定される。また他の時代の縞状鉄鉱層の報告値から、Co 濃度と Mn 濃度との正の相関は、29 億年前には見られることから、後期太古代には既に海水中の Co は Mn 酸化物によって固定化され、Co 濃度は低く保たれていた可能性が示唆される。Co は、タンパク質材料であるメチオニン合成を触媒するビタミン B12 に使われる元素であり、真核生物に比べて原核生物はその相対依存度は低い。真核生物や一部のシアノバクテリアなどの原核生物は、Co の機能を Zn で代用している。本研究で示された約 29 億年以降の Mn 酸化物への固定化にともなう海水 Co 濃度の減少によって、高い Co 依存性を持つ原核生物の中から、Co 依存性の低いシアノバクテリアが生まれ、真核生物の祖先となった可能性を示唆する。これは Co と Zn 酵素の発現遺伝子の系統解析を行なった先行研究からも支持される。

第 5 章では、第 2 章から 4 章にかけて行なった研究から縞状鉄鉱層の化学組成に影響を与える要素として砕屑粒子や水酸化鉄以外の化学沈殿物の影響が大きいことを示し、

その影響を考慮して推定された海水の遷移金属元素経年変化は地球史を通して酸化還元や供給源の変化に伴って経年変化してきたことを説明した。そしてその推定結果と化石記録や化学的な記録から制約される生物の出現・繁栄時期とを比較し、海水の遷移金属元素濃度変化は、様々な代謝や系統の生物の進化とほぼ同じ時期、あるいはそれよりも早い時期に起きたことを示した。このことから海洋の遷移金属元素濃度変化はそれを利用する生命の進化に影響を与えてきており、両者の共進化の結果が現在の子孫生物の金属元素利用能として記録されている可能性を示した。

Chapter I.

General Introduction

It is generally thought that the surface environments and life have coevolved on the earth. Especially, the redox potentials and partial pressure of oxygen fluctuate closely with the evolutions of metabolisms and body plans throughout the earth history (Kasting, 1987) (Fig. 1A). The anaerobic conditions during the Archean had ensured the prosperity of eukaryotic organisms such as methanogens and iron reducing bacteria (Ueno et al., 2006; Konhauser et al., 2009; Yoshiya et al., 2015), which perform anaerobic respiration (the method of acquiring energy by decomposing the organic matter into pyruvic acid without oxygen). Following the birth and prosperity of oxygenic phototrophs during the period from the Neoarchean to the Paleoproterozoic (Farquhar et al., 2011; Holland, 2006; Planavsky et al., 2014), the eukaryotes and the multicellular organisms have emerged at *ca.* 2.1 Ga (Han and Runnegar, 1992; Runnegar, 1991; Albani et al., 2010). They perform aerobic respiration (the method of acquiring much more energy by decomposing the organic matter into H_2O and CO_2). Many researchers think that the increases in redox potentials in the surface environments have provoked their emergence. It is because their aerobic respiration can be accomplished over a value of approximately 0.01 (1%) of the present atmospheric oxygen level (PAL). In addition, the steroid (which is a structural component of the eukaryotic cell essential for determining the fluidity of their cell membranes) and the collagen (which acts as a glue to strengthen the link

between the cells in the multicellular organisms) can be synthesized only under oxic conditions (Dean et al., 1967; Summons et al., 2006; Rittle and Green, 2010; Desmond and Gribaldo, 2010; Towe, 1970). Therefore, the fluctuation of bioavailable free oxygen in the surface environments throughout the Earth history might have an impact on the biological evolutions.

However, all organisms on the Earth are not only dependent on oxygen, but also on many "bioessential" elements, which are used for critical components of their living tissues, enzymes and other biomolecules. Especially, transitional elements within them are concerned with biological elements. And, it is known that their degrees of dependence on their transitional elements are different depending on their metabolic types and/or phylogenies (e.g. Zerkle et al., 2005; Dupont et al., 2006). For example, Ni is used for Cofactor F430, which catalyzes the release of the methane in the final step of methanogenesis. Therefore, methanogens, which are one of the earliest lives on the earth, use preferentially Ni-bearing enzymes relative to other metabolic-type organisms (Zerkle et al., 2005).

On the other hand, Co is also one of bioessential elements. Prokaryotes such as archaea and bacteria have a greater number of Co-binding proteins than eukaryotes (Dupont et al., 2006; Zhang and Gladyshev, 2010). Cobalt is used for vitamine B12 (Met

H), which catalyzes the synthesis of methionine, an essential amino acid. Most of prokaryotes can synthesize Met H, but eukaryotes cannot synthesize it. A part of eukaryotes can acquire and use Met H in symbiosis with Met H-sysnthesizing prokaryotes (Croft et al., 2005). On the other hand, some eukaryotes can use Zn-bearing enzyme (Met E) in place of Co for synthesis of methionine (Croft et al., 2005; Helliwell et al., 2011).

From the difference of dependences on the transitional elements between metabolic types and/or phylogenies, those element abundances in the surface environments could have influence on the timing of evolutions of organisms having specific metabolisms or belonging to specific taxa (Williams and Frausto da Silva, 2003; Zerkle et al., 2005; Dupont et al., 2006). Based on the differences of redox chemistries of those elements, the evolutions of those bioessential element abundances in the ocean have been inferred throughout the earth history (Saito et al., 2003; Zerkle et al., 2005; Anbar, 2008) (Fig. 1B). Those modeling studies are based on the simple redox-evolution model that anoxic ocean at the Archean have evolved into sulfidic ocean at the Proterozoic, finally into the oxic ocean at the Phanerozoic (Canfield, 1998). These estimates, for example, show that dissolved Ni was limited in the anoxic and/or sulfidic Archean and Proterozoic ocean because it is prone to be precipitated as sulfide minerals (NiS) under

anoxic conditions. On the other hand, those show that dissolved Co in the seawater were progressively decreased along with increased redox potentials in the ocean because Co chemical species change from dissolved divalent to undissolved trivalent forms under oxic conditions.

On the other hand, chemical compositions of the sedimentary rocks (e.g. the BIFs, carbonate rocks and black shales) could be key tools for decoding the secular variations of the seawater chemical compositions based on the solid material evidences. Particularly, the Banded Iron Formations (BIFs) are the chemical sedimentary rocks composed of alternating Fe-minerals and Si-minerals bands. Their occurrences are found in the geologic suites from 3.9 to 0.7 Ga except for the Middle Proterozoic (Klein and Beukes, 1992; Isley and Abbott, 1999; Komiya et al., 2015) (Fig. 2). Therefore, their geochemical studies could meet the purposes for the estimates of secular variations in seawater chemical compositions throughout the Precambrian. Their whole-rock chemical compositions are thought to preserve those of the contemporary seawater, from which they were precipitated. The most noteworthy elements are rare earth elements (REE) and Y. Their shale- or chondrite-normalized REE + Y patterns show characteristics anomalies similar to those of modern seawater or high-temperature hydrothermal fluid (e.g. Bau and Dulski, 1996; Bolhar et al., 2004). For example, they often have Y anomalies

(superchondritic Y/Ho ratios: > 27) and negative Ce anomalies (only if they were deposited under oxic conditions) similar to those of modern oxic seawater. In addition, the BIFs, which are thought to have been precipitated from solutions with hydrothermal effects, show positive Eu anomalies in similar to modern high-temperature hydrothermal fluid. Therefore, since the growing availability of the trace-element analyses by ICP-MS or -AES the at the 1980s, the magnitudes of their characteristic anomalies, negative Ce anomaly and positive Eu anomaly, have been used as the proxies for the redox and inputs of hydrothermal fluids in their sedimentary environments, respectively (e.g. Kato et al., 2006; Viehmann et al., 2015).

Since the 2000s, the compositions of bioessential and/or redox-sensitive element such as P, Cr, Co, Ni, Cu and U in the BIFs have been used as proxies for of seawater chemistry thorough the time (Bjerrum and Canfield, 2002; Swanner et al., 2014; Konhauser et al., 2011; Konhauser et al., 2009; Partin et al., 2013; Fru et al., 2016). The most famous ones of the previous studies have been performed by Konhauser and his colleagues (Konhauser et al., 2009; Mloszewska et al., 2012; Mloszewska et al., 2013; Pecoits et al., 2009; Haugaard et al., 2016). They showed secular variations of Ni/Fe ratios in the BIFs show that their ratios in the Archean are higher than those in the post-2.7Ga (Fig. 3). Based on the secular variations, Konhauser and his colleagues

estimated that the Archean seawater was more enriched in Ni contents due to higher hydrothermal Ni influx from komatiites to ocean, resulting in prosperity of methanogens because Ni is an essential element to form Cofactor F430.

However, the estimate is still controversial because the compiled Ni/Fe ratios of the BIFs are highly variable even in a single BIF sequence and because their chemical compositions are dependent on not only seawater composition but also various factors such as sedimentary rates (Kato et al., 1998; Kato et al., 2002), involvement of clastic and volcanic materials (Bau, 1993 Manikyamba et al., 1993; Pecoits et al., 2009; Frei and Polat, 2007; Viehmann et al., 2015a, b), secondary movement accompanied with metamorphism (Bau, 1993; Viehmann et al., 2015a, b) and kinetic of adsorption rates of the elements on the iron oxyhydroxides (Kato et al., 1998; Kato et al., 2002), other interference elements (Konhauser et al., 2009), and so on.

In general, the BIFs contain not only iron oxides (hematite and magnetite) and silica minerals (quartz), which are transformed from amorphous ferrihydrite and silica precipitated from seawater, but also carbonate and silicate minerals (Klein, 2005). The carbonate minerals are precipitated minerals from seawater or diagenetic minerals, and silicate minerals possibly originate from carbonate minerals precipitated from seawater, secondary minerals formed during diagenesis, metamorphism and alteration, and clastic

and volcanic material. As a result, the whole-rock trace element compositions are dependent on not only compositions of the iron oxides and quartz but also those of other minerals. The most predominant minerals of the other silicate minerals are Mg- and Ca-bearing minerals such as amphibole and carbonate minerals (Dymek and Klein, 1988; Mloszewska et al., 2012; Mloszewska et al., 2013). They have high REE and transition element contents but the effects of the involvement of the Mg- and Ca-bearing minerals on the whole rock compositions have not been fully evaluated yet.

The second component is derived from clastic and volcanic materials. They consist of clastic minerals such as detrital minerals of zircon, aluminosilicate minerals and quartz, aeolian dusts, and volcanic exhalative materials of tiny insoluble grains or colloidal particles. Some previous studies tried eliminating contamination of the clastic materials based on arbitrarily determined threshold values of some detritus-loving elements such as Al, Ti, Sc, Rb, Y, Zr, Hf and Th (e.g. Konhauser et al., 2009; Partin et al., 2013). However, even insignificant contaminations of clastic materials resulted in significant influence on the REE and transitional element compositions of the BIFs because they are much more abundant in clastic and exhalative materials relative to pure chemical sediments (Bolhar et al., 2004; Viehmann et al., 2015a, b), and are more

abundant than the index elements of Zr, Y and Hf in most clastic and volcanic materials except for zircon. Therefore, it is necessary to more strictly eliminate the contaminations.

In this Ph.D. thesis, I analyzed the whole-rock or mineral-scale chemical compositions of the BIFs with many Precambrian ages, and discussed the influence of above two components on their chemical compositions. Moreover, I estimated the chemical compositions of the BIFs free from the two components and seawater compositions, from which they were precipitated. Finally, I discussed the secular variations of their compositions and their influences on the biological evolutions.

In Chapter II of this thesis, I analyzed the whole-rock compositions of the Eoarchean BIFs in the Isua supracrustal belt (ISB). I discussed the relationships between their lithofacies and chemical compositions and influences of carbonate or silicate minerals other than Fe-oxide minerals on REE + Y and transitional-element contents. Moreover, I discussed the influences of the clastic or volcanic materials on the variations of chemical compositions of the BIFs rich in Fe-oxide minerals, based on the correlations of those elements with Al, Ti and HFSE contents. Finally, I estimated the compositions of the BIFs free from above contaminations, and reconstructed evolutions of seawater compositions (especially for Ni) through the time on the basis of comparison with the younger BIFs.

In Chapter III, I performed the mineralogical and geochemical studies of the Eoarchean BIFs in the Nulliak supracrustal rocks. Firstly, I described their lithofacies and mineralogy, and performed their chemical analysis for estimating the metamorphisms and their primary mineralogy. Secondly, I analyzed the whole-rock compositions of the BIFs, and discussed relationships between lithofacies and transitional-element contents. Moreover, I discussed the influences of the clastic or volcanic materials on the variations of chemical compositions of the BIFs rich in Fe-oxide minerals in the same manner with the study of the ISB BIFs of chapter II. Finally, I estimated the compositions of the BIFs free from above contaminations, and ascertained the Eoarchean seawater chemistry suggested by the geochemical studies of the ISB BIFs in the chapter II.

In Chapter IV, I analyzed the whole-rock and the mineral-scale chemical compositions of the Paleoproterozoic BIFs in the Hotazel Formation from the Transvaal Supergroup, South Africa. These BIFs are interlayered with the Mn rocks at the three stratigraphic horizons. Firstly, I analyzed the stratigraphic variations of REE + Y compositions from the lowermost BIFs to the lowest Mn rocks, and discussed their secondary movements at their diagenesis based on the correlations with their mineralogy and major element contents. And, I estimated the variations in the redox potentials and the influences of hydrothermal components at the sedimentary environments in

combination with their lithostratigraphies, based on negative Ce anomalies and positive Eu anomalies. Moreover, I estimated the transitional-element cycles and their seawater compositions in the Paleoproterozoic oceans on the basis of relationships between their lithofacies (the BIFs and Mn rocks) and transitioinal-element contents, and micro-scale distributions of those elements. And, based on above results, I estimated that Co bioavailability in the Paleoproterozoic ocean was limited because the element was removed by Mn-oxide minerals. Moreover, I estimated that Co fixations by Mn-oxide minerals in seawater are shown in the older ages (up to the late Archean) based on the correlations between Co and Mn contents in the older BIFs. Finally, I discussed the secular variations of those element seawater-compositions and their influences on the biological evolutions from the prokaryotes to the eukaryotes, which are thought to be occurred during the Paleoproterozoic (Han and Runnegar, 1992; Albani et al., 2010).

In Chapter V, I summarized above results from chapter II to chapter IV, and discussed whether the bioavailability of transitional elements in seawater have influences on biological evolutions.

References

Albani, A.E., Bengston, S., Canfield, D.E., Bekker, A., Macchiarelli, R., Mazurier, A., Hammarlund, E.U., Boulvais, P., Dupuy, J.J., Fontaine, C., Fürisch, F. T., Gaurhier-Lafaye, F., Janvier, P., Javaux, E., Ossa, F. O., Pierson-Wickmann, A. C., Riboulleau, A., Sardini, P., Vachard, D., Whitehouse, M., Meunier, Alain., 2010. Large colonial organisms with coornated growth in oxygenated environments 2.1Gyr ago. Nature 466, 100-104.

Anbar, A.D., 2008. Elements and Evolution. Science 322, 1481-1483.

Bau, M., 1993. Effects of syn- and post-depositional processes on the rare-earth element distribution in Precambrian iron-formations. European Journal of Mineralogy 5, 257-267.

Bau, M., Dulski, P., 1996. Distribution of yttrium and rare-earth elements in the Penge and Kuruman iron-formations, Transvaal Supergroup, South Africa. Precambarian Research 79, 37-55.

Bjerrum, C.J., Canfield, D.E., 2002. Ocean productivity before about 1.9 Gyr ago limited by phosphorus adsorption onto iron oxides. Nature 417, 159–162.

Bolhar, R., Kamber, B.S., Moorbarth, S., Fedo, C.M., Whitehouse, M.J., 2004. Characterisation of early Archaean chemical sediments by trace element signatures. Earth and Planetary Science Letters 222, 43-60.

Canfield, D.E., 1998. A new model for Proterozoic ocean chemistry. Nature 396, 450-453.

Croft, M.T., Lawrence, A.D., Raux-Deery, E., Waren, M.J., Smith, A.G., 2005. Algae acquire vitamin B12 through a symbiotic relationship with bacteria. Nature 438, 90-93.

Dean, P.D.G., Ortiz de Montellano, P.R., Bloch, K., Corey, E.J. 1967. A soluble 2,3-oxidosqualene sterol cyclase. Journal of Biological Chemistry 242, 3014-3015.

Desmond, E., Gribaldo, S., 2009. Phylogenomics od sterol synthesis: Insights into the origin, evolution, and diversity of a key eukaryotic feature. Genome Biology and Evoluton 1, 364-381.

Dupont, C.L., Yang, S., Palenik, B., Bourne, P.E., 2006. Modern proteomes contain putative imprints of ancient shifts in trace metal geochemistry. PNAS 47, 17822-17827.

Farquhar, J., Zerkle, A.L., Bekker, A., 2011. Geological constraints on the origin of oxygenic photosynthesis. Photosynthesis Research 107, 11-36.

Frei, R., Polat, A., 2007. Source heterogeneity for the major components of ~ 3.7 Ga Banded Iron Formations (Isua Greenstone Belt, Western Greenland): Tracing the nature of interacting water masses in BIF formation. Earth and Planetary Science Letters 253, 266-281.

Fru, E.C., Rodriguez, N.P., Partin, C.A., Lalonde, S.V., Andersson, P., Weiss, D.J., Albani, A.E., Rodushkin, I., Konhauser, K.O., 2016. Cu isotopes in marine black shales record the Great Oxidation Event. PNAS 113, 4941-4946.

Han, T.M., Runnegar, B., 1992. Megascopic eukaryotic algae from the 2.1-billion-year-old negaunee iron-formation, Michigan. Science 1992, 232-235.

Haugaard, R., Pecoits, E., Lalonde, S., Rouxel, O., Konhauser, K., 2016. The Joffre banded iron formation, Hamersley Group, Western Australia: Assessing the palaeoenvironment through detailed petrology and chemostratigraphy. Precambrian Research 273, 12-37.

Helliwell, K.E., Wheeler, G.L., Leptos, K.C., Goldstein, R.E., Smith, A.G., 2011, Insights into the evolution of vitamin B12 auxotrophy from sequenced algaeones. Molecular Biology and Evolution 28, 2921-2933.

Holland, H.D., 2006. The oxygenation of the atmosphere and oceans. Philosophical Transactions of The Royal Society B 361, 903-915.

Isley, A.E., Abbott, D.H., 1999. Plume-related mafic volcanism and the deposition of banded iron formations. Journal of Geophysical Research 104, 15461-15477.

Kasting, J.F., 1987. Theoretical constraints on oxygen and carbon dioxide concentrations in the Precambrian atmosphere. Precambrian Research 34, 205-229.

Kato, Y., Ohta, I., Tsunematsu, T., Watanabe, Y., Isozaki, Y., Maruyama, S., Imai, N., 1998. Rare earth element variations in mid-Archean banded iron formations: implications for the chemistry of ocean and continent and plate tectonics. Geochimica et Cosmochimica Acta 62, 3475-3497.

Kato, Y., Kano, T., Kunugiza, K., 2002. Negative Ce Anomaly in the Indian Banded Iron Formations: Evidence for the Emergence of Oxygenated Deep-Sea at 2.9-2.7 Ga. Resource Geology 52, 101-110.

Kato, Y., Yamaguchi, K.E., Ohmoto, H., 2006. Rare earth elements in Precambrian banded iron formations: Secular changes of Ce and Eu anomalies and evolution of atmospheric oxygen. In:Kesler, S.E., Ohmoto, H. (Eds.), Evolution of Early Earth's Atmosphere, Hydrosphere and Biosphere Constraints from Ore Deposits. Geological Society of America Memoir 198, Geological Society of America. 269-289.

Klein, C., Beukes, N.J., 1992. Time distribution, stratigraphy, and sedimentologic setting,

and geochemistry of Precambrian iron-formations. In:Schopf, J.W., Klein, C. (Eds), The Proterozoic Biosphere: A multidisciplinary Approach. Cambridge University Press, New York, 139-147.

Klein, C., 2005. Some Precambrian banded iron-formations (BIFs) from around the world: Their age, geologic setting, mineralogy, metamorphism, geochemistry, and origins. American Mineralogist 90, 1473-1499.

Konhauser, K.O., Pecoits, E., Lalonde, S.V., Papineau, D., Nisbet, E.G., Barley, M.E., Arndt, N.T., Zhanle, K., Kamber, B.S., 2009. Oceanic nickel depletion and a methanogen famine before the Great Oxidation Event. Nature 458, 750-753.

Konhauser, K.O., Lalonde, S.V., Planavsky, N.J., Pecoits, E., Lyons, T.W., Mojzsis, S.J., Rouxel, O.J., Barley, M.E., Rosìere, C., Fralick, P.W., Kump, L.R., Bekker, A., 2011. Aerobic bacterial pyrite oxidation and acid rock drainage during the Great Oxidation Event. Nature 478, 369-374.

Komiya, T., Yamamoto, S., Aoki, S., Sawaki, Y., Ishikawa, A., Tashiro, T., Koshida, K., Shimojo, M., Aoki, K., Collerson, K.D., 2015. Geology of the Eoarcehan, >3.95 Ga, Nulliak supracrustal rocks in the Saglek Block, northern Labrador, Canada: The oldest geological evidence for plate techtonics. Tectonophysics 662, 40-66.

Manikyamba, C., Balaram, V., Naqvi, S.M., 1993. Geochemical signatures of polygenetic origin of a banded iron formation (BIF) of the Archaean Sandur greenstone belt (schist belt) Karnataka nucleus, India. Precambrian Research 61, 137-164.

Mloszewska, A.M., Pecoits, E., Cates, N.L., Mojzsis, S.J., O'Neil, J., Robbins, L.J., Konhauser, K.O., 2012. The composition of Earth's oldest iron formations: The Nuvvuagittuq Supracrustal Belt (Québec, Canada). Earth and Planetary Science Letters 317-318, 331-342.

Mloszewska, A.M., Mojzsis, S.J., Pecoits, E., Papineau, D., Dauphas, N., Konhauser, K.O., 2013. Chemical sedimentary protoliths in the >3.75 Ga Nuvvuagittuq Supracrustal Belt (Québec, Canada). Gondwana Research 23, 574-594.

Nishizawa, M., Miyazaki, J., Makabe, A., Koba, K., Takai, K. 2014. Physiological and isotopic characteristics of nitrogen fixation by hyperthermophilic methanogens: Key insights into nitrogen anabolism of the microbial communities in Archean hydrothermal systems. Geochimica et Cosmochimica Acta 138, 117-135.

Partin, C.A., Lalonde, S.V., Planavsky, N.J., Bekker, A., Rouxel, O.J., Lyons, T.W., Konhauser, K.O., 2013. Uranium in iron formations and the rise of atmospheric oxygen. Chemical Geology 362, 82-90.

Pecoits, E., Gingras, M.K., Barley, M.E., Kappler, A., Posth, N.R., Konhauser, K.O., 2009. Petrography and geochemistry of the Dales Gorge banded iron formation:

Paragenetic sequence, source and implications for palaeo-ocean chemistry. Precambrian Research 172, 163-187.

Rittle, J., Green, M.T., 2010. Cytochrome P450 Compound I: Capture, Characterization, and C-H bond activation kinetics. Science 330, 933-937.

Runnegar, B., 1991. Precambrian oxygen levels estimated from the biochemistry and physiology of early eukaryotes. Paleogeography, Paleoclimatology, Paleoecology 97, 97-111.

Saito, M.A, Sigman, D.M., Morel, F. M. M., 2003, The bioinorganic chemistry of the ancient ocean: the co-evolution of cyanobacterial metal requirements and biogeochemical cycles at the Archean-Proterozoic boundary?. Inorganica Chimica Acta 356, 308-318.

Summons, R.E., Bradley, A.S., Jahnke, L.L. Waldbauer, J.R., 2006. Steroids, triterpenoids and molecular oxygen. Phylosophical Transcations of the Royal Society B Biologicak Sciences 361, 951-968.

Swanner, E.D., Planavsky, N.J., Lalonde, S.V., Robbins, L.J., Bekker, A., Rouxel, O.J., Saito, M. A., Kappler, A., Mojzsis, S.J., Konhauser, K.O., 2014. Cobalt and marine redox evolution. Earth and Planetary Science Letters 290, 253-263.

Towe, K.M., 1970. Oxygen-collagen priority and the early metazoan fossil record. PNAS 65, 781-788.

Ueno, Y., Yamada, K., Yoshida, N., Maruyama, S., Isozaki, Y., 2006. Evidence from fluid inclusions for microbial methanogenesis in the early Archeaean era. Nature 440, 516-519.

Yoshiya, K., Sawaki, Y., Hirata, T., Maruyama, S., Komiya, T., 2015. In-situ iron isotope analysis in pyrite in ~3.7 Ga sedimentary protoliths from the Isua supracrustal belt, southern West Greenland. Chemical Geology 401, 126-139.

Viehmann, S., Bau, M., Smith, A.J.B., Beukes, N.J., Dantas, E.L., Bühn, B., 2015a. The reliability of ~2.9 Ga old Witwatersrand banded iron formations (South Africa) as archives for Mesoarchean seawter: Evidence from REE and Nd isotope systematics. Journal of African Earth Sciences 111, 322-334.

Viehmann, S., Bau, M., Hoffmann, J.E., Münker, C., 2015b. Geochemistry of the Krivoy Rog Banded Iron Fomration, Ukline, and the impact of peak episodes of increased global magmatic activity on the trace element composition of Precambrian seawater. Precambrian Research 270, 165-180.

Williams, R.J.P., Frausto da Silva, J.J.R., 2003, Evolution was chemically constrained. Journal of theoretical biology 220, 323-343.

Zerkle, A.L., House, C.H., Brantley, S.L., 2005. Biogeochemical signatures through time

as inferred from whole microbial genomes. American Journal of Science 305, 467–502.

Zhang, Y., Gladyshev, V.N., 2010. General trends in trace element utilization revealed by comparative genomic analyses of Co, Cu, Mo, Ni, and Se. Journal of Biological Chemistry.

Figure captions

Figure 1. (A) Secular variations of pO_2 through geological time (Kasting, 1987) and the estimated ages of appearances of variable prokaryotes and eukaryotes, constrained by variable geological evidences. (B) Secular variations of some transitional-element compositions in seawater (modified from Anbar, 2008), estimated based on simple redox-potential evolution models (Canfield, 1998).

Figure 2. Schematic diagrams showing the relative abundance of Precambrian BIFs vs. time from Klein, 2005. Estimated abundances are relative to the Hamersley Group BIF volume taken as maximum.

Figure 3. Molar Ni/Fe ratios of the BIFs vs. age from Konhauser et al., 2009. Two stages are identified based on maximum Ni/Fe ratios, with the transition period indicated by a grey bar.

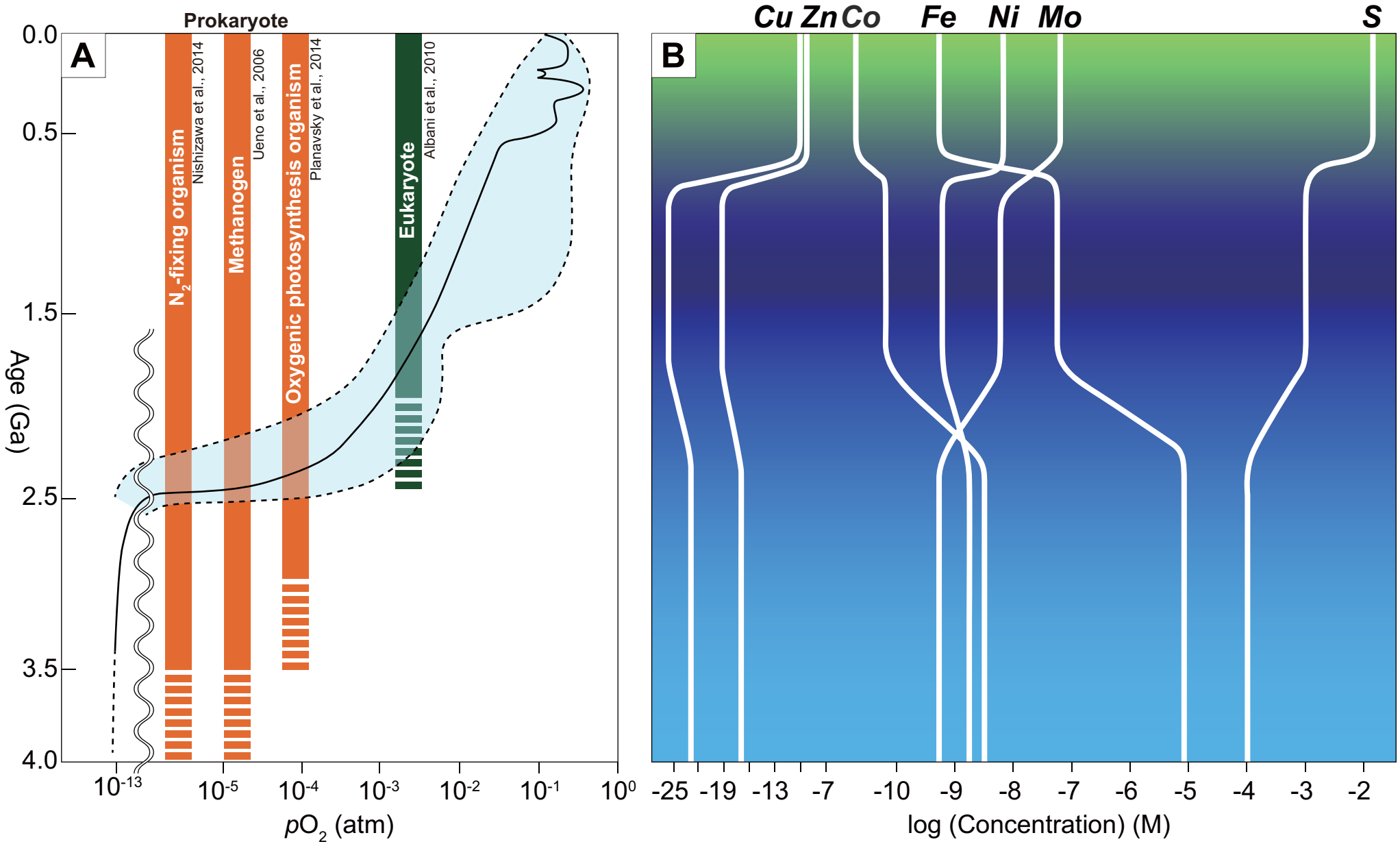
A
Prokaryote
N_2-fixing organism
Nishizawa et al., 2014
Methanogen
Ueno et al., 2006
Oxygenic photosynthesis organism
Planavsky et al., 2014
Eukaryote
Albani et al., 2010
Age (Ga)
0.0
0.5
1.5
2.5
3.5
4.0
10^{-13}
10^{-5}
10^{-4}
10^{-3}
10^{-2}
10^{-1}
10^{0}
pO_2 (atm)
B
Cu Zn Co Fe Ni Mo S
-25 -19 -13 -7 -10 -9 -8 -7 -6 -5 -4 -3 -2
log (Concentration) (M)

Figure. 1

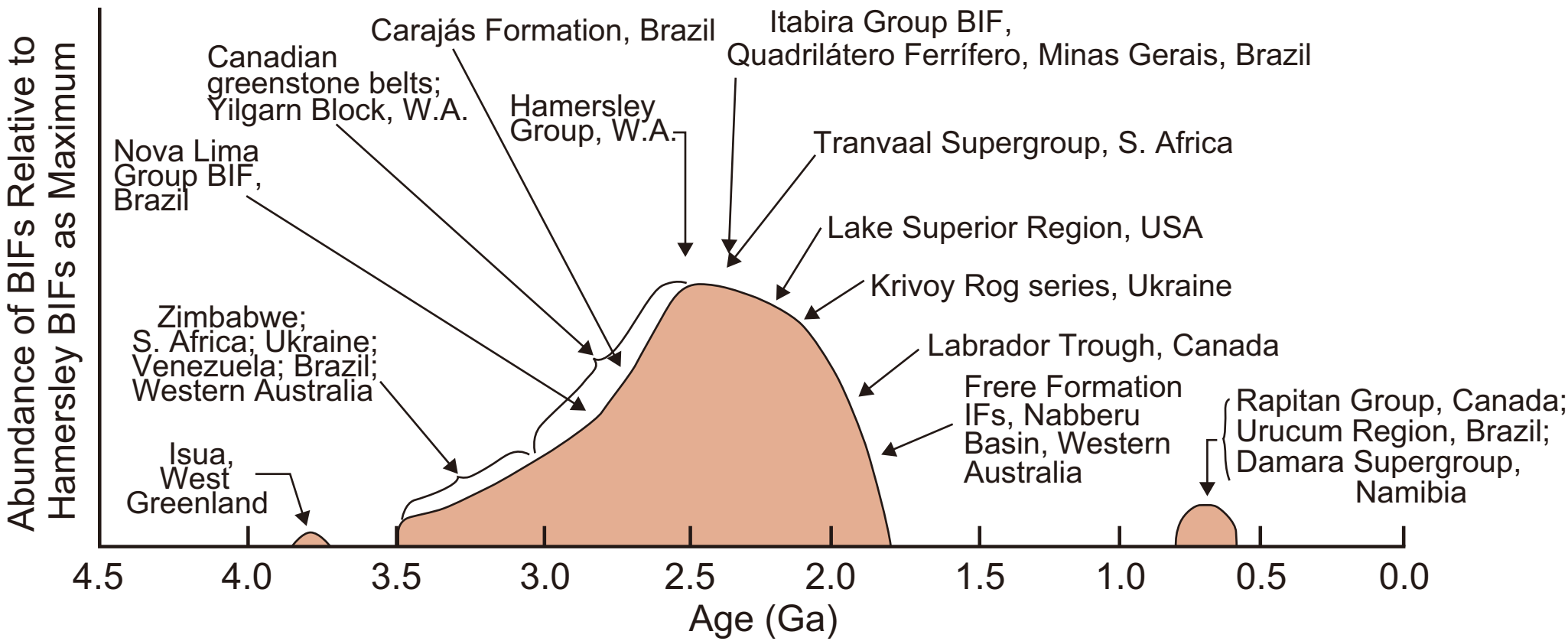
Abundance of BIFs Relative to Hamersley BIFs as Maximum
Carajás Formation, Brazil
Itabira Group BIF, Quadrilátero Ferrífero, Minas Gerais, Brazil
Canadian greenstone belts; Yilgarn Block, W.A.
Hamersley Group, W.A.
Tranvaal Supergroup, S. Africa
Nova Lima Group BIF, Brazil
Lake Superior Region, USA
Krivoy Rog series, Ukraine
Zimbabwe; S. Africa; Ukraine; Venezuela; Brazil; Western Australia
Labrador Trough, Canada
Frere Formation IFs, Nabberu Basin, Western Australia
Rapitan Group, Canada; Urucum Region, Brazil; Damara Supergroup, Namibia
Isua, West Greenland
4.5
4.0
3.5
3.0
2.5
2.0
1.5
1.0
0.5
0.0
Age (Ga)

Figure. 2

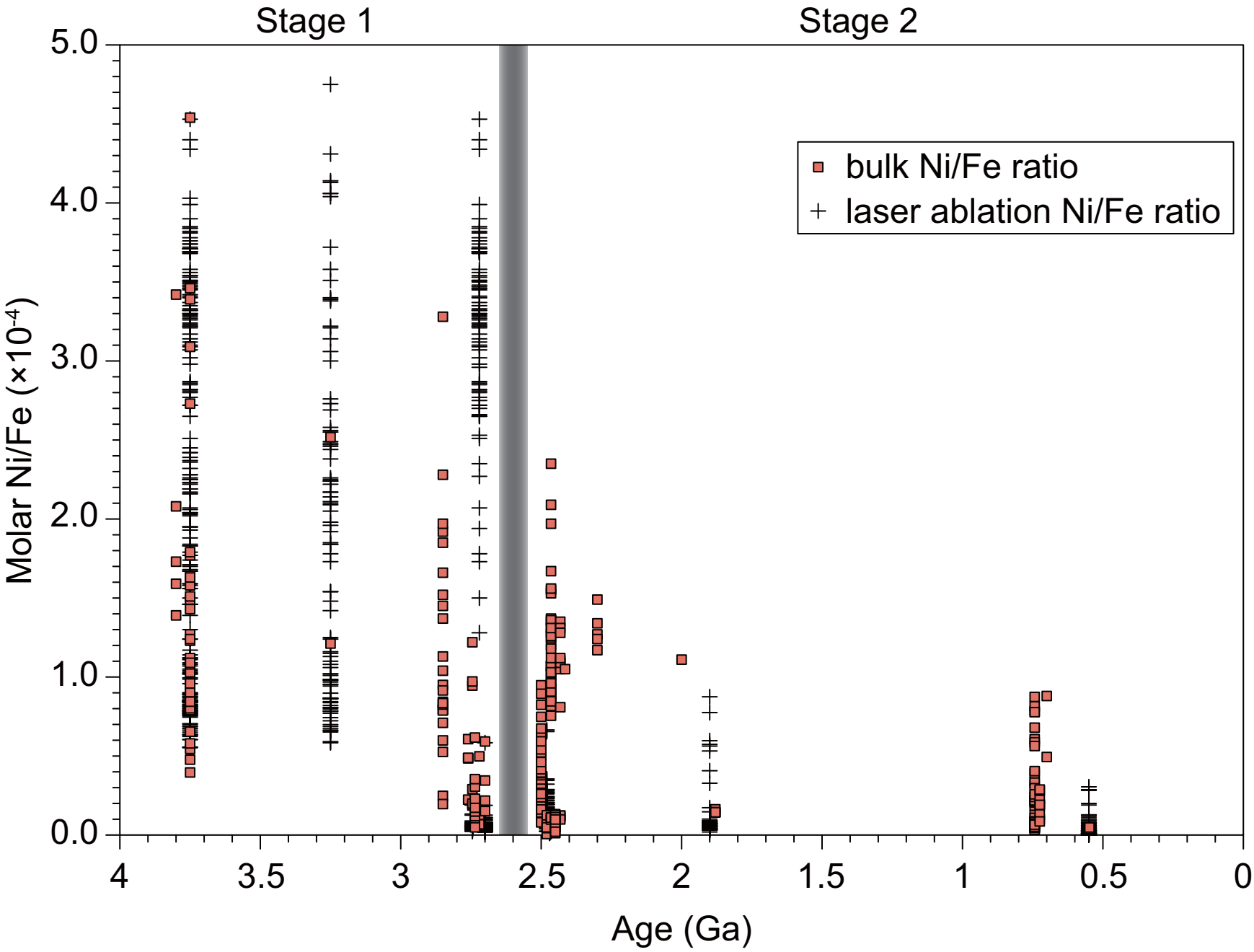
Stage 1
Stage 2
bulk Ni/Fe ratio
laser ablation Ni/Fe ratio
Molar Ni/Fe (×10-4)
Age (Ga)
5.0
4.0
3.0
2.0
1.0
0.0
4
3.5
3
2.5
2
1.5
1
0.5
0

Figure. 3

Chapter II.

Influence of contamination on banded iron formations in the Isua supracrustal belt, West Greenland: Estimate of the Eoarchean seawater compositions

Abstract

Banded Iron Formations (BIFs) are chemical sediments, ubiquitously distributed in the Precambrian supracrustal belts; thus their trace element compositions are helpful for deciphering geochemical evolution on the earth through the time. However, it is necessary to elucidate factors controlling the whole-rock compositions in order to decode the ancient seawater compositions because their compositions are highly variable.

I analyzed major and trace element contents of the BIFs in the 3.8-3.7 Ga Isua supracrustal belt (ISB), southern West Greenland. The BIFs are petrographically classified into four types: Black-, Gray-, Green- and White-types, respectively. The Green-type BIFs contain more amphiboles, and are significantly enriched in Co, Ni, Cu, Zn, Y, heavy rare earth element (HREE) and U contents. However, their bulk compositions are not suitable for estimate of seawater composition because the enrichment was caused by secondary mobility of metamorphic Mg, Ca and Si-rich fluid, involvement of carbonate minerals and silicate minerals of olivine and pyroxene and/or later silicification or contamination of volcanic and clastic materials. The White-type BIFs are predominant in quartz, and have lower transition element and REE contents. The Gray-type BIFs contain both quartz and magnetite. The Black-type BIFs are dominated by magnetite, and contain moderate to high transition element and REE contents. But,

positive correlations of V, Ni, Zn and U contents with Zr contents suggest that involvement of detrital, volcanic and exhalative materials influences on their contents. The evidence for significant influence of the materials on the transition element contents such as Ni in the BIFs indicates the transition element contents in the Archean ocean were much lower than previously estimated. I reconstructed secular variations of V, Co, Zn and U contents of BIFs through the time, which show Ni and Co contents decreased whereas V, Zn and U contents increased through the time. Especially, the Ni and Co contents drastically decreased in the Mesoarchean rather than around the Great Oxidation Event. On the other hand, the V, Zn and U contents progressively increased from the Mesoarchean to the Proterozoic.

Stratigraphical trends of the BIFs show increase in Y/Ho ratios and decrease in positive Eu anomaly upwards, respectively. The stratigraphic changes indicate that a ratio of hydrothermal fluid to seawater component gradually decrease through the deposition, and support the Eoarchean plate tectonics, analogous to their stratigraphic variations of seafloor metalliferous sediments at present and in the Mesoarchean.

1. Introduction

Coevolution of the surface environment and life through the time is one of the most significant features of the earth. Decoding of ocean chemistry in the early Earth is a key issue to understand the origin and evolution of life, but it is difficult to directly estimate the composition because ancient seawater cannot be preserved. The geochemistry of banded iron formations (BIFs) provides one of the powerful proxies to estimate the ancient seawater because they ubiquitously occur in the Archean, and contain high abundances of transitional metals and rare earth elements (REEs). Their REE + Y patterns and trace element compositions (e.g. Ni, Cr, Co and U) are considered to be related with contemporaneous ocean chemistry (e.g. Bau and Dulski, 1996; Bau and Dulski, 1999; Bjerrum and Canfield, 2002; Bolhar et al., 2004; Konhauser et al., 2009; Konhauser et al., 2011; Partin et al., 2013; Swanner et al., 2014). Konhauser and his colleagues showed that the Archean BIFs have higher Ni/Fe ratios than post-Archean BIFs and iron-oxide deposits, and suggested that the Archean seawater was more enriched in Ni contents due to higher hydrothermal Ni influx from komatiites to ocean, resulting in prosperity of methanogens because Ni is an essential element to form Cofactor F430 (Konhauser et al., 2009; Mloszewska et al., 2012; Mloszewska et al., 2013; Pecoits et al., 2009), which act as the enzyme catalyzing the release of methane in

the final step of methanogenesis. However, the estimate is still controversial because the compiled Ni/Fe ratios of the BIFs are highly variable even in a single BIF sequence and because their chemical compositions are dependent on not only seawater composition but also various factors such as sedimentary rates (Kato et al., 1998; Kato et al., 2002), involvement of clastic and volcanic materials (Bau, 1993 Manikyamba et al., 1993; Pecoits et al., 2009; Frei and Polat, 2007; Viehmann et al., 2015a, b), secondary movement accompanied with metamorphism (Bau, 1993; Viehmann et al., 2015a, b) and kinetic of adsorption rates of the elements on the iron oxyhydroxides (Kato et al., 1998; Kato et al., 2002), other interference elements (Konhauser et al., 2009), and so on.

In general, the BIFs contain not only iron oxides (hematite and magnetite) and silica minerals (quartz), which are transformed from amorphous ferrihydrite and silica precipitated from seawater, but also carbonate and silicate minerals (Klein, 2005). The carbonate minerals are precipitated minerals from seawater or diagenetic minerals, and silicate minerals possibly originate from carbonate minerals precipitated from seawater, secondary minerals formed during diagenesis, metamorphism and alteration, and clastic and volcanic material. As a result, the whole-rock trace element compositions are dependent on not only compositions of the iron oxides and quartz but also those of other minerals. The most predominant minerals of the other silicate minerals are Mg- and

Ca-bearing minerals such as amphibole and carbonate minerals (Dymek and Klein, 1988; Mloszewska et al., 2012; Mloszewska et al., 2013). They have high REE and transition element contents but the effects of the involvement of the Mg- and Ca-bearing minerals on the whole rock compositions have not been fully evaluated yet.

The second component is derived from clastic and volcanic materials. They consist of clastic minerals such as detrital minerals of zircon, aluminosilicate minerals and quartz, aeolian dusts, and volcanic exhalative materials of tiny insoluble grains or colloidal particles. Some previous studies tried eliminating contamination of the clastic materials based on arbitrarily determined threshold values of some detritus-loving elements such as Al, Ti, Sc, Rb, Y, Zr, Hf and Th (e.g. Konhauser et al., 2009; Partin et al., 2013). However, even insignificant contaminations of clastic materials resulted in significant influence on the REE and transitional element compositions of the BIFs because they are much more abundant in clastic and exhalative materials relative to pure chemical sediments (Bolhar et al., 2004; Viehmann et al., 2015a, b), and are more abundant than the index elements of Zr, Y and Hf in most clastic and volcanic materials except for zircon. Therefore, it is necessary to more strictly eliminate the contaminations.

The 3.8-3.7 Ga Isua supracrustal belt (ISB) in southern West Greenland contains one of the oldest sedimentary rocks including BIFs and cherts, and have a potential to

estimate the Eoarchean surface environments (Fig. 1). Thus, since early 1980s (Appel, 1980), many geochemical studies for the BIFs have been performed for their trace element compositions (Bolhar et al., 2004; Dymek and Klein, 1988), stable isotope ratios of S (Mojzsis et al., 2003; Whitehouse et al., 2005), Si (André et al., 2006) and Fe (Dauphas et al., 2004; Dauphas et al., 2007; Whitehouse and Fedo, 2007; Yoshiya et al., 2015), Pb isotope systematics (Frei et al., 1999; Frei and Polat, 2007; Moorbath et al., 1973) and Sm-Nd isotope systematics (Frei et al., 1999; Frei and Polat, 2007; Shimizu et al., 1990).

Dymek and Klein (1988) classified the BIFs into quartz-magnetite IF, amphibole-rich magnesian IF, calcite- and dolomite-rich carbonate IF and graphite-, ripidolite- and almandine-rich graphitic and aluminous IF, and analyzed the whole-rock REE compositions. They suggested that they were precipitated from seawater with inputs of high-temperature (> 300 ˚C) hydrothermal fluid because of positive Eu anomalies of the shale-normalized REE+Y patterns. Moreover, they showed that the graphitic and aluminous IFs have higher REE and transition element contents (e.g. Sc, V, Cr, Co, Ni, Cu, Zn, Y, REE and U) than others due to inputs of detrital materials. Bolhar et al. (2004) showed that PAAS-normalized REE + Y patterns of the BIFs share modern seawater-like character such as positive La ($La_{SN}/(3Pr_{SN} - 2Nd_{SN}) > 1$) and Y (Y/Ho > *ca.* 26)

anomalies and low LREE to HREE ratios ($La_{SN}/Yb_{SN} < 1$) with the exception of Eu ($Eu_{SN}/0.67Sm_{SN} + 0.33Tb_{SN}$) and Ce ($Ce_{SN}/(2Pr_{SN} - Nd_{SN})$) anomalies. However, the relationship of the patterns with lithofacies was still ambiguous due to lack of their mineralogical and major element composition data.

This study presents major and trace element contents of the BIFs systematically collected from stratigraphically lower to upper levels in the ISB to estimate the influences of lithofacies and involvement of clastic and volcanic materials on the whole-rock compositions, and to reconstruct evolutions of transition elements of seawater (e.g. V, Co, Ni and U) through the time. Moreover, we estimated the seawater and hydrothermal processes in the Archean oceans, and sedimentary environments of the ISB BIFs based on the relationship between stratigraphy and REE and Y compositions of the BIFs

2. Geological outline and the BIFs descriptions for this study

2.1. Geological outline of the Isua supracrustal belt

The 3.8-3.7 Ga Isua supracrustal belt (ISB) is located at approximately 150 km northeast of Nuuk, southern West Greenland. The southern West Greenland is underlain mainly by the Archean orthogneisses, supracrustal rocks and various types of intrusions, and is subdivide into three terranes: Akia, Akulleq and Tasiusarsuaq terranes from north to south (Fig. 1A). The Akulleq terrane is composed mainly of the Eoarchean Itsaq gneisses (3830-3660 Ma) and old supracrustal rocks (Akilia association), the Paleoarchean mafic intrusions (Ameralik dykes) and the Neoarchean Ikkattoq gneisses (2820 Ma) and young supracrustal rocks (Malene supracrustals) (Friend et al., 1988; McGregor et al., 1991; McGregor, 1993).

The ISB is the largest belt of the Akilia association and forms a 35 km long arcuate tract in the northern end of the Akulleq terrane (Fig. 1A). The ISB comprises 3.8-3.7 Ga volcanic and sedimentary rocks (Crowley et al., 2002; Crowley, 2003; Nutman et al., 1993; Nutman et al., 1996; Nutman et al., 2007; Nutman and Friend, 2009), and it is considered that it occurs as an enclave within the Itsaq Gneiss (Fig. 1B). The ISB is composed mainly of four lithofacies (Komiya et al., 1999): (1) mafic-felsic clastic sedimentary rocks including black shale and minor conglomerate, (2) chemical

sedimentary rocks of BIFs, chert and carbonate rocks, (3) basaltic and basaltic andesitic volcanic rocks including pillow lava, pillow breccia, and related intrusive rocks and (4) ultramafic rocks. They were subsequently intruded by the Paleoarchean Ameralik (Tarssartoq) dykes, and the Proterozoic N-S-trending high-Mg andesite dikes (Nutman, 1986).

Although it was previously considered that the ISB comprises volcano-sedimentary successions, it has, recently, been widely considered that it is composed of some tectonic slices bounded by faults (Appel et al., 1998; Komiya et al., 1999; Myers, 2001; Nutman, 1986; Nutman and Friend, 2009; Rollinson, 2002; Rollinson, 2003). But, the origins of the tectonic slices are controversial, and two ideas were mainly proposed: collision and amalgamation of allochthonous terranes and peeling and accretion of oceanic crusts during successive accretion of oceanic crusts, respectively (e.g. Komiya et al., 1999; Nutman and Friend, 2009). The former is that the slices or panels were formed after the intrusions of the granitic rocks, due to collision and amalgamation of some terranes with different geologic histories (e.g. Crowley, 2003; Nutman, 1986; Nutman et al., 1997a; Nutman and Friend, 2009; Rollinson, 2002; Rollinson, 2003). Especially, Nutman and the colleagues proposed that the ISB comprises two tectonic belts with different origins based on age distributions of detrital zircons in quartzite and

felsic sedimentary rocks and orthogneisses intruding into the supracrustal belts (Crowley, 2003; Nutman et al., 1997a; Nutman and Friend, 2009; Nutman et al., 2009). The latter is that the tectonic slices are bounded by layer-parallel faults and were formed during accretion of oceanic materials to a continental crust (Komiya et al., 1999).

The tectonic setting of the ISB is still controversial. Furnes and the colleagues showed an ophiolite-like stratigraphy including pillow lavas and sheeted dykes and estimated that they were formed in the intra-oceanic island arc or mid-oceanic ridge settings based on the geological occurrence and geochemistry of the greenstones (Furnes et al., 2007; Furnes et al., 2009). On the other hand, some groups suggested that the ISB was formed in a subduction zone environment because the greenstones share geochemical signatures with the modern boninites and island arc basalts (Dilek and Polat, 2008; Polat et al., 2002; Polat and Hofmann, 2003; Polat and Frei, 2005; Polat et al., 2015). In the case, the BIFs were formed in spreading fore-arc and intra-arc settings associated with trench rollback caused by young and hot oceanic crust (Dilek and Polat, 2008; Polat and Frei, 2005; Polat et al., 2015). Komiya and colleagues proposed that the depositional environment ranged from basaltic volcanism at a mid-oceanic ridge through deposition of deep-sea sediments (BIFs/chert) in an open sea to terrigenous sedimentation at the

subduction zone based on the OPS-like stratigraphy (Komiya et al., 1999; Komiya et al., 2015; Yoshiya et al., 2015).

The ISB suffered polyphase metamorphism from greenschist to amphibolite facies (Arai et al., 2015; Hayashi et al., 2000; Komiya et al., 2002; Myers, 2001; Nutman et al., 1984; Nutman, 1986; Rollinson, 2002; Rollinson, 2003; Rose et al., 1996; Rosing et al., 1996). Although it is still controversial whether the variation of mineral parageneses and compositions is due to progressive or retrogressive metamorphism (Nutman, 1986 #10), the variation of mineral parageneses and compositions of mafic and pelitic rocks in the northeastern area of the ISB suggested the progressive metamorphic zonation from greenschist (Zone A) through albite-epidote-amphibolite (Zone B) to amphibolite facies (Zones C and D). The metamorphic pressures and temperatures were estimated 5-7 kbar and 380-550 ˚C in Zones B to D by garnet-hornblende-plagioclase-quartz and garnet-biotite geothermobarometries (Arai et al., 2015; Hayashi et al., 2000; Komiya et al., 2002).

2.2. Geological characteristics of the BIFs

The BIFs and cherts occur as some layers throughout the ISB (Allaart, 1976; Komiya et al., 1999; Nutman, 1986; Nutman et al., 1996; Nutman et al., 1997b; Nutman

et al., 2002; Nutman and Friend, 2009). I studied the BIFs in the northeastern part of the ISB, corresponding to the metamorphic Zone A (Hayashi et al., 2000) (Fig. 1B, 2A). In this area, the supracrustal rocks have NE-trending strikes with E-dipping, and the stratigraphy of supracrustal rocks in each subunit is composed of pillow lava or massive lava greenstones overlain by BIFs and cherts. The BIFs, *ca.* 9 m thick, show mappable-scale syncline structures with underlying pillow lava and hyaloclastite-like greenstones (Fig. 2A, B, C). In this study, I analyzed the BIF samples from the bottom on the hyaloclastite-like greenstones to the top in one-side limb of the syncline structures.

2.3. Lithological characteristics of the BIFs for this study

The studied BIFs have sharply-bounded bands with several to tens millimeter thickness. The bands are varied in color even within an outcrop: black, white, gray and green in color, dependent on mineral assemblages but independent of their stratigraphy (Fig. 3). Mineral assemblages of the BIFs are composed mainly of magnetite + quartz + amphibole (Fig. 4), which are typical mineral assemblage of the moderately metamorphosed BIFs (Klein, 2005), but the modal abundances of the constituent minerals are varied so that their colors are variable.

The black bands are composed mainly of euhedral and anhedral magnetite. They are elongated in the direction parallel to their banding structure. Quartz, actinolitic amphiboles and ripidolitic chlorites are scattered among magnetites (Fig. 4A).

The white and gray bands are composed mainly of quartz, most of which show sutured grains boundary or wavy extinction suggestive of secondary deformation. Magnetites, amphiboles and subordinate amount of calcites ubiquitously occur among the quartz grains or as inclusions within the quartz grains (Fig. 4B). The gray-colored bands are enriched in magnetite as inclusions within quartz matrix relative to the white bands (Fig. 4B). Moreover, most of the bands are interbedded with thin nematoblastic amphibole (Fig. 4C), calcite (Fig. 4D) and magnetite layers.

The green bands consist mainly of alternating actinolite- and quartz-rich layers (Fig. 4E), and the amphiboles show a nematoblastic texture, forming the bands. Anhedral magnetites are scattered as inclusions within the amphibole and quartz. Calcites rarely occur as inclusions within amphiboles.

3. Analytical methods

I analyzed whole rock compositions of the BIFs from the bottom to the top of the BIF succession (Fig. 2C). The rocks samples were slabbed with a diamond-bladed rock saw to avoid visible altered parts and veins of quartz. Each rock piece consists of some mesobands with different colors, but was classified into four groups based on the colors of dominant bands: Black, White, Gray and Green-types, respectively. They were polished with a grinder for removing saw marks, and rinsed in an ultrasonic bath. They were crushed into small pieces with a hammer wrapped with plastic bags, and ground into powders by an agate mortar.

Major element compositions of the 36 samples were determined with an X-ray fluorescence spectrometry, RIGAKU 3270 (Rigaku Corp., Japan) at the Ocean Research Institute, the University of Tokyo. The analytical reproducibilities are better than 1.0 % for SiO_2, TiO_2, Al_2O_3, Fe_2O_3, MgO, CaO and K_2O, 1.2 % for P_2O_5, 1.4 % for MnO, and 1.6% for Na_2O, respectively. The details of XRF analytical procedure were described elsewhere (Kato et al., 1998).

Trace element compositions were determined by a Q-pole mass filter ICP mass spectrometer, iCAP Qc (Thermo Fisher Scientific Inc., USA) with a collision cell at the Kyoto University. The same rock powders as those for major-element analysis were

completely digested with 1 ml HF and 1 ml $HClO_4$ in a tightly sealed 7 ml Teflon PFA screw-cap beaker, heated at 120 ˚C during 12 hours with several sonication steps, and then evaporated at 120 ˚C for 12 hours, 165 ˚C for 12 hours and 195 ˚C for complete dry. The residues were repeatedly digested with 1 ml $HClO_4$ for removing fluoride, completely evaporated again, dissolved with 1 ml HCl and evaporated at 100 ˚C. The dried residues were digested and diluted in mixtures of 0.5 M HNO_3 and trace HF. Before analyses, indium and bismuth solutions were added for internal standards. As the external calibration standard, W-2, issued by USGS, was analyzed every two unknown samples. The preferred values of W-2 by Eggins et al. (Eggins et al., 1997), except for Tm (Dulski, 2001) were adopted. On the ICP-MS analysis, He + H_2 collision gas was introduced in order to eliminate molecular interferences, resulting in low oxide formation (CeO^+/Ce^+ < ~0.5%). The reproducibility and accuracies of the analytical protocol were verified with a USGS standard of BIR-1. The reproducibilities (RSD) were under than 5% (2sd) except for Li and Th (Supplementary Table 1). The REE and Y concentrations were normalized by PAAS (Post-Archean Australian Shale, Taylor and McLennan, 1985), and La, Ce and Eu anomalies, La/La*, Ce/Ce* and Eu/Eu*, were defined by $[La_{SN}/\{Pr_{SN}/(Pr_{SN}/Nd_{SN})^2\}]$, $[Ce_{SN}/\{Pr_{SN}/(Pr_{SN}/Nd_{SN})\}]$ and $[Eu_{SN}/(0.67Sm_{SN}+0.33Tb_{SN})]$.

4. Results

4.1. Major element abundances

Major element compositions of all analyzed samples are listed in Table 1. The BIFs are composed mainly of Fe_2O_3 and SiO_2 (Fig. 5A), similar to compositions of quartz-magnetite IFs (Dymek and Klein, 1988). The Black-type is enriched in Fe_2O_3 whereas the White-type in SiO_2 contents. The Gray- and Green-types have the intermediate compositions between the Black- and White-types on the Fe_2O_3 vs. SiO_2 diagram. The Green-type are off the SiO_2-Fe_2O_3 line because they contains more abundant other elements such as MgO (1-7%) and CaO contents (2-6%) (Fig. 5) so that they are similar to magnesian and carbonate IF (Dymek and Klein, 1988). All the types apparently lack Na_2O and K_2O contents, but contain trace amounts of P_2O_5. Most samples except for 60B and 150B have quite low Al_2O_3 contents, <1%.

4.2. Trace element abundances

Trace element compositions are also listed in Table 1. Fe_2O_3 variation diagrams of Y, Pr, Sm, Yb, Sc, V, Co, Ni, Cu, Zn, Rb, Sr, Ba, Zr, Hf, Th and U contents are shown in Figure 6. Although the Black-type BIFs have large variations in the trace element contents, they have higher maximum values than other types, except for some elements of

the Green-type. The Green-type BIFs are enriched in most REEs, transition elements of Co, Ni, Cu, Zn and U, and high field strength elements (HFSEs) of Zr, Hf and Th. The element contents of the White, Gray and Black-types increase with increasing iron contents except for Sr and Ba (Fig. 6). Some White- and Gray-types are extremely enriched in Sr (e.g. 179R) and Ba (e.g. 168R, 170R, 179R and 26GRY) relative to other samples (Fig. 6).

The PAAS-normalized REE+Y patterns of the Black-, White-, Gray- and Green-types are shown in Figure 7. All of them share some geochemical features: positive La anomalies (La/La* > 1), positive Eu anomalies (Eu/Eu* > 1), positive Y anomalies (Y/Ho > 26), and lack to slightly positive Ce anomalies (1 <Ce/Ce* <1.5) except for one sample (292W). Most of the Black-type BIFs except for three samples of 45B, 150B and 177B ($0.15 < Pr_{SN}/Yb_{SN} < 0.23$) display flat to slightly LREE-enriched REE+Y patterns ($0.30 < Pr_{SN}/Yb_{SN} < 0.99$) whereas the White- and Gray-type BIFs show flat to LREE-depleted REE+Y patterns ($0.07 < Pr_{SN}/Yb_{SN} < 0.39$) (Fig. 7). The REE+Y patterns of the Green-type is highly variable, and different from others in some characteristics. Most of them have much higher REE contents than others, and strongly HREE-enriched REE+Y patterns ($0.03 < Pr_{SN}/Yb_{SN} < 0.29$) (Fig. 7D).

5. Discussion

5.1. The relationship between the whole-rock trace element contents and lithofacies

The BIFs consist mainly of quartz and iron oxide minerals of hematite and magnetite. Because the quartz-rich BIFs and cherts have lower REE and transition metal contents, amounts of quartz apparently dilute their contents. And, the precursors of the iron-oxide minerals probably hosted the elements because the REE and transition metal contents basically increase with the iron contents, analogous to modern iron oxyhydroxides (German and Von Damm, 2003). However, all of the REE and transition elements, in fact, are not hosted by only the iron oxide minerals because the BIFs contain Ca- and Mg-bearing minerals as well as innegligible Zr and Al_2O_3 contents (Klein, 2005). The REEs, some transition elements of Co, Ni, Cu and Zn, alkaline earth metals of Sr and Ba, and HFSEs of Zr, Hf, U and Th are more abundant in Green-BIFs, and some White- and Gray-type BIFs than the Black-type BIFs at given Fe_2O_3 contents on their Fe_2O_3 variation diagrams and ternary plots (Fig. 6, 8). The overabundance indicates that minerals rather than the iron oxides, which are abundant in the Green-, White- and Gray-type BIFs, also contain the elements. All of the BIFs in the ISB contain amphiboles, and especially the Green-type BIFs contain more amphiboles (Fig. 4F), consistent with higher Mg and Ca contents (Fig. 5, 8). Because amphiboles, generally speaking, can host

various elements except for HFSEs (e.g. Taylor and McLennan, 1985), the enrichment of some trace elements in the Mg and Ca-rich BIFs of Green-type BIFs and some of White- and Gray-type BIFs are possibly due to the enrichment of amphiboles. The enrichment of those elements in amphibole-rich BIFs could be explained by two contrasting possibilities that Mg and Ca moved through metamorphic fluid during the metamorphism, or that Mg and Ca-bearing materials such as silicates, carbonate and exhalative materials were involved during the deposition.

Firstly, I consider the possibility of metasomatism by Mg, Ca and Si-rich metamorphic fluid into the BIFs. Because the metamorphism fluid, generally speaking, is more enriched in LREE (Bau, 1993, Viehmann et al., 2015b), the Green-type BIFs should be more enriched in LREE than the Black-type BIFs. However, the involvement of metamorphic fluid is not consistent with the REE patterns because the formers have LREE-depleted REE patterns (Fig. 7).

Alternatively, I consider that the enrichment of those elements is due to involvement of carbonate minerals, silicate minerals, volcanic and detrital materials, from which the amphiboles were subsequently formed during the metamorphism. Although the involvement of calcite with/without dolomite does not result in amphibole formation under the greenschist facies condition, amphibole and calcite are formed through the

reaction of quartz and dolomite, dependent on the XCO_2, under the amphibolite facies condition (Spear, 1993). On the other hand, contamination of volcanic and clastic materials with a higher ratio of MgO to CaO leads to formation of amphibole under even the greenschist facies condition (Spear, 1993). Because they have shale-normalized LREE-depleted REE patterns, the contamination results in depletion of LREE in the BIFs, consistent with those of the Green-type BIFs (Fig. 7).

Despite of the cause of amphibole formation, the occurrence of the amphibole is not in favor of estimate of ancient seawater composition because the BIFs contain any materials besides iron oxyhydroxide.

A previous work used not only quartz-magnetite IFs but also magnesian IFs with a lot of amphiboles to estimate compositions of the Eoarchean seawater, and their BIF sample with the highest Ni/Fe ratio is the magnesian IF (10-2A, Konhauser et al., 2009; Dymek and Klein, 1988). If the contaminants are not clastic or volcanic detritus but silicate minerals of olivine and pyroxene, the contamination increases Ni contents but not Zr and Al_2O_3 contents because they do not contain Zr and Al_2O_3. Figure 8F shows that Mg- and Ca-rich IFs are enriched in Ni relative to the iron-rich IFs. Because of significant influence of the Mg- and Ca-rich phases on whole rock compositions, only

White-, Gray- and Black-type BIFs with low Mg and Ca contents ((MgO+CaO)/Fe_2O_3 < 0.1) are considered hereafter.

5.2. Influence of involvement of clastic and volcanic materials on whole-rock trace element contents

5.2.1. Influence of their involvement on REE + Y and transitional element contents

Contamination of clastic and volcanic materials of silicate minerals, volcanic ashes and glass, and exhalative insoluble materials significantly disturbs seawater signatures of BIFs because the contaminants usually have higher REE, LILE, HFSE, and transition element contents (e.g. Bau, 1993). Generally speaking, Al^{3+}, Ti^{4+}, and HFSE are insoluble in aqueous solution (e.g. Andrews et al., 2004; Martin and Whitfield, 1983) and concentrated in clay minerals, weathering-resistant minerals such as zircon and some aluminous and titaniferous phases, REE-bearing minerals of monazite and apatite, volcanic glass and exhalative insoluble materials so that their abundances are often used as criteria for their involvement (e.g. Bau, 1993).

Previous works assumed the influence of involvement of clastic and volcanic materials on REE contents is negligible because Zr contents in their BIF samples are low, up to *ca.* 4.2 ppm (Bolhar et al., 2004), 10.2 ppm (Frei and Polat, 2007), *ca.* 2.2 (Friend et

al., 2008) and 3.1 ppm (Nutman et al., 2010). But, figure 9G displays that La contents are positively correlated with Zr contents even for Black- and White-type BIFs except for two Black-type BIFs (60B, 150B), and indicates that the LREE contents are influenced by the contaminants. The samples of 60B and 150B have relatively high Al_2O_3 (> 1%) and HFSE (Zr > 2 ppm) contents. And their Pr, V and Ni contents are lower than others at a given Zr content but are higher than the minimum value of the Black-type BIFs at the low Zr content (Fig. 9A, C, G). The feature indicates that the samples are also influenced by the contamination but the contaminants have different compositions with high Al_2O_3, HFSE and U contents from others. Similar observation was previously reported by Frei and Polat (2007), who mentioned that highly LREE-enriched BIFs have higher Rb contents possibly due to contamination of detrital clay minerals. Some of our samples also have higher Rb contents than 2 ppm so that the samples with high Rb contents are eliminated possibly due to the involvement of clay minerals hereafter.

On the other hand, MREE and HREE contents are not well correlated with Zr contents, especially for the Black-type BIFs (Fig. 9H, I), suggesting that the contaminants have relatively low MREE and HREE contents. It is well known that Y and Ho, which share trivalent oxidation state and similar ionic radii, are not fractionated in magmatic systems, but Ho is preferentially scavenged by suspended particles relative to Y in

aqueous systems. As a result, volcanic and clastic materials have almost chondritic values (*ca.* 26) whereas seawater and associated chemical sediments have superchondritic Y/Ho ratios (e.g. Alibo and Nozaki, 1999; Bau, 1996; Bolhar et al., 2005; Nozaki et al., 1997). Contamination of clastic and volcanic materials depresses the Y/Ho ratios of chemical sediments, but all of our studied BIFs have higher Y/Ho ratios than the chondritic value, and lack a negative correlation between Zr content and Y/Ho ratios (Fig. 9K). The characteristics suggest that the influence of the contamination on the elements was insignificant for the Black-type BIFs.

5.2.2. Estimate of Ni, U and other transitional elements of contamination-free BIFs

Konhauser and his colleagues suggested that the Archean ocean was enriched in Ni contents probably due to higher influx of hydrothermal fluids from Ni-rich komatiites because of higher Ni/Fe ratios of the Archean BIFs from 3.8 to 2.7 Ga, and proposed that the high Ni contents resulted in prosperity of methanogens with a Ni-bearing key enzyme and depression of activity of oxygen-producing bacteria (Konhauser et al., 2009; Mloszewska et al., 2012; Mloszewska et al., 2013; Pecoits et al., 2009). Konhauser et al. (2009) selected the BIFs with the low Ti, Zr, Th, Hf and Sc contents (< 20 ppm) and Al contents (Al_2O_3 < 1%) to avoid the contamination of clastic materials. But, the transition

element contents in the ISB BIFs, in fact, increase with the contaminations by the clastic and volcanic materials because “aluminous-graphitic IFs” with alumino-silicate minerals have higher contents of Al (0.57% < Al_2O_3 < 12.4%), HFSE (4.2ppm < Zr < 94.7ppm) and transitional elements (68.7ppm < Ni < 230.3ppm) relative to “quartz-magnetite IFs” (0.05% < Al_2O_3 < 2.66%, Zr < 21.9ppm, 10.8ppm < Ni < 48.6ppm) (Dymek and Klein, 1988). In addition, this study shows that even low-Zr content (< 2 ppm) samples have a positive correlation between Zr and Ni contents (Fig. 9C), and that the BIFs with higher Ca and Mg contents have the higher Ni/Fe ratios, as mentioned above. The facts indicate that the contamination more significantly influences on Ni contents of the BIFs than previously expected so that it is necessary to avoid the influence for estimate of ancient seawater composition. The Ni content of contamination-free BIFs can be ideally calculated from an intercept of a compositional variation of Ni contents on a Zr variation diagram, analogous to the modern iron oxyhydroxide (Sherrell et al., 1999). However, it is difficult to exactly determine another end-member(s) of the compositional variation, namely contaminant(s) because the compositional variation is more scattered at higher Zr contents. Therefore, I employed two methods to calculate the intercept. Firstly, assuming that the contaminant has only one component, the intercept was calculated from a regression line of all data of the Black-type BIFs with low Rb contents (< 2 ppm) and

magnetite-IFs with high iron contents (Fe_2O_3 > 60%, Frei & Polat, 2007) to obtain 18±12 ppm (Fig. 10A). Similar positive correlations are shown in younger BIFs. In the same way, the intercepts can be calculated to be 4.8±13, 0.83±1.4, 1.2±1.4 and 0.028±2.8 ppm for the 2.9, 2.7, 2.4 and 0.7 Ga BIFs, respectively (Fig. 10B, C, D). Secondly, the intercept was estimated from some regression lines covering all data of the Black-type BIFs and magnetite-IFs because the contaminants do not have only one composition but varied compositions, as mentioned above (Fig. 10A). The intercepts range from 18 to 22 for the ISB as well as from 4.5 to 7, from 0.36 to 2.8, from 0.16 to 1.6 and from 0.24 to 1.2 for the 2.9, 2.7, 2.4 and 0.7 Ga BIFs, respectively (Fig. 10B, C, D, E). Because the contaminants are highly varied, for example silicate minerals of olivine and pyroxene, clastic, volcanic, ultramafic and exhalative materials, carbonate minerals and clay minerals, it is considered that the latter method can obtain the compositions of contamination-free BIFs more accurately.

The uranium content of the contamination-free BIF can be also estimated from the Zr vs. U content diagram, analogous to the Ni contents of the contamination-free BIFs. A positive correlation of U contents with Zr contents for the Isua BIFs also indicate contamination-free BIFs have less uranium contents, and the U content is estimated to be from 0.0061 to 0.024 by the second method (Fig. 9J, 11A). Partin et al. (2013) excluded

BIF samples in the ISB and Nuvvuagittuq Supracrustal Belt (NSB) from their compilation because they considered that severely metamorphosed rocks less likely preserve a seawater signature of uranium content possibly due to late remobilization of uranium. In fact, some of them have significantly high U contents, up to 0.79 and 23.4 ppm for ISB and NSB, repetitively. But, the BIFs also show positive correlations of U contents with Al_2O_3 contents, and the minimum values are 0.04 and 0.02 ppm at the lowest Al_2O_3 contents for the ISB and NSB, respectively, so that the apparent high uranium contents can be explained by involvement of U-bearing contaminants. On the other hand, the U contents of contamination-free BIFs with low MgO and CaO contents ((CaO+MgO)/FeO < 0.1)) were estimated to be from 0.037 to 0.06, from 0.012 to 0.050, from 0.030 to 0.083 and from 0.025 to 0.07 ppm for 2.9, 2.7, 2.4 and 0.7 Ga BIFs based on the correlations of U contents with Zr contents, respectively (Fig. 11B, C, D).

Similarly, the vanadium contents of the BIFs are also correlated with Zr contents so that the variation is at least partially due to the involvement of the clastic and volcanic materials (Fig. 9A). The V contents of contamination-free BIFs are estimated to range from 0.88 to 1.2 ppm for the ISB BIFs, from 0.84 to 2.7 ppm at 2.4 Ga and from 8.0 to 9.1 ppm at 0.7 Ga, respectively (Fig. 12).

Zinc also displays a positive correlation with Zr contents for the Black-type BIFs, and the Zn contents of the contamination-free BIFs are estimated to be from 0 to 2 ppm at *ca.* 3.8 Ga, and from 0.8 to 7 ppm at 2.4 Ga at 0 ppm in Zr contents (Fig. 13). Cobalt contents in the Black-type BIFs with low Rb contents (< 2 ppm) and magnetite-IF (Fe_2O_3 > 60%) also form a positive correlation against Zr contents so that I can estimate the Co content of a contamination-free BIF from 0.34 to 1.8 ppm (Fig. 14). In the same way, the Co contents are estimated to be from 0.41 to 1 ppm, from 0.046 to 0.15 ppm and from 0 to 0.2 ppm at 2.9, 2.7 and 0.7 Ga, respectively (Fig. 14).

The secular changes of the vanadium, zinc and cobalt contents of contamination-free BIFs show the vanadium and zinc contents increased whereas the cobalt content through the time (Fig. 15B, C).

Other transition elements such as copper show no clear positive correlations with Zr contents (Fig. 9D), suggesting that minimal effects of the clastic and volcanic contaminations or highly variable compositions in the contaminants. The copper contents of the BIFs are highly scattered from 1.3 to 5.7 even for the Black-type BIFs (Fig. 9D). Although the Isua BIFs have low modal abundances of sulfide minerals, a few sulfide grains are found in some Isua BIFs (e.g. Dauphas et al., 2007; Mojzsis et al., 2003; Yoshiya et al., 2015). The scattering is possibly due to involvement of sulfides into the

BIFs for the enrichment or early deposition of the sulfide around hydrothermal vents, analogous to modern ferruginous sediments for depletion (German and Von Damm, 2003), respectively.

5.2.3. Trace element compositions of cherts and interference of silica adsorption in the transient element contents in the BIF

The amounts of Ni adsorbed on iron oxyhydroxide depend on not only Ni contents of seawater but also other compositions like Si contents (e.g. Konhauser et al., 2009). The Ni contents of the BIFs are well correlated with Fe_2O_3 contents because cherts and siliceous BIFs have lower Ni contents due to dilution of silica minerals (Fig. 6C). But, looking closely, there is an obvious gap of the Ni contents between the White- and Black-type BIFs (Fig. 6C, 9C). The gap is more obvious for V contents (Fig. 6A, 9A). Hindrance of adsorption of Ni on the iron-oxyhydroxide by dissolved Si possibly accounts for the obvious Ni-depletion in the cherts and siliceous BIFs. The apparent gap of Ni contents between the White- (siliceous) and Black-type (magnetite-dominant) BIFs suggests that the interference by the dissolved Si are more significant for the precipitation of the White-type BIFs whereas played an insignificant role on the Black-type BIFs possibly because the silica was under-saturated during the deposition of Black-type BIFs

due to higher dissolved iron contents. The characteristics that the gap for V contents on the Fe_2O_3 and Zr variation diagrams are larger than for Ni contents can be explained by the difference in degree of adsorption of Ni and V on iron hydroxide (Hein et al., 2000; Hein et al., 2003; Li, 1981; Li, 1982; Takahashi et al., 2015). The vanadium is more effectively influenced by the interference of silica.

5.3. The evolution of transition element contents of seawater throughout the time

Figure 15 show secular changes of V, Co, Ni, Zn and U contents of contamination-free BIFs through geologic time. The Ni and Co contents decrease whereas the V, Zn and U contents increase through the time. It is widely accepted that methanogen is one of the earliest microbial activity on the earth (e.g. Takai et al., 2006), and possibly played important roles on the surface environment because it is considered that the emergence of the methanogen supplied methane to compensate faint luminosity of the young Sun (Pavlov et al., 2000) and higher activity of the methanogen prevented oxidation of surface environment by oxygen-producing bacteria (Konhauser et al., 2009). Nickel is a bio-essential element for the methanogen because the nickel is held in a heterocyclic ring of an enzyme methyl coenzyme M reductase, Cofactor F430, (Jaun and Thauer, 2007; Ragdale, 2014). Konhauser et al. (2009) showed secular change of Ni

contents of the BIFs through the time, and proposed that methanogen had flourished before the Great Oxidation Event around 2.4 Ga because the seawater was enriched in Ni contents and that depression of methanogen activity due to decrease in the Ni content of seawater resulted in increase of atmospheric oxygen. Figure 15A shows a secular change of Ni contents of contamination-free BIFs through the time. The Archean iron deposits have slightly higher Ni contents than the post-Archean equivalents but much lower than previously estimated (Konhauser et al., 2009). In addition, the Ni contents apparently decreased in the Mesoarchean (*ca*. 2.7 Ga) rather than the Great Oxidation Event, inconsistent with the idea that the decrease in Ni contents of seawater caused the Great Oxidation Event through decline of methanogen activity. If the Ni content of seawater controlled the activity of methanogens, the activity declined from *ca.* 2.9 Ga to 2.7 Ga. Recently, some geochemical evidence suggested that the emergence and prosperity of oxygen-producing bacteria have already occurred around 2.7-3.0 Ga based on REE contents and Ce anomalies of carbonate minerals (Komiya et al., 2008), Fe isotopes of sulfides in carbonate rocks (Nishizawa et al., 2010) and Mo isotopes of the BIFs (Planavsky et al., 2014). The decline of dissolved Ni contents in seawater before 2.7 Ga is possibly related with the emergence of oxygen-producing bacteria.

Uranium has four valences, U^{3+}, U^{4+}, U^{5+} and U^{6+}, and forms an insoluble uranium oxide, uraninite, under reduced condition whereas forms soluble oxoacid and carbonate complexes under the oxic condition. The presence of uraninite in the clastic sedimentary rocks is considered as evidence for anoxic atmosphere until the Late Archean (e.g. Holland, 1994). Partin et al. (2013) compiled molar U/Fe ratios and U contents of the BIFs throughout the Earth history, and showed they increased up to 2.4×10^{-6} and *ca.* 400 ppm around 2.32 Ga in the Great Oxidation Event (GOE). They discussed that delivery of U^{6+} to ocean was increased due to oxidative continental weathering. The secular change of the uranium contents of the BIFs shows the uranium content stated to increase at least in the late Archean (Fig. 15D). The increase is possibly due to abrupt increase of continental growth and oxidative continental weathering because geological, geochemical and geobiological evidence suggests increase in oxygen content of seawater in the Late Archean (Bosak et al., 2009; Eigenbrode et al., 2008; Hayes, 1994; Komiya et al., 2008; Yoshiya et al., 2012). Our reconstructed secular change of uranium contents of BIFs supports U^{4+} oxidation around 2.9 to 2.7 Ga, suggested by lower Th/U ratios in the BIFs than an average continental crust value (Bau and Alexander, 2008).

Vanadium varies from +2 to +5 in the valance, is soluble as various vanadate compounds under oxic condition, and one of bioessential elements for some nitrogen-fixing microorganisms such as Azotobacter, algae and some metazoans of ascidians (e.g. Sigel and Sigel, 1995). Our estimate of secular variation of vanadium contents of BIFs indicates that the vanadium content of BIFs increased in the Late Archean (Fig. 15B), and suggests that dissolved vanadate influx into ocean possibly increased with increasing of oxidative continental weathering, analogous to the U contents. On the other hand, zinc occurs only as a divalent ion in natural environments, and is fixed as sulfide minerals under the sulfidic condition. It is well known that Zn is used for metallopeptidases, metallophosphatases and many other polymerases involved in DNA- and RNA-binding and synthesis (Lipscomb and Sträter, 1996). Our estimate of secular variation of Zn contents shows Zn contents of the BIFs increased in the Late Archean, and suggests that the Zr content of seawater increased since then, similar to the U and V contents (Fig. 15B).

Cobalt has +2 and +3 in the valence, and is also soluble as a divalent ion under the reducing environment, whereas oxidized and fixed as an insoluble trivalent ion by manganese deposits under the oxic condition. Cobalt is also one of the bioessential elements, and, for example, is involved in a vitamin B12 for synthesis of methionine.

Swanner et al. (2014) compiled Co/Ti ratios of the BIFs through the time, and showed that the ratio increased from *ca.* 2.8 to 1.8 Ga. They interpreted that the seawater was enriched in the Co content at that time due to high hydrothermal influx and low Co burial efflux. On the other hand, our result show the Co content decreased though the time (Fig. 15C).

5.4. Correlations of stratigraphy with Y/Ho ratios and Eu anomaly

Figure 16A shows an obvious correlation of Y/Ho ratios of the BIFs with the stratigraphic positions. All of the BIFs have higher Y/Ho ratios than a chondritic value (*ca.* 26), PAAS (*ca.* 27), an Archean mudstone (*ca.* 24, Taylor and McLennan, 1985), modern river waters (*ca.* 38, Nozaki et al., 1997) and modern hydrothermal fluid (*ca.* 32, Bau and Dulski, 1999), and similar values to modern seawaters from 43 to 80 (Nozaki et al., 1997). The Y/Ho ratios in Archean chemical sedimentary rocks are often used as a proxy of balance between seawater and hydrothermal fluid in a depositional environment (e.g. Alexander et al., 2008). The stratigraphically increasing trend of the Y/Ho ratios in the BIFs suggests that a seawater-like component with a high Y/Ho ratio increase progressively in the depositional environments of the BIFs.

Figure 16B shows relationship of the positive Eu anomalies of the BIFs with stratigraphic positions. Although more scattered than Y/Ho ratios, the positive Eu anomalies obviously decrease with increasing stratigraphic positions. Because modern hydrothermal fluids have distinct positive Eu anomalies in shale-normalized REE patterns (e.g. Bau and Dulski, 1999; German and Von Damm, 2003; Klinkhammer et al., 1994), the stratigraphically upward trend of Eu anomaly can be explained by decrease of a hydrothermal fluid component in the BIFs. Alternatively, decrease of high-temperature hydrothermal fluid component also accounts for the stratigraphically upward trend because the positive Eu anomaly is unique to high temperature (> 300 ˚C) hydrothermal fluids (e.g. Klinkhammer et al., 1994). However, increase of high-temperature hydrothermal fluid leads to higher influx of Fe and Mn compared with low-temperature components of Si, Ba and Ca so that REE and Ni contents adhering to the iron oxyhydroxide would decrease due to higher precipitation rates of iron oxyhydroxide. Because the REE and Ni contents are not correlated with the stratigraphic position, the former model is capable of explaining the stratigraphically upward trend.

Generally speaking, BIFs comprise two components of iron oxyhydroxide and silica, and they, at present, are transformed to magnetite and quartz in the ISB, respectively. A Nd isotope variation of black and white bands within a slabbed BIF

sample shows that the black bands have higher Nd isotope values and higher positive Eu anomalies than the white bands, and suggests that the black bands have more hydrothermal components than the white bands (Frei and Polat, 2007). The geochemical difference that the BIFs have higher silicon isotope values and higher positive Eu anomalies than cherts also suggest that the BIFs contain more hydrothermal components than chert (André et al., 2006). However, the stratigraphic upward trends of the Y/Ho ratios and positive Eu anomalies are inconsistent with the Nd and Si isotopes at a glance because the stratigraphic upward trends of Y/Ho ratios and positive Eu anomalies are apparently independent of their lithologies. However, it is considered that the Nd isotope variation of the BIF sample reflects variations within hydrothermal plumes in a short term because it was obtained from only *ca.* 10 cm long part of a BIF sequence. On the other hand, because our stratigraphic upward trends were obtained from almost the whole BIF sequence, the trends indicate the temporal change through the BIF deposition.

It is well known that a modern drilled metalliferous sedimentary sequence around the East Pacific Rise (EPR) also displays that positive Eu anomalies decrease with the stratigraphy upwards (Olivarez and Owen, 1991; Ruhlin and Owen, 1986). The compositional change of the EPR metalliferous sediments can be explained by decrease in ratios of hydrothermal to seawater components with increasing distance from a ridge

axis through ocean plate movement. The upward decrease of the positive Eu anomalies was also reported from the Mesoarchean BIFs in the Cleaverville area of the Pilbara craton, Western Australia, and was explained by change of depositional setting from mid-ocean ridge to continental margin (Kato et al., 1998). The stratigraphic upward trends of Y/Ho ratios and positive Eu anomalies of the BIFs in the ISB are also accounted for by change of depositional setting, analogous to the modern and Mesoarchean metalliferous sediments, and supports the ocean plate stratigraphy and possible accretionary complex model for the formation of the ISB (Furnes et al., 2007; Komiya et al., 1999). Because the greenstones have arc-affinity signatures such as Nb-depletion in the ISB (Dilek and Polat, 2008; Furnes et al., 2014; Polat et al., 2002), the ridge axis would be located in the suprasubduction setting (Komiya et al., 2015). On the other hand, recent reappraisal of the Nb-poor greenstones suggests that the Nb-depletion was partially due to crustal contamination or later metasomatism of Nb-poor fluids (Hoffmann et al., 2010). Further comprehensive studies should be necessary to determine the tectonic setting of the Isua supracrustal belt.

Conclusions

I petrographically classified BIFs in the Isua supracrustal belt into four types: Black-, Gray-, Green- and White-types, respectively. The amphibole-rich Green-type BIFs were enriched in REE + Y and transitional elements due to contamination of Mg and Ca-bearing minerals so that they are unsuitable for the estimate of seawater composition.

The magnetite-rich Black-type BIFs show positive correlations of LREE, transitional element (V, Co, Ni, Zn and U) contents with Zr contents, suggesting that the compositions also suffered from contaminations of volcanic, clastic and exhalative materials. Similar correlations are observed for 2.9, 2.7, 2.4 and 0.7 Ga BIFs. Nickel content of contamination-free BIFs in the Eoarchean, which is calculated from an intercept of a compositional variation of their contents on a Zr variation diagram, is much lower than previously estimated. Our reconstructed secular variation of Ni contents of BIFs shows that the Ni content had already decreased before 2.7 Ga, in contrast to previous works. I also reconstructed secular variations of V, Co, Zn and U contents of BIFs through the time, which shows Ni and Co contents decreased whereas V, Zn and U contents increased through the time. Especially, the Ni and Co contents drastically

decreased in the Mesoarchean whereas the V, Zn and U contents progressively increased from the Mesoarchean to the Proterozoic.

The BIFs increased in Y/Ho ratios and decreased in positive Eu anomalies stratigraphical upwards, analogous to modern metalliferous sediments on the spreading oceanic plate. The similarities suggest that the REE+Y stratigraphic variations of the BIFs can be also explained by decreasing of ratios of hydrothermal to seawater components with increasing distance from a middle oceanic ridge due to movement of oceanic plate. It supports the existence of ocean plate stratigraphy and an accretionary complex in the ISB as well as the Eoarchean plate tectonics.

References

Alibo, D.S., Nozaki, Y., 1999. Rare earth elements in seawater: Particle association, shale-normalization, and Ce oxidation. Geochimica et Cosmochimica Acta 63, 363-372.

Alibo, D.S., Nozaki, Y., 1999. Rare earth elements in seawater: Particle association, shale-normalization, and Ce oxidation. Geochimica et Cosmochimica Acta 63, 363-372.

Alexander, B. W., Bau, M., Andersson, P., Dulski, P., 2008. Continentally-derived solutes in shallow Archean seawater: Rare earth element and Nd isotope evidence in iron formation from the 2.9Ga Pongola Supergroup, South Africa/ Geochimica et Cosmochimica Acta 72, 378-394.

Allaart, J.H., 1976. The Pre-3760 m.y. old supracrustal rocks of the Isua area, central West Greenland, and the associated occurrence of quartz-banded ironstone. In: Windley, B.F. (Ed.), The early history of the Earth. John Wiley & Sons, London, pp. 177-189.

André, L., Cardinal, D., Alleman, L.Y., Moorbath, S., 2006. Silicon isotopes in ~3.8 Ga West Greenland rocks as clues to the Eoarchaean supracrustal Si cycle. Earth and Planetary Science Letters 245, 162-173.

Andrews, J.E., Brimblecombe, P., Jickells, T.D., Liss, P.S., Reid, B., 2004. An Introduction to Environmental Chemistry, second edition. Blackwell Science, Malden, USA, 296 pp.

Appel, P.W.U., 1980. On the early Archaean Isua iron-formation, West Greenland. Precambrian Research 11, 73-87.

Appel, P.W.U., Fedo, C.M., Moorbath, S., Myers, J.S., 1998. Recognizable primary volcanic and sedimentary features in a low-strain domain of the highly deformed, oldest known (≈ 3.7-3.8 Gyr) Greenstone Belt, Isua, West Greenland. Terra Nova 10, 57-62.

Arai, T., Omori, S., Komiya, T., Maruyama, S., 2015. Intermediate P/T-type regional metamorphism of the Isua Supracrustal Belt, southern west Greenland: The oldest Pacific-type orogenic belt? Tectonophysics 662, 22-39.

Baldwin, G.J., Turner, E.C., Kamber, B.S., 2012. A new depositional model for glaciogenic Neoproterozoic iron formation: insights from the chemostratigraphy and basin configuration of the Rapitan iron formation1Northwest Territories Geoscience Office Contribution 0052. Canadian Journal of Earth Sciences 49, 455-476.

Bau, M., 1993. Effects of syn- and post-depositional processes on the rare-earth element distribution in Precambrian iron-formations. European Journal of Mineralogy 5, 257-267.

Bau, M., 1996. Controls on the fractionation of isovalent trace elements in magmatic and aqueous systems: evidence from Y/Ho, Zr/Hf, and lanthanide tetrad effect. Contributions to Mineralogy and Petrology 123, 323-333.

Bau, M., Dulski, P., 1996. Distribution of yttrium and rare-earth elements in the Penge and Kuruman iron-formations, Transvaal Supergroup, South Africa. Precambrian Research 79, 37-55.

Bau, M., Dulski, P., 1999. Comparing yttrium and rare earths in hydrothermal fluids from the Mid-Atlantic Ridge: implications for Y and REE behaviour during near-vent mixing and for the Y/Ho ratio of Proterozoic seawater. Chemical Geology 155, 77-90.

Bau, M., Alexander, B.W., 2009. Distribution of high field strength elements (Y, Zr, REE, Hf, Ta, Th, U) in adjacent magnetite and chert bands and in reference standards FeR-3 and FeR-4 from the Temagami iron-formation, Canada, and the redox level of the Neoarchean ocean. Precambrian Research 174, 337-346.

Bjerrum, C.J., Canfield, D.E., 2002. Ocean productivity before about 1.9 Gyr ago limited by phosphorus adsorption onto iron oxides. Nature 417, 159-162.

Bolhar, R., Kamber, B.S., Moorbath, S., Fedo, C.M., Whitehouse, M.J., 2004. Characterisation of early Archaean chemical sediments by trace element signatures. Earth and Planetary Science Letters 222, 43-60.

Bolhar, R., Kamber, B.S., Moorbath, S., Whitehouse, M.J., Collerson, K.D., 2005. Chemical characterization of earth's most ancient clastic metasediments from the Isua Greenstone Belt, southern West Greenland. Geochimica et Cosmochimica Acta 69, 1555-1573.

Bosak, T., Liang, B., Sim, M.S., Petroff, A.P., 2009. Morphological record of oxygenic photosynthesis in conical stromatolites. Proceedings of the National Academy of Sciences 106, 10939-10943 %R 10.1073/pnas.0900885106.

Crowley, J.L., Myers, J.S., Dunning, G.R., 2002. Timing and nature of multiple 3700-3600 Ma tectonic events in intrusive rocks north of the Isua greenstone belt, southern West Greenland. Geological Society of America Bulletin 114, 1311-1325.

Crowley, J.L., 2003. U-Pb geochronology of 3810-3630 Ma granitoid rocks south of the Isua greenstone belt, southern West Greenland. Precambrian Research 126, 235-257.

Dauphas, N., van Zuilen, M., Wadhwa, M., Davis, A.M., Marty, B., Janney, P.E., 2004. Clues from Fe isotope variations on the origin of Early Archean BIFs from Greenland. Science 306, 2077-2080.

Dauphas, N., van Zuilen, M., Busigny, V., Lepland, A., Wadhwa, M., Janney, P.E., 2007. Iron isotope, major and trace element characterization of early Archean supracrustal rocks from SW Greenland: Protolith identification and metamorphic overprint. Geochimica et Cosmochimica Acta 71, 4745-4770.

Dilek, Y., Polat, A., 2008. Suprasubduction zone ophiolites and Archean tectonics. Geology 36, 431-432.

Dulski, P., 2001. Reference materials for geochemical studies: New analytical data by ICP-MS and critical discussion of reference values. Geostandards Newsletter 25, 87-125.

Dymek, R.F., Klein, C., 1988. Chemistry, petrology and origin of banded iron-formation lithologies from the 3800 Ma Isua supracrustal belt, West Greenland. Precambrian Research 39, 247-302.

Eggins, S.M., Woodhead, J.D., Kinsley, L.P.J., Mortimer, G.E., Sylvester, P., McCulloch, M.T., Hergt, J.M., Handler, M.R., 1997. A simple method for the precise determination of ≥ 40 trace elements in geological samples by ICPMS using enriched isotope internal standardisation. Chemical Geology 134, 311-326.

Eigenbrode, J.L., Freeman, K.H., Summons, R.E., 2008. Methylhopane biomarker hydrocarbons in Hamersley Province sediments provide evidence for Neoarchean aerobiosis. Earth and Planetary Science Letters 273, 323-331.

Frei, R., Bridgwater, D., Rosing, M.T., Stecher, O., 1999. Controversial Pb-Pb and Sm-Nd isotope results in the early Archean Isua (West Greenland) oxide iron formation: Preservation of primary signatures versus secondary disturbances. Geochimica et Cosmochimica Acta 63, 473-488.

Frei, R., Polat, A., 2007. Source heterogeneity for the major components of ~ 3.7 Ga Banded Iron Formations (Isua Greenstone Belt, Western Greenland): Tracing the nature of interacting water masses in BIF formation. Earth and Planetary Science Letters 253, 266-281.

Friend, C.R.L., Nutman, A.P., McGregor, V.R., 1988. Late Archaean terrane accretion in the Godthåb region, southern West Greenland. Nature 335, 535-538.

Friend, C.R.L., Nutman, A.P., Bennett, V.C., Norman, M.D., 2008. Seawater-like trace element signatures (REE + Y) of Eoarchaean chemical sedimentary rocks from southern West Greenland, and their corruption during high-grade metamorphism. Contributions to Mineralogy and Petrology 155, 229-246.

Furnes, H., de Wit, M., Staudigel, H., Rosing, M., Muehlenbachs, K., 2007. A vestige of Earth's oldest ophiolite. Science 315, 1704-1707.

Furnes, H., Rosing, M., Dilek, Y., de Wit, M., 2009. Isua supracrustal belt (Greenland) -A vestige of a 3.8 Ga suprasubduction zone ophiolite, and the implications for Archean geology. Lithos 113, 115-132.

Furnes, H., de Wit, M., Dilek, Y., 2014. Four billion years of ophiolites reveal secular trends in oceanic crust formation. Geoscience Frontiers 5, 571-603.

German, C.R., Von Damm, K.L., 2003. Hydrothermal processes, The Oceans and Marine Geochemistry. Vol. 6 Treatise on geochemistry (eds. Holland, H. D. and Turekian, K.K.). Elsevier-Pergamon, Oxford, pp. 181-222.

Haugaard, R., Pecoits, E., Lalonde, S., Rouxel, O., Konhauser, K., 2016. The Joffre banded iron formation, Hamersley Group, Western Australia: Assessing the palaeoenvironment through detailed petrology and chemostratigraphy. Precambrian Research 273, 12-37.

Hayashi, M., Komiya, T., Nakamura, Y., Maruyama, S., 2000. Archean regional metamorphism of the Isua supracrustal belt southern West Greenland: Implications for a driving force for Archean plate tectonics. International Geology Review 42, 1055-1115.

Hayes, J.M., 1994. Global methanotrophy at the Archean-Proterozoic transition. In: Bengtson, S. (Ed.), Early Life on Earth. Columbia University Press, New York, pp. 220-236.

Hein, J.R., Koschinsky, A., Bau, M., Manheim, F.T., Kang, J.-K., Roberts, L., 2000. Cobalt-rich ferromanganese crusts in the Pacific. In: Cronan, D.S. (Ed.), Handbook of marine mineral deposits. CRC, Boca Raton, pp. 239-279.

Hein, J.R., Koschinsky, A., Halliday, A.N., 2003. Global occurrence of tellurium-rich ferromanganese crusts and a model for the enrichment of tellurium. Geochimica et Cosmochimica Acta 67, 1117-1127.

Hoffmann, J.E., Münker, C., Polat, A., König, S., Mezger, K., Rosing, M.T., 2010. Highly depleted Hadean mantle reservoirs in the sources of early Archean arc-like rocks, Isua supracrustal belt, southern West Greenland. Geochimica et Cosmochimica Acta 74, 7236-7260.

Holland, H.D., 1994. Early Proterozoic atmospheric change. In: Bengtson, S. (Ed.), Early Life on Earth. Columbia University Press, New York, pp. 237-244.

Jaun, B., Thauer, R.K., 2007. Methyl-Coenzyme M Reductase and its Nickel Corphin Coenzyme F430 in Methanogenic Archaea. In: Sigel, A., Sigel, H., Sigel, R.K.O. (Eds.), Nickel and Its Surprising Impact in Nature, Metal Ions in Life Sciences

Vol. 2. John Wiley & Sons, Ltd, Chichester, UK, pp. 323-356.

Kato, Y., Ohta, I., Tsunematsu, T., Watanabe, Y., Isozaki, Y., Maruyama, S., Imai, N., 1998. Rare earth element variations in mid-Archean banded iron formations: implications for the chemistry of ocean and continent and plate tectonics. Geochimica et Cosmochimica Acta 62, 3475-3497.

Kato, Y., Kano, T., Kunugiza, K., 2002. Negative Ce Anomaly in the Indian Banded Iron Formations: Evidence for the Emergence of Oxygenated Deep-Sea at 2.9-2.7 Ga. Resource Geology 52, 101-110.

Klein, C., 2005. Some Precambrian banded iron-formations (BIFs) from around the world: Their age, geologic setting, mineralogy, metamorphism, geochemistry, and origins. American Mineralogist 90, 1473-1499.

Klinkhammer, G., German, C.R., Elderfield, H., Greaves, M.J., Mitra, A., 1994. Rare earth elements in hydrothermal fluids and plume particulates by inductively coupled plasma mass spectrometry. Marine Chemistry 45, 179-186.

Komiya, T., Maruyama, S., Masuda, T., Nohda, S., Hayashi, M., Okamoto, K., 1999. Plate tectonics at 3.8-3.7 Ga: Field evidence from the Isua accretionary complex, southern West Greenland. Journal of Geology 107, 515-554.

Komiya, T., Hayashi, M., Maruyama, S., Yurimoto, H., 2002. Intermediate-P/T type Archean metamorphism of the Isua supracrustal belt: Implications for secular change of geothermal gradients at subduction zones and for Archean plate tectonics. American Journal of Science 302, 804-826.

Komiya, T., Hirata, T., Kitajima, K., Yamamoto, S., Shibuya, T., Sawaki, Y., Ishikawa, T., Shu, D., Li, Y., Han, J., 2008. Evolution of the composition of seawater through geologic time, and its influence on the evolution of life. Gondwana Research 14, 159-174.

Komiya, T., Yamamoto, S., Aoki, S., Sawaki, Y., Ishikawa, A., Tashiro, T., Koshida, K., Shimojo, M., Aoki, K., Collerson, K.D., 2015. Geology of the Eoarchean, >3.95 Ga, Nulliak supracrustal rocks in the Saglek Block, northern Labrador, Canada: The oldest geological evidence for plate tectonics. Tectonophysics 662, 40-66.

Konhauser, K.O., Pecoits, E., Lalonde, S.V., Papineau, D., Nisbet, E.G., Barley, M.E., Arndt, N.T., Zahnle, K., Kamber, B.S., 2009. Oceanic nickel depletion and a methanogen famine before the Great Oxidation Event. Nature 458, 750-753.

Konhauser, K.O., Lalonde, S.V., Planavsky, N.J., Pecoits, E., Lyons, T.W., Mojzsis, S.J., Rouxel, O.J., Barley, M.E., Rosiere, C., Fralick, P.W., Kump, L.R., Bekker, A., 2011. Aerobic bacterial pyrite oxidation and acid rock drainage during the Great Oxidation Event. Nature 478, 369-373.

Liscomb, W.N., Sträter, N., 1996. Recent Advances in Zinc Enzymology. Chemical Reviews 96, 2375-2434.

Li, Y.H., 1981. Ultimate removal mechanisms of elements from the ocean. Geochimica et Cosmochimica Acta 45, 1659-1664.

Li, Y.H., 1982. Ultimate removal mechanisms of elements from the ocean (reply to a comment by M.W Whitfield and D.R. Turner). Geochimica et Cosmochimica Acta 46, 1993-1995.

Manikyamba, C., Balaram, V., Naqvi, S.M., 1993. Geochemical signatures of polygenetic origin of a banded iron formation (BIF) of the Archaean Sandur greenstone belt (schist belt) Karnataka nucleus, India. Precambrian Research 61, 137-164.

Martin, J.-M., Whitfield, M., 1983. The significance of the river input of chemical elements to the ocean. In: Wong, C.S., Boyle, E., Bruland, K.W., Burton, J.D., Goldberg, E.D. (Eds.), Trace metals in sea water, Volume 9 of the series NATO Conference Series. Plenum Press, New York, pp. 265-296.

McGregor, V.R., Friend, C.R.L., Nutman, A.P., 1991. The late Archean mobile belt through Godthåbsfjord, southern West Greenland: a continent-continent collision zone? Bulletin of the Geological Society of Denmark 39, 179-197.

McGregor, V.R., 1993. Descriptive text to 1:100000 Geological map of GREENLAND Qôrqut 64 V.1 Syd. Geological Survey of Greenland, Copenhagen, 40 pp.

Mloszewska, A.M., Pecoits, E., Cates, N.L., Mojzsis, S.J., O'Neil, J., Robbins, L.J., Konhauser, K.O., 2012. The composition of Earth's oldest iron formations: The Nuvvuagittuq Supracrustal Belt (Québec, Canada). Earth and Planetary Science Letters 317-318, 331-342.

Mloszewska, A.M., Mojzsis, S.J., Pecoits, E., Papineau, D., Dauphas, N., Konhauser, K.O., 2013. Chemical sedimentary protoliths in the >3.75 Ga Nuvvuagittuq Supracrustal Belt (Québec, Canada). Gondwana Research 23, 574-594.

Mojzsis, S.J., Coath, C.D., Greenwood, J.P., McKeegan, K.D., Harrison, T.M., 2003. Mass-independent isotope effects in Archean (2.5 to 3.8 Ga) sedimentary sulfides determined by ion microprobe analysis. Geochimica et Cosmochimica Acta 67, 1635-1658.

Moorbath, S., O'Nions, R.K., Pankhurst, R.J., 1973. Early Archaean age for the Isua Iron Formation, West Greenland. Nature 245, 138-139.

Myers, J.S., 2001. Protoliths of the 3.8-3.7 Ga Isua greenstone belt, West Greenland. Precambrian Research 105, 129-141.

Nishizawa, M., Yamamoto, H., Ueno, Y., Tsuruoka, S., Shibuya, T., Sawaki, Y., Yamamoto, S., Kon, Y., Kitajima, K., Komiya, T., Maruyama, S., Hirata, T., 2010.

Grain-scale iron isotopic distribution of pyrite from Precambrian shallow marine carbonate revealed by a femtosecond laser ablation multicollector ICP-MS technique: Possible proxy for the redox state of ancient seawater. Geochimica et Cosmochimica Acta 74, 2760-2778.

Nozaki, Y., Zhang, J., Amakawa, H., 1997. The fractionation between Y and Ho in the marine environment. Earth and Planetary Science Letters 148, 329-340.

Nutman, A.P., Allaart, J.H., Bridgwater, D., Dimroth, E., Rosing, M., 1984. Stratigraphic and geochemical evidence for the depositional environment of the early Archaean Isua supracrustal belt, southern West Greenland. Precambrian Research 25, 365-396.

Nutman, A.P., 1986. The early Archaean to Proterozoic history of the Isukasia area, southern West Greenland, 154. Grønlands geol. Unders. Bull., København, Denmark, 80 pp.

Nutman, A.P., Friend, C.R.L., Kinny, P.D., McGregor, V.R., 1993. Anatomy of an Early Archean gneiss complex: 3900 to 3600 Ma crustal evolution in southern West Greenland. Geology 21, 415-418.

Nutman, A.P., McGregor, V.R., Friend, C.R.L., Bennett, V.C., Kinny, P.D., 1996. The Itsaq Gneiss Complex of southern West Greenland; the world's most extensive record of early crustal evolution (3900-3600 Ma). Precambrian Research 78, 1-39.

Nutman, A.P., Bennett, V.C., Friend, C.R.L., Rosing, M.T., 1997a. ~ 3710 and ≥ 3790 Ma volcanic sequences in the Isua (Greenland) supracrustal belt; structural and Nd isotope implications. Chemical Geology 141, 271-287.

Nutman, A.P., Mojzsis, S., Friend, C.R.L., 1997b. Recognition of ≥3850 Ma water-lain sediments in West Greenland and their significance for the early Archaean Earth. Geochimica et Cosmochimica Acta 61, 2475-2484.

Nutman, A.P., Friend, C.R.L., Bennett, V.C., 2002. Evidence for 3650-3600 Ma assembly of the northern end of the Itsaq Gneiss Complex, Greenland: Implication for early Archaean tectonics. Tectonics 21, 10.1029/2000TC001203.

Nutman, A.P., Friend, C.R.L., Horie, K., Hidaka, H., 2007. The Itsaq Gneiss Complex of southern West Greenland and the construction of Eoarchaean crust at convergent plate boundaries. In: van Kranendonk, M.J., Smithies, R.H., Bennett, V.C. (Eds.), Earth's Oldest Rocks. Elsevier, Amsterdam, pp. 187-218.

Nutman, A.P., Friend, C.R.L., 2009. New 1:20,000 scale geological maps, synthesis and history of investigation of the Isua supracrustal belt and adjacent orthogneisses, southern West Greenland: A glimpse of Eoarchaean crust formation and orogeny. Precambrian Research 172, 189-211.

Nutman, A.P., Friend, C.R.L., Paxton, S., 2009. Detrital zircon sedimentary provenance ages for the Eoarchaean Isua supracrustal belt southern West Greenland: Juxtaposition of an imbricated ca. 3700 Ma juvenile arc against an older complex with 3920-3760 Ma components. Precambrian Research 172, 212-233.

Nutman, A.P., Friend, C.R.L., Bennett, V.C., Wright, D., Norman, M.D., 2010. ≥3700 Ma pre-metamorphic dolomite formed by microbial mediation in the Isua supracrustal belt (W. Greenland): Simple evidence for early life? Precambrian Research 183, 725-737.

Olivarez, A.M., Owen, R.M., 1991. The europium anomaly of seawaer: implications for fluvial versus hydrothermal REE inputs to the oceans. Chemical Geology 92, 317-328.

Partin, C.A., Lalonde, S.V., Planavsky, N.J., Bekker, A., Rouxel, O.J., Lyons, T.W., Konhauser, K.O., 2013. Uranium in iron formations and the rise of atmospheric oxygen. Chemical Geology 362, 82-90.

Pavlov, A.A., Kasting, J.F., Brown, L.L., Rages, K.A., Freedman, R., 2000. Greenhouse warming by CH_4 in the atmosphere of early Earth. J. Geophys. Res. 105, 11981–11990.

Pecoits, E., Gingras, M.K., Barley, M.E., Kappler, A., Posth, N.R., Konhauser, K.O., 2009. Petrography and geochemistry of the Dales Gorge banded iron formation: Paragenetic sequence, source and implications for palaeo-ocean chemistry. Precambrian Research 172, 163-187.

Planavsky, N.J., Asael, D., Hofmann, A., Reinhard, C.T., Lalonde, S.V., Knudsen, A., Wang, X., Ossa Ossa, F., Pecoits, E., Smith, A.J.B., Beukes, N.J., Bekker, A., Johnson, T.M., Konhauser, K.O., Lyons, T.W., Rouxel, O.J., 2014. Evidence for oxygenic photosynthesis half a billion years before the Great Oxidation Event. Nature Geoscience 7, 283-286.

Polat, A., Hofmann, A.W., Rosing, M., 2002. Boninite-like volcanic rocks in the 3.7-3.8 Ga Isua greenstone belt, West Greenland: geochemical evidence for intra-oceanic subduction zone processes in the early Earth. Chemical Geology 184, 231-254.

Polat, A., Hofmann, A.W., 2003. Alteration and geochemical patterns in the 3.7-3.8 Ga Isua greenstone belt, West Greenland. Precambrian Research 126, 197-218.

Polat, A., Frei, R., 2005. The origin of early Archean banded iron formations and of continental crust, Isua, southern West Greenland. Precambrian Research 138, 151-175.

Polat, A., Wang, L., Appel, P.W.U., 2015. A review of structural patterns and melting processes in the Archean craton of West Greenland: Evidence for crustal growth

at convergent plate margins as opposed to non-uniformitarian models. Tectonophysics 662, 67-94.

Ragdale, S.W., 2014. Biochemistry of Methyl-Coenzyme M Reductase: The Nickel Metalloenzyme that Catalyzes the Final Step in Synthesis and the First Step in Anaerobic Oxidation of the Greenhouse Gas Methane. In: Kroneck, P.M.H., Sosa Torres, M.E. (Eds.), The Metal-Driven Biogeochemistry of Gaseous Compounds in the Environment. Metal Ions in Life Sciences 14. Springer, pp. 125-145.

Rollinson, H., 2002. The metamorphic history of the Isua Greenstone Belt, West Greenland. In: Fowler, C.M.R., Ebinger, C.J., Hawkesworth, C.J. (Eds.), The early Earth: Physical, Chemical, and Biological Development. Geological Society, London, Special Publications, 199, pp. 329-350.

Rollinson, H., 2003. Metamorphic history suggested by garnet-growth chronologies in the Isua Greenstone Belt, West Greenland. Precambrian Research 126, 181-196.

Rose, N.M., Rosing, M.T., Bridgwater, D., 1996. The origin of metacarbonate rocks in the Archaean Isua supracrustal belt, West Greenland. American Journal of Science 296, 1004-1044.

Rosing, M.T., Rose, N.M., Bridgwater, D., Thomsen, H.S., 1996. Earliest part of Earth's stratigraphic record: A reappraisal of the > 3.7 Ga Isua (Greenland) supracrustal sequence. Geology 24, 43-46.

Ruhlin, D.E., Owen, R.M., 1986. The rare-earth element geochemistry of hydrothermal sediments from the East Pacific Rise: Exhumation of a seawater scavenging mechanism. Geochimica et Cosmochimica Acta 50, 393-400.

Sherrell, R.M., Field, M.P., Ravizza, G., 1999. Uptake and fractionation of rare earth elements on hydrothermal plume particles at 9° 45′ N, East Pacific Rise. Geochimica et Cosmochimica Acta 63, 1709-1722.

Shimizu, H., Umemoto, N., Masuda, A., Appel, P.W.U., 1990. Sources of iron-formations in the Archean Isua and Malene supracrustals, West Greenland: Evidence from La-Ce and Sm-Nd isotopic data and REE abundances. Geochimica et Cosmochimica Acta 54, 1147-1154.

Sigel, H., Sigel, A. (Eds.), 1995. Vanadium and its role in life, Metal ions in biological systems volume 31. Marcel Dekker, Inc., New York, 779 pp.

Spear, F.S., 1993. Metamorphic phase equilibria and pressure-temperature-time paths. Mineralogical Society of America, Washington, D. C., 799 pp.

Swanner, E.D., Planavsky, N.J., Lalonde, S.V., Robbins, L.J., Bekker, A., Rouxel, O.J., Saito, M.A., Kappler, A., Mojzsis, S.J., Konhauser, K.O., 2014. Cobalt and marine redox evolution. Earth and Planetary Science Letters 390, 253-263.

Szilas, K., Kelemen, P.B., Rosing, M.T., 2015. The petrogenesis of ultramafic rocks in the > 3.7 Ga Isua supracrustal belt, southern West Greenland: Geochemical evidence for two distinct magmatic cumulate trends. Gondwana Research 28, 565-580.

Takahashi, Y., Ariga, D., Fan, Q., Kashiwabara, T., 2015. Systematics of Distributions of Various Elements Between Ferromanganese Oxides and Seawater from Natural Observation, Thermodynamics, and Structures. In: Ishibashi, J.-i., Okino, K., Sunamura, M. (Eds.), Subseafloor Biosphere Linked to Hydrothermal Systems: TAIGA Concept. Springer Japan, Tokyo, pp. 39-48.

Takai, K., Nakamura, K., Suzuki, K., Inagaki, F., Nealson, K.H., Kumagai, H., 2006. Ultramafics-Hydrothermalism-Hydrogenesis-HyperSLiME (UltraH3) linkage: a key insight into early microbial ecosystem in the Archean deep-sea hydrothermal systems. Paleontological Research 10, 269-282.

Taylor, S.R., McLennan, S.M., 1985. The continental crust: Its composition and evolution. Blackwell, Oxford, 312 pp.

Trendall, A.F., Morris, R.C., 1983. Iron Formation: Facts and Problems. Developments in Precambrian geology, Vol. 6. Elsevier, Amsterdam, 572 pp.

Viehmann, S., Bau, M., Smith, A.J.B., Beukes, N.J., Dantas, E.L., Bühn, B., 2015a. The reliability of ~2.9 Ga old Witwatersrand banded iron formations (South Africa) as archives for Mesoarchean seawter: Evidence from REE and Nd isotope systematics. Journal of African Earth Sciences 111, 322-334.

Viehmann, S., Bau, M., Hoffmann, J.E., Münker, C., 2015b. Geochemistry of the Krivoy Rog Banded Iron Fomration, Ukline, and the impact of peak episodes of increased global magmatic activity on the trace element composition of Precambrian seawater. Precambrian Research 270, 165-180.

Whitehouse, M.J., Kamber, B.S., Fedo, C.M., Lepland, A., 2005. Integrated Pb- and S-isotope investigation of sulphide minerals from the early Archaean of southwest Greenland. Chemical Geology 222, 112-131.

Whitehouse, M.J., Fedo, C.M., 2007. Microscale heterogeneity of Fe isotopes in >3.71 Ga banded iron formation from the Isua Greenstone Belt, southwest Greenland. Geology 35, 719-722.

Yoshiya, K., Nishizawa, M., Sawaki, Y., Ueno, Y., Komiya, T., Yamada, K., Yoshida, N., Hirata, T., Wada, H., Maruyama, S., 2012. *In situ* iron isotope analyses of pyrite and organic carbon isotope ratios in the Fortescue Group: Metabolic variations of a Late Archean ecosystem. Precambrian Research 212-213, 169-193.

Yoshiya, K., Sawaki, Y., Hirata, T., Maruyama, S., Komiya, T., 2015. *In-situ* iron isotope

analysis of pyrites in ~ 3.7 Ga sedimentary protoliths from the Isua supracrustal belt, southern West Greenland. Chemical Geology 401, 126-139.

Figure captions

Figure 1. (A) A geological map of the Southern West Greenland, which comprises Akia, Akulleq and Tasiussarsuaq Terranes. The Akulleq Terrane is composed of Ikkattoq gneiss, Amîtsoq gneiss, supracrustal rocks and post-collision Qôrqut granite, in the southern West Greenland (modified from McGregor, 1993). The Isua supracrustal belt (the ISB) is located in the northeastern part. (B) A geological map of the northeastern part of the Isua supracrustal belt (modified after Komiya et al., 1999). Our studied area is located in the northeastern part (Fig. 2).

Figure 2. (A) A geological map of our studied area (modified after Komiya et al., 1999). (B) A cross section along A-B on the Fig. 2A. (C) Stratigraphy and sample positions of the BIF sequence, which overlies basaltic hyaloclastite and pillow lavas.

Figure 3. The slabbed sections of BIF samples. (A) Alternation of black, white and gray bands, and (B) Alternation of black and green bands. B: black band, W: white band, GRY: gray band, and GRN: green band.

Figure 4. Photomicrographs of the BIFs in plane polarized light. (A) A magnified photo of a black layer, which is composed mainly of magnetite, accompanied with quartz, amphibole and chlorite. (B) A gray-colored bands, showing scattered magnetite within quartz matrix. (C) Alternation of black, magnetite-rich bands and white, quartz-rich bands with thin amphibole-rich layers with a nematoblastic texture. (D) Interbedded calcite and amphibole layers interbedded within quartz layer. (E) A magnified photo of a greenish band, which consists of alternating amphibole and quartz with scattered magnetite. Mgt: magnetite, Qz: quartz, Amp: actinolitic amphibole, Chl: ripidolitic chlorite, Hem: hematite and Carb: carbonate mineral (calcite).

Figure 5. Fe_2O_3 variation diagrams for (A) SiO_2, (B) MgO, (C) CaO contents along with compositional variations of BIFs from a literature (Dymek and Klein, 1988).

Figure 6. Fe_2O_3 variation diagrams for (A) V, (B) Co, (C) Ni, (D) Cu, (E) Zn, (F) Rb, (G) Sr, (H) Y, (I) Zr, (J) Ba, (K) Pr, (L) Sm, (M) Yb, (N) Th and (O) U contents.

Figure 7. PAAS-normalized REE + Y patterns for (A) Black-type, (B) White-type, (C) Gray-type and (D) Green-type BIFs.

Figure 8. Ternary plots of (A) Co-(Mg+Ca)-Fe, (B) Ni-(Mg+Ca)-Fe, (C) Cu-(Mg+Ca)-Fe, (D) Zn-(Mg+Ca)-Fe, (E) Y-(Mg+Ca)-Fe, (F) Pr-(Mg+Ca)-Fe, (G) Sm-(Mg+Ca)-Fe, (H) Yb-(Mg+Ca)-Fe, and (I) U-(Mg+Ca)-Fe contents, along with compositional variations of BIFs from a literature except for Pr (Dymek and Klein, 1988).

Figure 9. Zr variation diagrams of (A) V, (B) Co, (C) Ni, (D) Cu, (E) Zn, (F) Y, (G) Pr, (H) Sm, (I) Yb, (J) U and (K) Y/Ho ratio. Small circles mean samples with high (MgO+CaO)/Fe_2O_3 ratios (> 0.1).

Figure 10. Zr variation diagrams of Ni contents: (A) BIFs in the ISB with low Al_2O_3 (< 1%) and Rb (< 2 ppm) contents and low (MgO+CaO)/Fe_2O_3 ratios (< 0.1), including the magnetite-IFs (Frei and Polat, 2007), (B) 2900 Ma Witwatersrand Iron Formations, South Africa (Viehmann et al., 2015a), (C) 2736 Ma Temagami Iron Formations, Canada (Bau and Alexander, 2009), (D) 2450 Ma Joffre iron formations, Western Australia (Haugaard et al., 2016) with low (MgO+CaO)/Fe_2O_3 ratios (<0.1) and (E) 743 Ma Rapitan iron formations, Canada (Baldwin et al., 2012) with low Al_2O_3 (< 1%), Zr contents (< 10 ppm) and (MgO+CaO)/Fe_2O_3 ratios (< 0.1). Blue, green and brown arrows mean the directions of compositions in ultramafic rocks, basaltic rocks and clastic sedimentary rocks in the ISB, respectively (Bolhar et al., 2005; Polat and Hofmann, 2003; Szilas et al., 2015). Red line and area enclosed with blue dotted line mean linear regression line and prediction area (1 σ). Gray area mean are encompassing the all data.

Figure 11. Zr variation diagrams of U contents: (A) BIFs in the ISB, (B) 2900 Ma Witwatersrand Iron Formations, South Africa, (C) 2736 Ma Temagami Iron Formations, Canada (D) 2450 Ma Joffre iron formations, Western Australia and (E) 743 Ma Rapitan iron formations, Canada. The symbols are same as those in Fig. 10.

Figure 12. Zr variation diagrams of V contents: (A) BIFs in the ISB, (B) 2450 Ma Joffre iron formations, Western Australia and (C) 743 Ma Rapitan iron formations, Canada. The symbols are same as those in Fig. 10.

Figure 13. Zr variation diagrams of Zn contents: (A) BIFs in the ISB and (B) 2450 Ma Joffre iron formations, Western Australia. The symbols are same as those in Fig. 10.

Figure 14. Zr variation diagrams of Co contents: (A) BIFs in the ISB, (B) 2900 Ma Witwatersrand Iron Formations, South Africa, (C) 2736 Ma Temagami Iron Formations, Canada, (D) 2450 Ma Joffre iron formations, Western Australia and (E) 743 Ma Rapitan iron formations, Canada. The symbols are same as those in Fig. 10.

Figure 15. Secular variations of (A) Ni, (B) V and Zn, (C) Co and (D) U contents. The inlet figures show compilations of BIF compositions for Ni (Konhauser et al., 2009), Co (Swanner et al., 2014) and U (Partin et al., 2013), respectively.

Figure 16. Correlations of (A) Y/Ho ratios and (B) positive Eu anomalies with the stratigraphic positions from the underlying basaltic lavas (Fig. 2).

Supplementary Table 1. Analytical data of a standard, BIR-1

	BIR-1 (n = 29)	RSD (%, 2sd)	Reference values*
Li (ppm)	3.23	17	3.32
Sc (ppm)	43.9	5.0	43.8
V (ppm)	316	1.4	322
Co (ppm)	54	1.9	53
Ni (ppm)	173	1.9	175
Cu (ppm)	122	2.0	113
Zn (ppm)	68	3.0	65
Rb (ppm)	0.209	4.8	0.195
Sr (ppm)	108.0	3.9	106.4
Y (ppm)	16.50	1.4	16.20
Zr (ppm)	14.60	2.3	14.47
Nb (ppm)	0.559	2.4	0.558
Ba (ppm)	6.54	1.3	6.52
La (ppm)	0.607	1.4	0.604
Ce (ppm)	1.889	1.2	1.897
Pr (ppm)	0.378	1.5	0.378
Nd (ppm)	2.39	1.1	2.38
Sm (ppm)	1.119	1.9	1.117
Eu (ppm)	0.524	0.50	0.524
Gd (ppm)	1.850	1.6	1.850
Tb (ppm)	0.374	1.7	0.379
Dy (ppm)	2.55	1.7	2.53
Ho (ppm)	0.585	1.2	0.585
Er (ppm)	1.730	1.8	1.734
Tm (ppm)	0.25	2.4	0.25
Yb (ppm)	1.650	2.6	1.649
Lu (ppm)	0.249	1.7	0.247
Hf (ppm)	0.566	0.82	0.562
Ta (ppb)	41	3.6	41
Th (ppb)	30.0	7.2	30.2
U (ppb)	10.1	3.4	10.0

*Reference values for Tm (Dulski, 2001) and others (Eggins et al., 1997)

Table 1. Whole-rock major and trace element data for the BIFs in the Isua supracrustal belt

Sample No.	9B	18B	45B	54B	60B	90B	138B	150B	177B	193B	236B	258B	277B	291B	312B	7W	48W	65W	216W	256W	292W	168R	170R	179R	26GRY	61GRY	89GRY	187GRY	236GRY	260GRY	303GRY	11GRN	60GRN	259GRN	268GRN	327GRN
Type	Black	Black	Black	Black	Black	Black	Black	Black	Black	Black	Black	Black	Black	Black	Black	White	White	White	White	White	White	White	White	White	Gray	Gray	Gray	Gray	Gray	Gray	Gray	Green	Green	Green	Green	Green
Distance* (m)	0.30	0.75	1.68	2.13	2.33	3.30	4.44	4.72	5.20	5.54	6.33	6.85	7.43	7.81	8.38	0.21	1.82	2.50	5.85	6.79	7.85	5.08	5.13	5.32	1.11	2.41	3.25	5.46	6.29	6.93	8.15	0.39	2.37	6.88	7.17	8.78
SiO_2 (wt%)	17.2	11.4	10	11.7	9.9	9.8	17.4	7.8	9.2	9.7	9.0	12.8	11.6	8.6	13.1	85.3	97.9	86.8	89.2	92.2	95.6	74.3	79.2	63.3	89.2	88.7	85.9	81.4	53.2	63.6	88.5	64.8	37.0	45.7	82.2	62.6
Al_2O_3 (wt%)	0.7	0.8	0.7	0.7	1.5	0.8	0.9	1.0	0.7	0.9	0.7	0.8	0.7	0.7	0.8	-	-	-	-	-	-	-	-	-	-	-	-	-	-	-	-	-	0.7	-	-	-
TiO_2 (wt%)	0.10	0.11	0.12	0.12	0.11	0.11	0.12	0.12	0.10	0.12	0.11	0.12	0.12	0.12	0.11	-	-	-	-	-	-	-	-	-	-	-	-	-	-	-	-	-	-	-	-	-
$Fe_2O_3^t$ (wt%)**	80.4	84.7	85.5	83.8	85.4	84.8	77.2	87.4	88.0	87.3	87.9	82.5	83.8	85.6	84.4	13.6	1.45	11.3	9.97	5.40	3.95	24.3	19.2	34.3	10.4	10.5	11.8	17.7	42.2	32.7	10.7	31.3	52.3	47.3	12.9	23.9
MgO (wt%)	0.68	0.107	1.65	1.86	1.56	2.37	2.34	2.00	1.01	1.00	1.17	1.74	1.86	2.20	0.74	0.42	0.10	1.05	0.32	1.12	0.11	0.56	0.42	0.90	0.09	0.25	1.21	0.07	2.21	1.76	0.36	1.07	5.44	3.71	2.42	6.81
MnO (wt%)	0.1	1.5	0.12	0.12	0.12	0.12	0.12	0.12	0.12	0.11	0.11	0.12	0.12	0.13	0.10	0.02	0.01	0.04	0.02	0.03	0.02	0.04	0.03	0.05	0.02	0.02	0.02	0.02	0.08	0.06	0.02	0.03	0.12	0.12	0.05	0.12
CaO (wt%)	0.67	1.36	1.66	1.59	1.26	1.93	1.85	1.59	0.87	0.90	1.04	1.80	1.67	2.29	0.74	0.29	0.15	0.65	0.32	0.93	0.15	0.56	0.38	1.19	0.11	0.21	0.89	0.17	1.90	1.57	0.34	2.24	4.42	2.60	1.99	5.88
Na_2O (wt%)	-	-	-	-	-	-	-	-	-	-	-	-	-	-	-	-	-	-	-	-	-	-	-	-	-	-	-	-	-	-	-	-	-	-	-	-
K_2O (wt%)	-	-	-	-	-	-	-	-	-	-	-	-	-	-	-	-	-	-	-	-	-	-	-	-	-	-	-	-	-	-	-	-	-	-	-	-
P_2O_5 (wt%)	-	-	0.20	-	-	0.11	0.08	-	-	-	-	0.22	-	0.30	-	-	-	-	-	-	-	-	-	-	-	-	-	-	0.08	-	-	-	-	-	-	0.29
Total (wt%)	99.89	99.95	99.92	99.90	99.88	100.01	99.98	100.04	99.99	99.99	99.98	100.10	99.89	99.94	100.02	99.67	99.61	99.81	99.83	99.68	99.83	99.77	99.21	99.73	99.79	99.67	99.85	99.39	99.67	99.64	99.87	99.41	99.93	99.44	99.58	99.56
Loss of ignition																	0.29	0.02		0.08	0.08				0.05							0.29			0.12	
Gain of ignition	2.06	2.47	2.63	2.41	2.47	2.44	2.38	2.30	2.34	2.84	2.73	2.39	2.29	2.51	2.55	0.16			0.14			0.31	0.46	0.52		0.16	0.13	0.45	1.02	0.71	0.16		1.08	1.05		0.09
Li (ppm)	0.75	0.39	0.33	0.31	0.34	1.09	1.47	1.19	0.72	1.15	0.69	0.44	0.32	0.35	0.19	0.43	0.49	0.43	0.73	0.54	0.59	0.57	0.67	0.71	0.37	0.30	0.36	0.67	0.64	0.60	0.35	0.73	0.87	0.57	0.50	0.63
Sc (ppm)	0.22	0.34	0.31	0.39	0.21	0.33	0.85	0.72	0.22	0.77	0.37	0.59	0.45	0.43	0.18	0.02	0.02	0.08	0.04	0.04	0.01	0.05	0.05	0.13	0.04	0.04	0.07	0.02	0.14	0.02	0.05	0.55	1.10	0.29	0.16	0.65
V (ppm)	3.43	2.39	1.98	3.01	2.29	2.31	3.76	2.10	1.71	3.73	3.33	3.23	2.34	2.00	1.97	0.16	0.04	0.430	0.07	0.04	0.07	0.19	0.29	0.37	0.18	0.34	0.23	0.29	0.82	0.11	0.20	0.56	0.45	0.77	0.44	0.32
Co (ppm)	2.9	4.1	4.7	4.3	4.2	1.3	4.5	4.3	5.7	4.5	4.8	2.9	3.7	4.9	3.8	0.82	0.30	0.61	0.30	0.35	0.51	0.79	1.1	1.4	1.5	0.66	0.27	1.0	1.7	0.78	0.87	6.9	4.9	3.1	2.5	6.1
Ni (ppm)	24	24	28	26	24	39	94	41	39	52	54	41	25	36	21	5.2	1.9	4.0	1.4	1.8	3.5	4.7	6.0	7.0	11	3.3	7.9	7.0	18	3.4	3.2	41	38	20	13	51
Cu (ppm)	2.61	2.09	0.67	1.57	0.80	0.09	0.13	0.03	0.02	0.03	1.20	0.25	0.25	0.23	0.17	0.88	2.40	2.77	1.16	0.90	0.69	0.23	0.31	0.34	2.55	1.07	2.35	0.20	1.51	0.71	0.57	4.67	2.89	1.17	11.70	4.32
Zn (ppm)	12	26	27	25	24	47	63	68	100	60	52	29	25	31	12	6.1	5.3	6.1	5.1	13	9.0	19.9	26.5	29.5	17	4.9	14	31	39	13	8.8	110	110	48	57	80
Rb (ppm)	0.92	0.38	0.36	0.62	0.22	3.23	2.30	1.36	2.07	1.97	1.14	0.43	0.61	0.44	0.26	0.05	0.02	0.06	0.06	0.06	0.04	0.20	0.21	0.33	0.06	0.04	0.08	0.38	0.24	0.09	0.07	0.12	0.15	0.20	0.16	0.27
Sr (ppm)	0.91	1.74	4.11	2.07	2.00	3.77	8.33	6.18	3.27	6.39	4.51	4.32	2.88	6.56	1.14	0.47	0.68	0.95	1.95	1.44	0.55	6.10	3.96	23.41	0.50	0.58	1.13	2.56	3.08	0.76	0.67	4.78	5.26	3.98	2.25	8.28
Y (ppm)	3.26	4.04	7.47	7.00	2.60	4.57	7.38	8.28	5.44	11.94	11.50	6.51	4.67	8.98	3.28	3.50	1.54	1.14	1.44	4.69	2.01	3.53	3.88	6.28	8.87	1.17	1.51	4.13	8.90	2.57	4.43	38.70	24.60	7.09	10.60	19.10
Zr (ppm)	0.96	1.03	0.64	0.94	2.08	1.00	2.00	2.78	0.25	1.50	0.97	1.59	1.11	0.70	0.48	0.05	0.09	0.21	0.14	0.06	0.05	0.10	0.12	0.29	0.06	0.13	0.11	0.08	0.18	0.05	0.08	0.48	0.77	0.38	0.23	0.27
Nb (ppm)	0.09	0.10	0.09	0.12	0.13	0.10	0.06	0.11	0.09	0.08	0.06	0.06	0.04	0.04	0.03	0.01	0.00	0.02	0.00	0.00	0.00	0.02	0.02	0.03	0.01	0.01	0.02	0.01	0.02	0.00	0.00	0.11	0.08	0.09	0.02	0.02
Ba (ppm)	2.41	2.44	2.30	2.58	2.38	6.76	9.35	10.66	8.41	16.19	8.27	3.02	2.90	3.59	2.88	1.35	1.06	3.28	3.11	1.27	3.38	11.09	15.47	16.11	2.13	1.25	1.46	13.5	3.92	4.17	1.03	6.50	3.11	15.40	3.99	1.27
La (ppm)	3.40	2.67	1.77	3.45	1.34	4.96	10.40	1.16	0.27	5.91	3.55	8.03	3.63	9.30	1.62	0.34	0.54	0.14	0.78	0.81	0.32	0.29	0.53	0.48	0.61	0.35	0.09	0.35	2.98	0.27	0.34	2.58	0.31	0.94	0.79	5.69
Ce (ppm)	4.89	3.87	2.71	5.67	1.76	6.56	13.87	1.75	0.65	8.92	4.35	10.58	4.64	9.48	2.26	0.53	0.69	0.23	0.87	1.14	0.37	0.54	0.80	0.84	1.17	0.51	0.16	0.57	3.79	0.48	0.54	4.95	1.00	1.52	1.33	11.36
Pr (ppm)	0.503	0.397	0.323	0.573	0.181	0.625	1.35	0.226	0.102	0.831	0.448	1.02	0.448	0.821	0.24	0.0743	0.0715	0.024	0.0831	0.119	0.06	0.07	0.103	0.12	0.178	0.056	0.0241	0.0831	0.396	0.0543	0.0696	0.739	0.212	0.184	0.151	0.907
Nd (ppm)	1.72	1.38	1.40	2.13	0.688	2.07	4.30	1.06	0.57	2.69	1.69	3.38	1.48	2.6	0.91	0.407	0.274	0.11	0.324	0.51	0.254	0.344	0.474	0.616	0.949	0.216	0.138	0.404	1.52	0.282	0.338	4.04	1.52	0.86	0.744	3.72
Sm (ppm)	0.207	0.228	0.342	0.363	0.134	0.293	0.559	0.330	0.176	0.430	0.358	0.406	0.180	0.357	0.163	0.155	0.054	0.037	0.068	0.133	0.060	0.092	0.111	0.167	0.336	0.050	0.047	0.103	0.313	0.092	0.108	1.314	0.811	0.272	0.262	0.831
Eu (ppm)	0.147	0.198	0.311	0.272	0.119	0.243	0.359	0.279	0.174	0.338	0.336	0.228	0.121	0.254	0.117	0.153	0.0598	0.0340	0.0580	0.131	0.0478	0.0838	0.107	0.146	0.331	0.0465	0.0544	0.0952	0.2970	0.0856	0.0990	1.38	0.793	0.240	0.255	0.636
Gd (ppm)	0.230	0.311	0.537	0.476	0.208	0.381	0.622	0.530	0.311	0.646	0.603	0.418	0.242	0.505	0.189	0.286	0.099	0.064	0.098	0.250	0.108	0.164	0.198	0.313	0.604	0.078	0.089	0.202	0.552	0.167	0.193	2.427	1.516	0.355	0.530	1.310
Tb (ppb)	34.9	53.8	91.0	79.2	33.7	53.7	92.5	93.6	51.1	107	95.7	60.3	38.2	73.5	30.1	49.7	17.8	11.5	15.7	41.6	17.0	26.8	30.5	54.6	120	14.1	16.1	32.8	86.2	29.4	39.3	407	296	59.8	105	207
Dy (ppm)	0.247	0.379	0.617	0.535	0.223	0.359	0.596	0.651	0.358	0.786	0.666	0.396	0.266	0.512	0.203	0.343	0.138	0.083	0.106	0.303	0.119	0.193	0.220	0.409	0.905	0.099	0.121	0.242	0.602	0.208	0.299	2.963	2.262	0.425	0.816	1.408
Ho (ppb)	80.0	96.4	160.0	136.0	58.8	89.8	144.0	163.0	93.9	204.0	177.0	102.0	69.9	134.0	49.0	85.1	37.8	21.2	26.9	80.3	32.4	52.5	58.6	106	237	25	32	70	151	55	76	780.0	590.0	114.0	218.0	348.0
Er (ppm)	0.201	0.298	0.471	0.415	0.181	0.286	0.448	0.512	0.283	0.666	0.558	0.326	0.227	0.432	0.151	0.266	0.128	0.069	0.081	0.243	0.103	0.164	0.189	0.342	0.780	0.078	0.103	0.208	0.476	0.171	0.257	2.470	1.923	0.362	0.715	1.059
Tm (ppb)	31	46	68	61	28	43	71	73	38	98	76	49	31	62	23	36	19	10	11	34	15	22	26	50	120	12	15	28	62	25	40	350	300	56	100	150
Yb (ppm)	0.194	0.311	0.437	0.386	0.186	0.283	0.448	0.463	0.220	0.647	0.465	0.326	0.208	0.416	0.148	0.219	0.118	0.0746	0.0664	0.210	0.101	0.141	0.160	0.328	0.747	0.0764	0.104	0.175	0.365	0.155	0.270	2.18	2.12	0.392	0.648	0.969
Lu (ppb)	36.8	51.2	70.0	63.3	33.5	49.5	73.8	74.1	34.6	109	73.7	57.7	34.3	69.7	25.9	35.9	18.7	12.2	9.9	33.3	18.5	23.1	28.1	50.2	121	12.2	16.2	29.2	61.5	25.5	45.8	364	327	67.9	108	160
Hf (ppb)	16.9	18.4	12.9	35.5	46.5	23.3	40.1	55.2	4.76	27.6	22.0	29.1	21.8	15.7	6.99	1.28	1.18	4.21	3.13	1.78	1.22	2.55	2.95	6.80	2.16	3.29	2.71	1.77	3.59	0.71	1.33	22.2	36.0	14.4	7.4	12.7
Ta (ppb)	4.54	3.30	2.79	4.92	5.11	2.69	2.64	4.65	2.55	4.74	3.08	3.25	1.19	1.37	1.11	0.59	0.19	0.89	0.18	0.34	0.14	0.69	0.85	1.18	0.66	0.70	0.54	0.63	0.60	0.21	0.18	5.56	2.37	2.21	1.38	2.61
Th (ppb)	70.6	20.0	31.0	37.4	43.5	85.1	188	125	23.6	99.4	38.5	65.3	49.8	39.8	20.2	2.42	3.09	13.1	4.44	3.00	8.39	3.79	4.53	9.05	4.75	10.6	8.91	6.29	14.3	4.74	4.01	25.2	20.4	56.7	36.4	37.0
U (ppb)	17.0	19.5	12.8	36.5	31.7	12.5	32.5	23.7	11.0	16.6	18.0	6.16	6.88	11.2	6.37	4.01	14.7	7.9	2.7	5.60	9.23	9.48	7.78	9.08	19.6	8.20	3.44	6.04	13.6	20.6	4.52	58.6	21.5	12.5	18.2	65.9
Y/Ho	40.8	41.9	46.7	51.5	44.2	50.9	51.3	50.8	57.9	58.5	65.0	63.8	66.8	67.0	66.9	41.1	40.7	53.8	53.5	58.4	62.0	67.2	66.2	59.2	37.4	46.6	47.3	59.0	58.9	47.1	58.3	49.6	41.7	62.2	48.6	54.9
Pr_{PAAS}/Yb_{PAAS}	0.816	0.401	0.232	0.467	0.306	0.694	0.945	0.154	0.146	0.404	0.303	0.985	0.678	0.621	0.510	0.107	0.191	0.101	0.394	0.178	0.187	0.156	0.202	0.115	0.0750	0.231	0.0729	0.149	0.342	0.110	0.0811	0.107	0.0314	0.147	0.0733	0.294
La/La*	1.43	1.48	1.87	1.52	1.93	1.59	1.43	2.04	1.46	1.35	2.04	1.56	1.61	2.06	1.76	2.47	1.99	2.25	2.60	2.25	1.73	1.80	1.98	1.94	1.75	1.67	2.15	1.79	1.99	2.45	2.10	1.89	1.37	2.04	2.29	1.91
Ce/Ce*	1.03	1.05	1.13	1.14	1.14	1.08	1.02	1.12	1.10	1.08	1.13	1.06	1.06	1.13	1.11	1.21	1.15	1.37	1.27	1.27	0.80	1.17	1.12	1.12	1.09	1.08	1.18	1.03	1.13	1.42	1.16	1.13	1.06	1.20	1.34	1.59
Eu/Eu*	3.36	3.58	3.54	3.19	3.56	3.80	3.06	3.19	3.68	3.16	3.64	2.79	2.90	3.11	3.28	3.48	3.87	3.28	3.55	3.52	3.00	3.38	3.69	3.06	3.28	3.53	3.95	3.28	3.62	3.30	3.03	3.78	3.22	3.76	3.03	3.07

*Distance from the bottom on the greenstones

**Total iron as Fe_2O_3

La/La*, Ce/Ce* and Eu/Eu*are defined by $[La/\{Pr/(Pr/Nd)^2\}]_{PAAS}$, $[Ce/\{Pr/(Pr/Nd)\}]_{PAAS}$ and $[Eu/(0.67Sm+0.33Tb)]_{PAAS}$, respectively.

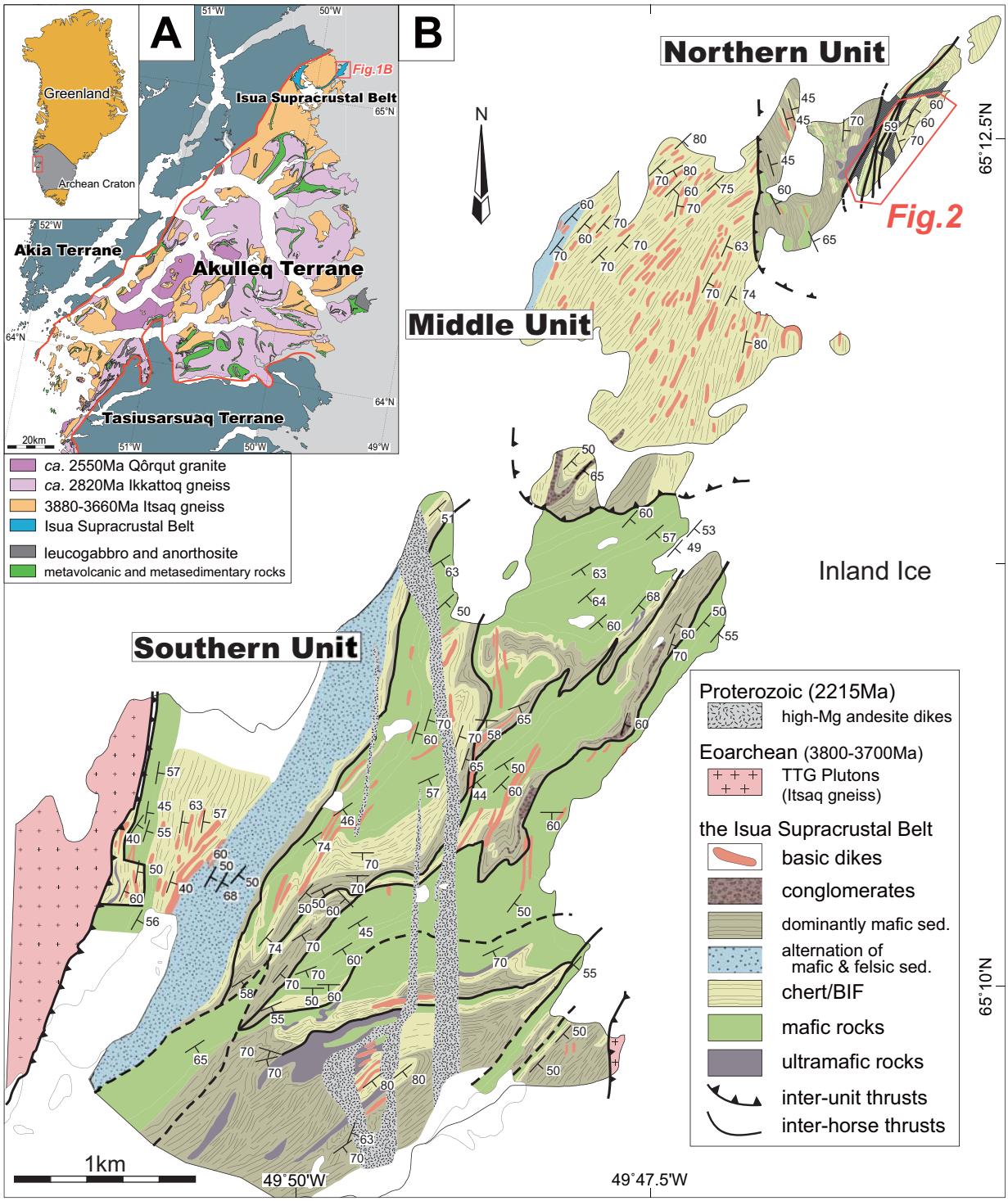
A
B
Greenland
Archean Craton
Fig.1B
Isua Supracrustal Belt
Akia Terrane
Akulleq Terrane
Tasiusarsuaq Terrane
ca. 2550Ma Qôrqut granite
ca. 2820Ma Ikkattoq gneiss
3880-3660Ma Itsaq gneiss
Isua Supracrustal Belt
leucogabbro and anorthosite
metavolcanic and metasedimentary rocks
Northern Unit
Middle Unit
Southern Unit
Fig.2
Inland Ice
N
1km
49°50'W
49°47.5'W
65°12.5'N
65°10'N
Proterozoic (2215Ma)
high-Mg andesite dikes
Eoarchean (3800-3700Ma)
TTG Plutons
(Itsaq gneiss)
the Isua Supracrustal Belt
basic dikes
conglomerates
dominantly mafic sed.
alternation of
mafic & felsic sed.
chert/BIF
mafic rocks
ultramafic rocks
inter-unit thrusts
inter-horse thrusts

Figure. 1

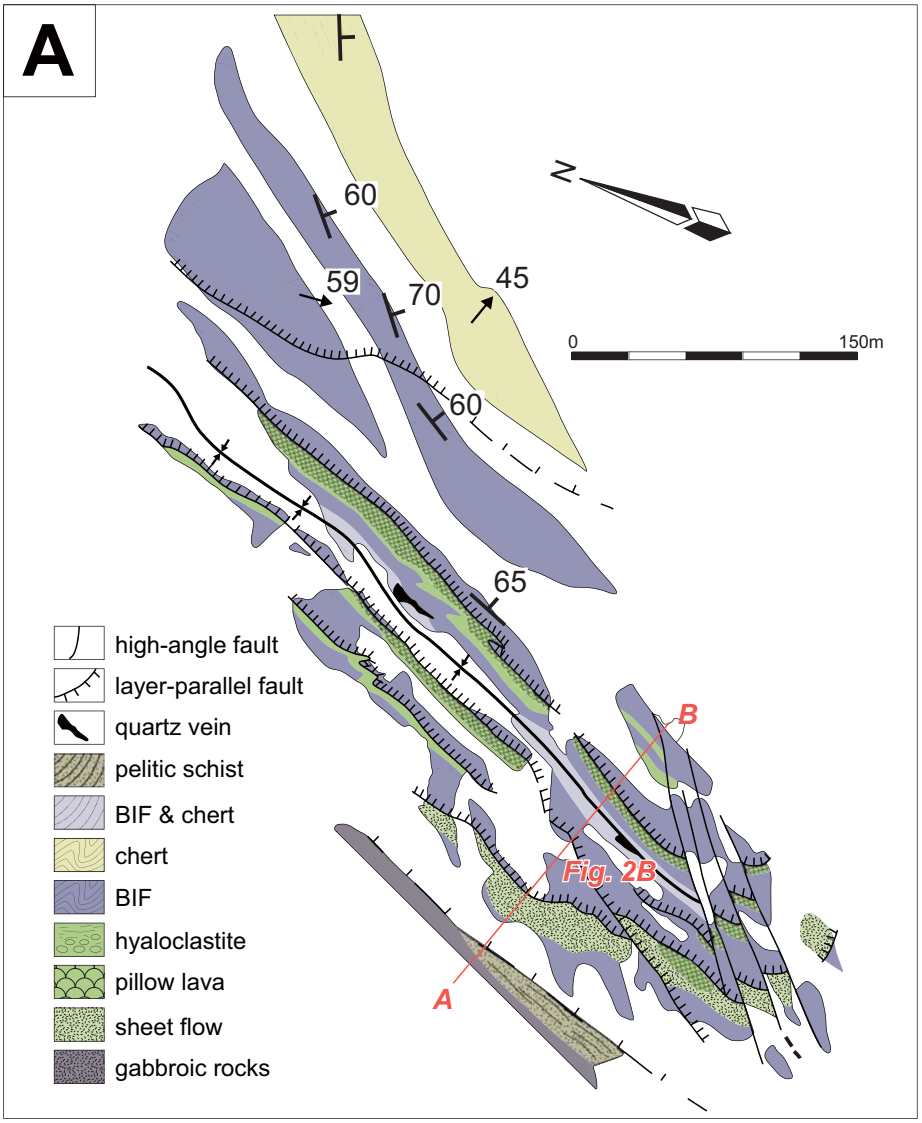
A
N
60
59
70
45
60
65
0
150m
high-angle fault
layer-parallel fault
quartz vein
pelitic schist
BIF & chert
chert
BIF
hyaloclastite
pillow lava
sheet flow
gabbroic rocks
B
Fig. 2B
A

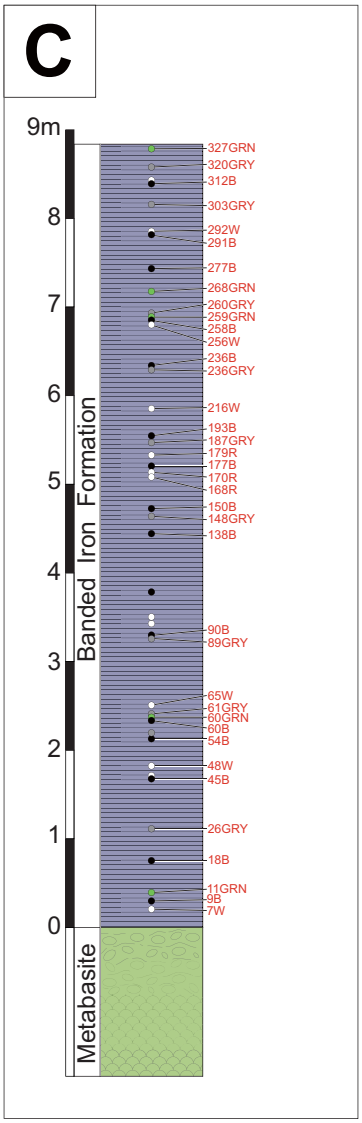
C
9m
8
7
6
5
4
3
2
1
0
Banded Iron Formation
Metabasite
327GRN
320GRY
312B
303GRY
292W
291B
277B
268GRN
260GRY
259GRN
258B
256W
236B
236GRY
216W
193B
187GRY
179R
177B
170R
168R
150B
148GRY
138B
90B
89GRY
65W
61GRY
60GRN
60B
54B
48W
45B
26GRY
18B
11GRN
9B
7W

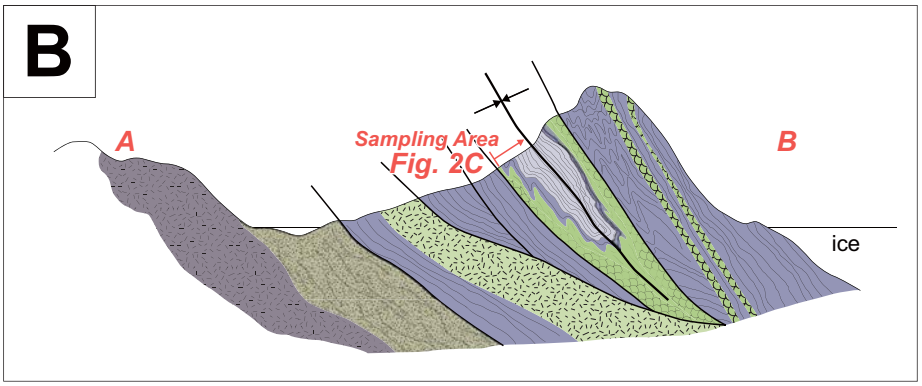
B
A
Sampling Area
Fig. 2C
B
ice

Figure. 2

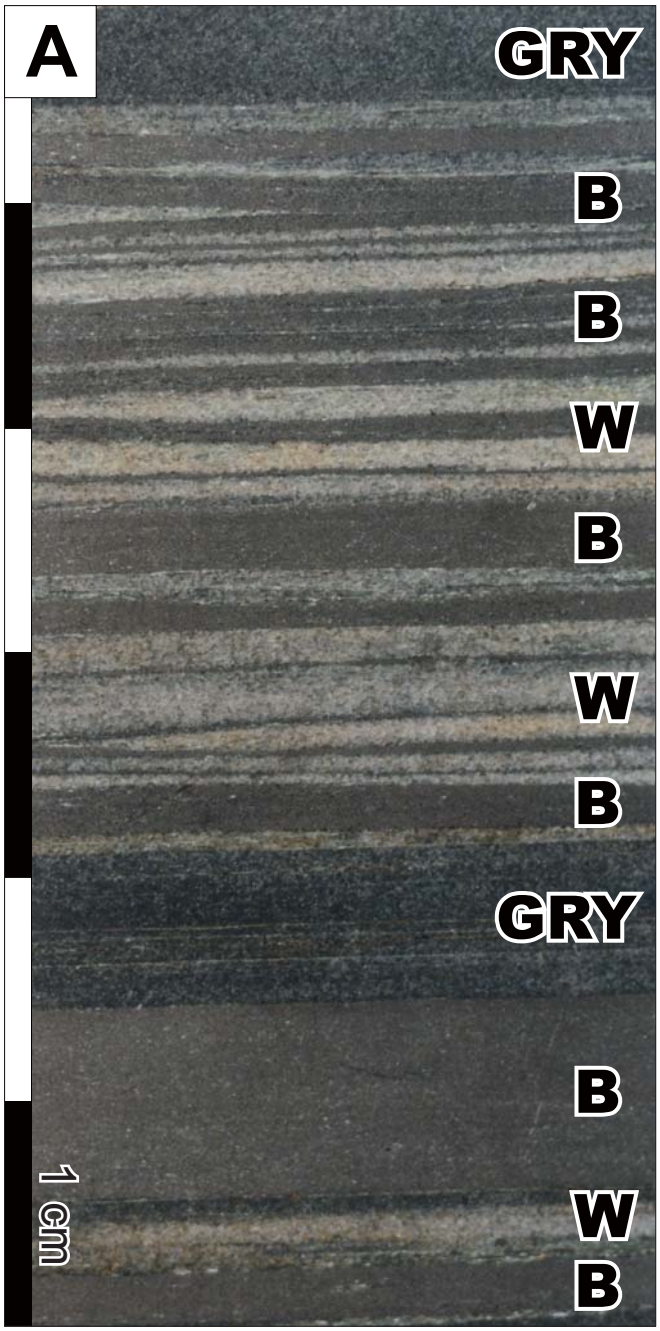

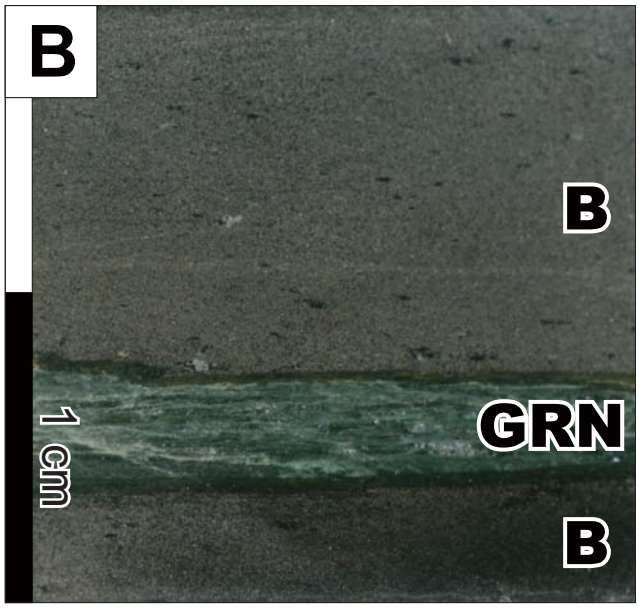

Figure. 3

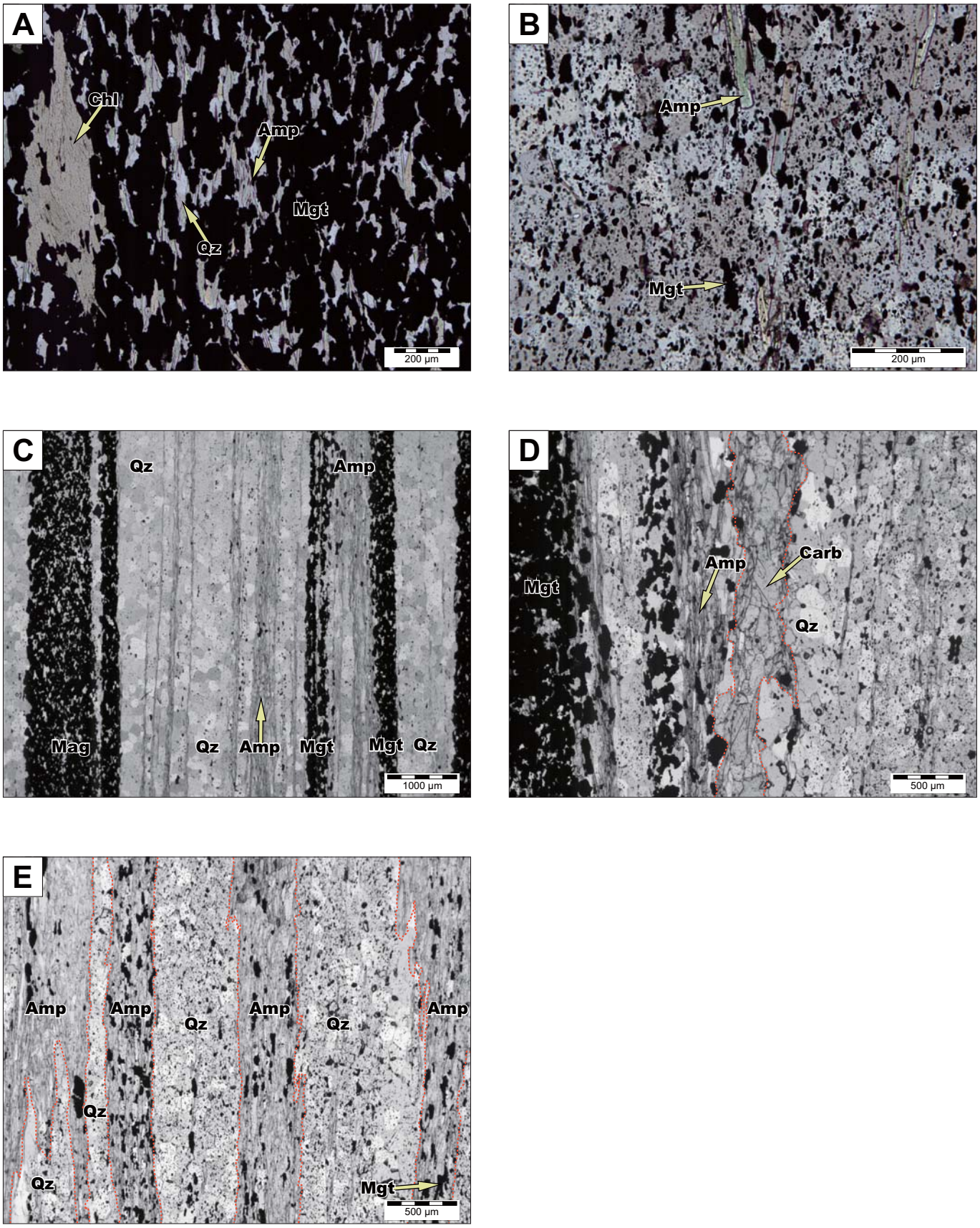
A
Chl
Amp
Mgt
Qz
200 µm
B
Amp
Mgt
200 µm
C
Qz
Amp
Mag
Qz
Amp
Mgt
Mgt
Qz
1000 µm
D
Mgt
Amp
Carb
Qz
500 µm
E
Amp
Amp
Qz
Amp
Qz
Amp
Qz
Qz
Mgt
500 µm

Figure. 4

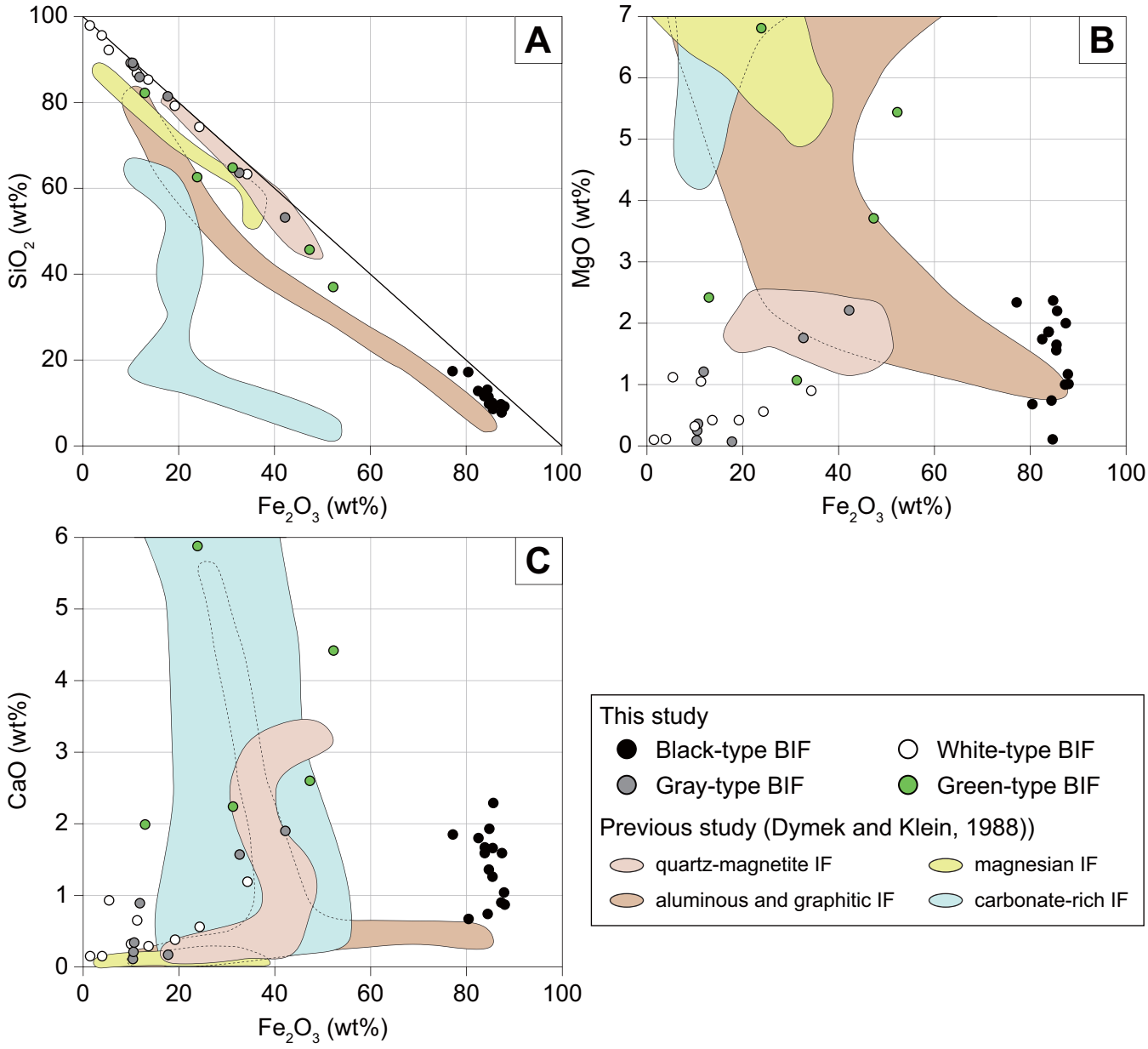
A
B
C
SiO2 (wt%)
MgO (wt%)
CaO (wt%)
Fe2O3 (wt%)
This study
Black-type BIF
White-type BIF
Gray-type BIF
Green-type BIF
Previous study (Dymek and Klein, 1988))
quartz-magnetite IF
magnesian IF
aluminous and graphitic IF
carbonate-rich IF

Figure. 5

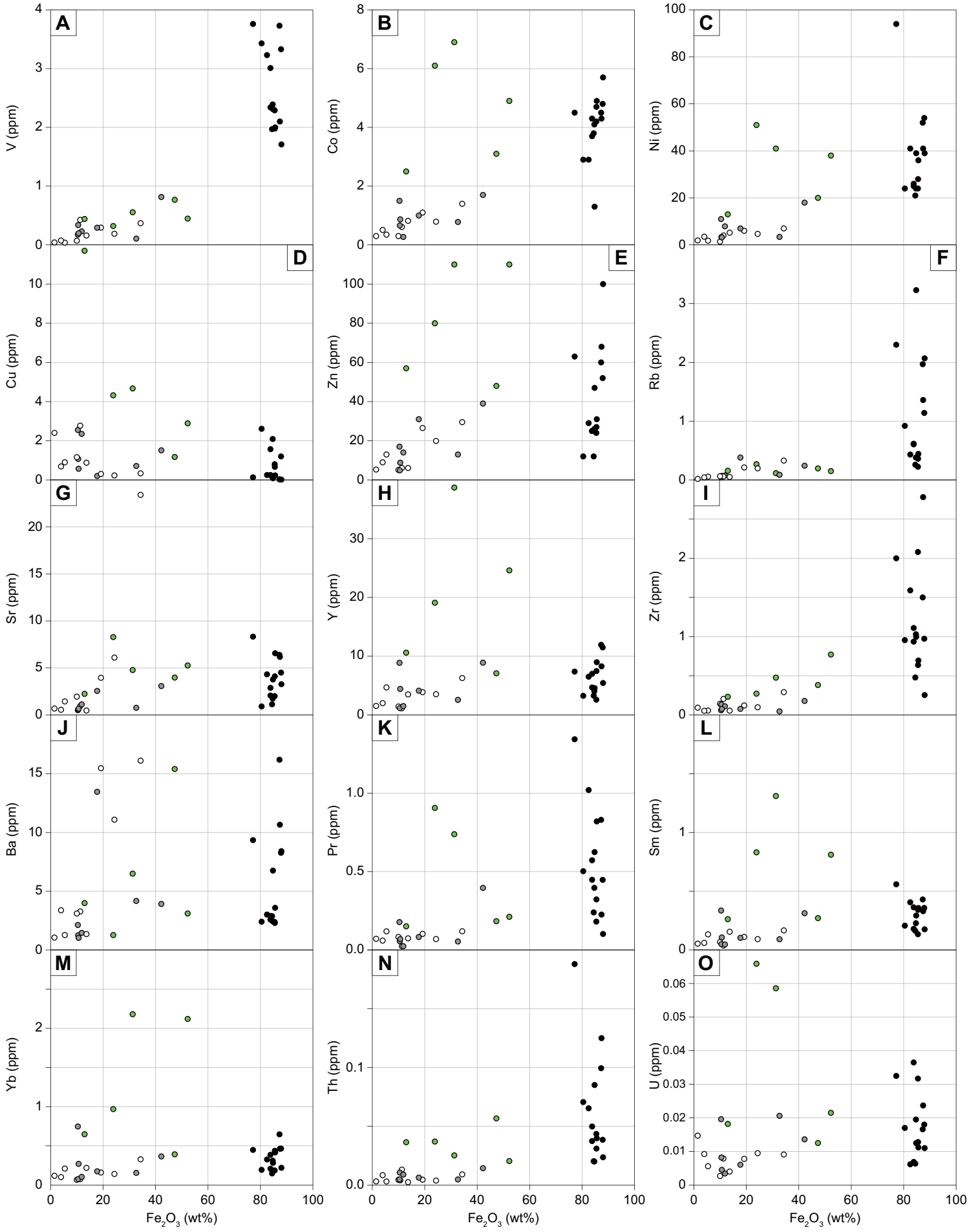
A
V (ppm)
B
Co (ppm)
C
Ni (ppm)
D
Cu (ppm)
E
Zn (ppm)
F
Rb (ppm)
G
Sr (ppm)
H
Y (ppm)
I
Zr (ppm)
J
Ba (ppm)
K
Pr (ppm)
L
Sm (ppm)
M
Yb (ppm)
N
Th (ppm)
O
U (ppm)
Fe2O3 (wt%)
Fe2O3 (wt%)
Fe2O3 (wt%)

Figure. 6

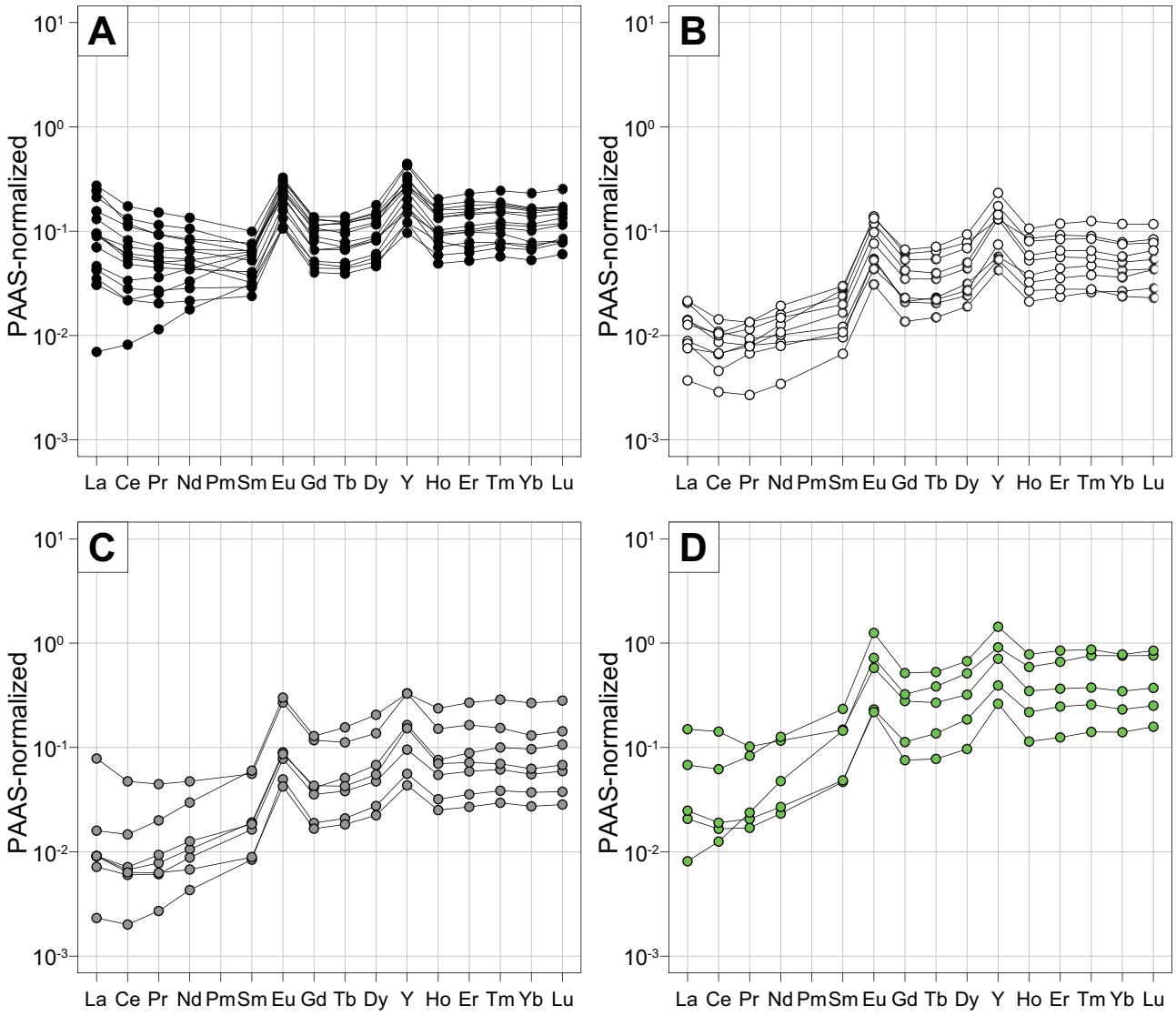
A
B
C
D
PAAS-normalized
10^{1}
10^{0}
10^{-1}
10^{-2}
10^{-3}
La Ce Pr Nd Pm Sm Eu Gd Tb Dy Y Ho Er Tm Yb Lu

Figure. 7

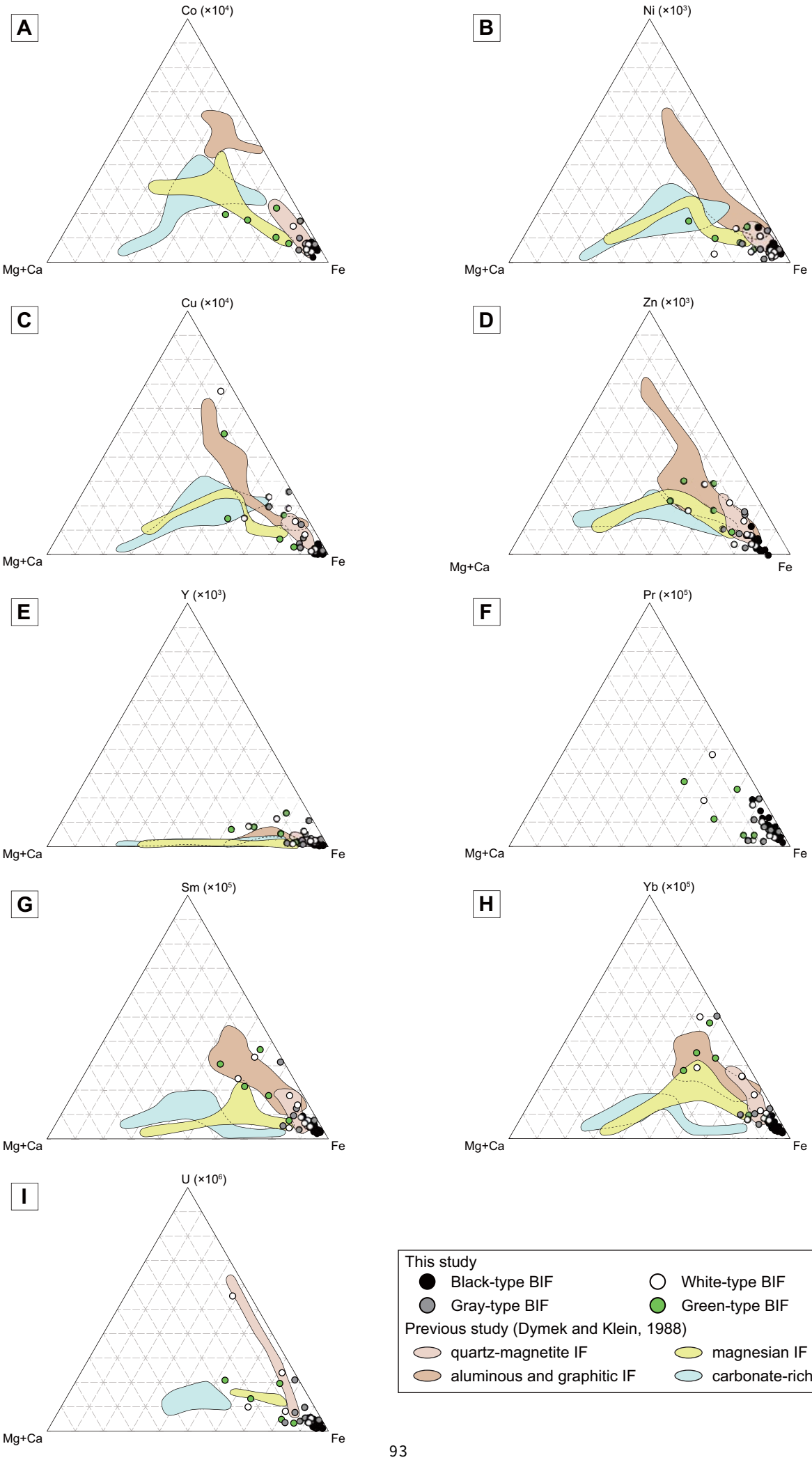
A
Co (×10⁴)
Mg+Ca
Fe
B
Ni (×10³)
Mg+Ca
Fe
C
Cu (×10⁴)
Mg+Ca
Fe
D
Zn (×10³)
Mg+Ca
Fe
E
Y (×10³)
Mg+Ca
Fe
F
Pr (×10⁵)
Mg+Ca
Fe
G
Sm (×10⁵)
Mg+Ca
Fe
H
Yb (×10⁵)
Mg+Ca
Fe
I
U (×10⁶)
Mg+Ca
Fe
This study
Black-type BIF
White-type BIF
Gray-type BIF
Green-type BIF
Previous study (Dymek and Klein, 1988)
quartz-magnetite IF
magnesian IF
aluminous and graphitic IF
carbonate-rich IF

Figure. 8

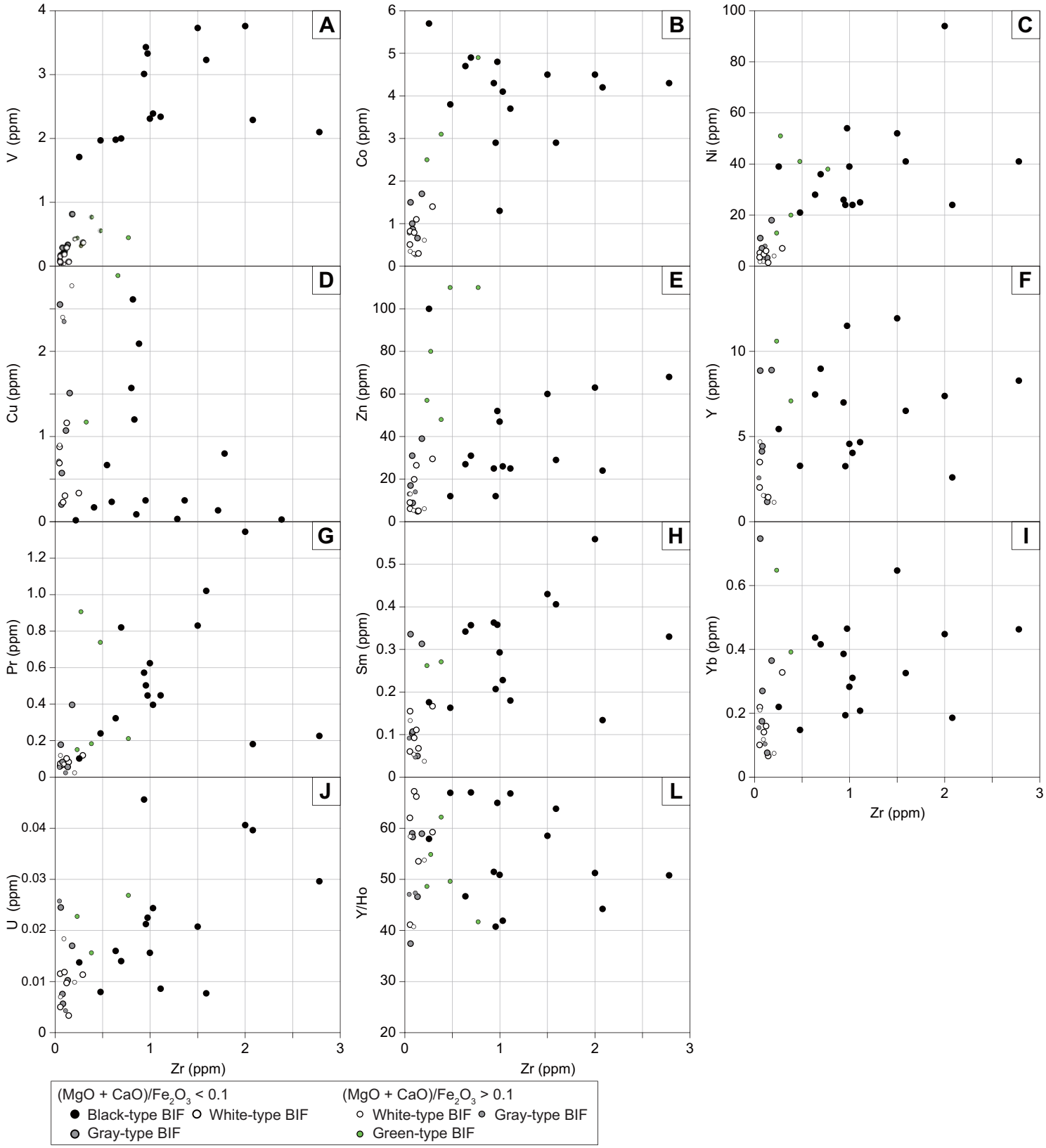
A
V (ppm)
B
Co (ppm)
C
Ni (ppm)
D
Cu (ppm)
E
Zn (ppm)
F
Y (ppm)
G
Pr (ppm)
H
Sm (ppm)
I
Yb (ppm)
J
U (ppm)
L
Y/Ho
Zr (ppm)
Zr (ppm)
(MgO + CaO)/Fe2O3 < 0.1
Black-type BIF
White-type BIF
Gray-type BIF
(MgO + CaO)/Fe2O3 > 0.1
White-type BIF
Gray-type BIF
Green-type BIF

Figure. 9

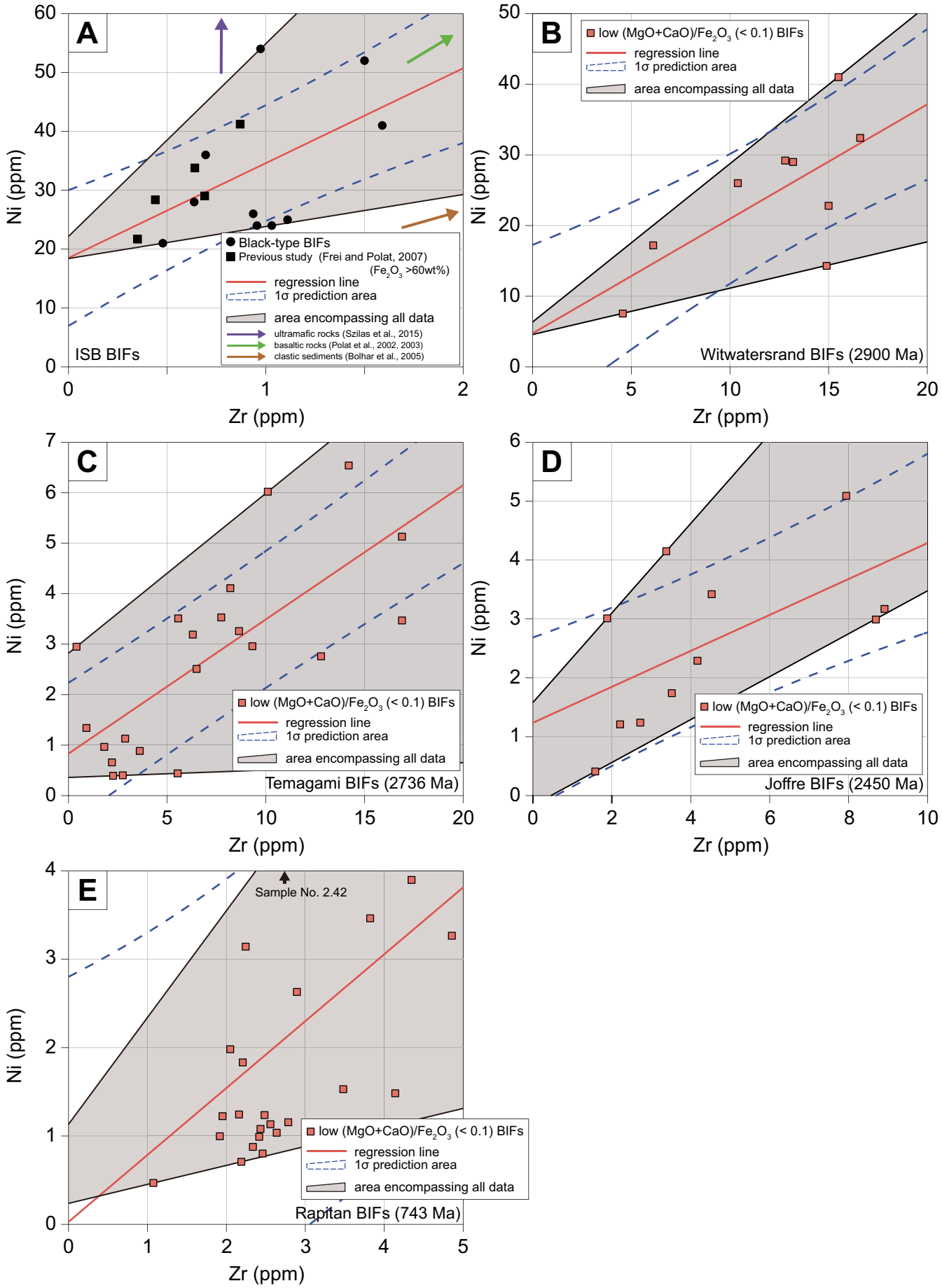
A
Ni (ppm)
Zr (ppm)
Black-type BIFs
Previous study (Frei and Polat, 2007)
(Fe_2O_3 >60wt%)
regression line
1σ prediction area
area encompassing all data
ultramafic rocks (Szilas et al., 2015)
basaltic rocks (Polat et al., 2002, 2003)
clastic sediments (Bolhar et al., 2005)
ISB BIFs
B
low (MgO+CaO)/Fe_2O_3 (< 0.1) BIFs
regression line
1σ prediction area
area encompassing all data
Witwatersrand BIFs (2900 Ma)
C
low (MgO+CaO)/Fe_2O_3 (< 0.1) BIFs
regression line
1σ prediction area
area encompassing all data
Temagami BIFs (2736 Ma)
D
low (MgO+CaO)/Fe_2O_3 (< 0.1) BIFs
regression line
1σ prediction area
area encompassing all data
Joffre BIFs (2450 Ma)
E
Sample No. 2.42
low (MgO+CaO)/Fe_2O_3 (< 0.1) BIFs
regression line
1σ prediction area
area encompassing all data
Rapitan BIFs (743 Ma)

Figure. 10

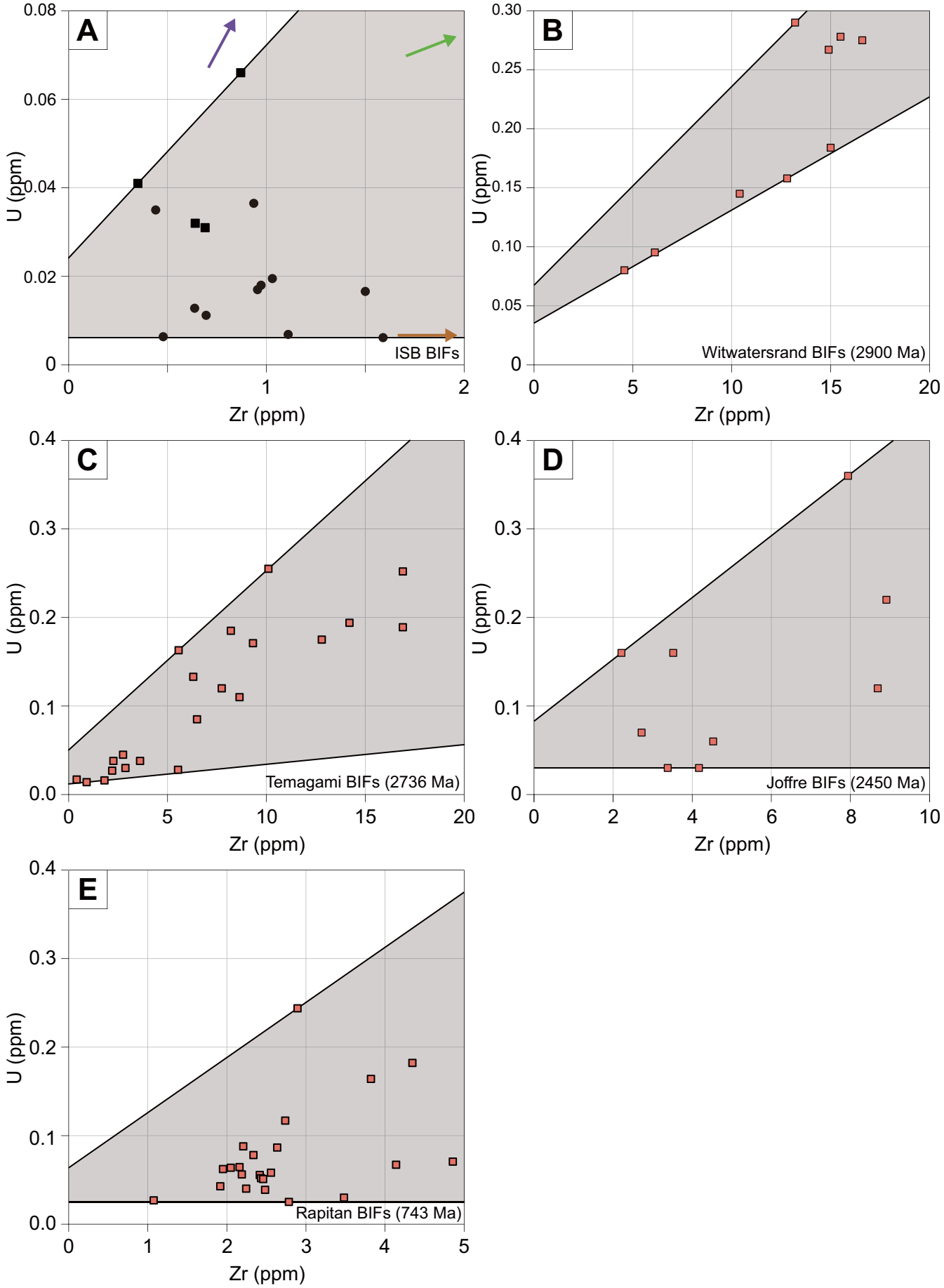
A
ISB BIFs
U (ppm)
Zr (ppm)
B
Witwatersrand BIFs (2900 Ma)
U (ppm)
Zr (ppm)
C
Temagami BIFs (2736 Ma)
U (ppm)
Zr (ppm)
D
Joffre BIFs (2450 Ma)
U (ppm)
Zr (ppm)
E
Rapitan BIFs (743 Ma)
U (ppm)
Zr (ppm)

Figure. 11

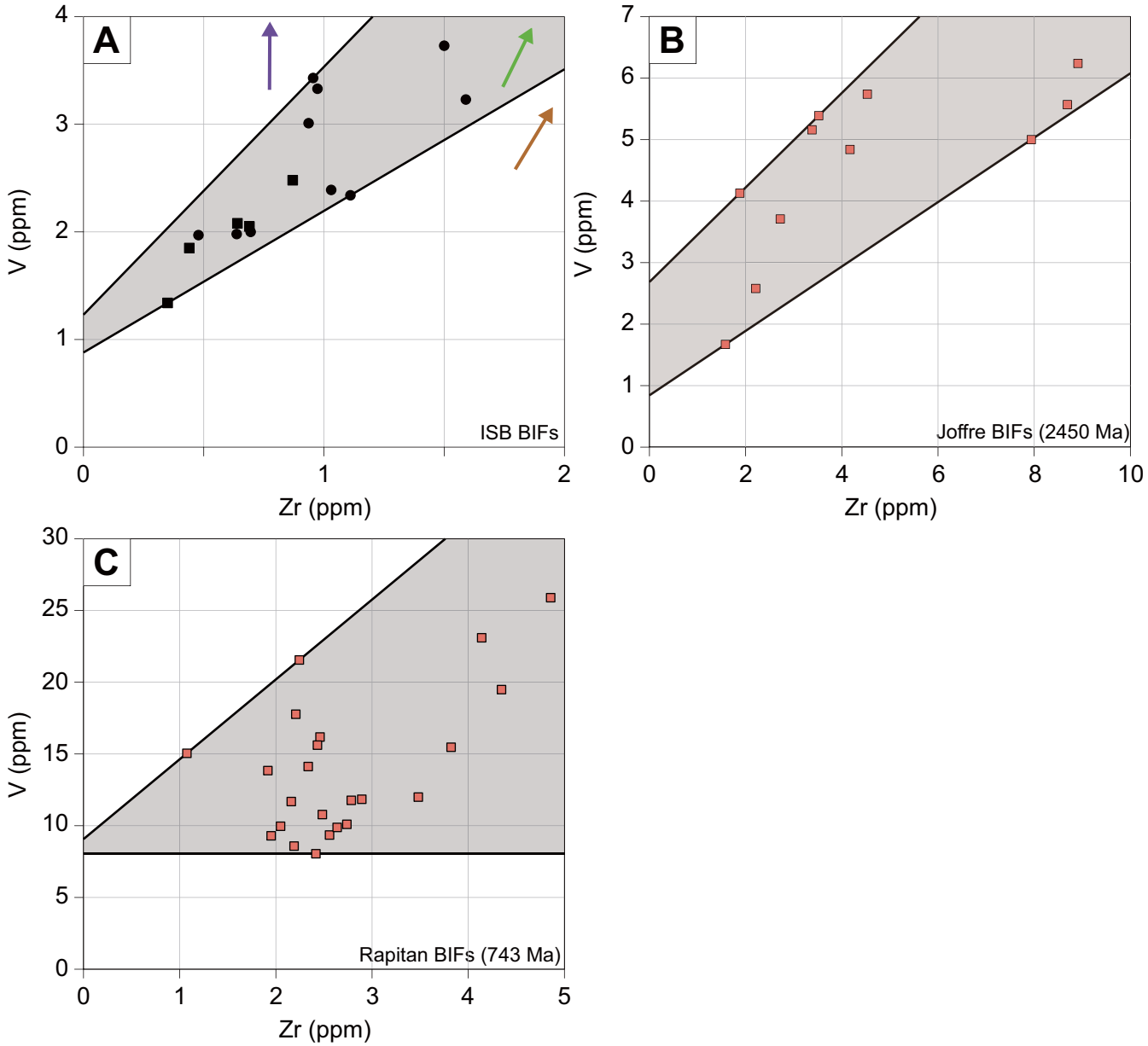
A
ISB BIFs
V (ppm)
Zr (ppm)
0
1
2
3
4
B
Joffre BIFs (2450 Ma)
V (ppm)
Zr (ppm)
0
2
4
6
8
10
1
3
5
7
C
Rapitan BIFs (743 Ma)
V (ppm)
Zr (ppm)
0
1
2
3
4
5
10
15
20
25
30

Figure. 12

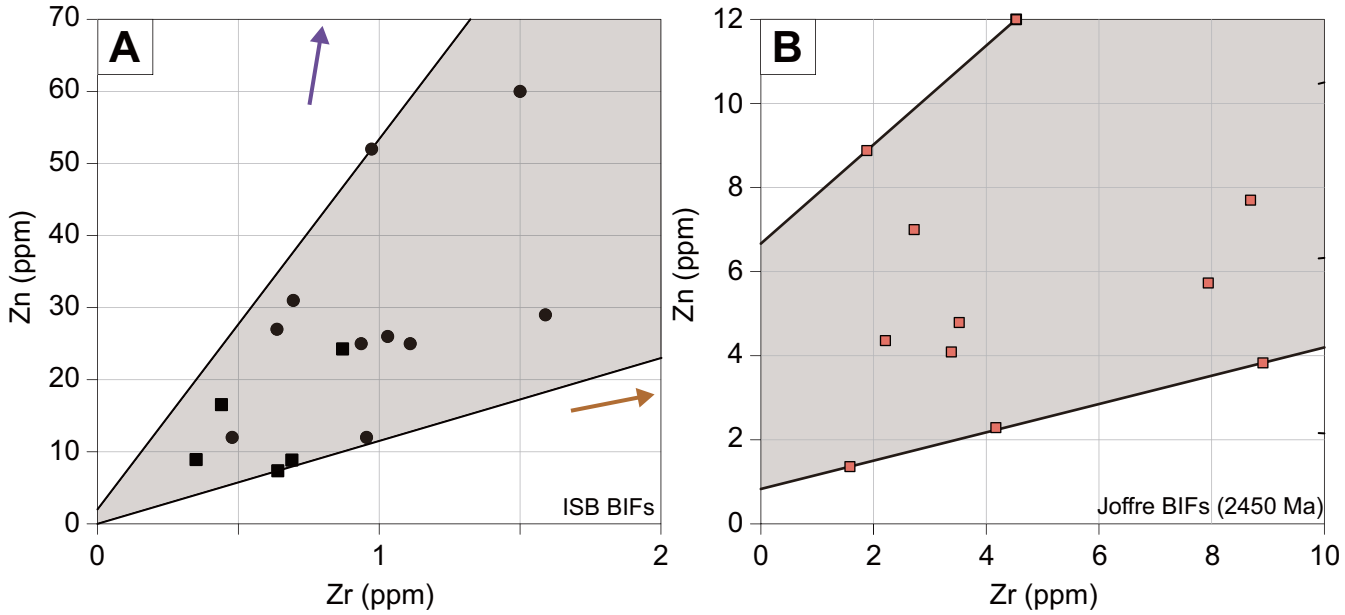
A
Zn (ppm)
Zr (ppm)
ISB BIFs
0
10
20
30
40
50
60
70
0
1
2
B
Zn (ppm)
Zr (ppm)
Joffre BIFs (2450 Ma)
0
2
4
6
8
10
12
0
2
4
6
8
10

Figure. 13

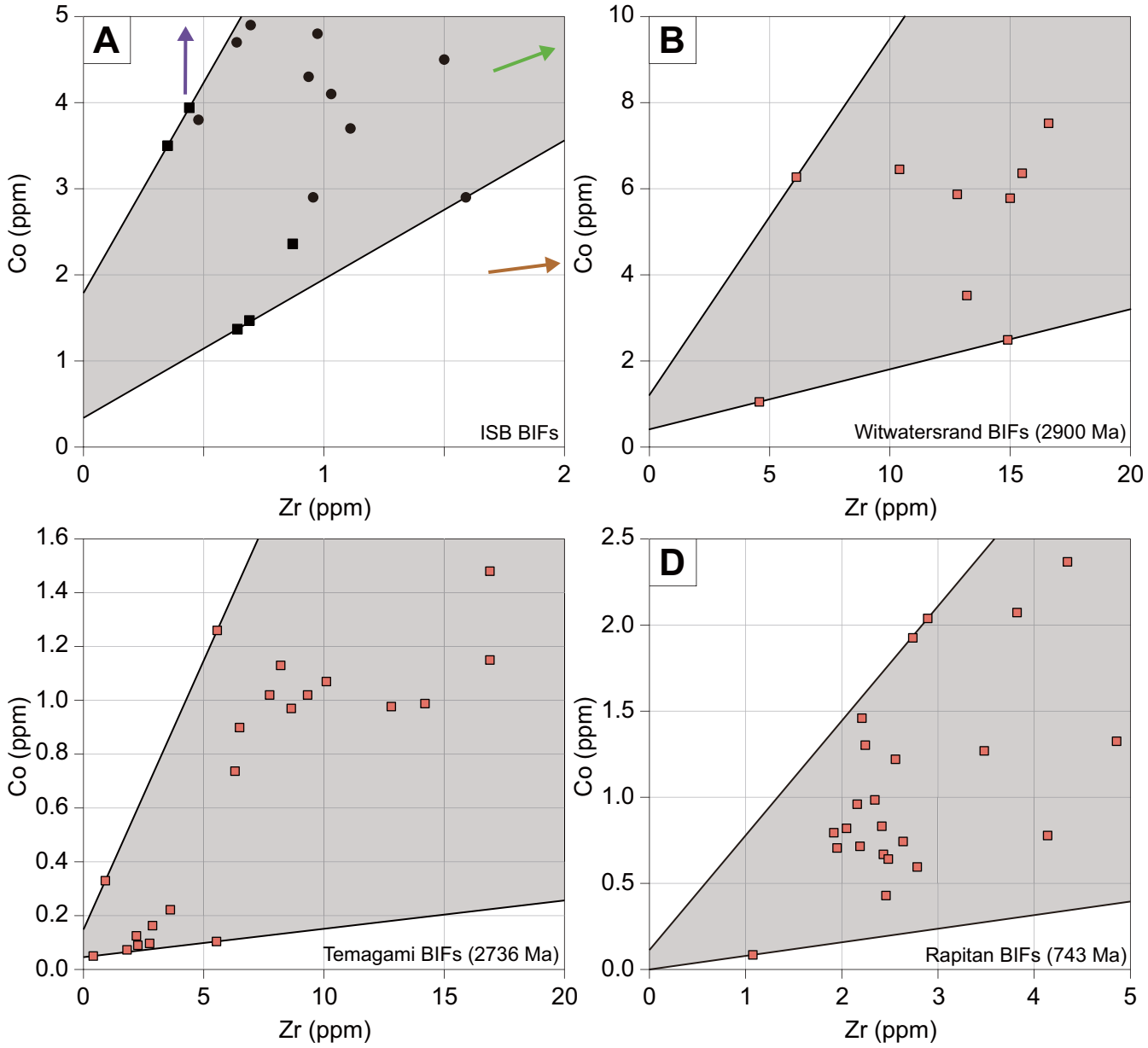
A
ISB BIFs
Co (ppm)
Zr (ppm)
B
Witwatersrand BIFs (2900 Ma)
Co (ppm)
Zr (ppm)
Temagami BIFs (2736 Ma)
Co (ppm)
Zr (ppm)
D
Rapitan BIFs (743 Ma)
Co (ppm)
Zr (ppm)

Figure. 14

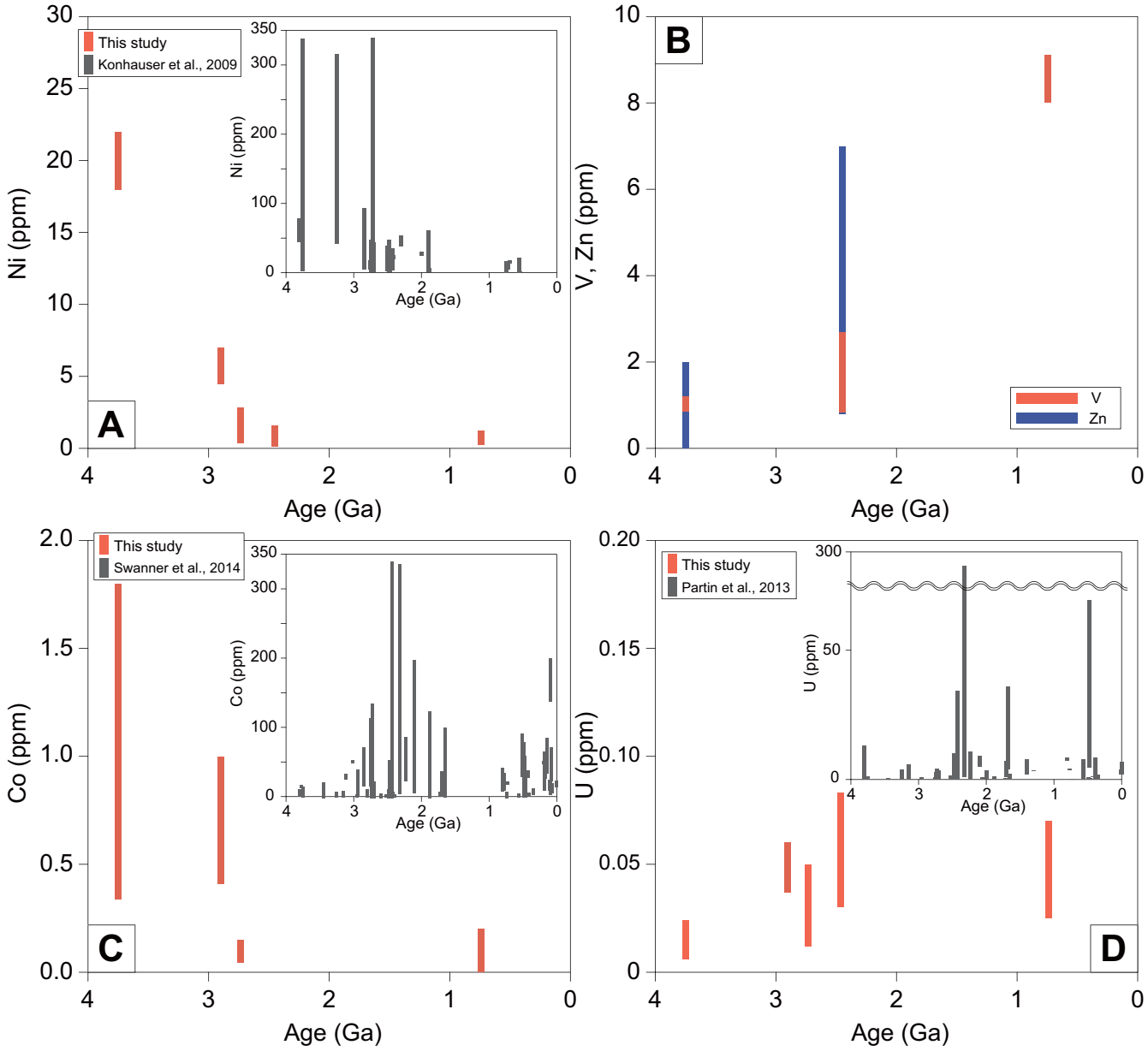
A
This study
Konhauser et al., 2009
Ni (ppm)
Age (Ga)
B
V
Zn
V, Zn (ppm)
Age (Ga)
C
This study
Swanner et al., 2014
Co (ppm)
Age (Ga)
D
This study
Partin et al., 2013
U (ppm)
Age (Ga)

Figure. 15

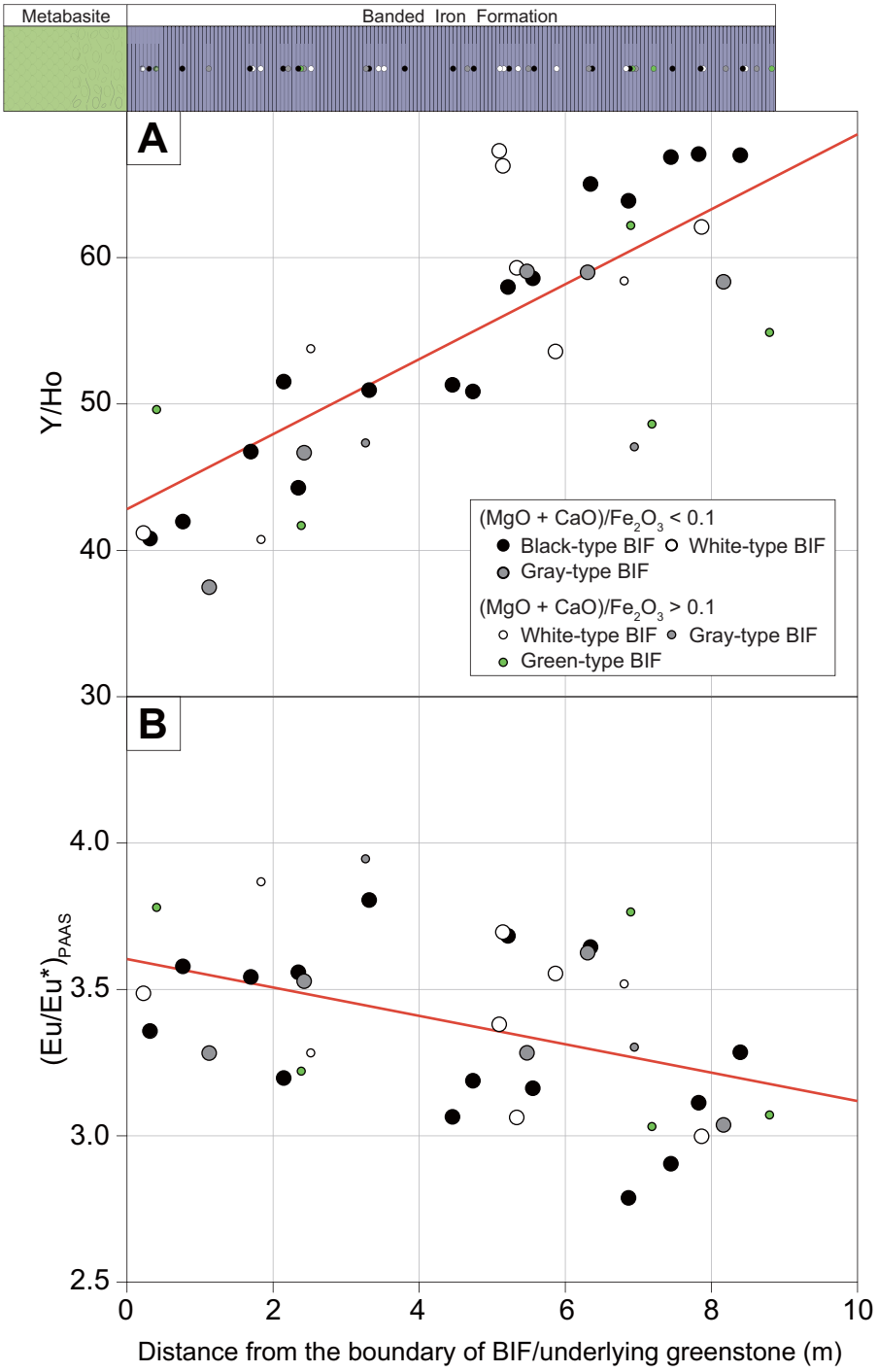
Metabasite
Banded Iron Formation
A
B
Y/Ho
(Eu/Eu*)PAAS
(MgO + CaO)/Fe2O3 < 0.1
Black-type BIF
White-type BIF
Gray-type BIF
(MgO + CaO)/Fe2O3 > 0.1
White-type BIF
Gray-type BIF
Green-type BIF
Distance from the boundary of BIF/underlying greenstone (m)

Figure. 16

Chapter III.

Occurrence and geochemistry of the oldest banded iron formation in the Saglek Block, Northern Labrador, Canada

Abstract

The chemical compositions of the Eoarchean banded iron formations (BIFs) might provide the chemical compositions of the Eoarchean seawater, where the early life inhabited. In this study, we performed geological, petrographical and geochemical study of BIFs of the Eoarchean Nulliak supracrustal rocks in Northern Labrador, Canada.

The BIFs in the Nulliak Island, which are interlayered with mafic rocks, are composed of magnetite, quartz, orthopyroxene and clinopyroxene. They have higher bulk Fe contents than the Pangertok Inlet BIFs. On the other hand, the BIFs in the Pangertok Inlet, which are accompanied with mafic and carbonate rocks, comprises magnetite, quartz and clinopyroxene. They have higher normative opal and dolomite components than the Nulliak Island BIFs, suggesting that carbonate and silica minerals were more precipitated at their depositional environment. The mineralogical difference of both BIFs is probably due to difference of XCO_2 of the metamorphic fluid.

The BIFs show positive correlations of rare earth element (REE) and transitional element (V, Cr, Ni, Cu, U) contents with Zr contents, suggesting that involvement of clastic and volcanic materials influenced on their contents. The contamination-free BIFs

have low V, Cr and U contents, suggesting that the Eoarchean seawater had quite low V, Cr and U contents possibly because of the anoxic conditions of ocean and terrestrial environments. On the other hand, Ni contents in contamination-free BIFs are higher than those of the Late Archean BIFs, suggesting that the Eoarchean seawater was enriched in dissolved Ni, as suggested by previous studies.

Differences in the Post-Archean Australian Shale (PAAS)-normalized REE + Y compositions, namely Eu and Y anomalies, and normative carbonate and opal components between the BIFs in the Pangertok Inlet and Nulliak Island suggest that they were precipitated from mixing of alkaline, Si-rich, hydrothermal fluid with acidic-neutral ambient seawater near hydrothermal vent sites, and the former, especially, was more strongly influenced by the hydrothermal fluid.

1. Introduction

The Earth is a dynamic planet, where oceans cover the surface and many organisms actively inhabit. It is widely considered that the ocean existed *ca*. 3.9-3.8 Ga from geological evidence such as chemical sedimentary rocks and pillow basalts in *ca.* 3.8 Ga Isua supracrustal belt, West Greenland (Komiya et al., 1999; Nutman et al., 1984) and chemical sedimentary rocks in *ca.* 3.9 Ga Nulliak supracrustal rocks (Komiya et al., 2015; Shimojo et al., 2016). In addition, recent oxygen isotope analyses of the Hadean zircons suggest that the ocean has already existed *ca.* 4.2 Ga (Valley et al., 2002; Wilde et al., 2001). On the other hand, some geochemical evidence indicates that organisms already existed in the Eoarchean ocean (Mojzsis et al., 1996; Ohtomo et al., 2014; Rosing, 1999; Ueno et al., 2002), but it is still obscure how the Eoarchean surface environment such as the seawater compositions of bio-essential elements was suitable for the early life.

A banded iron formation (BIF) is a chemical sediment with alternating iron and silica-rich bands, and mainly occurred before the Paleoproterozoic (Isley and Abbott, 1999; Klein and Beukes, 1992). Because some of them have diagnostic rare earth element and Y (REE+Y) patterns, namely positive La and Y anomalies, it is considered that they were precipitated from the ocean with/without hydrothermal fluid (Bau and Dulski, 1996;

Bau and Dulski, 1999; Bolhar et al., 2004). In that case, their compositions possibly provide a good proxy of ancient seawater compositions of bio-essential or redox-sensitive elements (e.g. P, Ni, Cr, Co and U) (e.g. Bjerrum and Canfield, 2002; Konhauser et al., 2009; Konhauser et al., 2011; Partin et al., 2013; Swanner et al., 2014). Recently, Konhauser and his colleagues suggested that the Archean seawater was more enriched in Ni contents due to higher hydrothermal Ni influx from komatiites to ocean based on higher molar Ni/Fe ratios in the Archean BIFs than post-Archean BIFs and iron-oxide deposits, and implied that the enrichment of Ni contents resulted in prosperity of methanogens because Ni is an essential element to form a Cofactor F430 (Haugaard et al., 2016; Konhauser et al., 2009; Konhauser et al., 2011; Mloszewska et al., 2012; Mloszewska et al., 2013; Pecoits et al., 2009).

However, the Ni/Fe ratios of the BIFs are highly variable, and range from 3.96×10^{-5} to 4.54×10^{-4} for *ca.* 3.8 Ga BIFs in the Isua supracrustal belt (ISB) so that the minimum value is almost comparable to those of the post-Archean BIFs (Konhauser et al., 2009). Generally speaking, compositions of BIFs depend on not only chemical compositions and physicochemical conditions of contemporaneous ocean but also their lithofacies because the BIFs also contain silicate, carbonate and sulfide minerals as well as iron-oxide and silica minerals. The precursors of the iron-oxide, silica and carbonate

minerals were precipitated from seawater, but the silicate minerals were formed during the diagenesis, metamorphism and alteration, or derived from clastic and volcanic materials (Klein, 2005). The silica minerals virtually do not contain REE and transition elements but the carbonate and silicate minerals usually host them very much. As a result, amphibole-rich BIFs are enriched in REE, Y and transition elements so that an amphibole-rich, Magnesian IF has the highest molar Ni/Fe ratio in the ISB (Konhauser et al., 2009). It is necessary to obtain a composition of a contamination-free BIF with only iron-oxide minerals and to correct the involvement of clastic and volcanic materials in order to estimate the ancient seawater. Previous works selected the BIFs with lower Al (< 1wt%) and HFSE (< 20 ppm) contents (e.g. Konhauser et al., 2009), but recent reinvestigation of the BIFs in the ISB showed that even the BIFs with the low Al_2O_3 and Zr contents form a positive correlations of REE and transition elements with the Al_2O_3 and Zr contents possibly due to the contamination (Aoki et al., 2016; Viehmann et al., 2015). Aoki and others (2016) proposed an alternative method to obtain a composition of a contamination-free BIF based on the regression lines between the transition metals and Zr contents.

The Eoarchean supracrustal rocks including the BIFs are found only in some areas of the Akilia Island, Isua supracrustal belt, Nuvvuagittuq supracrustal belt and Nulliak

supracrustal rocks (Komiya et al., 2015; Mojzsis et al., 1996; Nutman, 1986; O'Neil et al., 2007; Ryan and Martineau, 2012). The BIFs in the Isua supracrustal belt have been well studied for their trace element compositions (Aoki et al., 2016; Bolhar et al., 2004; Dymek and Klein, 1988), stable isotope ratios of S (Mojzsis et al., 2003; Whitehouse et al., 2005), Si (André et al., 2006) and Fe (Dauphas et al., 2004; Dauphas et al., 2007; Whitehouse and Fedo, 2007; Yoshiya et al., 2012; Yoshiya et al., 2015), Pb isotope systematics (Frei et al., 1999; Frei and Polat, 2007; Moorbath et al., 1973) and Sm-Nd isotope systematics (Frei et al., 1999; Frei and Polat, 2007; Shimizu et al., 1990). However, the origin of the BIF in the Akilia Island is still controversial whether chemical sedimentary rocks or metasomatized ultramafic rocks (e.g. Fedo and Whitehouse, 2002). The BIFs in the Nuvvuagittuq supracrustal rocks have diagnostic positive La and Y anomalies of chemical sedimentary rocks, but because the Y anomaly ranges from 1.09 to 1.70 and is much smaller than those in the ISB, it is considered that the BIF was possibly formed in an environment with more hydrothermal fluid component (Mloszewska et al., 2012; Mloszewska et al., 2013).

Recent reappraisal of U-Pb dating of zircons from the Uivak Gneisses intruding into the Nulliak supracrustal rocks showed that the supracrustal rocks were formed over 3.9 Ga so that the geochemical study allows us to estimate a >3.9 Ga seawater

composition (Shimojo et al., 2016). Nutman and others (1989) reported the REE and HFSE contents of the BIFs in the Nulliak Island and Pangertok Inlet areas and suggested that the chemical compositions reflect contemporaneous seawater because they have diagnostic Y anomalies. However, the high HFSE contents, ranging from 7.2 to 75.4 ppm in Zr contents, indicate that they severely suffered from contamination of clastic and volcanic materials. In addition, they did not cite a cause of geological, chemical and mineralogical differences between oxide-type BIFs in the Nulliak Island and carbonate-type BIF in the Pangertok Inlet.

In this study, we described geological and mineralogical differences between the BIFs in the Nulliak Island and Pangertok Inlet in the Saglek Block, and performed geochemical analyses of them to estimate the Eoarchean seawater composition.

2. Geological outlines of the Saglek-Hebron area and the Nulliak supracrustal rocks

The Saglek-Hebron area is located in the northeastern part of the Labrador Peninsula, northeast Canada, and is underlain by the early Archean granite-greenstone belt terrain, called the Saglek Block (Fig. 1A, B). The Saglek Block is a western margin of the North Atlantic Craton from the Scotland through the southern part of Greenland to the Labrador. Geological and geochronological similarities indicate that it correlates with the Akulleq terrane including the Eoarchean Akilia association and Itsaq Gneiss Complex in West Greenland (Bridgwater and Schiøtte, 1991) (Fig. 1A). This area is underlain by the Early to Late Archean suites including granitoid, sedimentary rocks, volcanic rocks and ultramafic rocks, mafic dikes and young granite (Bridgwater et al., 1975; Bridgwater and Schiøtte, 1991; Collerson and Bridgwater, 1979; Collerson, 1983; Komiya et al., 2015; Schiøtte et al., 1989a). The Archean rocks are mainly subdivided into two groups based on crosscutting relationships of mafic to ultramafic Mesoarchean dykes, called the Saglek dyke (Bridgwater et al., 1975): a pre-Saglek dyke suite of the Nulliak supracrustal rocks and Uivak Gneisses, and a post-Saglek suite of the Upernavik supracrustal rocks and Lister Gneiss, respectively.

The Uivak Gneisses are subdivided into two groups based on their petrographic observation, ages and crosscutting relationships: Uivak I and II suites, respectively. The Uivak I orthogneiss, generally speaking, is characterized by grayish color and relatively fine-grained, and tonalitic-trondhjemitic composition (Bridgwater and Collerson, 1976; Collerson et al., 1976; Schiøtte et al., 1989a; Schiøtte et al., 1989b). On the other hand, the Uivak II gneiss suite comprises porphyritic granodioritic and associated dioritic gneisses, commonly contains megacrysts of feldspar, and has relatively darker color than the Uivak I gneiss due to high iron contents (Bridgwater and Collerson, 1976; Collerson et al., 1976). The age of the protolith of the Uivak orthogneiss was equivocal (Collerson, 1983; Krogh and Kamo, 2006; Regelous and Collerson, 1996; Schiøtte et al., 1989a; Schiøtte et al., 1989b), and previous works suggested that the protolith of Uivak I was formed at 3634-3732 Ma (Krogh and Kamo, 2006; Schiøtte et al., 1989a; Schiøtte et al., 1989b) or over 3.8 Ga (Regelous and Collerson, 1996) whereas protolith of Uivak II around 3760 Ma (Wanless et al., 1979). However, recent reappraisal of geological occurrence and detailed zircon geochronology of Uivak Gneisses in the St. John's Harbor South area showed that the Uivak gneisses comprise at least five generations, and the oldest generation (the Iqaluk Gneiss) has over 3.9 Ga age (Komiya et al., 2016; Shimojo et al., 2016).

The Nulliak supracrustal rocks are composed mainly of ultramafic rocks, mafic volcanic and intrusive rocks, chemical sedimentary rocks of BIFs, chert, carbonate rocks and clastic sedimentary rocks of conglomerate and pelitic rocks. Because the supracrustal rocks are intruded by the Uivak gneisses, the supracrustal rocks were formed before the Uivak gneiss. The supracrustal rocks in the St John's Harbour South and Pangertok Inlet consist of piles of fault-bounded blocks, which are composed of the ultramafic rocks, mafic rocks and sedimentary rocks in ascending order, similar to modern ophiolites. In addition, small-scale duplex structures are found over the areas. The presence of duplex structures and an ophiolite sequence suggests that the > 3.9 Ga Nulliak supracrustal belts originate from an accretionary complex (Komiya et al., 2015).

These supracrustal rocks and orthogneisses underwent multiple metamorphic events. Based on the disturbance of whole-rock isotopic systems on Uivak gneisses and U-Pb ages of rims of zircons, at least two metamorphic events occurred at 3600 Ma (Bridgwater and Collerson, 1976; Schiøtte et al., 1989a; Schiøtte et al., 1989b) and at 2800-2700 Ma (Collerson, 1983; Schiøtte et al., 1989a; Schiøtte et al., 1989b). A major, sub-vertical, NS-trending fault, the Handy fault, runs from Handy Island through St. Jones Harbour to the south, and separates two metamorphic terranes based on indicative metamorphic minerals such as a orthopyroxene in gneisses and basic rocks, and the Early

Archean rocks were suffered from the granulite facies metamorphism in the western part whereas sub-granulite facies rocks are sporadically preserved in the eastern part (Bridgwater et al., 1975; Collerson et al., 1976; Schiøtte et al., 1986).

3. Geological occurrence of the BIFs in the Nulliak supracrustal rocks

Previous geological works showed that BIFs occur only in the Nulliak Island, its opposite coast, Pangertok Inlet and the south of St. John's Harbour (Ryan and Martineau, 2012), but recent reinvestigation found the BIFs in Big Island and Shuldham Island, which have been considered as the Upernavik supracrustal rocks (Komiya et al., 2015). On the other hand, the reinvestigation revealed that the putative BIFs in the south of St. John's Harbour area and the south of the Pangertok Inlet are derived from mafic rocks metasomatized by thin granitic intrusions.

3.1. Occurrence of the BIFs in the Nulliak Island

Supracrustal rocks occur in southwestern part of the Nulliak Island (Fig. 1B, 2A). The supracrustal rocks are composed of ultramafic rocks, mafic rocks (garnet amphibolites) and BIFs, and they mostly strike NW-SE and dip moderately to gently west. The supracrustal body is bounded by the Uivak gneiss on both the eastern and western sides, and was also intruded by the Uivak gneiss in the center to form two belts (Fig. 2A). The supracrustal rocks belong to the Nulliak supracrustal rocks because the supracrustal rocks and Uivak gneisses are intruded by the Saglek dykes. Recently, U-Pb dating of the Uivak Gneiss showed that the Uivak Gneisses in the Nulliak Island and the opposite side

have *ca.* 3.75 and 3.85 Ga ages, respectively (Komiya et al., 2016). Moreover, their rocks are intruded by many, thin N-S trending granitic intrusions all over the area.

The supracrustal body comprises two layer-parallel-fault-bounded successions with similar lithostratigraphies, which consist of mafic rock units interlayered with thin BIF layers on the ultramafic bodies. At least eight BIF layers are interlayered with the mafic rock units, and they mostly occur as 0.3 - 3 m-thick layers except for a very thick, *ca.* 31.5 m thick, layer along the southwest shore of the island (Fig. 2A, B, C). The figures 2B and 2C show a sketch map and photographs of an outcrop at the southwest shore. The BIF succession is composed of two parts, bounded by a basaltic layer in the middle part. The lower part of each BIF layer is interlayered with thin basaltic layers, suggesting they were deposited almost simultaneously or at the late stage of basaltic volcanism. The BIFs comprise alternation of two bands: 0.1 to 3 cm-thick Fe-rich black bands and 0.1 to 1 cm-thick Si-rich white bands, respectively (Fig. 2D). The former is composed mainly of magnetite and iron-bearing silicates whereas the latter comprises quartz. Because intraformational folds are observed in some places, original sedimentary structures are still preserved in the outcrop (Fig. 2E).

3.2. Occurrence of the BIFs and cherts in the Pangertok Inlet

A supracrustal body occurs at the eastern side of the Pangertok Inlet (Fig. 1B, 3A). Because two Saglek dykes are intruded into the supracrustal body and the orthogneiss, the supracrustal rocks and orthogneisses belong to the Nulliak supracrustal rocks and Uivak gneiss, respectively (Komiya et al., 2015). The supracrustal body forms antiform, and occurs as an enclave within the Uivak Gneiss. They generally show strikes from 20°W to 20°E with dips to SW by 10 to 60° on the western limb, whereas dip to SE by 30 to 70° on the eastern limb. The supracrustal rocks consist of ultramafic rocks, mafic rocks, BIFs, chert and carbonate rocks. They show lithostratigraphic repetition from mafic rocks through carbonate rocks to BIFs on the both limbs. Occurrence of branching of carbonate and BIF layers in the western limb suggests that the supracrustal belt comprises some fault-bounded subunits with similar lithostratigraphy of mafic rocks, carbonate rocks, and BIFs in ascending order (Komiya et al., 2015).

Seven thin (< 3m thick) BIF layers are present in the Pangertok Inlet area, and they do not directly overlie mafic rocks but occur on carbonate rocks, in contrast to those in the Nulliak Island (Fig. 3B). They are composed of alternation of two lithologies: 0.1 to 1 cm-thick Fe-rich blackish to greenish bands and 0.1 to 3cm-thick Si-rich white bands (Fig. 3C). The former is composed mainly of magnetite and Fe-silicates whereas the latter

consists of quartz. The BIFs in this area have more Si-rich bands relative to the BIFs in the Nulliak Island.

4. Sample preparation and analytical methods of the BIFs

For chemical analysis, I prepared 103 BIF samples in the Nulliak Island, including 32 samples in the sketched outcrop (Fig. 2B), and 92 BIF and ferruginous chert samples in the Pangertok Inlet (Fig. 3A).

Mineral compositions were obtained by an electron probe microanalyzer, JXA-8800 (JEOL Ltd., Japan), at the University of Tokyo. The electron probe analyses were performed with accelerating voltage of 15-20 kV, 12-20 nA beam current and focused beam. The oxide ZAF correction method was applied.

The samples were slabed with a diamond-bladed rock saw for major and trace element analyses. Twenty-two samples in the sketched outcrop and 3 samples in other outcrops of the Nulliak Island, and 13 samples in the Pangertok Inlet were selected based on macroscopic observations of the slabs (Fig. 2A, Fig. 3A). They were polished with a grinder to remove saw marks, and rinsed in an ultrasonic bath. They were crushed into small pieces in plastic bags with a hammer, and hand-picked fresh pieces without altered parts and veins were ground into powders by an agate mortar.

Major element compositions were obtained with an X-ray fluorescence spectrometry of RIX2100 (Rigaku Corp., Japan) equipped with Rh tube at the Tokyo Institute of Technology. The measurement was carried out on fused glass beads at the

acceleration voltage of 50 kV and the current of 50 mA. To prepare the fused glass beads, rock powder samples were heated at 110 ˚C for 24 hours to remove adsorbed water, and 0.4000 g sample was mixed with 4.0000 g $Li_2B_4O_7$ flux and fused at about 1150˚C for 8 min in a Pt crucible. A calibration curve was constructed using 21 geochemical reference samples issued by the Geological Survey of Japan and Bureau of Analysed Samples, including BIF standards (EURONORM-CRM No. 884-1, EURONORM-CRM No. 682-2 and BCS-CRM No. 517). The reproducibility (95% reliability) of measurement on relative scale was better than 1.0% for SiO_2, TiO_2, Al_2O_3, Fe_2O_3, MnO, MgO, CaO, and K_2O, 1.2% for P_2O_5, and 1.7% for Na_2O, respectively.

Trace element abundances were measured with a Q-pole mass filter ICP mass spectrometer, iCAP Qc (Thermo Fisher Scientific Inc., USA) with a collision cell, at the Kyoto University. The analytical method, accuracy and precision were described elsewhere (Aoki et al., 2016). The rare earth element and yttrium (REE+Y) concentrations were normalized to Post-Archaean Australian Average Shale (PAAS, Taylor and McLennan, 1985), and La, Ce and Eu anomalies, La/La*, Ce/Ce* and Eu/Eu*, were defined by $[La/(3Pr-2Nd)]_{PAAS}$, $[Ce/(2Pr-Nd)]_{PAAS}$ and $[Eu/(0.67Sm+0.33Tb)]_{PAAS}$, respectively.

5. Results

*5.1. Petrography and mineral compositions of the BIF*s

The BIFs in the Nulliak Island are composed of magnetite, orthopyroxene, clinopyroxene and quartz with subordinate amounts of cummingtonite, hornblende, pyrite and apatite (Fig. 4). The white bands mainly comprise large quartz (10 to 1000 μm across), which has anhedral and euhedral forms and shows wavy extinction and sutured grain boundaries (Fig. 4A). The magnetite ubiquitously occurs as inclusions within the quartz in the white bands. On the other hand, the black bands consist mainly of magnetite, orthopyroxene and clinopyroxene with subordinate amounts of quartz, cummingtonite and hornblende (Fig. 4A). The magnetite, orthopyroxene and clinopyroxene display anhedral and subhedral shapes, and the magnetite forms bands and clear lineage boundaries between the black and white bands. Some magnetite and quartz occur as inclusions within the pyroxenes. The pyroxenes are present as discrete grains, and parallel to subparallel to the bands. Most of clinopyroxene grains have exsolution lamellae of orthopyroxene (Fig. 4C, D). Most of them run along two crystallographic planes of (001) and (100) in the host clinopyroxene. The cummingtonite occurs along the rims of some orthopyroxene grains, and the occurrence suggests that they were possibly

formed during the retrogression (Fig. 4C). The hornblende occurs in black bands of aluminous (Al_2O_3 > 1%) BIFs such as LAD317 (Fig. 4B).

The mineral compositions are shown in Table 1. The compositions of the orthopyroxene and clinopyroxene grains and orthopyroxene lamellae are shown in figure 6A. The clinopyroxene has diopside and hedenbergite compositions: $Wo_{41.6\text{-}46.6}En_{24.7\text{-}29.9}Fs_{24.4\text{-}29.9}$. The orthopyroxene grains have $Wo_{0.1\text{-}3.1}En_{32.1\text{-}40.2}Fs_{59.0\text{-}67.8}$ compositions, whereas the orthopyroxene lamellae have $Wo_{0.0\text{-}1.4}En_{30.5\text{-}35.2}Fs_{63.7\text{-}69.0}$ compositions.

The BIFs and cherts in the Pangertok Inlet contain magnetite, clinopyroxene and quartz (Fig. 4E). The white bands are mainly composed of anhedral quartz with minor magnetite, and the quartz shows sutured grain boundaries, subgrains and wavy extinction due to strong deformation. Most of the magnetite grains occur as inclusions within the quartz. The black bands mainly comprise magnetite, clinopyroxene and quartz. Some magnetite and quartz grains occur as inclusions within the pyroxenes. No orthopyroxene grains and lamellae are found in the Pangertok Inlet BIFs. The magnetite has anhedral, elongated shape, and the clinopyroxene forms anhedral to subhedral. The clinopyroxenes have diopside and hedenbergite compositions: $Wo_{42.9\text{-}50.4}En_{18.7\text{-}43.9}Fs_{8.8\text{-}36.9}$ (Fig. 5B, Table 2).

5.2. Whole rock compositions of the BIFs

Major element compositions of the BIFs are listed in Table 3, 4 and Fig. 7, respectively. The BIFs are composed mainly of Fe_2O_3 and SiO_2 (Fig. 6A) with minor amounts of MgO and CaO (Fig. 7B, C). Some of the BIFs have high Al_2O_3 contents (> 1%), and low Na_2O, K_2O and P_2O_5 contents (< 0.1 %). But four BIFs with high Al_2O_3 contents in the Pangertok Inlet (LAD710, LAD714, LAD905 and LAD909) have high potassium contents (> 0.1%). The BIFs in the Nulliak Island have higher Fe_2O_3 than those in the Pangertok Inlet. The BIFs in the Pangertok Inlet have higher (Mg + Ca)/Fe ratios because of their low iron contents (Fig. 6D).

Trace element compositions of the BIFs are listed in Table 3 and 4. The Fe_2O_3 variation diagrams of V, Cr, Co, Ni, Cu, Zn, Sr, Y, Zr, Pr, Sm, Yb and U contents are shown in Figures 8. The V, Cr, Co, Ni, Zn, Y, and REE contents increase with increasing iron contents in the Pangertok Inlet. The PAAS-normalized REE + Y patterns are shown in Figure 9. Most BIFs show positive La anomalies except for LAD288, LAD294, LAD297, LAD310 and LAD905, and positive Eu anomalies except for LAD288. All of the BIFs show positive Y anomalies on the REE+Y patterns. In general, the BIFs in the Pangertok Inlet show larger positive Eu anomalies especially for LAD11, KAD729, LAD736, LAD740, LAD903, LAD904, LAD911, and less variable and lower Y/Ho

ratios (*ca*. 40-50) than those in the Nulliak Island. Moreover, their patterns are depleted in LREE relative to HREE ($(Pr/Yb)_{PAAS} < 1$) except for LAD 905.

6. Discussion

6.1. Mineral paragenesis of the BIFs

Previous work suggested that the Nulliak supracrustal rocks and surrounding Uivak Gneisses were metamorphosed under granulite facies condition in the western side of the Handy Fault whereas under the amphibolite facies condition in the northern part of the eastern side and under amphibolite-granulite facies transition in the southern part (Schiøtte et al., 1986). Therefore, the BIFs in the Pangertok Inlet suffered from the granulite facies metamorphism whereas the BIFs in the Nulliak Island were metamorphosed under the amphibolite-granulite facies transition (Schiøtte et al., 1986). On the other hand, deformation is relatively weak or parallel to the layering so that some are massive, but most clearly display black and white bands, and even intraformational layering (Fig. 2D, 3C).

Clinopyroxene and orthopyroxene are index minerals of upper upper-amphibolite and granulite facies metamorphism in a BIF system (Klein, 2005). Figure 9 shows mineral parageneses under the granulite (A) and upper amphibolite facies conditions (B) in a SiO_2-CaO-MgO-H_2O-CO_2 (CMS-HC) system (Spear, 1993). The BIFs mainly contain SiO_2, Fe_2O_3, FeO, MgO and CaO contents with quite small amounts of TiO_2, Al_2O_3, Cr_2O_3, MnO, Na_2O, K_2O and P_2O_5 contents (Table 3, 4), and mainly comprise magnetite, quartz, amphibole and two pyroxenes, as mentioned above (Fig. 4). Assuming

that all of the iron exists as the magnetite, the magnetite and water are excess phases and Ti, Al, Cr, Na, K and P are negligible, parageneses of the BIFs can be shown on a SiO_2-CaO-MgO plane of the SiO_2-Fe_2O_3-CaO-MgO-H_2O-CO_2 system. Addition of dolomite to BIFs of silica phase and magnetite makes the BIFs to be plotted around an SiO_2-Di line on a SiO_2-CaO-MgO plane so that the mineral parageneses are characterized by quartz, diopside, tremolite and magnetite under the upper amphibolite facies condition (Fig. 9B). A decomposition of the tremolite results in appearance of orthopyroxene or coexistence of clinopyroxene with orthopyroxene (Fig. 9A), and temperature of the reaction strongly depends on XCO_2, ranging from 920 ˚C at XCO_2=0.0 to 600 ˚C at XCO_2=0.95 (Spear, 1993).

The BIFs in the Nulliak Island and Pangertok Inlet areas are plotted around the SiO_2-Di line on the pseudoternary diagram of SiO_2-CaO-MgO (Fig. 9), but the former contains magnetite, quartz, clinopyroxene and orthopyroxene whereas the latter contains only magnetite, quartz and clinopyroxene. The difference of the mineral parageneses between them cannot be explained by difference in their bulk compositions because both have similar compositions (Fig. 9). In addition, the presence of orthopyroxene in the BIFs of the Nulliak Island apparently contradicts the estimated metamorphic grade from parageneses of mafic rocks, which display amphibolite facies condition in the eastern side

of the Handy Fault, whereas granulite facies condition in the western side (Bridgwater et al., 1975; Collerson et al., 1976; Schiøtte et al., 1986; Schiøtte et al., 1989a; Schiøtte et al., 1989b). But, the inconsistency can be explained by strong dependence of tremolite decomposition on CO_2 partial pressure because high XCO_2 of metamorphic fluid results in orthopyroxene-in at much lower temperature (Spear, 1993). In addition, there are orthopyroxene lamellae within clinopyroxenes in BIFs of the Nulliak Island (Fig. 4C, D). We obtained the minimum temperature of the metamorphism at 640-710 ˚C based on a two-pyroxene thermometry for the orthopyroxene lamellae and host clinopyroxenes (Fonarev et al., 1991), consistent with garnet-biotite thermometry for the pelitic gneisses in eastern side of St. John's Harbour and Big Island (Tashiro et al., 2016). The comparison of the two-pyroxene and garnet-biotite thermometers with the coexistence of clinopyroxene and orthopyroxene indicates that the XCO_2 ranged from 0.85 to 0.9 for the metamorphism (Spear, 1993). The quite high XCO_2 value suggests the BIFs with/without underlying altered basaltic crusts contained much amounts of carbonate minerals and they were decomposed during the metamorphism (c.f. Kitajima et al., 2001; Nakamura and Kato, 2004; Shibuya et al., 2007).

6.2. Estimate of the Eoarchean seawater composition based on the whole-rock compositions of the BIFs

6.2.1. Relationships of rare earth and transitional element contents with the lithofacies

The BIFs are composed mainly of quartz and iron-oxide minerals such as hematite and magnetite. It is considered that the quartz was recrystallized from amorphous silica precipitate. The precursor mineral of magnetite cannot be well constrained based on only petrological and geochemical observations of this study, but it is considered that they were derived primarily from iron oxyhydroxide such as ferrihydrite because the Eoarchean BIFs have high iron isotopic ratios (Dauphas et al., 2004; Dauphas et al., 2007; Whitehouse and Fedo, 2007; Yoshiya et al., 2015). The BIFs in the Nulliak supracrustal rocks are composed mainly of Fe_2O_3 and SiO_2 (Fig. 6A), and positive correlations of the REE and transitional element contents with Fe_2O_3 contents suggest that a precursor of the magnetite mainly hosted the elements, analogous to modern iron oxyhydroxide (German and Von Damm, 2003).

The BIFs contain not only magnetite and quartz but also pyroxene and amphibole with small amounts of apatite and sulfide minerals (Fig. 4). The precursor of the apatite is probably hydroxyl-fluorapatite, and the pyrite originates from sulfide and an iron-oxyhydroxide mineral, analogous to those in the Isua supracrustal belt (Yoshiya et

al., 2015). The amphibole and pyroxene were mainly derived from dolomite because the BIFs are plotted along the SiO_2-Di tie-line as mentioned above (Fig. 9).

Assuming that precursors of the quartz, magnetite, apatite and sulfide are an opal with an $SiO_2 \cdot nH_2O$ composition, ferrihydrite with an FeO(OH) composition, hydroxyl-fluorapatite with a $Ca_5(PO_4,CO_3)_3(OH,O,F)$ composition, carbonate with a $CaCO_3$-$CaMg(CO_3)_2$ composition, and pyrites with an FeS_2 composition, respectively, we calculated normative modal compositions of the precursors in the BIFs (see the Appendix). However, we neglected the normative sulfide in our calculation because the modal sulfide contents are negligible low in the BIFs of the Nulliak supracrustal rocks.

The BIFs of the Pangertok Inlet have higher normative opal (75-91%) and slightly higher carbonate (2.7-12%) contents than those of the Nulliak Island (60-76% and 4.8-11%, respectively) so that opal and dolomite were more precipitated in the depositional environment of the Pangertok Inlet BIFs. In addition, higher normative dolomite to ferrihydrite ratios of the BIFs in Pangertok Inlet suggest that the carbonates were more dominant than iron-oxide minerals during the deposition (Fig. 6D). Generally speaking, the phosphate contains high REE and Sr contents whereas the pyrite is enriched in transition elements such as Ni, Zn and Co. Besides, the dolomite and calcite also have high REE, Sr and transitional element contents so that the involvement should disturb

their abundances in BIFs. However, no apparent correlations of the REE and transition element contents with normative dolomite contents suggest the involvement of carbonate minerals was insignificant influence on their contents (Fig. 10).

6.2.2. Influence of clastic contamination on the whole-rock compositions in the BIFs

Contamination of volcanic materials of silicate minerals, ash and glass, exhalative insoluble materials and detritus at the BIF deposition masks their seawater chemical signatures because the contaminants usually have higher REE, LILE, HFSE, and transition element contents. Generally speaking, Al^{3+}, Ti^{4+}, and HFSE are insoluble in aqueous solution (e.g. Andrews et al., 2004; Martin and Whitfield, 1983) and concentrated in clay minerals, weathering-resistant minerals such as zircon and some aluminous and titaniferous phases, REE-bearing minerals of monazite and apatite, volcanic glass and exhalative insoluble materials so that the HFSE abundances are often used as criteria for their involvement (e.g. Bau, 1993).

Positive correlations between transitional element (V, Cr, Ni, Cu, U) and HFSE (e.g. Zr, Nb, Hf, Th) contents suggest that their abundances of the BIFs were derived partly from the clastic or volcanic materials (Fig. 11A, B, D, E, K). In addition, obvious positive correlations of Co and Zn contents with Zr contents in the BIFs of the Pangertok

Inlet indicate that they were also derived from clastic materials. On the other hand, influence of the involvement of clastic or volcanic materials on the Co contents of the BIFs in the Nulliak Island is probably minimal because of lack of correlation between their Co and Zr contents (Fig. 11C).

Positive correlations of REE and Y contents with Zr contents are also obvious, and the La anomalies for the BIFs in Nulliak Island and positive Eu anomalies for both BIFs decrease with increasing their Zr contents (Fig. 11L, M), consistent with contamination of volcanic and clastic materials such as Archean mudstone with lower Eu/Sm ratios (Bau, 1993). The Y/Ho ratios in the BIFs of the Nulliak Island also decrease with their increasing Zr contents. Because Y and Ho behave as geochemical twins with trivalent valence and similar ionic radii in magmatic processes, igneous rocks and associated clastic rocks have chondritic Y/Ho ratios (ca. 26). On the other hand, seawater and their associated chemical sediments have superchondritic Y/Ho ratios (> 26) because Ho is preferentially adsorbed and removed by particulate matter in seawater (e.g. Alibo and Nozaki, 1999; Bau, 1996; Bolhar et al., 2005; Nozaki et al., 1997). The negative correlation between Y/Ho ratios and Zr contents in the BIFs of the Nulliak Island indicate the contamination of clastic or volcanic materials, but influence of the contamination on the Y/Ho ratios of the BIFs in the Pangertok Inlet is relatively insignificant because the

ratios are almost constant regardless of the Zr contents (Fig. 11N).

6.3. Estimate of transitional element contents in the Eoarchean seawater

Previous studies showed that pre-2.7 Ga BIFs have higher Ni contents than younger BIF and iron deposits, and interpreted that Archean seawater had higher Ni contents due to higher influx of Ni-rich hydrothermal fluid from komatiite (Haugaard et al., 2016; Konhauser et al., 2009; Konhauser et al., 2011; Mloszewska et al., 2012; Mloszewska et al., 2013; Pecoits et al., 2009). They used three criteria to choose the BIFs without influence of clastic contamination: (1) < 1wt% Al, (2) < 20ppm Ti, Zr, Th, Hf and Sc and (3) lack of co-variations of Zr versus Y/Ho, Y/Ho versus Ce/Ce* and Th versus La/La*. However, the criteria are still insufficient because the magnetite-rich BIFs in the 3.8 Ga ISB also show positive correlations of LREE and some transitional elements with Zr contents even under those threshold values (Aoki et al., 2016).

Because the BIFs in the Nulliak Island have more iron contents, namely magnetite contents, than those in the Pangertok Inlet, we, hereafter, used the compositions of the BIFs in the Nulliak Island to estimate composition of seawater. A positive correlation between Zr and Ni contents in the Nulliak Island BIFs suggest that all the nickel was not derived from adsorption on iron-oxyhydroxide but partially originated from clastic or volcanic materials so that it is necessary to remove the influence of the involvement of

those materials to estimate paleo-seawater composition. There are two methods to obtain the Ni content of a contamination-free BIF. The first method is to calculate the Ni content from an intercept of a linear regression line along the compositional trend of Ni contents on a Zr variation diagram, analogous to the modern iron oxyhydroxide (Sherrell et al., 1999). However, the method is based on an assumption that the Ni variation is due to input from a single clastic or volcanic material source. The second method is to obtain the contamination-free composition from the intercepts of some regression lines, which encompass all the data. The method is on a basis of consideration that the contaminant sources are multiple because the BIF have highly variable Ni contents at a given Zr content and contaminant candidates of supracrustal rocks such as metaperidotite, amphibolite, carbonate rock and metapelites are highly variable in Ni to Zr ratios (Nutman et al., 1989).

The contamination-free Ni content of the Nulliak Island BIFs is 29 ± 10 ppm (1σ), and ranges from 10 to 30 ppm for the first and second methods, respectively (Fig. 12C). The value is similar to that estimated from magnetite-rich BIFs in the ISB and higher than those from post-2.7 Ga BIFs (Aoki et al., 2016), which suggests that the 3.9 Ga Saglek seawater had higher dissolved Ni content than the Late Archean seawater and supports the Eoarchean Ni-rich seawater (Konhauser et al., 2009).

Uranium varies from +3 to +6 in the valence, and forms insoluble tetravalent uranium compounds such as uraninite under an anoxic condition whereas hexavalent compounds under an oxic condition. Partin et al. (2013) suggested that dissolved U content of seawater increased around the Great Oxidation Event (GOE) from 2.4 to 2.1 Ga due to oxidative continental weathering and consequent enhanced U (VI) delivery to seawater based on the Precambrian BIFs and Phanerozoic iron-rich sediments. They excluded some of BIFs, which suffered from super-greenschist facies metamorphisms including the Eoarchean BIFs from the Isua supracrustal belt and the Nuvvuagittuq supracrustal belt, because it is assumed that they lost seawater U signatures due to secondary mobilizations. However, a positive correlation between U and Zr contents of the Nulliak Island BIFs suggests that a variation of the U contents can be explained by the contamination. Because a uranium content of the contamination-free BIF is 0.0327 ± 0.0366 ppm, and ranges from 0.01 to 0.06 ppm for the first and second methods, respectively, uranium adsorbed on the oxyhydroxide was almost negligible so that dissolved uranium was minimal in the Eoarchean ocean (Fig. 12E).

Vanadium also has some valences from +2 to +5, and is soluble as various vanadate compounds under the oxic condition. And, it is one of bioessential elements for some nitrogen-fixing microorganisms. A vanadium content of a contamination-free BIF

is estimated to be 4.06 ± 2.09 ppm (1σ), and from 3 to 5 ppm from the first and second method, respectively (Fig. 12A), almost comparable to an estimated value of a contamination-free BIF in the ISB (Aoki et al., 2016). Although available data of vanadium contents of younger BIFs are few, a value estimated from the Neoproterozoic Rapitan IFs is higher than those from the Eoarchean BIFs, suggesting that the dissolved vanadium content in seawater increases with increasing oxidation through the time (Aoki et al., 2016).

Chromium is also multivalent from +3 to +6 in the valence, and occurs as trivalent compounds in chromite or sulfide minerals under the reducing or acidic environment whereas forms soluble hexavalent compounds such as chromate anion (CrO_4^-) under the oxic environment. Frei et al. (2009) proposed that isotopically heavy trivalent ^{53}Cr in the continental crust was preferentially oxidized into tetravalent forms and were supplied into the ocean at ca. 2.8-2.6 and 0.74-0.55 Ga because the BIFs at that time have high $\delta^{53}Cr$ values than igneous rocks, and that riverine influx of chromium into the ocean in the Eoarchean was limited due to anoxic surface environment because the BIFs in the ISB have similar $\delta^{53}Cr$ values to igneous rocks. Konhauser et al. (2011) showed increases in Cr contents and Cr/Ti ratios of BIFs around the GOE based on a compilation of Cr contents and Cr/Ti ratios in the Precambrian iron formations and

Phanerozoic iron-rich sediments, and interpreted that the high Cr contents and Cr/Ti ratios were caused by increase in dissolved Cr content of seawater due to oxidation of sulfide minerals by aerobic-respiring, chemolithoautotrophic bacteria in the continental crust. However, they could not obtain reliable Cr contents of the Eoarchean BIFs because showed that the BIFs in the ISB are significantly influenced by contamination of chromite-bearing clastic or volcanic materials; thus it is still open whether the Eoarchean BIFs and seawater was enriched in Cr contents because chromite-bearing ultramafic volcanic rocks (komatiite) were more pervasive in the early Earth, analogous to Ni contents in the Eoarchean BIFs. A obvious positive correlation between Zr and Cr contents in the BIFs of the Nulliak supracrustal rocks suggests that the chromium was sourced from clastic or volcanic materials (Fig. 11B), and a Cr content of the contamination-free BIF is estimated to be 14 ± 4.9 ppm (1σ) and 5 to 20 ppm by the first and second methods, respectively (Fig. 12B). Those values are significantly lower than those of the BIFs around GOE (up to 3500 ppm) (Konhauser et al., 2011), and indicate that dissolved Cr content was much lower in the Eoarchean Ocean.

Copper is one of bioessential elements of denitrifying microbes for nitrite reductase, and has some valences from +1 to +2 and is soluble as bivalent compounds under oxic condition. An estimated contamination-free Cu content of the Nulliak BIFs is

0.70 ± 3.71 ppm by first method, or ranges from 0 to 3 ppm by second method so that copper adsorbed on the oxyhydroxide is almost negligible (Fig. 12D). Recently, Chi Fru et al. (2016) showed δ^{65}Cu values of the black shales changed from negative to positive around the GOE, and interpreted that, before GOE, dissolved Cu was low due to limited oxidative weathering of continental Cu sulfide, and mass precipitation of the BIFs. The former supplies ^{65}Cu into the ocean whereas the latter scavenges ^{65}Cu from the ocean. Our estimate also indicates that the Archean seawater was depleted in Cu content, but the quite low Cu contents of the BIFs suggest the latter process was insignificant.

6.4. The depositional environment of the BIFs in the Nulliak supracrustal rocks and the contemporaneous seawater chemistry

Superchondritic Y/Ho ratios (> 26) and positive Eu anomalies are characteristic of modern seawater and hydrothermal fluid, respectively (e.g. Alibo and Nozaki, 1999; Bau and Dulski, 1999; Nozaki et al., 1997). Therefore, the value in chemical sediment is often used to estimate a mixing ratio between seawater and hydrothermal fluid in a depositional environment (Alexander et al., 2008; Kato et al., 1998; Sugahara et al., 2010). However, the REE and Y contents in BIFs of the Nulliak supracrustal rocks are significantly influenced by magmatic and clastic materials because Y/Ho

ratios are well correlated with Zr contents so that the correction is necessary (Fig. 8, 11). The estimated contamination-free BIFs range from 50 to 60 and from 40 to 50 in Y/Ho ratios, and from 2.0 to 2.5 and from 2.0 to 4.0 in positive Eu anomalies for the Nulliak Island and Pangertok Inlet BIFs, respectively. Because the contamination-free BIF in the Pangertok Inlet has a lower Y/Ho ratio and higher Eu anomaly than that in the Nulliak Island, the BIFs in the Pangertok Inlet were probably precipitated under the environment with more hydrothermal fluid component. On the other hand, higher ratios of normative carbonate components to iron-oxyhydroxide components of the BIFs in the Pangertok Inlet than those in the Nulliak Island suggest that the hydrothermal environments were more saturated in carbonate minerals compared with ambient seawater in the Eoarchean ocean.

There are two ideas of the depositional settings of the BIFs, which account for the difference in the major element and REE compositions of the BIFs in the Pangertok Inlet and Nulliak Island. The first idea assumes that the environment near a hydrothermal vent site was shallower than carbonate compensation depth (CCD), similar to modern ridge environments. In this case, the BIFs in the Pangertok Inlet were formed at shallower environment

than the CCD near the hydrothermal vent sites whereas the BIFs in the Nulliak Island were deposited at a deeper area, distal to the hydrothermal vent sites. However, the model cannot explain why silica minerals were more precipitated in the depositional environment of the Pangertok Inlet.

Another idea is that BIFs with higher normative carbonate and silica components were formed by mixing of alkaline and SiO_2-rich high-temperature hydrothermal fluid with ambient seawater. This model is based on a thermodynamic calculation of phase equilibria in hydrothermally altered Archean basalts (Shibuya et al., 2010). They proposed that a highly alkaline hydrothermal fluids with a high total [CO_2] content (pH > 11, [ΣCO_2] > 0.2 mol/kg) was spouted in an Archean subseafloor basalt-hosted hydrothermal system, in contrast to acidic hydrothermal fluid (pH < 5, [ΣCO_2] < 0.02 mol/kg) of modern MORB-hosted hydrothermal systems (Charlou et al., 2000; Ding et al., 2005; Merlivat et al., 1987; Seyfried et al., 1991). The alkaline fluid was enriched in Si, and depleted in Fe and Ca contents whereas acidic-neutral and anoxic Archean seawater was enriched in Fe and Ca contents (Shibuya et al., 2010). The mixing of the alkaline hydrothermal fluid with the ambient seawater makes the hydrothermal vent site saturated with

Fe and Ca, and eventually iron-oxyhydroxide and carbonate precipitated. In addition, the high silica content of the alkaline hydrothermal fluid leads to more precipitation of silica minerals near the vent site. In this model, the BIFs of the Pangertok Inlet were precipitated near the alkaline hydrothermal vent sites, whereas the BIFs in the Nulliak Island were deposited distal to the alkaline hydrothermal vents.

Conclusion

The Eoarchean banded iron formations of the Nulliak supracrustal rocks occur in the Nulliak Island, Pangertok Inlet, Big Island and Shuldham Island. The BIFs in the Nulliak Island and the Pangertok Inlet are geologically and petrographically different from each other. The former is interlayered with the mafic rocks, and is composed mainly of magnetite, quartz, orthopyroxene and clinopyroxene. The latter is accompanied with mafic and carbonate rocks, and comprises magnetite, quartz and clinopyroxene. Their mineral parageneses cannot be explained by difference in their metamorphic grades or bulk compositions, but possibly by the difference of XCO_2 of metamorphic fluid. The latter was metamorphosed under the higher XCO_2 condition.

Both the BIFs show positive correlations of transitional element (V, Cr, Ni, Cu and U) contents with Zr contents, suggesting that those compositions are influenced by the contaminations of volcanic or clastic materials at the depositions. We estimated the compositions of contamination-free BIFs from the intercepts of compositional variations encompassing all the data at 0 ppm of Zr contents. The contamination-free BIFs have quite low V, Cr, Cu and U contents, suggesting that the Eoarchean seawater was depleted in those elements possibly because the Eoarchean ocean and terrestrial environments were anoxic. On the other hand, Ni was abundantly dissolved in the Eoarchean ocean

because Ni content in the contamination-free BIF is higher than those of the post-2.7Ga BIFs.

The BIFs in the Pangertok Inlet have higher normative opal and dolomite components than those in the Nulliak Island, suggesting that dolomite and silica minerals were more precipitated in the former's depositional environment. Because the REE and Y contents are also positively correlated with Zr contents, their contents were also influenced by contamination of clastic and volcanic materials. The PAAS-normalized REE + Y patterns of the BIFs with low Zr contents are characterized by positive La, Eu and Y anomalies, similar to modern seawater and hydrothermal fluids. In addition, the contamination-free BIF of the Pangertok Inlet has higher Eu positive anomaly than that of the Nulliak Island, indicating that the former was precipitated at an environment more strongly influenced by high-temperature hydrothermal fluid. The combination of higher Eu anomaly and more normative dolomite and silica mineral components for the Pangertok Inlet BIFs suggests that they were precipitated from mixing of alkaline, Si-rich, hydrothermal fluid with acidic-neutral ambient seawater near hydrothermal vent sites.

References

Alexander, B.W., Bau, M., Andersson, P., Dulski, P., 2008. Continentally-derived solutes in shallow Archean seawater: Rare earth element and Nd isotope evidence in iron formation from the 2.9 Ga Pongola Supergroup, South Africa. Geochimica et Cosmochimica Acta 72, 378-394.

Alibo, D.S., Nozaki, Y., 1999. Rare earth elements in seawater: Particle association, shale-normalization, and Ce oxidation. Geochimica et Cosmochimica Acta 63, 363-372.

André, L., Cardinal, D., Alleman, L.Y., Moorbath, S., 2006. Silicon isotopes in ~3.8 Ga West Greenland rocks as clues to the Eoarchaean supracrustal Si cycle. Earth and Planetary Science Letters 245, 162-173.

Andrews, J.E., Brimblecombe, P., Jickells, T.D., Liss, P.S., Reid, B., 2004. An Introduction to Environmental Chemistry, second edition. Blackwell Science, Malden, USA, 296 pp.

Aoki, S., Morinaga, C., Kato, Y., Hirata, T., Komiya, T., 2016. Influence of contamination on banded iron formations in the Isua supracrustal belt, West Greenland: Reevaluation of the Eoarchean seawater compositions. Geoscience Frontiers submitted.

Bau, M., 1993. Effects of syn- and post-depositional processes on the rare-earth element distribution in Precambrian iron-formations. European Journal of Mineralogy 5, 257-267.

Bau, M., 1996. Controls on the fractionation of isovalent trace elements in magmatic and aqueous systems: evidence from Y/Ho, Zr/Hf, and lanthanide tetrad effect. Contributions to Mineralogy and Petrology 123, 323-333.

Bau, M., Dulski, P., 1996. Distribution of yttrium and rare-earth elements in the Penge and Kuruman iron-formations, Transvaal Supergroup, South Africa. Precambrian Research 79, 37-55.

Bau, M., Dulski, P., 1999. Comparing yttrium and rare earths in hydrothermal fluids from the Mid-Atlantic Ridge: implications for Y and REE behaviour during near-vent mixing and for the Y/Ho ratio of Proterozoic seawater. Chemical Geology 155, 77-90.

Bjerrum, C.J., Canfield, D.E., 2002. Ocean productivity before about 1.9 Gyr ago limited by phosphorus adsorption onto iron oxides. Nature 417, 159-162.

Bolhar, R., Kamber, B.S., Moorbath, S., Fedo, C.M., Whitehouse, M.J., 2004. Characterisation of early Archaean chemical sediments by trace element

signatures. Earth and Planetary Science Letters 222, 43-60.

Bolhar, R., Kamber, B.S., Moorbath, S., Whitehouse, M.J., Collerson, K.D., 2005. Chemical characterization of earth's most ancient clastic metasediments from the Isua Greenstone Belt, southern West Greenland. Geochimica et Cosmochimica Acta 69, 1555-1573.

Bridgwater, D., Collerson, K.D., Hurst, R.W., Jesseau, C.W., 1975. Field characters of the early Precambrian rocks from Saglek, coast of Labrador, Report of activities, part A. Geological Survey of Canada, Paper 75-1A, pp. 287-296.

Bridgwater, D., Collerson, K.D., 1976. The major petrological and geochemical characters of the 3,600 m.y. Uivak gneisses from Labrador. Contributions to Mineralogy and Petrology 54, 43-59.

Bridgwater, D., Schiøtte, L., 1991. The Archaean gneiss complex of northern Labrador. A review of current results, idea and problems. Bulletin of the Geological Society of Denmark 39, 153-166.

Charlou, J.L., Donval, J.P., Douville, E., Jean-Baptiste, P., Radford-Knoery, J., Fouquet, Y., Dapoigny, A., Stievenard, M., 2000. Compared geochemical signatures and the evolution of Menez Gwen (37˚50'N) and Lucky Strike (37˚17'N) hydrothermal fluids, south of the Azores Triple Junction on the Mid-Atlantic Ridge. Chemical Geology 171, 49-75.

Chi Fru, E., Rodríguez, N.P., Partin, C.A., Lalonde, S.V., Andersson, P., Weiss, D.J., El Albani, A., Rodushkin, I., Konhauser, K.O., 2016. Cu isotopes in marine black shales record the Great Oxidation Event. Proceedings of the National Academy of Sciences 113, 4941-4946.

Collerson, K.D., Jesseau, C.W., Bridgwater, D., 1976. Crustal development of the Archaean Gneiss Complex: Eastern Labrador. In: Windley, B.F. (Ed.), The Early History of the Earth based on the proceeding of a NATO advanced study institute held at the university of Leicester 5-11 April, 1975. John Wiley & Sons, London, pp. 237-253.

Collerson, K.D., Bridgwater, D., 1979. Metamorphic development of early Archaean tonalitic and trondhjemitic gneisses: Saglek area, Labrador. In: Barker, F. (Ed.), Trondhjemites, dacites, and related rock. Elsevier, Amsterdam.

Collerson, K.D., 1983. Ion microprobe zircon geochronology of the Uivak Gneisses: Implications for the evolution of early terrestrial crust in the North Atlantic Craton. In: Ashwal, L.D., Card, K.D. (Eds.), Abstracts for Early Crustal Genesis Field Workshop, Lunar and Planetary Institute, Houston, TX, Technical Report 83-03, pp. 28-33.

Dauphas, N., van Zuilen, M., Wadhwa, M., Davis, A.M., Marty, B., Janney, P.E., 2004. Clues from Fe isotope variations on the origin of Early Archean BIFs from Greenland. Science 306, 2077-2080.

Dauphas, N., van Zuilen, M., Busigny, V., Lepland, A., Wadhwa, M., Janney, P.E., 2007. Iron isotope, major and trace element characterization of early Archean supracrustal rocks from SW Greenland: Protolith identification and metamorphic overprint. Geochimica et Cosmochimica Acta 71, 4745-4770.

Ding, K., Seyfried Jr, W.E., Zhang, Z., Tivey, M.K., Von Damm, K.L., Bradley, A.M., 2005. The in situ pH of hydrothermal fluids at mid-ocean ridges. Earth and Planetary Science Letters 237, 167-174.

Dymek, R.F., Klein, C., 1988. Chemistry, petrology and origin of banded iron-formation lithologies from the 3800 Ma Isua supracrustal belt, West Greenland. Precambrian Research 39, 247-302.

Fedo, C.M., Whitehouse, M.J., 2002. Metasomatic origin of quartz-pyroxene rock, Akilia, Greenland, and implications for Earth's earliest life. Science 296, 1448-1452.

Fonarev, V.I., Graphchikov, A.A., Konilov, A.N., 1991. A consistent system of geothermometers for metamorphic complexes. International Geology Review 33, 743-783.

Frei, R., Bridgwater, D., Rosing, M.T., Stecher, O., 1999. Controversial Pb-Pb and Sm-Nd isotope results in the early Archean Isua (West Greenland) oxide iron formation: Preservation of primary signatures versus secondary disturbances. Geochimica et Cosmochimica Acta 63, 473-488.

Frei, R., Polat, A., 2007. Source heterogeneity for the major components of ~ 3.7 Ga Banded Iron Formations (Isua Greenstone Belt, Western Greenland): Tracing the nature of interacting water masses in BIF formation. Earth and Planetary Science Letters 253, 266-281.

Frei, R., Gaucher, C., Poulton, S.W., Canfield, D.E., 2009. Fluctuations in Precambrian atmospheric oxygenation recorded by chromium isotopes. Nature 461, 250-253.

German, C.R., Von Damm, K.L., 2003. Hydrothermal processes, The Oceans and Marine Geochemistry. Vol. 6 Treatise on geochemistry (eds. Holland, H. D. and Turekian, K.K.). Elsevier-Pergamon, Oxford, pp. 181-222.

Haugaard, R., Pecoits, E., Lalonde, S., Rouxel, O., Konhauser, K., 2016. The Joffre banded iron formation, Hamersley Group, Western Australia: Assessing the palaeoenvironment through detailed petrology and chemostratigraphy. Precambrian Research 273, 12-37.

Isley, A.E., Abbott, D., 1999. Plume-related mafic volcanism and the deposition of

banded iron formation. Journal of Geophysical Research 104, 15461-15477.

Kato, Y., Ohta, I., Tsunematsu, T., Watanabe, Y., Isozaki, Y., Maruyama, S., Imai, N., 1998. Rare earth element variations in mid-Archean banded iron formations: implications for the chemistry of ocean and continent and plate tectonics. Geochimica et Cosmochimica Acta 62, 3475-3497.

Kitajima, K., Maruyama, S., Utsunomiya, S., Liou, J.G., 2001. Seafloor hydrothermal alteration at an Archean mid-ocean ridge. Journal of Metamorphic Geology 19, 583-600.

Klein, C., Beukes, N.J., 1992. 4.2. Time distribution, stratigraphy, and sedimentologic setting, and geochemistry of Precambrian iron-formation. In: Schopf, J.W., Klein, C. (Eds.), The Proterozoic Biosphere: A Multidisciplinary Study. Cambridge University Press, New York, pp. 139-146.

Klein, C., 2005. Some Precambrian banded iron-formations (BIFs) from around the world: Their age, geologic setting, mineralogy, metamorphism, geochemistry, and origins. American Mineralogist 90, 1473-1499.

Komiya, T., Maruyama, S., Masuda, T., Nohda, S., Hayashi, M., Okamoto, K., 1999. Plate tectonics at 3.8-3.7 Ga: Field evidence from the Isua accretionary complex, southern West Greenland. Journal of Geology 107, 515-554.

Komiya, T., Yamamoto, S., Aoki, S., Sawaki, Y., Ishikawa, A., Tashiro, T., Koshida, K., Shimojo, M., Aoki, K., Collerson, K.D., 2015. Geology of the Eoarchean, >3.95 Ga, Nulliak supracrustal rocks in the Saglek Block, northern Labrador, Canada: The oldest geological evidence for plate tectonics. Tectonophysics 662, 40-66.

Komiya, T., Yamamoto, S., Aoki, S., Koshida, K., Shimojo, M., Sawaki, Y., Aoki, K., Sakata, S., Yokoyama, D.T., Maki, K., Ishikawa, A., Hirata, T., Collerson, K.D., 2016. A prolonged granitoid formation in Saglek Block, Labrador: Zonal growth and crustal reworking of continental crust in the Eoarchean. Geoscience Frontiers in press.

Konhauser, K.O., Pecoits, E., Lalonde, S.V., Papineau, D., Nisbet, E.G., Barley, M.E., Arndt, N.T., Zahnle, K., Kamber, B.S., 2009. Oceanic nickel depletion and a methanogen famine before the Great Oxidation Event. Nature 458, 750-753.

Konhauser, K.O., Lalonde, S.V., Planavsky, N.J., Pecoits, E., Lyons, T.W., Mojzsis, S.J., Rouxel, O.J., Barley, M.E., Rosiere, C., Fralick, P.W., Kump, L.R., Bekker, A., 2011. Aerobic bacterial pyrite oxidation and acid rock drainage during the Great Oxidation Event. Nature 478, 369-373.

Krogh, T.E., Kamo, S.L., 2006. Precise U-Pb zircon ID-TIMS ages provide an alternative interpretation to early ion microprobe ages and new insight into Archean crustal

processes, norther Labrador. In: Reimold, W.U., Gibson, R.L. (Eds.), Processes on the Early Earth. Geological Society of America Special Paper 405, Boulder, Colorado, pp. 91-103.

Martin, J.-M., Whitfield, M., 1983. The significance of the river input of chemical elements to the ocean. In: Wong, C.S., Boyle, E., Bruland, K.W., Burton, J.D., Goldberg, E.D. (Eds.), Trace metals in sea water, Volume 9 of the series NATO Conference Series. Plenum Press, New York, pp. 265-296.

Merlivat, L., Pineau, F., Javoy, M., 1987. Hydrothermal vent waters at 13 ˚N on the East Pacific Rise: isotopic composition and gas concentration. Earth and Planetary Science Letters 84, 100-108.

Mloszewska, A.M., Pecoits, E., Cates, N.L., Mojzsis, S.J., O'Neil, J., Robbins, L.J., Konhauser, K.O., 2012. The composition of Earth's oldest iron formations: The Nuvvuagittuq Supracrustal Belt (Québec, Canada). Earth and Planetary Science Letters 317-318, 331-342.

Mloszewska, A.M., Mojzsis, S.J., Pecoits, E., Papineau, D., Dauphas, N., Konhauser, K.O., 2013. Chemical sedimentary protoliths in the >3.75 Ga Nuvvuagittuq Supracrustal Belt (Québec, Canada). Gondwana Research 23, 574-594.

Mojzsis, S.J., Arrhenius, G., McKeegan, K.D., Harrison, T.M., Nutman, A.P., Friend, C.R.L., 1996. Evidence for life on Earth before 3,800 million years ago. Nature 385, 55-59.

Mojzsis, S.J., Coath, C.D., Greenwood, J.P., McKeegan, K.D., Harrison, T.M., 2003. Mass-independent isotope effects in Archean (2.5 to 3.8 Ga) sedimentary sulfides determined by ion microprobe analysis. Geochimica et Cosmochimica Acta 67, 1635-1658.

Moorbath, S., O'Nions, R.K., Pankhurst, R.J., 1973. Early Archaean age for the Isua Iron Formation, West Greenland. Nature 245, 138-139.

Nakamura, K., Kato, Y., 2004. Carbonatization of oceanic crust by the seafloor hydrothermal activity and its significance as a CO_2 sink in the Early Archean. Geochimica et Cosmochimica Acta 68, 4595-4618.

Nozaki, Y., Zhang, J., Amakawa, H., 1997. The fractionation between Y and Ho in the marine environment. Earth and Planetary Science Letters 148, 329-340.

Nutman, A.P., Allaart, J.H., Bridgwater, D., Dimroth, E., Rosing, M., 1984. Stratigraphic and geochemical evidence for the depositional environment of the early Archaean Isua supracrustal belt, southern West Greenland. Precambrian Research 25, 365-396.

Nutman, A.P., 1986. The early Archaean to Proterozoic history of the Isukasia area,

southern West Greenland, 154. Grønlands geol. Unders. Bull., København, Denmark, 80 pp.

Nutman, A.P., Fryer, B.J., Bridgwater, D., 1989. The early Archaean Nulliak (supracrustal) assemblage, northern Labrador. Canadian Journal of Earth Science 26, 2159-2168.

O'Neil, J., Maurice, C., Stevenson, R.K., Larocque, J., Cloquet, C., David, J., Francis, D., 2007. The Geology of the 3.8 Ga Nuvvuagittuq (Porpoise Cove) Greenstone Belt, Northeastern Superior Province, Canada. In: van Kranendonk, M.J., Smithies, R.H., Bennett, V.C. (Eds.), Earth's Oldest Rocks. Developments in Precambrian Geology. Elsevier, Amsterdam, pp. 219-250.

Ohtomo, Y., Kakegawa, T., Ishida, A., Nagase, T., Rosing, M.T., 2014. Evidence for biogenic graphite in early Archaean Isua metasedimentary rocks. Nature Geoscience 7, 25-28.

Partin, C.A., Lalonde, S.V., Planavsky, N.J., Bekker, A., Rouxel, O.J., Lyons, T.W., Konhauser, K.O., 2013. Uranium in iron formations and the rise of atmospheric oxygen. Chemical Geology 362, 82-90.

Pecoits, E., Gingras, M.K., Barley, M.E., Kappler, A., Posth, N.R., Konhauser, K.O., 2009. Petrography and geochemistry of the Dales Gorge banded iron formation: Paragenetic sequence, source and implications for palaeo-ocean chemistry. Precambrian Research 172, 163-187.

Regelous, M., Collerson, K.D., 1996. ^{147}Sm-^{143}Nd, ^{146}Sm-^{142}Nd systematics of Early Archaean rocks and implications for crust-mantle evolution. Geochimica et Cosmochimica Acta 60, 3513-3520.

Rosing, M.T., 1999. ^{13}C-depleted carbon microparticles in > 3700-Ma sea-floor sedimentary rocks from West Greenland. Science 283, 674-676.

Ryan, B., Martineau, Y., 2012. Revised and coloured edition of 1992 map showing the Geology of the Saglek Fiord - Hebron Fiord area, Labrador (NTS 14L/2,3,6,7). Scale: 1:100000. Newfoundland Department of Mines and Energy, Geological Survey Branch, Map 92-18B and Geological Survey of Canada, Open File 2466.

Schiøtte, L., Bridgwater, D., Collerson, K.D., Nutman, A.P., Ryan, A.B., 1986. Chemical and isotopic effects of late Archaean high-grade metamorphism and granite injection on early Archaean gneisses, Saglek-Hebron, northern Labrador. In: Dawson, J.B., Hall, D.A., Wedepohl, K.H. (Eds.), The nature of the lower continental crust. Geological Society of London, London, pp. 261-273.

Schiøtte, L., Compston, W., Bridgwater, D., 1989a. U-Th-Pb ages of single zircons in Archaean supracrustals from Nain Province, Labrador, Canada. Canadian Journal

of Earth Science 26, 2636-2644.

Schiøtte, L., Compston, W., Bridgwater, D., 1989b. Ion probe U-Th —Pb zircon dating of polymetamorphic orthogneisses from northern Labrador, Canada. Canadian Journal of Earth Science 26, 1533-1556.

Seyfried, W.E., Ding, K., Berndt, M.E., 1991. Phase equilibria constraints on the chemistry of hot spring fluids at mid-ocean ridges. Geochimica et Cosmochimica Acta 55, 3559-3580.

Sherrell, R.M., Field, M.P., Ravizza, G., 1999. Uptake and fractionation of rare earth elements on hydrothermal plume particles at 9° 45′ N, East Pacific Rise. Geochimica et Cosmochimica Acta 63, 1709-1722.

Shibuya, T., Kitajima, K., Komiya, T., Terabayashi, M., Maruyama, S., 2007. Middle Archean ocean ridge hydrothermal metamorphism and alteration recorded in the Cleaverville area, Pilbara Craton, Western Australia. Journal of Metamorphic Geology 25, 751-767.

Shibuya, T., Komiya, T., Nakamura, K., Takai, K., Maruyama, S., 2010. Highly alkaline; high-temperature hydrothermal fluids in the early Archean ocean. Precambrian Research 182, 230-238.

Shimizu, H., Umemoto, N., Masuda, A., Appel, P.W.U., 1990. Sources of iron-formations in the Archean Isua and Malene supracrustals, West Greenland: Evidence from La-Ce and Sm-Nd isotopic data and REE abundances. Geochimica et Cosmochimica Acta 54, 1147-1154.

Shimojo, M., Yamamoto, S., Sakata, S., Yokoyama, T.D., Maki, K., Sawaki, Y., Ishikawa, A., Aoki, K., Aoki, S., Koshida, K., Tashiro, T., Hirata, T., Collerson, K.D., Komiya, T., 2016. Occurrence and geochronology of the Eoarchean, ~3.9 Ga, Iqaluk Gneiss in the Saglek Block, northern Labrador, Canada: Evidence for the oldest supracrustal rocks in the world. Precambrian Research in press.

Spear, F.S., 1993. Metamorphic phase equilibria and pressure-temperature-time paths. Mineralogical Society of America, Washington, D. C., 799 pp.

Sugahara, H., Sugitani, K., Mimura, K., Yamashita, F., Yamamoto, K., 2010. A systematic rare-earth elements and yttrium study of Archean cherts at the Mount Goldsworthy greenstone belt in the Pilbara Craton: Implications for the origin of microfossil-bearing black cherts. Precambrian Research 177, 73-87.

Swanner, E.D., Planavsky, N.J., Lalonde, S.V., Robbins, L.J., Bekker, A., Rouxel, O.J., Saito, M.A., Kappler, A., Mojzsis, S.J., Konhauser, K.O., 2014. Cobalt and marine redox evolution. Earth and Planetary Science Letters 390, 253-263.

Tashiro, T., Ishida, A., Hori, M., Igisu, M., Sano, Y., Komiya, T., 2016. The earliest trace

of life from the oldest (>3.9 Ga) sedimentary rocks from northern Labrador, Canada. Nature submitted.

Taylor, S.R., McLennan, S.M., 1985. The continental crust: Its composition and evolution. Blackwell, Oxford, 312 pp.

Ueno, Y., Yurimoto, H., Yoshioka, H., Komiya, T., Maruyama, S., 2002. Ion microprobe analysis of graphite from ca. 3.8 Ga metasediments, Isua supracrustal belt, West Greenland: Relationship between metamorphism and carbon isotopic composition. Geochimica et Cosmochimica Acta 66, 1257-1268.

Valley, J.W., Peck, W.H., King, E.M., Wilde, S.A., 2002. A cool early Earth. Geology 30, 351-354.

Viehmann, S., Bau, M., Hoffmann, J.E., Münker, C., 2015. Geochemistry of the Krivoy Rog Banded Iron Formation, Ukraine, and the impact of peak episodes of increased global magmatic activity on the trace element composition of Precambrian seawater. Precambrian Research 270, 165-180.

Wanless, R.K., Bridgwater, D., Collerson, K.D., 1979. Zircon age measurements for Uivak II gneisses from the Saglek area, Labrador. Canadian Journal of Earth Science 16, 962-965.

Wasteneys, H.A., Wardle, R.J., Krogh, T.E., 1996. Extrapolation of tectonic boundaries across the Labrador shelf: U-Pb geochronology of well samples. Canadian Journal of Earth Sciences 33, 1308-1324.

Whitehouse, M.J., Kamber, B.S., Fedo, C.M., Lepland, A., 2005. Integrated Pb- and S-isotope investigation of sulphide minerals from the early Archaean of southwest Greenland. Chemical Geology 222, 112-131.

Whitehouse, M.J., Fedo, C.M., 2007. Microscale heterogeneity of Fe isotopes in >3.71 Ga banded iron formation from the Isua Greenstone Belt, southwest Greenland. Geology 35, 719-722.

Wilde, S.A., Valley, J.W., Peck, W.H., Graham, C.M., 2001. Evidence from detrital zircons for the existence of continental crust and oceans on the Earth 4.4 Gyr ago. Nature 409, 175-178.

Yoshiya, K., Nishizawa, M., Sawaki, Y., Ueno, Y., Komiya, T., Yamada, K., Yoshida, N., Hirata, T., Wada, H., Maruyama, S., 2012. *In situ* iron isotope analyses of pyrite and organic carbon isotope ratios in the Fortescue Group: Metabolic variations of a Late Archean ecosystem. Precambrian Research 212-213, 169-193.

Yoshiya, K., Sawaki, Y., Hirata, T., Maruyama, S., Komiya, T., 2015. In-situ iron isotope analysis of pyrites in ~ 3.7 Ga sedimentary protoliths from the Isua supracrustal belt, southern West Greenland. Chemical Geology 401, 126-139.

Figure Captions

Figure 1. (A) Archean terranes of the North Atlantic Craton in Labrador and western Greenland (modified after Wasteneys et al., 1996), showing that the Saglek Block is equivalent to the Akulleq Terrane in the West Greenland (Bridgwater and Schiøtte, 1991). (B) A map of the Saglek-Hebron area.

Figure 2. (A) A geological map of the southwestern part of the Nulliak Island (Komiya et al. (2015)) and localities of the analyzed BIFs. The area is underlain by the supracrustal rocks and Uivak Gneiss, intruded by the Saglek dykes and young granitic intrusions. The supracrustal rocks are composed of ultramafic and mafic rocks, interlayered with many thin BIF layers. (B) A sketch map of a large outcrop with ~31.5 m thickness along a southwest shore of the Nulliak Island. (C) A photograph of the outcrop. (D) Alternation of Fe-oxide- and silicate-rich black bands and quartz-dominant white bands. (E) An intraformational fold.

Figure 3. (A) A geological map of the Pangertok Inlet area (Komiya et al. (2015)) and localities of analyzed samples. Two NS-trending supracrustal belts run within the Iqaluk-Uivak Gneiss body, intruded by the Saglek dykes. The supracrustal rocks have mafic and ultramafic rocks, cherts, carbonate rocks, BIFs and pelitic rocks. (B) The BIFs occur on the carbonate rocks. (C) Alternation of Fe-oxide- and silicate-rich black bands and quartz-rich white bands. The white bands are thicker than those in the Nulliak Island.

Figure 4. Photomicrographs and BSE images of the BIFs in the Nulliak Island ((A), (B) (C), and (D)) and Pangertok Inlet (E). (A) A plane-polarized image of alternation of magnetite+pyroxene and quartz layers. (B) A plane-polarized image of an aluminous BIF, which contain hornblende together with magnetite and pyroxene. (C) A BSE image of pyroxene with orthopyroxene lamellae, magnetite and quartz. Orthopyroxene grains in the matrix are rimmed with cummingtonite. (D) A BSE image of clinopyroxene with bidirectional orthopyroxene lamellae. (E) A plane-polarized image of alternating quartz+magnetite+clinopyroxene and quartz layers.

Figure 5. Compositions of orthopyroxene, clinopyroxene and orthopyroxene lamellae within clinopyroxene in BIFs of the Nulliak Island (A) and clinopyroxene in BIFs of the Pangertok Inlet (B).

Figure 6. Variation diagrams of Fe_2O_3 contents for (A) SiO_2, (B) MgO and (C) CaO contents. (D) A ternary plot of Fe-Ca-Mg.

Figure 7. Variation diagrams of Fe_2O_3 contents for (A) V, (B) Cr, (C) Co, (D) Ni, (E) Cu, (F) Zn, (G) Sr, (H) Y, (I) Zr, (J) Pr, (K) Sm, (L) Yb and (M) U contents.

Figure 8. Post-Archean Australian shale (PAAS)-normalized REE + Y diagrams for BIFs in the Nulliak Island (A) and BIFs in the Pangertok Inlet (B).

Figure 9. Ternary diagrams for a CaO-MgO-SiO_2-H_2O-CO_2 (CMSHC) system projected from H_2O and CO_2 with nominal mineral compositions (Spear, 1993) for BIFs in the Nulliak Island (A) and BIFs in the Pangertok Inlet (B), respectively.

Figure 10. Variation diagrams of normative modal compositions of dolomite with (A) V, (B) Cr, (C) Co, (D) Ni, (E) Cu, (F) Zn, (G) Y, (H) Pr, (I) Sm, (J) Yb and (K) U contents. The calculation method of normative dolomite compositions is written in the text and appendix.

Figure 11. Zirconium variation diagrams of (A) V, (B) Cr, (C) Co, (D) Ni, (E) Cu, (F) Zn, (G) Y, (H) Pr, (I) Sm, (J) Yb, (K) U contents, (L) La anomalies (La/La*), (M) Eu anomalies (Eu/Eu*) and (N) Y/Ho ratios.

Figure 12. Zirconium variation diagrams of (A) V, (B) Cr, (C) Ni, (D) Cu, (E) Zn and (F) U contents. Purple and green arrows mean the directions of metaperidotite and amphibolite compositions in the Nulliak supracrustal rocks (Nutman et al., 1989). Red lines and areas enclosed with blues line mean regression lines and prediction areas (1σ), respectively. Gray areas mean areas encompassing the all data.

APPENDIX

Calculation of normative mineral compositions for BIFs.

All of iron is as Fe_2O_3. Molecular proportions are obtained by dividing weight percent of oxides by molecular weight. The normative modal compositions are combined according to the following:

Pyrites: $FeS_2 = 1/2SO_2$

Hydroxyl-fluorapatite: $Ca_5(PO_4,CO_3)_3(OH,O,F) = 2/3P_2O_5$

If $(CaO-10/3P_2O_5)>MgO$

Dolomite: $CaMg(CO_3)_2 = MgO$

Calcite: $CaCO_3 = (CaO-10/3P_2O_5)-MgO$

Silica mineral (opal): $SiO_2 \cdot nH_2O = SiO_2$

Ferrihydrite: $FeO(OH) = 1/2Fe_2O_3-1/2SO_2$

If $(CaO-10/3P_2O_5)<MgO$

Dolomite: $CaMg(CO_3)_2 = CaO$

Contaminant: MgO-CaO

Silica mineral (opal): $SiO_2 \cdot nH_2O = SiO_2-(MgO-CaO)$

Ferrihydrite: $FeO(OH) = 1/2Fe_2O_3-1/2SO_2$

Proportions of ferrihydrite, silica mineral, carbonates, pyrites and contaminant are then normalized to 100%.

Table.1 Major-element compositions of minerals in the BIFs of the Nulliak Island

Sample No.	LAD310						LAD317					LAD323		LAD330				
mineral	magnetite	quartz	cpx	opx	host cpx	opx lamellae in host cpx	magnetite	quartz	amphibole	host cpx	opx	host cpx	opx	magnetite	quartz	amphibole (rim of opx)	host cpx	opx
n	10	7	16	13	1	1	5	7	11	10	13	7	15	8	9	3	6	18
SiO_2(wt%)	0.09	100.05	51.59	50.03	51.78	49.99	0.08	99.92	41.60	50.84	49.78	50.90	49.74	0.09	100.45	52.24	51.54	49.41
TiO_2	0.07	0.01	0.01	0.01	0.02	0.00	0.08	0.00	0.19	0.02	0.01	0.00	0.01	0.05	0.00	0.01	0.00	0.01
Al_2O_3	0.64	0.01	0.70	0.41	0.77	0.36	1.54	0.01	12.22	1.51	0.73	0.91	0.36	0.42	0.01	0.49	0.64	0.39
Cr_2O_3	0.01	0.01	0.01	0.00	0.00	0.00	0.01	0.03	0.01	0.01	0.01	0.03	0.00	0.01	0.01	0.00	0.01	0.06
FeO*	91.70	0.02	15.71	33.97	16.01	35.86	91.49	0.01	22.63	15.50	34.42	16.73	34.67	92.04	0.02	29.12	16.28	34.44
MnO	0.20	0.01	1.29	3.08	1.31	3.28	0.16	0.00	0.45	0.87	2.13	2.01	4.36	0.14	0.01	3.62	1.33	3.33
NiO	0.01	0.02	0.01	0.01	0.00	0.00	0.01	0.01	0.02	0.02	0.01	0.02	0.01	0.03	0.02	0.02	0.01	0.01
MgO	0.03	0.01	9.24	11.69	8.65	10.31	0.04	0.00	6.85	9.61	12.54	8.17	10.26	0.00	0.00	11.03	9.22	11.49
CaO	-	0.00	21.13	0.80	21.10	0.96	0.00	0.01	11.32	21.50	0.83	20.26	1.00	0.00	0.00	0.98	20.65	0.88
Na_2O	0.01	0.01	0.33	0.02	0.33	0.03	0.01	0.01	1.35	0.48	0.01	0.38	0.02	0.01	0.01	0.04	0.32	0.02
K_2O	-	0.00	0.01	0.01	0.00	0.00	0.01	0.01	1.69	0.00	0.01	0.00	0.00	0.01	0.00	0.00	0.01	0.01
Total	92.77	100.15	100.22	100.04	100.18	100.79	93.46	100.03	98.42	100.51	100.47	99.63	100.45	92.82	100.53	97.56	100.23	100.00
Formula proportions calculated on the basis of 24 oxygens (O=23 as for amphibole)																		
Si	0.02	11.99	7.97	8.00	8.00	8.01	0.02	11.99	6.35	7.83	7.91	7.96	8.00	0.02	12.00	7.55	7.97	7.94
Ti	0.01	0.00	0.00	0.00	0.00	0.00	0.01	0.00	0.02	0.00	0.00	0.00	0.00	0.01	0.00	0.00	0.00	0.00
Al	0.18	0.00	0.13	0.08	0.14	0.07	0.42	0.00	2.20	0.27	0.14	0.17	0.07	0.11	0.00	0.08	0.12	0.07
Al(4)	-	-	0.04	0.00	0.00	0.00	-	-	1.65	0.23	0.10	0.04	0.00	-	-	0.08	0.04	0.07
Al(6)	-	-	0.09	0.08	0.14	0.07	-	-	0.55	0.05	0.03	0.13	0.07	-	-	0.00	0.08	0.01
Cr	0.00	0.00	0.00	0.00	0.00	0.00	0.00	0.00	0.00	0.00	0.00	0.00	0.00	0.00	0.00	0.00	0.00	0.01
Fe	17.73	0.00	2.03	4.54	2.07	4.80	17.49	0.00	2.89	1.99	4.57	2.19	4.66	17.81	0.00	3.52	2.11	4.63
Fe(2)	5.95	-	1.98	4.54	2.07	4.80	5.96	-	2.41	1.67	4.50	2.16	4.66	5.96	-	0.95	2.06	4.57
Fe(3)	11.78	-	0.05	0.00	0.00	0.00	11.53	-	0.48	0.32	0.07	0.03	0.00	11.84	-	2.56	0.05	0.06
Mn	0.04	0.00	0.17	0.42	0.17	0.44	0.03	0.00	0.06	0.11	0.29	0.27	0.59	0.03	0.00	0.44	0.17	0.45
Ni	0.00	0.00	0.00	0.00	0.00	0.00	0.00	0.00	0.00	0.00	0.00	0.00	0.00	0.01	0.00	0.00	0.00	0.00
Mg	0.01	0.00	2.13	2.79	1.99	2.46	0.01	0.00	1.56	2.21	2.97	1.91	2.46	0.00	0.00	2.38	2.13	2.75
Ca	0.00	0.00	3.50	0.14	3.49	0.16	0.00	0.00	1.85	3.55	0.14	3.40	0.17	0.00	0.00	0.15	3.42	0.15
Na	0.01	0.00	0.10	0.01	0.10	0.01	0.01	0.00	0.40	0.14	0.00	0.12	0.01	0.00	0.00	0.01	0.10	0.01
K	0.00	0.00	0.00	0.00	0.00	0.00	0.00	0.00	0.33	0.00	0.00	0.00	0.00	0.00	0.00	0.00	0.00	0.00
total	17.99	12.00	16.02	15.97	15.97	15.96	18.00	12.01	15.80	16.11	16.02	16.01	15.97	17.99	12.00	14.97	16.02	16.02
XFe**	-	-	0.16	0.58	0.27	0.61	-	-	-	0.22	0.59	0.28	0.59	-	-	-	0.26	0.58

*Total iron as FeO

**XFe=Fe(II)/(Fe(II)+Mg+Ca+Mn)

Table.1 (continued)

Sample No.	LAD330				LAE42					LAE44					
mineral	host cpx No.1	opx lamella in	host cpx No.1	host cpx No.2	opx lamella in host cpx No.2	magnetite	quartz	opx	host cpx	opx lamellae in host cpx	magnetite	quartz	cpx	opx	host cpx	opx lamellae in host cpx
n	2		2	2	1	9	10	2	2	5	6	7	13	4	5	2
SiO_2(wt%)	51.53		50.30	51.67	49.55	0.11	99.89	48.71	50.17	48.24	0.08	100	51.06	49.59	50.89	49.38
TiO_2	0.00		0.01	0.00	0.01	0.05	0.01	0.03	0.00	0.02	0.08	0.02	0.00	0.03	0.01	0.00
Al_2O_3	0.62		0.37	0.64	0.31	0.49	0.01	0.30	0.53	0.31	0.68	0.00	0.69	0.40	0.68	0.31
Cr_2O_3	0.02		0.03	0.00	0.00	0.01	0.01	0.02	0.01	0.00	0.01	0.02	0.02	0.01	0.04	0.01
FeO*	16.87		35.27	16.34	36.20	92.56	0.02	38.27	18.44	38.69	92.07	0.04	16.72	35.52	16.84	37.61
MnO	1.22		2.81	1.29	2.98	0.06	0.01	1.93	0.76	2.00	0.15	0.00	1.04	2.52	1.05	2.50
NiO	0.00		0.00	0.01	0.00	0.01	0.02	0.00	0.01	0.01	0.01	0.02	0.02	-	0.01	0.01
MgO	9.23		10.89	9.01	10.24	0.01	0.00	10.11	8.58	9.83	0.02	0.00	8.70	10.97	8.68	9.57
CaO	20.12		0.89	20.93	0.52	0.00	0.01	0.74	21.21	0.86	0.00	0.01	21.28	0.97	21.24	0.64
Na_2O	0.23		0.02	0.37	0.04	0.01	0.01	0.00	0.41	0.02	0.01	0.00	0.35	0.01	0.34	0.01
K_2O	0.01		0.00	0.00	0.00	0.00	0.01	0.01	0.01	0.01	0.01	0.00	0.00	0.01	0.01	0.02
Total	100.05		100.60	100.46	99.83	93.31	99.99	100.15	100.31	100.00	93.12	100.25	100.05	100.04	99.94	100.05
Formula proportions calculated on the basis of 24 oxygens (O=23 as for amphibole)																
Si	7.99		8.03	7.98	8.02	0.03	11.99	7.92	7.86	7.89	0.02	12.00	7.94	7.98	7.93	8.01
Ti	0.00		0.00	0.00	0.00	0.01	0.00	0.00	0.00	0.00	0.01	0.00	0.00	0.00	0.00	0.00
Al	0.11		0.07	0.12	0.06	0.13	0.00	0.10	0.22	0.15	0.19	0.00	0.13	0.08	0.12	0.06
Al(4)	0.01		0.00	0.03	0.00	-	-	0.10	0.22	0.15	-	-	0.09	0.01	0.10	0.00
Al(6)	0.10		0.07	0.09	0.06	-	-	0.00	0.00	0.00	-	-	0.04	0.06	0.02	0.06
Cr	0.00		0.00	0.00	0.00	0.00	0.00	0.00	0.00	0.00	0.00	0.00	0.00	0.00	0.00	0.00
Fe	2.19		4.71	2.11	4.90	17.80	0.00	5.21	2.42	5.29	17.73	0.00	2.17	4.78	2.19	5.11
Fe(2)	2.19		4.71	2.05	4.90	5.98	-	5.12	2.07	5.14	5.97	-	2.03	4.78	2.02	5.11
Fe(3)	0.00		0.00	0.06	0.00	11.82	-	0.09	0.35	0.15	11.76	-	0.15	0.00	0.17	0.00
Mn	0.16		0.38	0.17	0.41	0.01	0.00	0.27	0.10	0.28	0.029	0.00	0.14	0.34	0.14	0.34
Ni	0.00		0.00	0.00	0.00	0.00	0.00	0.00	0.00	0.00	0.00	0.00	0.00	0.00	0.00	0.00
Mg	2.13		2.59	2.07	2.47	0.00	0.00	2.45	2.00	2.40	0.01	0.00	2.02	2.63	2.02	2.32
Ca	3.34		0.15	3.46	0.09	0.00	0.00	0.13	3.56	0.15	0.00	0.00	3.55	0.17	3.55	0.11
Na	0.07		0.01	0.11	0.01	0.01	0.00	0.00	0.12	0.01	0.00	0.00	0.11	0.00	0.10	0.00
K	0.00		0.00	0.00	0.00	0.00	0.00	0.00	0.00	0.00	0.00	0.00	0.00	0.00	0.00	0.00
total	15.99		15.94	16.02	15.96	17.99	12.00	16.04	16.16	16.08	18.00	12.00	16.05	15.98	16.06	15.96
XFe**	0.29		0.63	0.27	0.66			0.66	0.27	0.67			0.27	0.63	0.27	0.68

*Total iron as FeO

**XFe=Fe(II)/(Fe(II)+Mg+Ca+Mn)

Table.2 Major-element compositions of minerals in the BIFs of the Pangertok Inlet

Sample No.	LAD11	LAD714			LAD729	LAD740			LAD904
mineral	cpx	magnetite	quartz	cpx	cpx	magnetite	quartz	cpx	cpx
n	30	8	13	11	14	12	17	15	17
SiO_2(wt%)	53.17	0.12	100.02	50.46	52.34	0.02	100.33	52.87	53.03
TiO_2	0.01	0.08	0.01	0.01	0.01	0.02	0.01	0.01	0.01
Al_2O_3	0.33	0.12	0.01	2.01	0.99	0.05	0.00	0.51	0.74
Cr_2O_3	0.01	0.02	0.01	0.01	0.01	0.02	0.01	0.02	0.01
FeO*	8.68	91.95	0.03	19.14	11.79	92.66	0.06	12.06	10.58
MnO	0.69	0.07	0.01	0.42	0.72	0.13	0.01	0.87	0.61
NiO	0.02	0.02	0.01	0.03	0.01	0.00	0.01	0.01	0.02
MgO	13.78	0.01	0.00	6.31	11.01	0.01	0.00	11.19	12.28
CaO	22.38	0.00	0.01	21.00	22.08	0.00	0.01	21.64	22.20
Na_2O	0.67	0.02	0.03	0.63	0.87	0.02	0.01	0.59	0.76
K_2O	0.01	0.02	0.02	0.01	0.00	0.00	0.01	0.01	0.01
Total	99.92	92.43	100.17	100.22	100.06	92.95	100.46	99.97	100.47
Formula proportions calculated on the basis of 24 oxygens									
Si	7.98	0.04	11.99	7.89	7.96	0.01	11.99	8.03	7.97
Ti	0.00	0.02	0.00	0.00	0.00	0.01	0.00	0.00	0.00
Al	0.07	0.04	0.00	0.37	0.18	0.02	0.00	0.09	0.13
Al(4)	0.07	-	-	0.11	0.08	-	-	0.00	0.06
Al(6)	0.00	-	-	0.26	0.10	-	-	0.09	0.07
Cr	0.00	0.01	0.00	0.00	0.00	0.01	0.00	0.00	0.00
Fe	1.09	23.84	0.00	2.50	1.50	23.92	0.01	1.53	1.33
Fe(2)	0.83	7.97	-	2.46	1.26	7.06	-	1.45	1.12
Fe(3)	0.26	15.87	-	0.04	0.24	15.96	-	0.08	0.21
Mn	0.09	0.02	0.00	0.06	0.09	0.02	0.00	0.11	0.08
Ni	0.00	0.00	0.00	0.00	0.00	0.00	0.00	0.00	0.00
Mg	3.08	0.00	0.00	1.47	2.49	0.01	0.00	2.53	2.75
Ca	3.60	0.00	0.00	3.52	3.60	0.00	0.00	3.52	3.58
Na	0.20	0.01	0.01	0.19	0.26	0.02	0.00	0.17	0.22
K	0.00	0.01	0.00	0.00	0.00	0.00	0.00	0.00	0.00
total	16.09	23.99	12.01	16.01	16.08	24.01	12.01	16.01	16.07
XFe**	0.11			0.33	0.17			0.19	0.15

*Total iron as FeO

**XFe=Fe(II)/(Fe(II)+Mg+Ca+Mn)

Table.3 Whole-rock major and trace element data for the BIFs in the Nulliak Island

Sample No.	LAD285	LAD286	LAD287	LAD288	LAD291	LAD292	LAD294	LAD297	LAD301	LAD305	LAD308	LAD310	LAD313	LAD317	LAD318	LAD323	LAD324	LAD325	LAD330-3	LAD330-1	LAD331	LAD332	LAE42	LAE44	LAA311
SiO_2 (wt%)	49.4	48.4	39.1	39.5	39.7	35.7	44.4	40.5	45.6	36.3	32.4	41.9	37.3	48.9	41.4	39.6	38.6	35.2	44.1	38.9	42.2	43.4	38.3	41.8	42.5
Al_2O_3 (wt%)	1.16	1.18	1.48	0.91	0.49	0.34	1.50	0.69	0.36	0.56	0.53	0.89	0.48	1.36	0.47	0.61	0.28	0.41	0.32	0.48	1.03	1.62	0.70	0.74	0.82
TiO_2 (wt%)	0.03	0.03	0.13	0.13	0.02	0.02	0.05	0.02	0.02	0.01	0.01	0.02	0.01	0.08	0.02	0.02	0.02	0.02	0.01	0.02	0.04	0.05	0.02	0.03	0.04
Fe_2O_3 (wt%)*	46.0	44.8	50.0	54.0	52.2	58.5	48.5	52.9	49.5	59.0	62.2	52.4	57.6	44.7	52.1	55.7	55.8	60.1	47.5	56.9	50.0	52.1	56.8	53.2	52.3
MgO (wt%)	1.92	2.38	2.34	2.81	2.71	2.45	1.80	2.29	2.39	2.69	2.79	2.79	2.47	2.81	2.83	1.92	2.60	2.15	2.81	2.73	2.79	2.74	2.65	2.47	2.75
MnO (wt%)	0.41	0.51	0.72	0.91	0.95	1.01	0.34	0.85	0.43	1.31	1.35	0.69	1.19	0.48	0.95	1.19	0.95	1.40	0.66	0.85	0.66	0.61	0.50	0.54	0.55
CaO (wt%)	2.73	4.12	5.88	4.01	3.88	3.71	4.00	4.19	3.29	3.37	3.90	3.68	3.68	3.59	4.03	3.48	3.67	3.13	5.85	2.84	2.79	2.36	4.04	3.54	3.51
Na_2O (wt%)	-	0.02	0.00	-	-	-	0.05	-	-	-	-	-	-	-	-	-	-	-	-	-	-	-	-	-	-
K_2O (wt%)	0.07	0.09	0.07	0.02	0.01	0.01	0.23	0.01	0.02	-	-	0.00	-	0.04	0.02	0.00	0.00	0.00	-	-	0.02	0.02	-	-	-
P_2O_5 (wt%)	0.04	0.04	0.06	0.06	0.05	0.06	0.04	0.05	0.05	0.06	0.06	0.05	0.05	0.04	0.05	0.06	0.05	0.06	0.04	0.05	0.05	0.05	0.05	0.05	0.04
Loss of ignition																					1.20				
Gain of ignition	1.25	1.58	0.32	2.12	0.05	1.90	1.20	1.51	1.90	2.89	3.30	3.51	2.59	1.98	1.87	1.69	2.01	2.87	1.65	3.02		3.20	3.65	2.50	3.20
Total (wt%)	100.51	99.99	99.46	100.23	99.96	99.90	99.71	99.99	99.76	100.41	99.94	98.91	100.19	100.02	100.00	100.89	99.96	99.60	99.64	99.75	100.78	99.75	99.41	99.87	99.31
Li (ppm)	3.06	4.66	5.52	3.96	4.81	2.63	8.56	5.86	8.21	5.42	6.23	7.60	5.66	8.38	7.63	5.38	8.59	4.50	10.35	7.59	11.26	9.45	4.28	3.61	4.34
Sc (ppm)	1.35	1.41	1.64	1.18	0.73	0.92	1.75	1.36	1.34	0.84	0.84	1.02	0.68	2.85	1.12	0.92	1.01	1.18	0.78	0.85	0.92	1.96	0.92	0.96	1.36
V (ppm)	9.76	10.02	14.40	11.06	6.07	4.38	13.88	6.20	8.32	5.76	4.99	6.74	5.10	18.89	7.44	6.14	7.05	7.56	6.09	5.80	7.48	13.91	7.48	6.36	10.68
Cr (ppm)	32	29	31	25	16	17	40	25	25	19	16	24	16	44	23	23	19	24	22	22	37	41	15	12	23
Co (ppm)	8.7	10.2	19.2	15.1	13.5	2.4	12.6	13.7	11.1	14.2	10.2	12.3	9.0	10.3	11.8	14.0	11.5	16.3	9.2	12.0	14.0	16.9	13.3	16.1	10.4
Ni (ppm)	46	50	50	30	23	17	50	33	42	28	33	37	28	47	39	40	37	44	40	45	56	63	22	22	40
Cu (ppm)	5.33	10.66	11.71	13.07	1.92	6.97	7.24	4.40	8.48	2.99	0.60	1.14	0.71	14.61	6.04	0.34	4.70	0.46	4.49	0.98	2.04	6.43	0.17	1.19	0.182
Zn (ppm)	66	97	175	192	169	26	135	148	105	141	121	236	170	53	147	98	113	115	63	61	115	79	166	70	159
Ga (ppm)	2.89	3.28	7.9	15.77	3.10	1.11	4.07	3.54	2.98	1.74	1.53	0.75	1.34	4.20	2.08	0.48	1.84	0.39	0.53	2.07	2.87	3.99	3.32	6.12	2.05
Rb (ppm)	1.90	2.88	2.97	1.09	1.28	3.35	1.34	0.69	1.77	0.16	0.26	0.25	0.16	2.40	1.96	1.00	0.36	0.65	0.31	0.52	1.43	0.70	0.15	0.24	0.16
Sr (ppm)	11.2	18.4	26.8	9.5	11.5	23.0	7.8	5.7	17.2	22.5	19.0	5.3	10.6	11.7	8.3	19.3	21.6	16.7	13.0	7.9	6.8	2.0	7.0	4.6	6.9
Y (ppm)	5.40	7.60	9.91	10.92	7.29	5.94	6.81	8.64	8.04	7.96	9.14	7.55	7.96	6.78	8.51	8.78	8.28	8.02	9.11	7.19	8.16	9.98	7.39	7.38	8.21
Zr (ppm)	15.65	10.65	11.64	12.61	2.99	5.01	13.43	12.71	7.64	5.71	3.71	10.54	1.78	26.84	4.85	3.31	6.48	3.12	4.17	3.78	12.25	20.74	4.02	5.62	11.16
Nb (ppm)	0.94	1.33	1.19	1.27	0.74	0.25	1.19	0.88	0.63	0.56	0.37	0.98	0.39	1.21	0.68	0.43	0.45	0.45	0.58	0.60	0.74	1.67	0.93	0.78	0.67
Ba (ppm)	34.5	29.4	56.3	9.6	16.4	19.2	15.9	6.2	0.2	0.7	1.7	1.1	0.2	69.1	8.1	3.2	1.4	0.4	2.8	4.4	24.8	5.2	2.7	2.4	0.6
La (ppm)	3.10	3.97	2.70	4.59	2.26	2.08	4.47	3.86	3.31	2.62	2.64	2.98	2.45	2.91	3.710	2.70	2.69	2.49	3.21	2.80	2.49	2.42	2.26	1.53	2.51
Ce (ppm)	5.78	7.89	6.37	12.50	3.99	2.91	9.67	8.89	5.65	4.33	4.37	7.72	4.68	6.83	5.680	4.80	4.85	4.39	5.02	4.79	5.230	5.89	3.99	2.94	5.21
Pr (ppm)	0.654	0.906	0.830	1.827	0.433	0.333	1.15	1.169	0.643	0.551	0.469	1.085	0.541	0.873	0.655	0.569	0.580	0.529	0.606	0.549	0.658	0.781	0.433	0.333	0.618
Nd (ppm)	2.35	3.35	3.41	7.70	1.61	1.38	4.13	4.34	2.40	2.23	1.84	4.25	2.01	3.54	2.390	2.32	2.29	2.12	2.43	2.12	2.60	3.27	1.61	1.51	2.49
Sm (ppm)	0.471	0.625	0.794	1.811	0.326	0.296	0.757	0.889	0.505	0.454	0.363	0.868	0.376	0.779	0.453	0.481	0.465	0.471	0.492	0.409	0.611	0.703	0.326	0.286	0.542
Eu (ppm)	0.132	0.208	0.250	0.273	0.179	0.141	0.228	0.180	0.164	0.168	0.176	0.174	0.161	0.177	0.183	0.196	0.173	0.179	0.206	0.161	0.199	0.208	0.179	0.179	0.184
Gd (ppm)	0.569	0.699	0.912	1.582	0.484	0.404	0.786	0.888	0.613	0.557	0.539	0.769	0.526	0.815	0.610	0.628	0.614	0.614	0.640	0.566	0.739	0.842	0.484	0.474	0.701
Tb (ppb)	80.6	111.8	147.7	232.9	71.3	56.0	114.9	127.9	95.3	86.6	77.3	115.4	77.1	123.6	94.6	96.0	93.6	96.7	105.1	81.1	124.4	133.5	71.3	68.5	110.6
Dy (ppm)	0.516	0.703	0.975	1.337	0.513	0.376	0.726	0.786	0.617	0.568	0.514	0.701	0.518	0.733	0.620	0.618	0.636	0.611	0.692	0.544	0.776	0.862	0.513	0.432	0.743
Ho (ppb)	121	171	233	283	135	91	161	180	154	147	140	166	133	161	160	158	162	155	177	137	188	213	135	124	181
Er (ppm)	0.375	0.527	0.692	0.794	0.411	0.263	0.484	0.552	0.461	0.462	0.436	0.502	0.417	0.495	0.493	0.474	0.501	0.466	0.543	0.428	0.583	0.675	0.411	0.351	0.543
Tm (ppb)	52.8	76.1	97.8	109.3	57.6	35.0	69.3	73.0	70.0	63.1	62.1	72.6	58.7	68.3	71.0	65.6	68.2	62.9	75.1	60.5	82.4	98.1	57.6	46.9	75.2
Yb (ppm)	0.339	0.493	0.629	0.698	0.370	0.224	0.453	0.471	0.427	0.405	0.381	0.460	0.352	0.445	0.430	0.399	0.441	0.391	0.469	0.378	0.540	0.618	0.370	0.289	0.482
Lu (ppb)	52.1	77.9	101.4	104.9	60.8	34.3	71.6	74.7	66.4	68.8	62.2	73.8	61.0	69.5	73.0	66.9	71.8	66.4	76.0	63.0	81.0	101.0	61.0	50.0	79.0
Hf (ppm)	0.36	0.30	0.33	0.28	0.07	0.19	0.38	0.27	0.19	0.17	0.12	0.16	0.07	0.58	0.13	0.09	0.16	0.19	0.16	0.17	0.28	0.46	0.16	0.19	0.26
Ta (ppb)	74	78	75	105	44	16	93	39	31	21	19	25	18	73	45	16	49	22	34	44	46	62	28	52	30
Th (ppm)	0.826	0.764	0.066	0.402	0.228	0.140	0.912	0.216	0.451	0.222	0.414	0.171	0.119	0.864	0.242	0.187	0.190	0.286	0.365	0.215	0.534	0.931	0.256	0.200	0.151
U (ppb)	183.8	124.0	47.7	77.4	40.5	44.7	151.0	100.5	97.6	98.4	50.8	29.6	27.0	156.3	33.9	52.6	63.4	81.4	69.2	73.0	105.2	121.9	32.3	34.9	17.9
Y/Ho	44.6	44.4	42.5	38.6	54.0	65.3	42.3	48.0	52.2	54.1	65.3	45.5	59.8	42.1	53.2	55.6	51.1	51.7	51.5	52.5	43.4	46.9	54.7	59.5	45.4
La/La*	1.11	1.09	1.07	0.90	1.31	2.11	0.91	0.83	1.31	1.49	1.61	0.78	1.14	1.05	1.37	1.52	1.35	1.43	1.61	1.40	1.11	1.08	1.31	2.25	1.25
Ce/Ce*	0.98	1.00	1.00	0.92	1.06	1.15	0.93	0.87	1.02	1.00	1.14	0.87	1.00	1.00	0.98	1.08	1.03	1.04	1.04	1.05	0.98	1.00	1.06	1.33	1.07
Eu/Eu*	1.32	1.54	1.44	0.78	2.34	2.16	1.48	1.02	1.47	1.67	2.09	1.03	1.88	1.10	1.76	1.81	1.64	1.66	1.80	1.75	1.43	1.34	2.34	2.56	1.49

*Total iron as Fe_2O_3

La/La*, Ce/Ce* and Eu/Eu*are defined by $[La/(3Pr-2/Nd)]_{PAAS}$, $[Ce/(2Pr-Nd)]_{PAAS}$ and $[Eu/(0.67Sm+0.33Tb)]_{PAAS}$, respectively.

Table.4 Whole-rock major and trace element data for the BIFs in the Pangertok Inlet

Sample No.	LAD11	LAD710	LAD713	LAD714	LAD728	LAD729	LAD736	LAD740	LAD903	LAD904	LAD905	LAD909	LAD911
SiO_2 (wt%)	68.2	48.3	51.2	52.6	56.4	61.5	75.7	75.7	56.1	56.8	68.5	60.5	55.8
Al_2O_3 (wt%)	0.72	1.77	0.56	1.45	1.01	0.49	0.20	0.33	0.59	0.58	0.91	0.93	0.56
TiO_2 (wt%)	0.04	0.06	0.01	0.08	0.02	0.01	<D.L.	0.00	0.00	0.03	0.05	0.06	0.02
Fe_2O_3 (wt%)*	28.4	45.6	41.8	38.9	30.7	30.0	16.9	18.5	38.8	34.0	28.8	35.5	37.8
MgO (wt%)	1.78	2.37	3.94	1.78	4.42	3.08	2.46	1.98	2.39	3.41	1.70	1.38	2.76
MnO (wt%)	0.13	0.13	0.17	0.17	0.43	0.31	0.23	0.21	0.15	0.24	0.12	0.08	0.18
CaO (wt%)	2.62	3.29	4.34	6.15	7.69	5.96	3.97	3.66	3.97	5.85	1.84	1.88	4.32
Na_2O (wt%)	-	0.06	-	0.07	0.14	0.03	-	-	0.01	-	-	-	-
K_2O (wt%)	0.02	0.32	0.04	0.22	0.03	0.00	-	0.03	0.02	0.03	0.17	0.24	0.03
P_2O_5 (wt%)	0.02	0.08	0.05	0.04	0.02	0.02	0.02	0.01	0.02	0.01	0.02	0.02	0.02
Loss of ignition							0.28						
Gain of ignition	1.90	2.15	2.50	1.62	1.60	1.52		0.12	2.50	0.30	1.98	0.79	1.85
Total (wt%)	100.03	99.83	99.61	99.84	99.26	99.88	99.76	100.30	99.55	100.65	100.13	99.80	99.64
Li (ppm)	17.02	7.84	2.64	9.98	32.40	27.4	9.06	5.00	9.29	13.96	8.47	4.71	9.14
Sc (ppm)	0.68	1.86	0.92	2.12	0.87	0.81	0.16	0.48	0.63	0.84	1.01	0.91	0.73
V (ppm)	7.69	8.38	4.38	11.89	4.52	3.33	1.00	3.24	3.80	4.98	6.45	7.84	3.84
Cr (ppm)	8	38	17	48	18	11	4	9	18	13	29	22	16
Co (ppm)	2.2	5.8	2.4	4.9	3.0	1.4	2.1	0.8	1.2	2.2	2.8	2.3	1.6
Ni (ppm)	11	27	17	34	20	12	15	7	14	14	22	22	16
Cu (ppm)	0.29	1.43	6.96	1.31	0.82	0.08	3.98	0.34	2.55	2.81	4.45	3.05	1.58
Zn (ppm)	41	72	26	150	28	27	16	9	15	28	25	16	21
Ga (ppm)	6.69	9.95	1.11	6.17	3.13	2.83	0.66	0.69	1.35	2.63	3.25	2.71	1.97
Rb (ppm)	1.07	20.80	3.35	8.53	1.31	0.26	0.16	0.96	0.86	1.07	9.37	15.15	1.06
Sr (ppm)	5.5	14.1	23.0	18.0	9.5	5.8	5.9	8.0	7.2	8.6	6.8	5.47	5.30
Y (ppm)	2.93	5.33	3.94	5.07	4.16	1.77	1.25	1.16	3.22	3.07	2.71	2.42	2.85
Zr (ppm)	4.01	9.69	9.01	20.18	9.18	4.91	1.80	2.91	4.54	3.57	4.42	1.29	1.81
Nb (ppm)	0.16	4.60	0.25	1.59	0.44	0.17	0.11	0.22	0.20	0.22	0.54	0.49	0.19
Ba (ppm)	6.8	48.2	49.2	291.3	158.6	5.6	14.4	56.2	27.8	43.3	307.7	210.9	39.2
La (ppm)	1.58	4.25	2.08	3.56	2.95	1.18	0.71	0.88	1.59	1.77	2.00	1.51	1.76
Ce (ppm)	2.73	6.81	3.01	6.43	5.23	2.29	1.10	1.62	2.82	3.08	4.65	3.31	3.11
Pr (ppm)	0.289	0.771	0.353	0.822	0.588	0.269	0.121	0.181	0.330	0.346	0.609	0.408	0.353
Nd (ppm)	1.06	2.73	1.38	3.19	2.18	1.00	0.45	0.65	1.21	1.31	2.34	1.60	1.33
Sm (ppm)	0.201	0.542	0.296	0.640	0.407	0.181	0.088	0.107	0.238	0.260	0.423	0.303	0.257
Eu (ppm)	0.184	0.200	0.141	0.174	0.173	0.125	0.077	0.088	0.135	0.153	0.148	0.119	0.140
Gd (ppm)	0.280	0.657	0.404	0.629	0.445	0.184	0.122	0.132	0.316	0.310	0.402	0.356	0.303
Tb (ppb)	44.3	91.5	55.8	93.3	58.9	28.1	17.9	16.9	46.2	45.5	54.5	45.1	44.8
Dy (ppm)	0.287	0.539	0.376	0.535	0.373	0.167	0.126	0.108	0.302	0.274	0.316	0.268	0.274
Ho (ppb)	72	127	91	117	86	41	31	25	71	65	71	60	65
Er (ppm)	0.215	0.366	0.263	0.327	0.260	0.117	0.097	0.076	0.212	0.191	0.203	0.181	0.188
Tm (ppb)	30.1	53.8	35.4	45.8	36.4	15.9	13.1	10.6	30.4	26.9	28.0	26.5	27.5
Yb (ppm)	0.175	0.328	0.224	0.292	0.214	0.109	0.084	0.059	0.190	0.159	0.173	0.165	0.172
Lu (ppb)	29.7	51.1	34.3	46.5	35.0000	17.2	14.8	9.7	30.2	24.6	27.3	24.5	27.1
Hf (ppm)	0.10	0.38	0.19	0.62	0.16	0.12	0.03	0.07	0.09	0.10	0.15	0.07	0.06
Ta (ppb)	4	380	16	40	38	8	7	12	9	11	39	29	9
Th (ppm)	0.047	0.497	0.140	0.255	0.167	0.080	0.042	0.071	0.052	0.074	0.019	0.047	0.182
U (ppb)	13.3	96.3	44.7	27.6	44.0	27.6	36.7	7.4	2.4	41.4	5.6	9.4	59.6
Y/Ho	40.7	42.0	43.3	43.3	48.4	43.2	40.3	46.4	45.4	47.2	38.4	40.3	44.2
La/La*	1.33	1.25	1.67	1.21	1.25	1.10	1.48	1.14	1.17	1.34	0.89	1.06	1.29
Ce/Ce*	1.07	0.97	1.04	0.95	1.02	0.98	1.05	0.99	0.97	1.05	0.91	0.99	1.03
Eu/Eu*	3.89	1.75	2.16	1.36	2.13	3.37	3.85	3.99	2.54	2.75	1.82	1.95	2.55

*Total iron as Fe_2O_3

La/La*, Ce/Ce* and Eu/Eu*are defined by $[La/(3Pr-2/Nd)]_{PAAS}$, $[Ce/(2Pr-Nd)]_{PAAS}$ and $[Eu/(0.67Sm+0.33Tb)]_{PAAS}$, respectively.

Table.5 Two pyroxene thermometer in the BIFs of the Nulliak Island

Sample No.	Mineral Pair	n	XFe*	T(°C)**
LAD310	host cpx No.1	1	0.27	701
	opx lamellae in host cpx No.1	1	0.61	
LAD330	host cpx No.1	2	0.29	713
	opx lamellae in host cpx No.1	2	0.63	
	host cpx No.2	2	0.27	658
	opx lamellae in host cpx No.2	1	0.66	
LAE42	host cpx No.1	2	0.27	650
	opx lamellae in host cpx No.1	5	0.67	
LAE44	host cpx No.1	5	0.27	643
	opx lamellae in host cpx No.1	2	0.68	

*XFe=Fe(II)/(Fe(II)+Mg+Ca+Mn)

**two pyroxene thermometer from Fonarev and Graphchikov, 1991

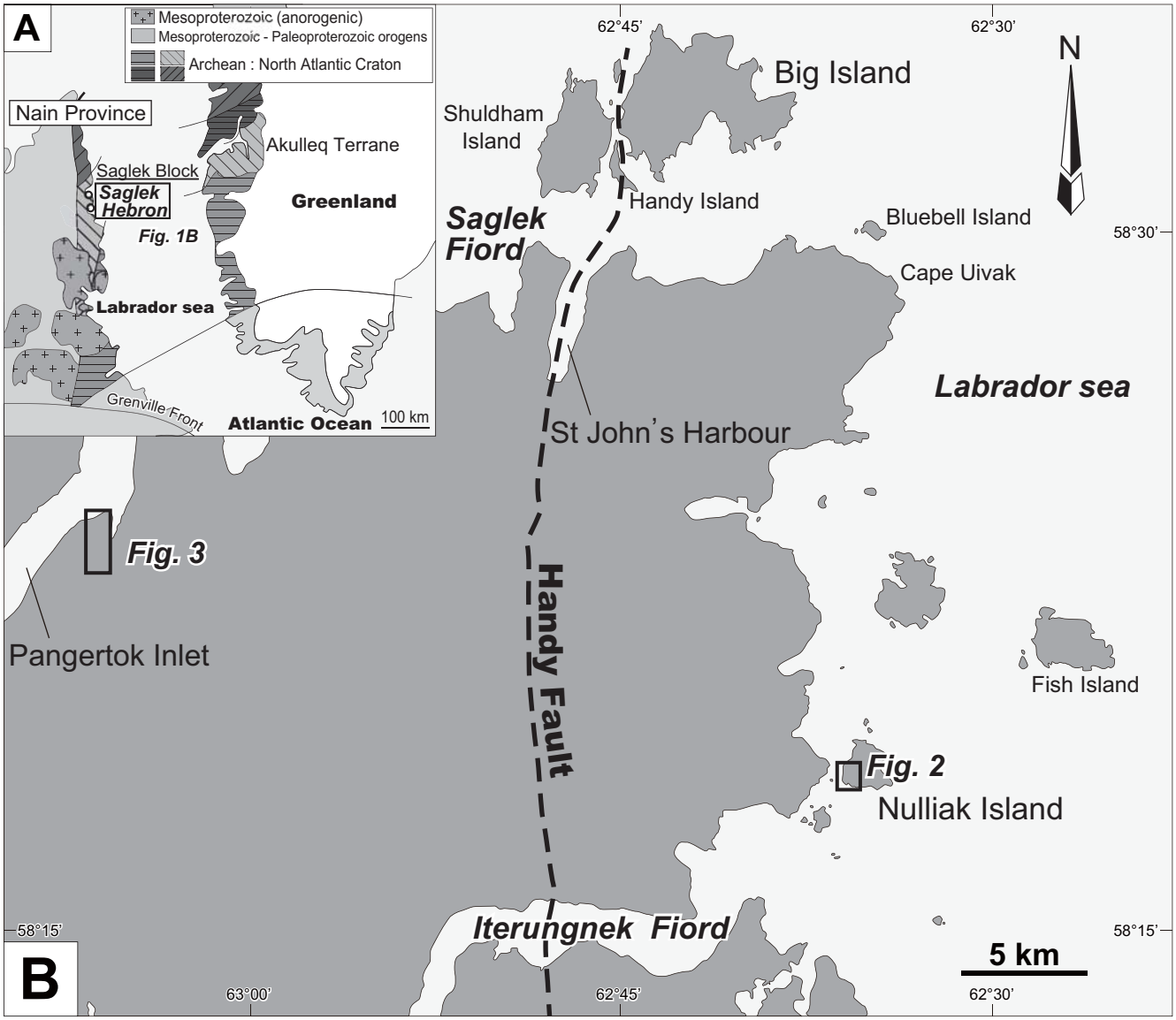
A
Mesoproterozoic (anorogenic)
Mesoproterozoic - Paleoproterozoic orogens
Archean : North Atlantic Craton
Nain Province
Akulleq Terrane
Saglek Block
Saglek
Hebron
Fig. 1B
Greenland
Labrador sea
Grenville Front
Atlantic Ocean
100 km
62°45'
62°30'
N
Big Island
Shuldham
Island
Handy Island
Saglek
Fiord
Bluebell Island
58°30'
Cape Uivak
Labrador sea
St John's Harbour
Fig. 3
Handy Fault
Pangertok Inlet
Fish Island
Fig. 2
Nulliak Island
58°15'
Iterungnek Fiord
B
5 km
63°00'
62°45'
62°30'
58°15'

Figure. 1

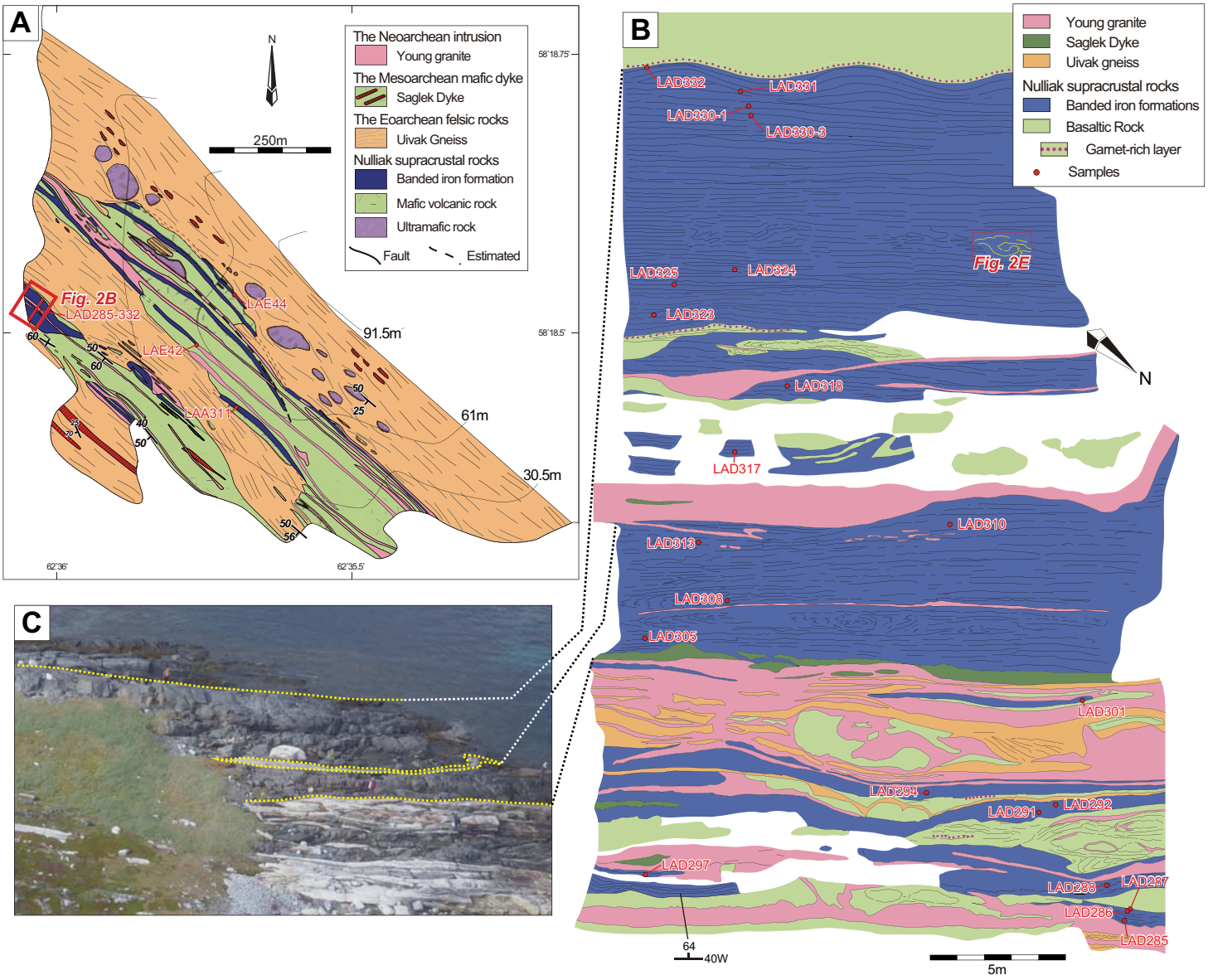
A
N
250m
The Neoarchean intrusion
Young granite
The Mesoarchean mafic dyke
Saglek Dyke
The Eoarchean felsic rocks
Uivak Gneiss
Nulliak supracrustal rocks
Banded iron formation
Mafic volcanic rock
Ultramafic rock
Fault
Estimated
Fig. 2B
LAD285-332
LAE44
LAE42
LAA311
91.5m
61m
30.5m
58°18.75'
58°18.5'
62°36'
62°35.5'
B
Young granite
Saglek Dyke
Uivak gneiss
Nulliak supracrustal rocks
Banded iron formations
Basaltic Rock
Garnet-rich layer
Samples
LAD332
LAD331
LAD330-1
LAD330-3
LAD325
LAD324
LAD323
Fig. 2E
LAD318
LAD317
LAD310
LAD313
LAD308
LAD305
LAD301
LAD294
LAD291
LAD292
LAD297
LAD288
LAD287
LAD286
LAD285
N
64
40W
5m
C
D
White band(quartz)
Black band
(magnetite + Fe-silicate)
50 cm
E
none-fold layer
intraformational folding
50 cm

Figure. 2

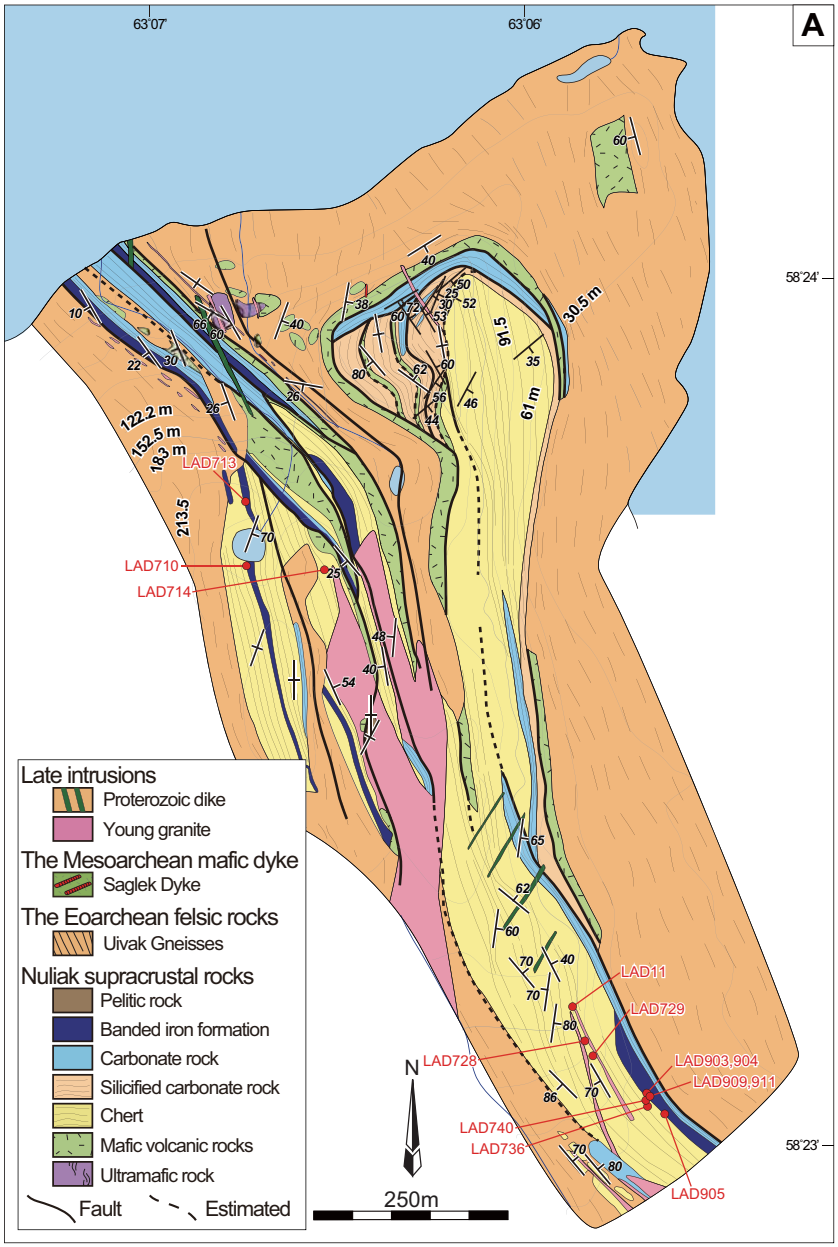
A
63°07'
63°06'
58°24'
58°23'
LAD713
LAD710
LAD714
LAD11
LAD729
LAD728
LAD903,904
LAD909,911
LAD740
LAD736
LAD905
122.2 m
152.5 m
183 m
213.5
91.5
30.5 m
61 m
N
250m
Late intrusions
Proterozoic dike
Young granite
The Mesoarchean mafic dyke
Saglek Dyke
The Eoarchean felsic rocks
Uivak Gneisses
Nuliak supracrustal rocks
Pelitic rock
Banded iron formation
Carbonate rock
Silicified carbonate rock
Chert
Mafic volcanic rocks
Ultramafic rock
Fault
Estimated

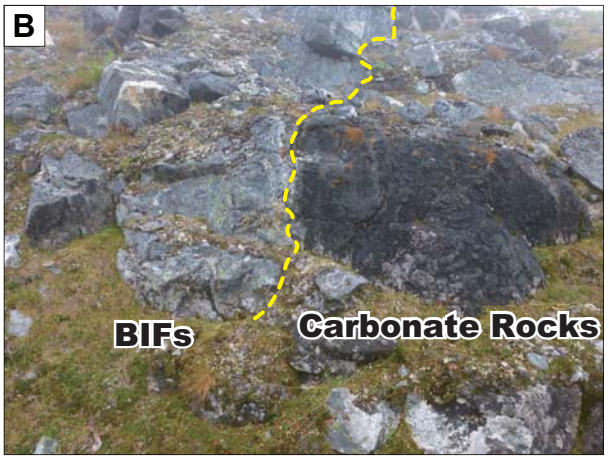
B
BIFs
Carbonate Rocks

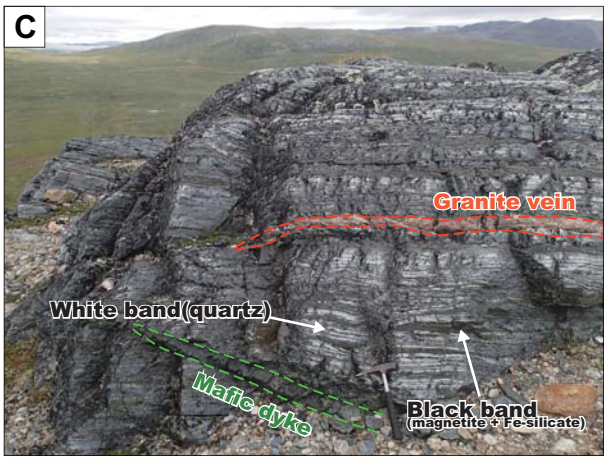
C
Granite vein
White band(quartz)
Mafic dyke
Black band
(magnetite + Fe-silicate)

Figure. 3

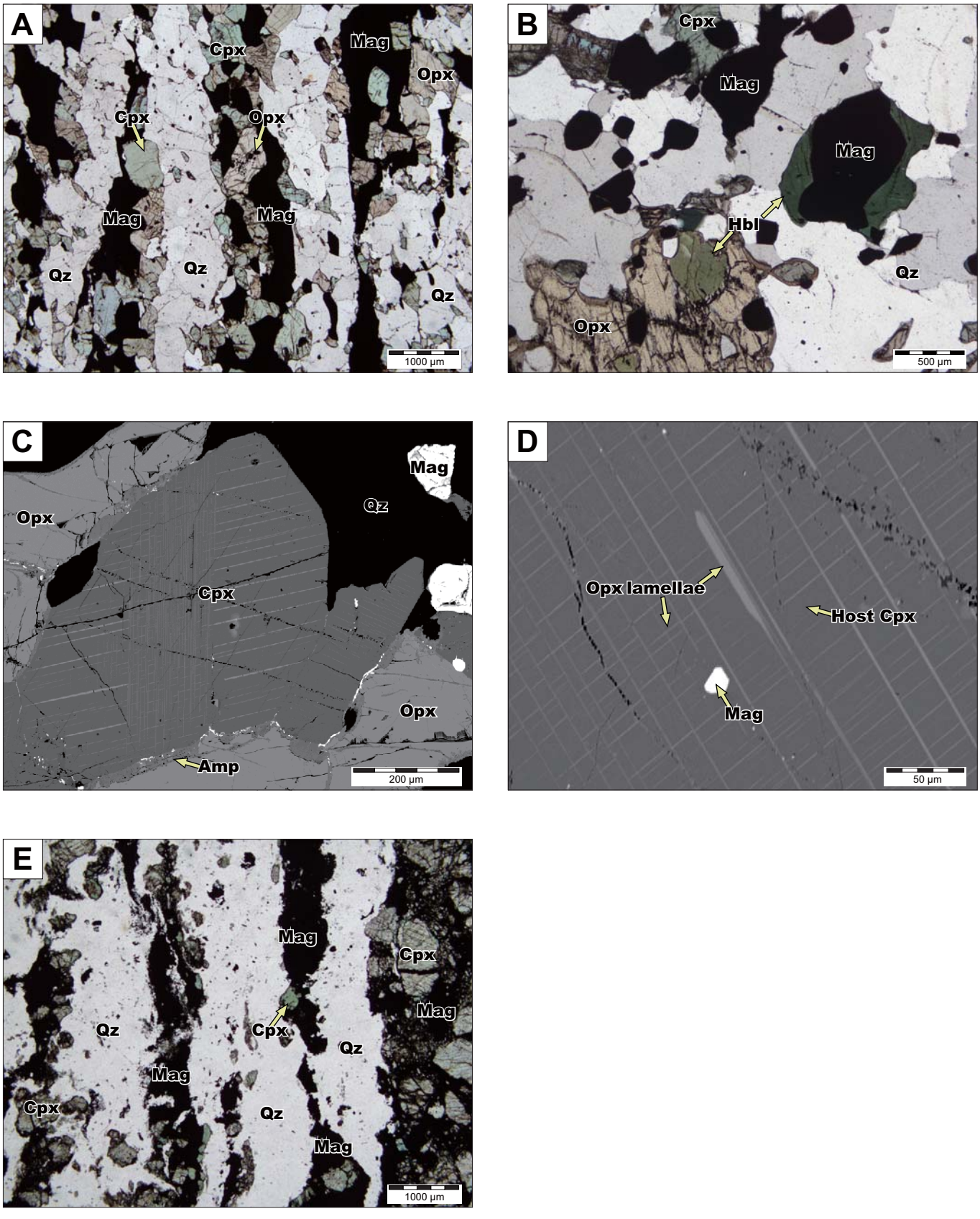
A
Cpx
Mag
Opx
Cpx
Opx
Mag
Mag
Qz
Qz
Qz
1000 µm
B
Cpx
Mag
Mag
Hbl
Qz
Opx
500 µm
C
Mag
Qz
Opx
Cpx
Opx
Amp
200 µm
D
Opx lamellae
Host Cpx
Mag
50 µm
E
Mag
Cpx
Mag
Qz
Cpx
Qz
Mag
Cpx
Qz
Mag
1000 µm

Figure. 4

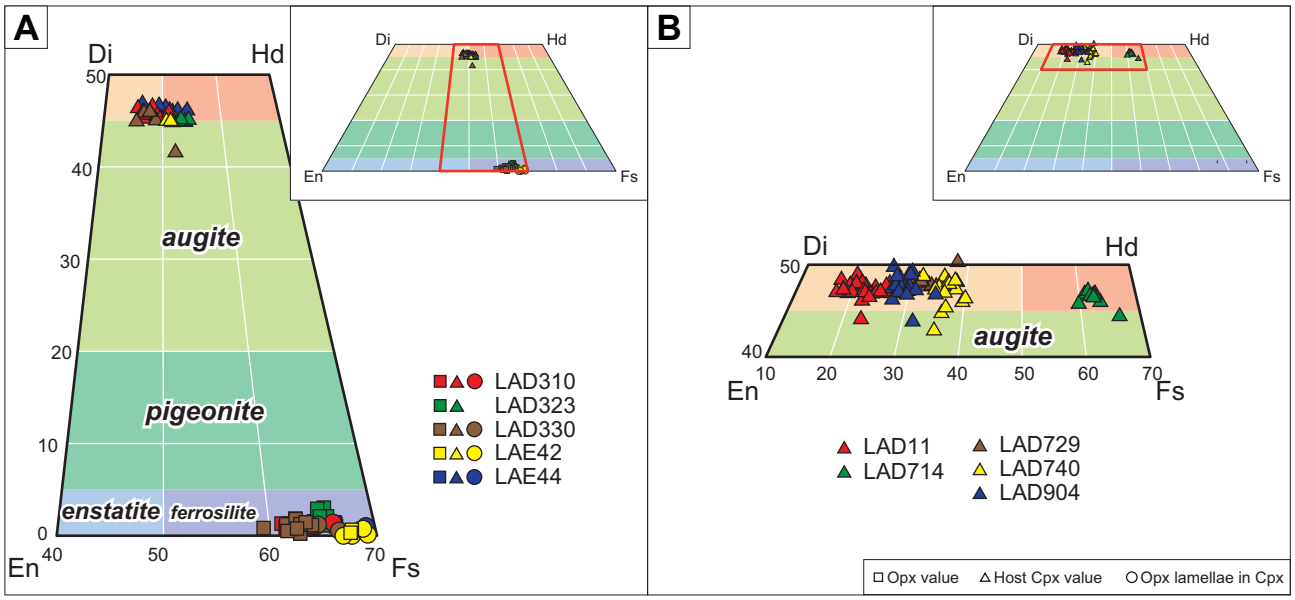
A
Di
Hd
En
Fs
augite
pigeonite
enstatite
ferrosilite
LAD310
LAD323
LAD330
LAE42
LAE44
B
augite
LAD11
LAD714
LAD729
LAD740
LAD904
Opx value
Host Cpx value
Opx lamellae in Cpx

Figure. 5

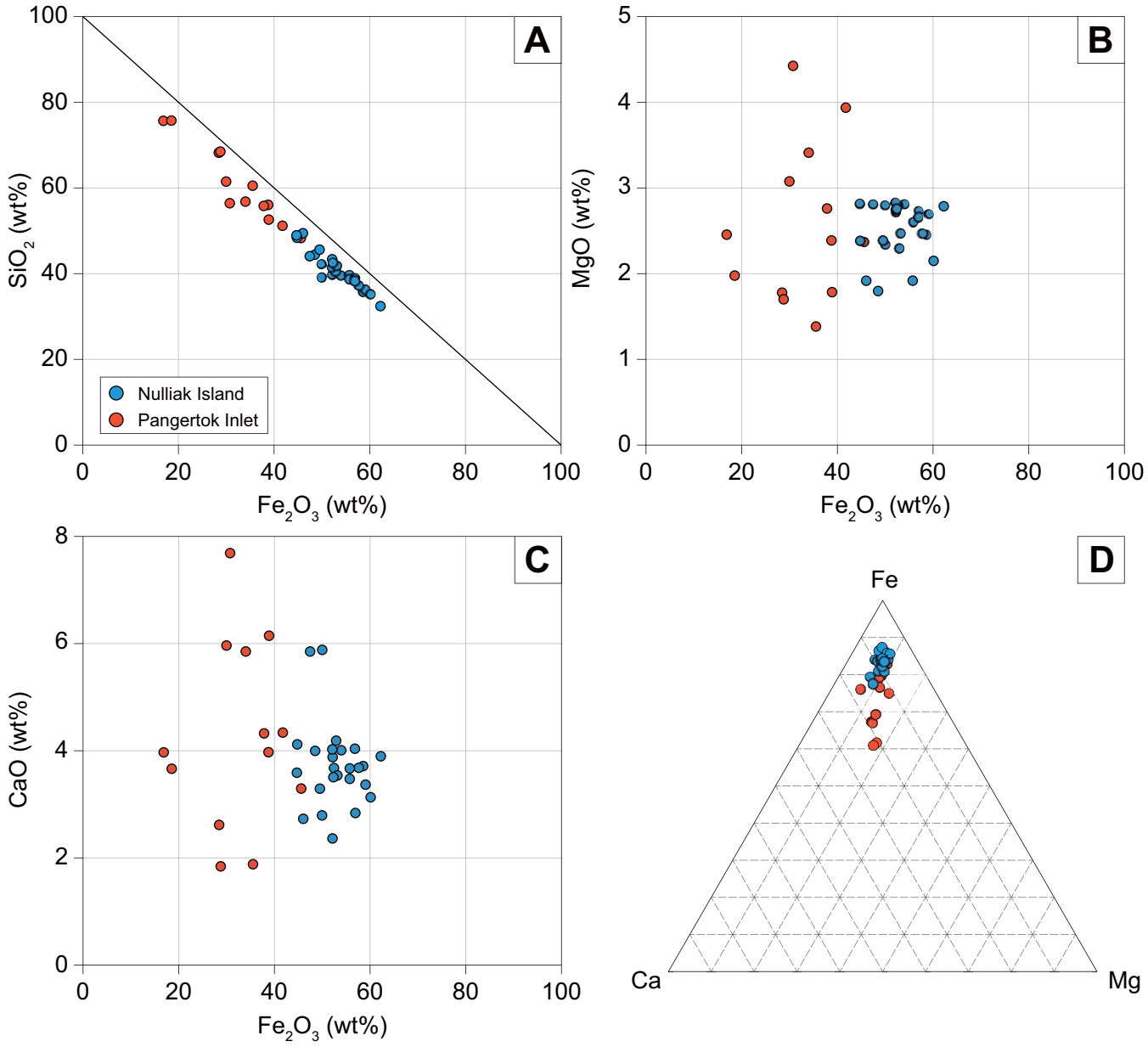
A
B
C
D
SiO2 (wt%)
MgO (wt%)
CaO (wt%)
Fe2O3 (wt%)
Nulliak Island
Pangertok Inlet
Fe
Ca
Mg

Figure. 6

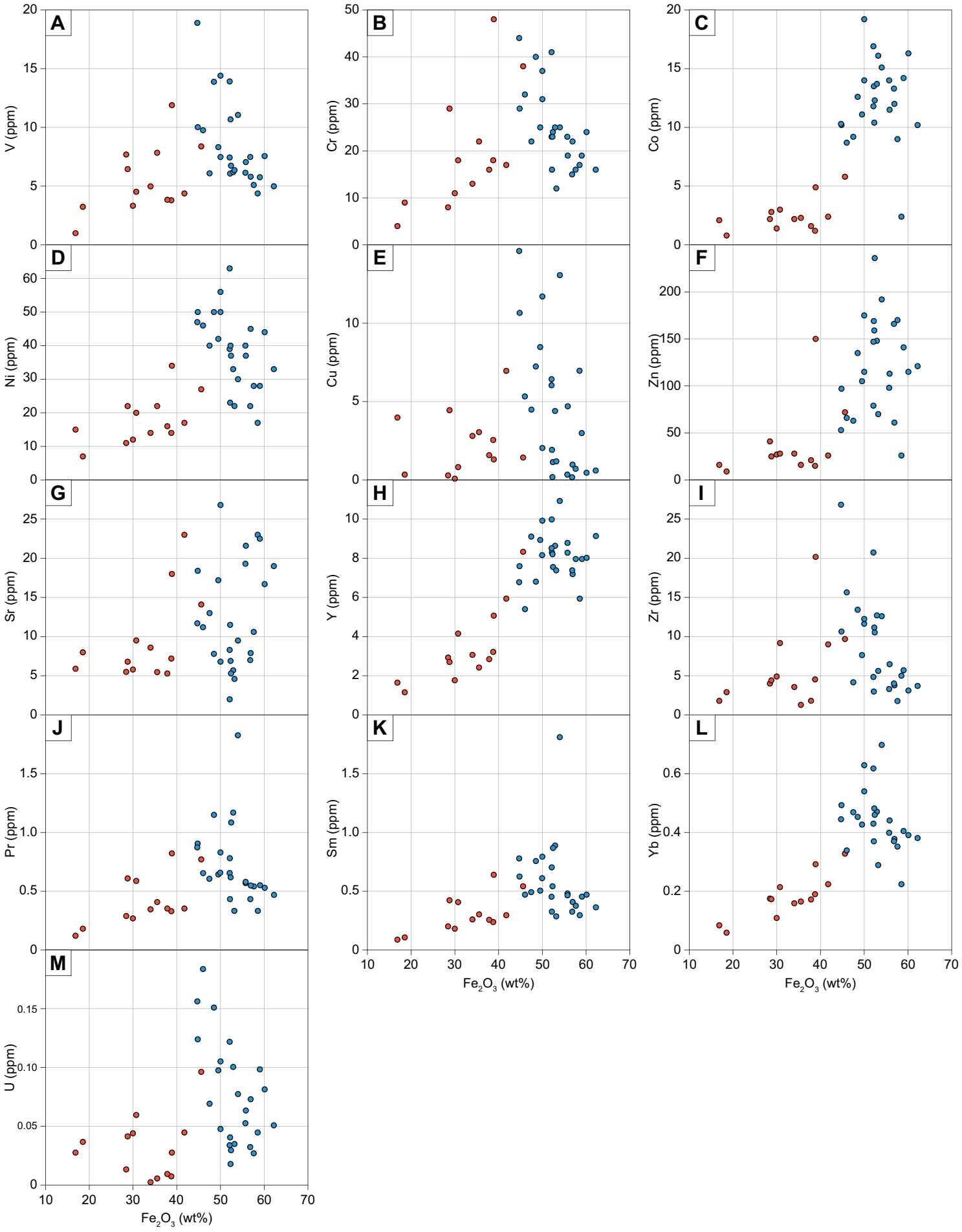
A
V (ppm)
B
Cr (ppm)
C
Co (ppm)
D
Ni (ppm)
E
Cu (ppm)
F
Zn (ppm)
G
Sr (ppm)
H
Y (ppm)
I
Zr (ppm)
J
Pr (ppm)
K
Sm (ppm)
L
Yb (ppm)
M
U (ppm)
Fe2O3 (wt%)
Fe2O3 (wt%)
Fe2O3 (wt%)

Figure. 7

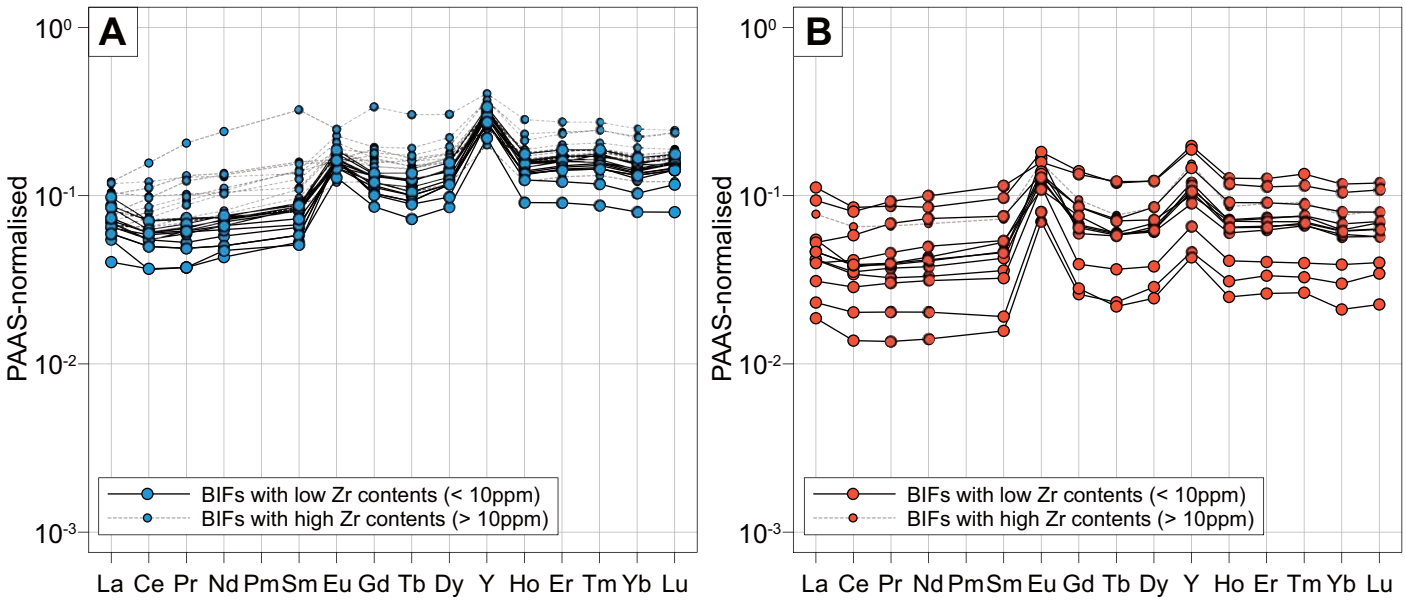
A
B
PAAS-normalised
10^{0}
10^{-1}
10^{-2}
10^{-3}
La Ce Pr Nd Pm Sm Eu Gd Tb Dy Y Ho Er Tm Yb Lu
BIFs with low Zr contents (< 10ppm)
BIFs with high Zr contents (> 10ppm)

Figure. 8

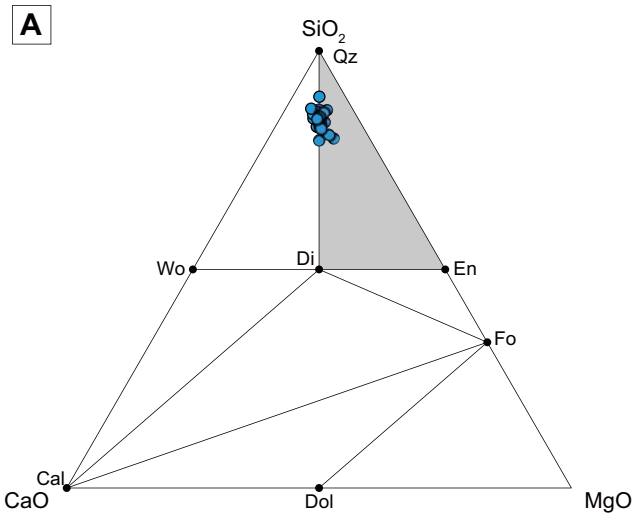
A
SiO2
Qz
Wo
Di
En
Fo
Cal
CaO
Dol
MgO

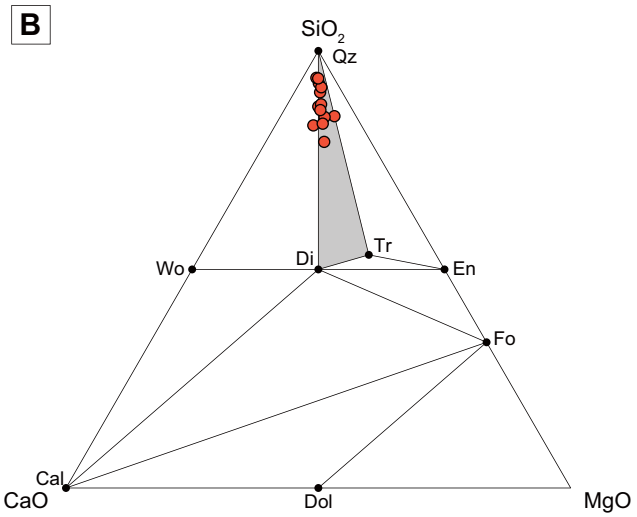
B
SiO2
Qz
Tr
Wo
Di
En
Fo
Cal
CaO
Dol
MgO

Figure. 9

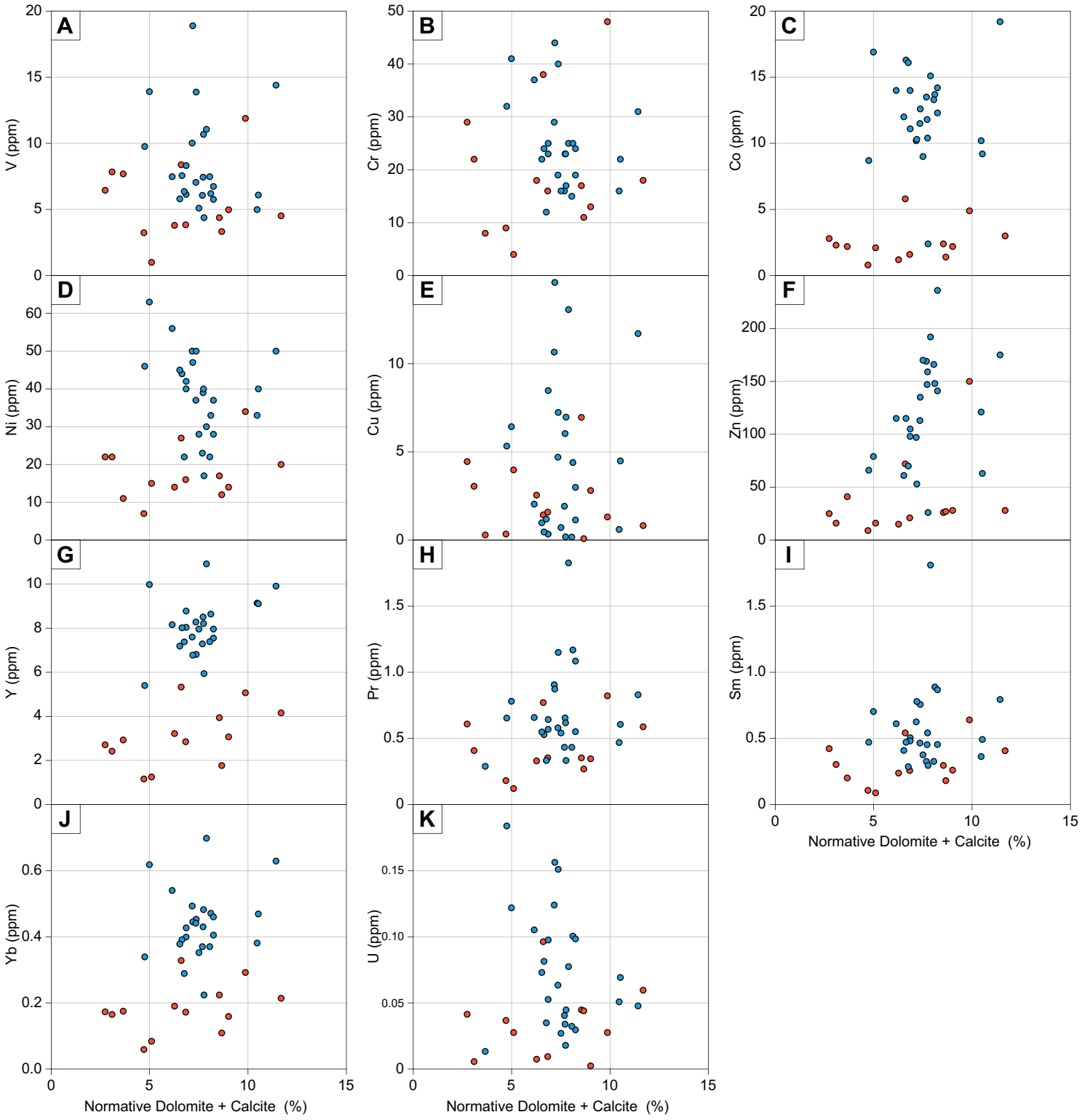
A
V (ppm)
B
Cr (ppm)
C
Co (ppm)
D
Ni (ppm)
E
Cu (ppm)
F
Zn (ppm)
G
Y (ppm)
H
Pr (ppm)
I
Sm (ppm)
J
Yb (ppm)
K
U (ppm)
Normative Dolomite + Calcite (%)
Normative Dolomite + Calcite (%)
Normative Dolomite + Calcite (%)

Figure. 10

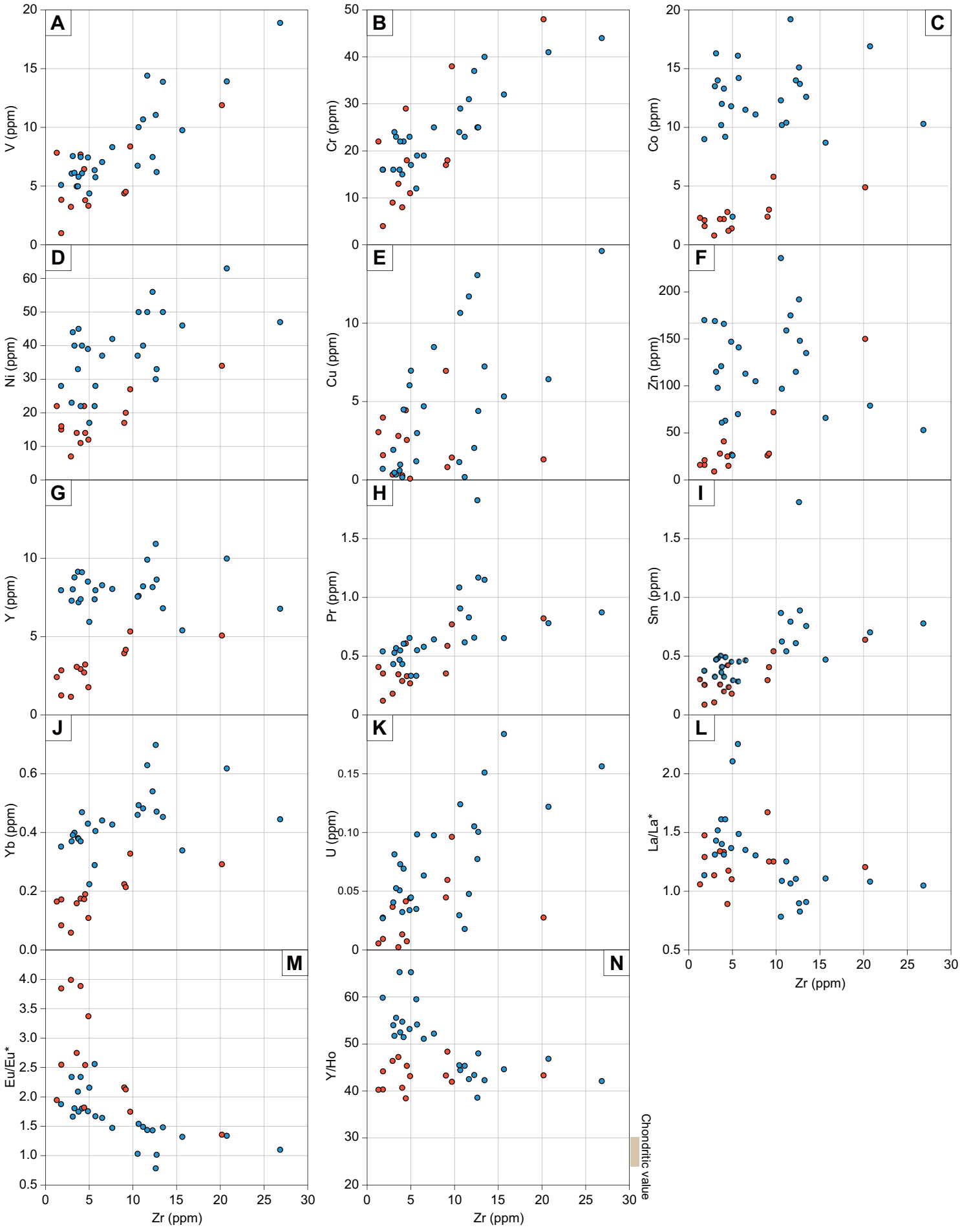
A
V (ppm)
B
Cr (ppm)
C
Co (ppm)
D
Ni (ppm)
E
Cu (ppm)
F
Zn (ppm)
G
Y (ppm)
H
Pr (ppm)
I
Sm (ppm)
J
Yb (ppm)
K
U (ppm)
L
La/La*
M
Eu/Eu*
N
Y/Ho
Zr (ppm)
Zr (ppm)
Zr (ppm)
Chondritic value

Figure. 11

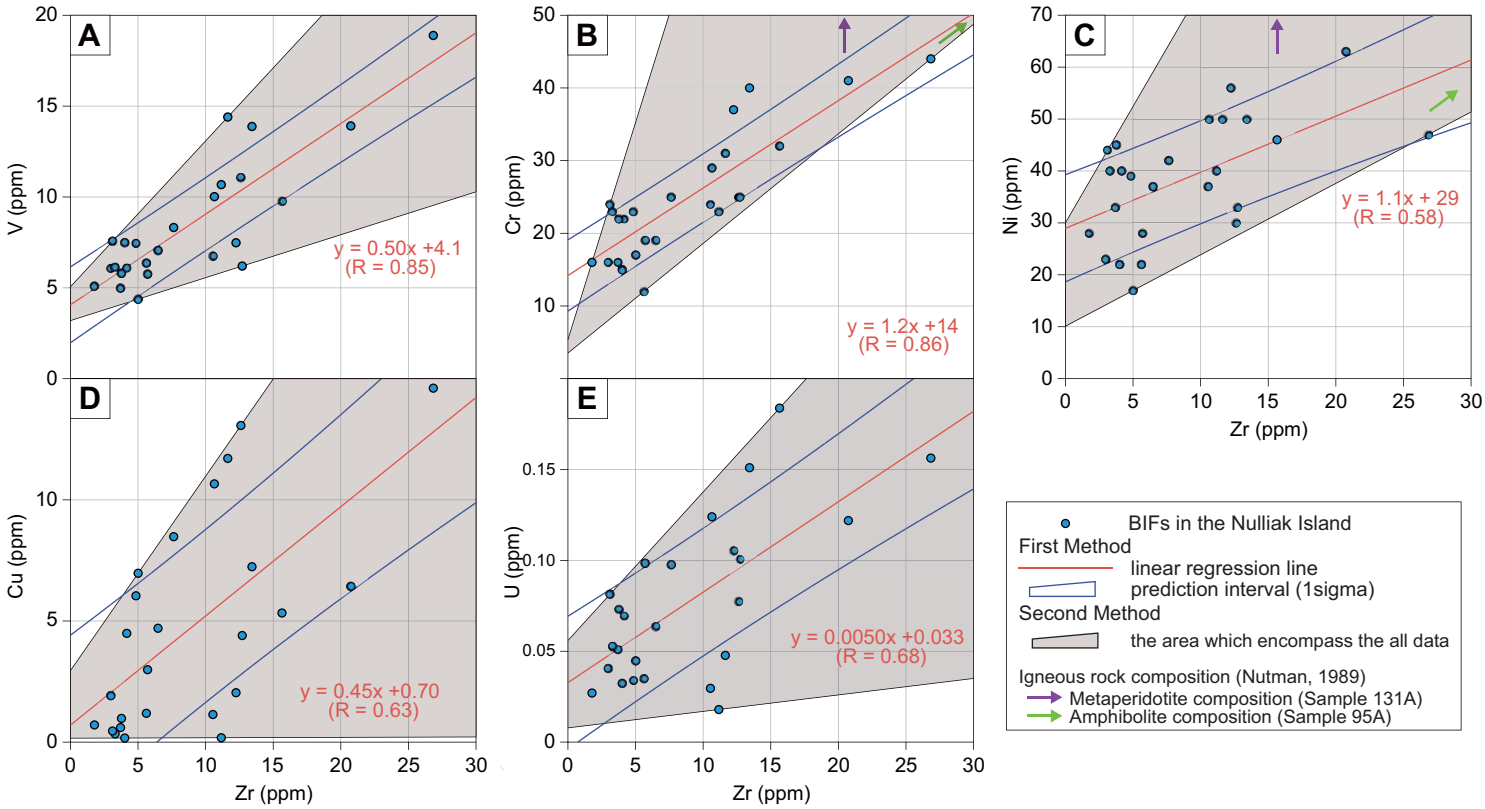
A
V (ppm)
y = 0.50x +4.1
(R = 0.85)
B
Cr (ppm)
y = 1.2x +14
(R = 0.86)
C
Ni (ppm)
y = 1.1x + 29
(R = 0.58)
D
Cu (ppm)
y = 0.45x +0.70
(R = 0.63)
E
U (ppm)
y = 0.0050x +0.033
(R = 0.68)
Zr (ppm)
BIFs in the Nulliak Island
First Method
linear regression line
prediction interval (1sigma)
Second Method
the area which encompass the all data
Igneous rock composition (Nutman, 1989)
Metaperidotite composition (Sample 131A)
Amphibolite composition (Sample 95A)

Figure. 12

Chapter IV.

The petrographical and geochemical characteristics of the BIFs in the Hotazel Formation from Transvaal Supergroup: Implications for redox and hydrothermal contributions in their sedimentary environments and bioavailability of transitional elements in Paleoproterozoic Ocean

Abstract

The chemical sedimentary rocks such as the banded iron formations (BIFs) might provide the evidences for the seawater chemical evolutions such as bioavailability of transitional elements, which are used as bio-essential elements. The Paleoproterozoic Hotazel Formation in the Transvaal Supergroup, South Africa, are composed of the BIFs, which are interlayered with the manganese rocks at three stratigraphic horizons. In this study, I analyzed their chemical compositions in the lower part of the Hotazel Formation, at whole-rock and mineral scale.

The stratigraphic variations of Fe, Ca, Mn and REE + Y whole-rock compositions from the lower most BIFs to the lowest manganese rocks suggest that their sedimentary environment was transited from hydrothermally-dominated ferruginous deep to oxic shallow water, as suggested by the previous studies.

Positive correlations of Mn whole-rock contents with of Co, Ni and Zn contents suggest that those transitional elements primarily existed in Mn-oxide minerals (precursor minerals of Mn-bearing minerals in the BIFs and manganese rocks). In other words, Mn-oxide minerals could be sink for those elements in the Paleoproterozoic

ocean same as the modern oxic ocean. On the other hand, Co contents in Mn-poor BIFs were very low and Co exists not in the Fe-oxide minerals but in Al-bearing clastic materials. Similar positive correlations of Mn or Al contents with Co contents were shown in Co-rich BIFs from Neoarchean to Paleoproterozoic, and the BIFs no with correlations have less Co contents than those from Eoarchean to Middle Archean, suggesting that dissolved divalent Co was limited in those oceans because it was oxidized and fixed as tetravalent forms within the Mn-oxide minerals, as opposed to the previous study.

On the other hand, Zn and Cu exist abundantly in the Fe-oxide minerals within Mn-poor BIFs relative to the Eoarchean BIFs, which have little Zn and Cu in Fe-oxide minerals, suggesting that those dissolved elements were increased under oxic conditions.

Bioavailabilities of Co and Zn are different between prokaryotic and eukaryotic organisms. Decrease in bioavailable Co and increase in Zn in the oceans suggested from the chemical compositions of the Neoarchean to Paleoproterozoic BIFs including the Hotazel Formation might be influential to the evolutions to the eukaryotic

organisms, which use preferentially Zn-containing enzymes in place of Co.

1. Introduction

It is generally thought that the Earth's ocean have evolved from anoxic to oxic environments from 3.9 - 3.7 billion years ago to the present, which sedimentary rocks are recognized. Throughout the Precambrian era, oxidation has developed not progressively but sharply at two major periods around the Paleoproterozoic and the Neoproterozoic, based on mineralogical, paleontological and geochemical evidences (Cloud, 1968; Walker, 1977; Walker, 1982; Kasting, 1987; Han and Runnegar, 1992; Schidlowski et al., 1976; Farquhar et al., 2000; Pavlov and Kasting, 2002).

The first oxidation event called the Great Oxidation Event (GOE) had been occurred from 2.45 to 2.1 Ga. At the early stage of the GOE (2.45 to 2.32 Ga), atmospheric oxygen level reached over 10^{-5} PAL indicated by the loss of mass-independent sulfur isotope fractionation (S-MIF) (Pavlov and Kasting, 2002; Farquhar et al., 2000; Bekker et al., 2004; Guo et al., 2009).

Around the GOE, major biological evolutions might have occurred. Even though only geochemical or morphological evidences for prokaryotes have been reported in the Archean geological suites (Rosing et al., 1996; Ohtomo et al., 2014;

Yoshiya et al., 2015; Schopf, 1992; Ueno et al., 2006; Shen et al., 2001; Yoshiya et al., 2012), the macro-scale fossils thought to be eukaryotes and multicellular organisms are found in the 2.1 Ga sedimentary rocks (Han and Runnegar, 1992; Albani et al., 2010). Because aerobic respiration done by eukaryotic organisms can be achieved over 10^{-2} PAL oxygen partial pressures, and steroid and collagen, which are respectively used for eukaryotic cell membranes and multicellular extracellular matrix, can be synthesized only under oxic conditions, increasing oxygen might have inspired the appearance of eukaryotes.

On the other hand, the distribution of life might be also controlled by the availability of bioessential elements (e.g. P, Fe, Mn, Ni, Co, Cu, Mo), which are used as cofactors catalyzing metabolic reactions. Those abundances in ocean could also have influence on the timing of origin and evolution of prokaryotic and eukaryotic organisms because their degrees of dependences on those elements are different between phylogenies (Zerkle et al., 2005; Dupont et al., 2006). Based on the differences of redox chemistries of those elements, the differences of the requirements for bioessential elements by modern organisms and the timing of their origins, the evolutions of those

bioessential element abundances in the ocean have been inferred throughout the Earth history (Saito et al., 2003; Zerkle et al., 2005; Anbar, 2008). However, those estimates have low temporal resolution and do not take account of the variations of supply sources of those elements such as oceanic or continental crust in material circulation because they are based only on the simple redox-evolution model that anoxic ocean at the Archean have evolved into sulfidic ocean at the Proterozoic, finally into the oxic ocean at the Phanerozoic (Canfield, 1998).

In contrast to above modeling studies, the geochemical studies of the sedimentary rocks could be proxies for the contemporary seawater chemical compositions. Particularly, the banded iron formations (BIFs), which are chemical sedimentary rocks composed of alternating Fe-oxide and silica bands, are useful for the estimates throughout the Precambrian because their occurrences are found in the geologic suites from 3.9 to 0.7 Ga except for the Middle Proterozoic (Klein and Beukes, 1992; Isley and Abbott, 1999; Komiya et al., 2015). Moreover, as shown by their diagnostic shale- or chondrite-normalized rare earth element (REE) + yttrium (Y) patterns, some of their chemical compositions are thought to preserve those of seawater,

from which they were precipitated (e.g. Bau and Dulski, 1996; Bolhar et al., 2004). Actually, their compositions can be also used as proxies for bioessential elements such as P, Co, Ni, Cu and Zn of seawater chemistry thorough the time (Bjerrum and Canfield, 2002; Swanner et al., 2014; Konhauser et al., 2009; Fru et al., 2016; Robbins et al., 2013). However, it requires attention for the interpretation of their analyzed values because they are controlled not only by chemical compositions and physicochemical conditions of contemporaneous ocean but also their lithofacies and constituent minerals. In generally, the BIFs contain not only Fe oxides (hematite and magnetite) and silica minerals (quartz), which are transformed from amorphous Fe oxyhydroxide and silica precipitated from seawater, but also other chemical precipitates and clastic or volcanic materials (Klein, 2005). Accordingly, the BIFs chemical compositions do not necessarily reflect the adsorbents on Fe oxyhydroxide in the seawater. Therefore we have to estimate amount of transitional elements existing in the Fe-oxide minerals more strictly based on correlations of those transitional elements with other elements prone to be distributed in those constituent minerals.

The Paleoproterozoic Kalahari manganese field in the Northern Cape

Province, South Africa, contains the largest and oldest manganese ore deposits, which represent the major land-based manganese resources (Roy, 1981; Beukes, 1983; Gutzmer et al., 1997; Cairncross et al., 1997; Kirschvink et al., 2002). The manganese deposits are hosted by the BIFs, known as the Hotazel Formation. At the lower stratigraphic positions than the Hotazel Formation, there are the glacial deposits suggestive of the global glaciations known as the Makganyene Formation. Those lithostratigraphies suggest that the surface redox state became oxidative after the global glaciation because trivalent manganese has a high oxidation potential (Kirschvink et al., 2002).

The petrographic or geochemical studies in the Hotazel Formation have been performed since Kleyenstüber (1984). However, most previous studies have concentrated on metallogeny or economic geology forming high-grade manganese or iron ores associated with secondary element movements caused by hydrothermal alterations (Kleyenstüber, 1985; Beukes et al., 1995; Gutzmer and Beukes, 1995; Gutzmer and Beukes, 1997; Tsikos et al., 2003; Chetty, 2008; Chetty and Gutzmer, 2012). On the other hand, there are not many geochemical studies for estimating their

sedimentary processes and paleoenvironments at Paleoproterozoic (Tsikos and Moore, 1997; Schneiderhan et al., 2006; Tsikos et al., 2010).

Tsikos and Moore (1997) presented the petrography of the BIFs, and analyzed their major and trace element (including REE+Y) contents from the lowest- to the highest stratigraphic parts of the Hotazel Formation sporadically. They showed that upper parts of the BIFs show higher CaO contents and modern-seawater like REE patterns (no positive Eu anomalies and strong enrichments in heavy REE relative to light REE) in contrast with lower parts, implying a transition to shallower oxic conditions of their sedimentary environments.

Schneiderhan et al. (2006) reported the chemostratigraphies of major and trace element contents except for REE + Y, stable isotopes ($\delta^{18}O_{carb}$, $\delta^{13}C_{carb}$ and $\delta^{13}C_{org}$) and $^{87}Sr/^{86}Sr$ ratios from the underlying Ongeluk Formation composed of andesitic basalts through the Hotazel Formation including the manganese rocks and the BIFs to the overlying Mooidraai Formation composed of carbonate rocks. Based on the increasing trends of inorganic carbon contents, $\delta^{13}C_{carb}$ and CaO contents from the lowermost Hotazel Formation BIFs to the Mooidraai Formation dolomite, they

estimated that precipitation of Ca-carbonate minerals were becoming increased due to transition to shallower parts of their sedimentary environments in similar to Tsikos et al (1997). Moreover, with the variations of $^{87}Sr/^{86}Sr$ isotopes within the Hotazel Formation, they predicted a layered Paleoproterozoic ocean with hydrothermally-dominated anoxic ferruginous deep water and oxygenated shallow water mass.

Tsikos et al. (2010) reported Fe isotope ($\delta^{57}Fe$) stratigraphies of the BIF layers, and showed that their $\delta^{57}Fe$ values stratigraphically decrease to the lowest values (-4‰) in the Precambrian BIFs with decreasing Fe/Mn ratios from the BIFs to manganese rocks. They suggested that dissolved Fe (II) pool in the ocean was becoming small due to precipitation of isotopically heavy Fe (III)-oxyhydroxide on the assumption of Rayleigh fractionation model, and dissolved Mn (II) contents were increased relative to dissolved Fe (II).

However, temporal variations of degree of inputs by hydrothermal fluids and redox chemistry in their sedimentary environments, and their correlations with the lithostratigraphies have not been known. Strontium isotopic ratios ($^{87}Sr/^{86}Sr$) by Schneiderhan et al. (2006) could decode the mass balance between hydrothermal fluids

and continental runoff in the Paleoproterozoic ocean, but those values are apparently variable irrespective of the lithofacies in the Hotazel Formation. In addition, those ratios are prone to be altered by the post-depositional fluids carrying radiogenic Sr (Brand and Veizer, 1980, 1981). On the other hand, REE + Y stratigraphies including the BIFs and manganese rocks might fulfill these purposes because they are less likely to be altered secondarily, but REE + Y abundances and patterns have been reported sporadically in the stratigraphies by Tsikos and Moore (1997), Chetty (2008) and Chetty and Gutzmer (2012) so far.

And, even though bioessential transitional element contents of the BIFs are reported by Tsikos and Moore (1997) and Schneiderhan et al. (2006), analysis by Tsikos and Moore (1997) was performed by XRF, and precisions and accuracies of the analyzed values of low-content elements are not reliable to discuss. The values reported by Schneiderhan et al. (2006) are mainly from the Ca- or Mn-rich BIFs, and it is unclear whether those elements are primarily derived from adsorbents on Fe oxyhydroxide (precursor minerals of Fe-oxide minerals in the BIFs) or other minerals. It is unfavorable to compare with the values of the BIFs with other ages for discussing the

secular variations of seawater compositions.

For this study, I analyzed chemical compositions in the lower parts of the Hotazel Formation. Based on their REE + Y stratigraphies, we reconstructed the temporal variations of redox potentials and influences by hydrothermal fluids and/or seawater in their sedimentary environments, which explain the variability of the lithofacies in the Hotazel Formation. Moreover, based on relationship between their transitional-element contents and lithofacies, and on their comparison with those from other-aged BIFs, I discussed the bioavailability of some transitional elements in Paleoproterozoic oceans and influences on the eukaryotic evolutions.

2. Geology of the Hotazel Formation in the Postmasburg Group, Transvaal Supergroup

The Transvaal Supergroup on the Kaapvaal Craton is a Neoarchean to Paleoproterozoic stratigraphic unit, which cover northern South Africa and southern Botswana (Beukes, 1986). In South Africa, it consists of two major structural basins, the eastern half called the Transvaal Basin and the western half called the Griqualand West Basin (Fig. 1A).

In the Griqualand West Basin, the Transvaal Supergroup is subdivided into two major units, the Ghaap and Postmasburg Groups. The Ghaap Group uncomformably overlies the basement of the Ventersdorp Supergroup, Neoarchean volcano-sedimentary succession (van der Westhuizen et al., 1991). The Ghaap Group, which spans the age bracket 2.64-2.45 Ga, are composed of four conformable subgroups; siliciclastic and carbonate ramp following the flooding of the basement of the Kaapvaal Craton (the Schmidtsdrif Subgroup), an extensive basal carbonate platform (the Campbellrand Subgroup), microbanded to granular iron formations (the Asbesheuwels Subgroup) and iron formations and siliciclastic rocks (the Koegas

Subgroup) in ascending order by time (Beukes, 1983; Beukes and Smit, 1987; Sumner, 1997; Sumner and Beukes, 2006; Schröder et al., 2011). The Koegas Subgroup is uncomformably overlain by the Makganyene Formation from the Postmasburg Group in shallow-water sections (Schröder et al., 2011).

The Postmasburg Group is composed of four conformable formations; the Makganyene, the Ongeluk, the Hotazel and the Mooidraai Formation in ascending order by time. The lower-most Makganyene Formation is consists of glacial diamictite overlain by the Ongeluk basaltic andesites showing pillow shape, massive lava flow or hyaloclastite textures. The glacial deposits and the volcanics often interfinger with each other, and small volcanic fragments are present in the upper-most part of the Makganyene Formation (Evans et al., 1997), suggesting that they were formed during much of the same time. Moreover, a paleomagnetic study shows that the Ongeluk volcanics were formed within tropical latitude of 11 ± 5° (Evans et al., 1997). The existence of glacial deposits at low-latitude areas suggests that the global glaciation event might occur (Kirschvink et al., 2000; Evans et al., 1997). The Hotazel Formation, overlying the Ongeluk basaltic andesites, is composed mainly of the BIFs laterally

interlayered with three manganese-rock layers (Tsikos and Moore, 1997). The formation is well preserved ~60 km north of the town of Kuruman in the Northern Cape Province as an erosional relict, which is often known as the Kalahari manganese field (KMF). The BIFs are characterized by the oxide- (hematite and magnetite), carbonate- (calcite, dolomite, siderite and ankerite) and silicate (quartz, minnesotaite and stilplnomelane) lithofacies (Tsikos and Moore, 1997; Tsikos et al., 2003; Schneiderhan et al., 2006). On the other hand, the manganese-rock layers are composed mainly of Mn-silicate (braunite and jacobsite) and Mn-carbonate minerals (kutnohorite, rhodochrosite and Mn calcite). The Fe- and Mn carbonate minerals in them are thought to be diagenetic-origin reduced by organic matters, and originated possibly from the Fe (III)- and Mn (IV)-oxide minerals (Tsikos et al., 2003; Schneiderhan et al., 2006). The lowermost of the formation are often characterized by glacially drop stones and sand stones suggestive of the end of the glaciation, and the following Fe- and Mn oxide depositions of the Hotazel Formation suggestive of evolutions into the oxic conditions in their depositional environments, because tetravalent Mn has a high oxidation potential (Kirschvink et al., 2000). The Hotazel Formation is conformably overlain by

the Mooidraai Formation, which is composed mainly of dolostones. The Hotazel BIFs show parallel laminations, suggesting that they were deposited under deep marine conditions below storm wave basin; on the other hand, the Mooidraai Formation are composed of poorly sorted carbonate breccias with carbonate rhythmites deposited potentially on a foreslope in the lower part, and overlain by smoothly laminated stromatolite and microbialaminite deposited from shelf and lagoonal to supratidal environments (Kunzmann et al., 2014). Shallowing upward at the depositional environments from the Hotazel Formation to the Mooidraai Formation are also supported by the increasing Ca contents upward in the Hotazel Formation (Tsikos et al., 1997; Schneiderhan et al., 2006). The Hotazel and Mooidraai Formation constitute the Voëlwater Subgroup (Beukes, 1983). The geochronological studies of the Postmasburg Group have not constrained the depositional age of the Hotazel iron formations fully. The Ongeluk basaltic andesites underlying the Hotazel Formation yields 2222 ± 12 Ma of whole-rock Pb-Pb age (Cornel et al., 1996); on the other hand, the Mooidraai dolomite yields 2394 ± 26 Ma of whole-rock Pb-Pb age (Bau et al., 1999) and 2492± 23 Ma (Fairey et al., 2013) of whole-rock U-Pb age. In the northern and western parts of

the Kalahari manganese field, the Voëlwater Subgroup is uncomformably overlain by the basal Mapedi Formation of the late Paleoproterozoic Olifaentshoek Supergroup (Beukes and Smit, 1987; Fig. 1B), which are mainly composed of shales, quartzites and minor conglomerates.

3. Petrological and mineralogical descriptions of drill-core sample "GL-137"

For this study, we recovered the drill-core sample "GL-137" near the Gloria Manganese Mine in the Kalahari manganese field (KMF; Fig. 1B). The GL-137 covers from the uppermost Ongeluk Formation to the lower parts of the Mooidraai Formation. In the Hotazel Formation of GL-137, the three manganese-rock layers are interlayered within the BIFs. The boundaries between the BIFs and manganese rocks are transitional, and marked by the hematite and Mn-bearing carbonate lutites (FeMn lutite). These stratigraphic characters are in common with the stratigraphies of other Gloria and other KMF mines (e.g. Tsikos et al., 2003; Schneiderhan et al., 2006; Tsikos et al., 2010).

In this study, we analyzed the lower stratigraphic part of GL-137 from the BIFs above the Ongeluk basaltic andesites to the carbonate rocks above the lowest manganese-rock layer (Fig. 3A).

The stratigraphic lowest parts in the BIFs immediately above the Ongeluk basaltic andesites are composed of the banding structures of reddish and black bands (Fig. 3B). From microscopic observations and elemental mapping by EPMA, reddish

layers are composed mainly of microcrystalline quartz with subordinate amounts of very fine-grained hematite, and rounded quartz minerals (> 30 μm) occur in places. On the other hand, black layers are composed of microcrystalline hematite. Moreover, submicron to several tens of micrometer apatites are scattered in places (Fig. 4A). In the middle stratigraphic horizons of the BIF layer, the BIFs with reddish and black bands and the BIFs with white and black bands alternate with each other. The contacts between them are sharp. The formers are similar to the lowest BIFs in lithofacies, and consist of alternating bands of quartz and hematite. On the other hand, the white layers in the latter are composed of microcrystalline quartz, and the black layers are composed mainly of coarse-grained magnetite elongated in the direction of the bedding planes (Fig. 3C). Fibrous or layered minnesotaite occur ubiquitously irrespective of reddish and black layers, and apatite grains exist in places (Fig. 4B). The upper parts of the BIF layer are seemingly similar to the reddish BIFs in the lower parts, and are composed of alternating reddish and black bands (Fig. 3D). However, the black bands are composed of hematite and carbonate minerals. > 100μm-grained hematite grains occur within a fine-grained matrix of Mn-bearing ankerite and dolomite (Fig. 4C). In addition, > 50μm

ovoid structures composed of kutnohorite occur in places. The reddish layers are mainly composed of microcrystalline quartz often interlayered with thin ankerite layers. In this paper, we call the BIFs with black and reddish bands and those with black and white bands as Hematite-Jasper Iron Formation and Magnetite-Quartz Iron Formation, respectively.

The FeMn lutite layer (Fig. 3E), the transitional zone between the BIFs and manganese rocks, show massive structures. They are composed mainly of kutnohorite, which are typically surrounded by minute hematite. Lizardite grains are scattered in patches (Fig. 4D).

Manganese-rock layer show alterations of black and brownish bands (Fig. 3F). The former bands are composed mainly of kutnohorite interlayered with thin braunite layers. On the other hand, the latter are composed of calcite or dolomite. Oval-shaped ankerite containing lizardite occur in patches (Fig. 4E).

The carbonate rocks located immediately above the upper FeMn lutite layer are composed of alternating of white and black bands (Fig. 3G). The white bands are composed of kutnohorite and lizardite. On the other hand, the black bands are composed

of granular hematite (Fig. 4F).

4. Analytical methods

4.1. Analysis of whole-rock chemical compositions by ICP-MS

For determining whole-rock chemical compositions, the powder samples were prepared at first. The core samples were cut by a diamond cutter along the layers. The cut rock chips were polished with a grinder for removing saw marks, and rinsed in an ultrasonic bath. They were wrapped with plastic bags and crushed into small pieces with a hammer. In the small pieces, fresh fragments with no alterations and veins are carefully handpicked and divided into up to three parts, which are finally ground to powders by an agate mortar.

Their chemical compositions were determined by the Q-pole mass filter ICP mass spectrometer, the Agilent 7700 (Agilent Technologies, Inc., Santa Clara, USA) with a collision cell at the Gakushuin University. For sample digestions and preparations of analyzed solutions, 18.2 MΩ de-ionised water by a Milli-Q system (Merck Millipore, Billerica, USA) and ultra-high purity acids “Ultrapur” (Kanto Chemical Co., Inc., Tokyo, Japan) were used following the digestion methods of “Acid digestion” by Awaji et al. (2006) with a few modifications. The 50 mg sample powder

was completely dissolved with 2 ml of conc. HF + 2 ml of conc. HNO_3 + 1 ml of conc. $HClO_4$ in a tightly sealed 7 ml Teflon PFA screw-cap beaker in an ultrasonic bath for five to ten days to achieve completely digestion, and then evaporated at 120 ˚C for 12 hours, 165 ˚C for 12 hours and 195 ˚C for complete dry. The residues were repeatedly digested with 1 ml of conc. $HClO_4$ + 1 ml of H_2O for removing fluoride completely, completely evaporated again, dissolved with 2 ml of conc. HCl and completely evaporated at 100 ˚C. The dried residues were digested and diluted in mixtures of 0.5 M HNO_3 and trace HF. Before analyses, indium and bismuth solutions were added for internal standards. As the external calibration standard, W-2, issued by USGS, was analyzed every two unknown samples. The preferred values of W-2 by Eggins et al. (1997), except for Tm (Dulski, 2001) were adopted. On the ICP-MS analysis, He collision gas was introduced in order to eliminate molecular interferences, resulting in low oxide formation (CeO^+/Ce^+ < ~0.7%). The reproducibility and accuracies of the analytical protocol were verified with a USGS standard of BIR-1. The averages, relative standard deviations and differences from previously reported values are given in Supplementary Table 1. The REE and Y concentrations were normalized by PAAS

(Post-Archean Australian Shale, Taylor and McLennan, 1985), and La, Ce and Eu anomalies, La/La*, Ce/Ce* and Eu/Eu*, were defined by [$La_{SN}/(3Pr_{SN}/-2Nd_{SN})$], [$Ce_{SN}/(2Pr_{SN}-Nd_{SN})$] and [$Eu_{SN}/(0.67Sm_{SN}+0.33Tb_{SN})$].

4.2. Analysis of spatial element distributions by LA-ICP-MS

We acquired the two-dimensional distribution mappings of the elements in the BIFs with LA-ICP-MS at Gakushuin University. For this analysis, we prepared the thin section of the BIFs corresponding to the lowermost BIFs immediately the Ongeluk formations (Fig. 3B: JPN5A-1, JPN5A-2, JPN5A-3, JPN5C-1, JPN5C-2), which has less Mn and Ca contents in whole-rock chemical compositions and recrystallization structures scarcely. I analyzed the area, which includes the alternating of hematite and quartz bands, for discussing whether REE + Y and transitional elements are concentrated in Fe oxide or other minerals.

The laser ablation system consists of a 213-nm solid-state laser-ablation system, an NWR-213 (Electro Scientific Industries, Inc., Portland, US). For the analysis, the ablations of sample surfaces were conducted by pulsing the laser at 20 Hz and with

a 30-μm circular ablation spot with moving the samples mounted on a motorized stage at 60 μm/sec in perpendicular direction to the BIF bandings to create a continuous transect (total: 50 transects).

The ablated material was transported into the triple Q-pole mass filter ICP mass spectrometer, the Agilent 8800 (Agilent Technologies, Santa Clara, US), using helium as the carrier gas at a flow rate of 800ml/min. In this study, masses ^{23}Na, ^{24}Mg, ^{27}Al, ^{29}Si, ^{31}P, ^{39}K, ^{43}Ca, ^{47}Ti, ^{55}Mn, ^{57}Fe, ^{59}Co, ^{60}Ni, ^{63}Cu, ^{66}Zn, ^{89}Y, ^{141}Pr, ^{172}Yb were analyzed by the single mass-filter mode of the Agilent 8800. Integration time per each analysis cycle was 0.25s. Background counts were measured at the beginning and the end of each transect analysis, and subtracted from sample counts. For external calibration, SRM610 glass, issued by NIST, was analyzed at the beginning and the end of total analyses. For obtaining the correction factors by SRM610, the ratios of each count of analyzed elements of SRM610 to total counts of all elements each cycle were divided by the ratios of the contents of each element to the total contents of all elements. The preferred values of SRM610 by Pearce (1997) were adopted for the purpose.

Each count of the elements in the sample was divided by total counts of all

elements each cycle, which are normalized to 100 %, for calibrating the variations of ablated volumes associated with the instrumental drift and the differences of ablated minerals. Finally, those values in the sample were multiplied by the correction factors by SRM610 for obtaining the spatial distributions of absolute contents.

5. Results

5.1. Whole-rock compositions

Whole-rock chemical compositions of all analyzed samples are listed in Table. 1. Stratigraphic variations of Fe, Mn and Ca contents are illustrated in Fig. 5. The BIFs under the manganese-rock layer have higher Fe (19-45%), and lower Mn (0-17%) and Ca (0.1-2.8%) contents relative to other lithofacies. On the other hand, manganese rocks have higher Mn (29-35%) and Ca (7-12%), and lower Fe (2.5-5.8%) contents. The FeMn lutites underlying or overlying the manganese rock show intermediate compositions of Fe (9.5-17%), Mn (16-21%) and Ca (6.1-11%) between above both lithofacies. The carbonate rocks overlying the manganese-rock layer have higher Ca (12%) and Mn (12-14%), and lower Fe contents (12-13%) than the BIFs underlying the manganese rocks. P contents are variable in the BIFs underlying the manganese-rock layers (0.0068-0.22 %), and lower in other lithofacies (< 0.016%). Mg contents are variable independent of the lithofacies. The BIFs underlying the manganese rocks have 0.037-6.4% of Mg. On the other hands, the manganese rocks have 1.4-2.8%. FeMn lutite have 2.5- 4.3%. The carbonate rocks have 3.3-3.6%.

From the plots of Fe vs. REE + Y contents, LREE and MREE contents of the BIFs show increasing trends with Fe contents roughly, even though five samples (JPN5C-1, JPN5C-2, JPN6C, JPN6D-1, JPN6D-2) have markedly higher abundances of those elements relative to other BIFs with similar Fe contents (Fig. 6A, B). On the other hand, their HREE and Y contents increase with increasing Fe contents, but JPN6C have higher abundances relative to other BIFs (Fig. 6C). These REE + Y contents of the BIFs are also positively correlated with P contents (Fig. 6D, E, F). In FeMn lutites and manganese rocks, their LREE and MREE contents increase with increasing Mn contents (Fig. 6G, H); on the other hands, their HREE and Y contents are variable irrespective of Mn contents (Fig. 6I). The PAAS-normalized REE + Y patterns are commonly characterized by positive La anomalies ($La/La^* > 1$), superchondritic Y/Ho ratios (> 26) and depletion of LREE relative to HREE (Fig. 7). The distinct positive Eu anomalies ($Eu/Eu^* = 2.0\text{-}2.1$) are shown only in the lowermost BIFs (JPN5A-1, JPN5A-2, JPN5A-3, JPN5C-1, JPN5C-2), and are not shown in other samples at upper stratigraphic horizons, even though subtle anomalies ($Eu/Eu^* = 1.4\text{-}1.5$) are shown in the carbonate rocks above the manganese-rock layer (JPN19A, JPN19B) (Fig. 7A, E,

8B). The negative Ce anomalies (Ce/Ce* = 0.65 – 0.88) are shown in manganese rocks layer and overlying FeMn lutites (Fig. 7C, D, 8A).

Within the transitional elements, Ni, Zn and Co contents of all analyzed samples increase with increasing Mn contents, even though the BIFs composed of magnetite and quartz bandings (JPN6B-2, JPN6C, JPN6D-1, JPN6D-2) have higher Zn contents than others with similar Mn contents (Fig. 9B, C, E). In addition, those Co, Ni and Zn-rich samples are also enriched in Ca (Fig. 11B, C, E). Those three elements do not seemingly show positive correlations with Fe contents (Fig. 10B, C, E). Uranium (U) contents increase roughly with Mn and Ca contents (Fig. 9F, 11F), but the contents in the BIFs are also positively correlated with Fe contents (Fig. 10F). Vanadium (V) contents, except for FeMn-lutite samples, increase roughly with Fe contents (Fig. 10A), but not correlated with Mn and Ca contents (Fig. 9A, 11A). FeMn-lutite samples have higher contents of V than other samples, and Fe-rich samples in them show higher abundances (Fig. 10A). Copper (Cu) contents are variable irrespective of Fe, Mn, Ca and other element contents (Fig. 9D, 10D, 11D).

5.2. Micro-scale distributions of elements of the BIFs

The elemental distribution maps by LA-ICP-MS and variation diagrams between the elements of the BIFs immediately above the Ongeluk Formation (Fig. 3B) are shown in Fig. 12, 13, 14 and 15. Similar to elemental mapping by EPMA (Fig. 4A), spatial distributions of Fe and Si alternate with each other (Fig. 12A, B). On the other hand, the enrichments of Mg, Al, P, Ca, Ti and Mn exist as layer or patch irrespective of Fe distributions are in places (Fig. 12C, D, E, F, G, H), which are often consistent with each other. The variation diagrams between above elements in a representative transect of the analyzed area show that those element contents increase with Fe contents, but some points have higher contents relative to others with similar Fe contents (Fig. 13A, B, C, D, E). In the same transect, some points with higher contents often have higher Al contents (Fig. 14A, B, C, D). In addition, the P and Ca contents of the transect are positively correlated with each other (Fig. 15A).

The enrichments of REE + Y (Y, Pr and Yb) exist as spots or layer, which are roughly consistent with the Fe-rich bands (Fig. 12M, N, Q). And, their enrichment layers are also consistent with those of Al, Ca and P (Fig. 12E, F, M, N, O). The

variation diagrams of Fe vs. REE + Y in a representative transect show that those element contents increase with Fe contents, but some points have higher contents relative to other points with similar Fe contents (Fig. 13I, J, K). In addition, some of those points with higher contents have higher Al and Ca contents (Fig. 14I, J, K, 15B, C, D).

The some transitional elements (Ni, Cu, Zn) are distributed in the Fe-rich bands (Fig. 12J, K, L). The some enriched patches of them, especially for Ni, are consistent with enriched patches or layer of Mg, Al, Ti and Mn in places (Fig. 12C, D, G, H). On the other hand, much of Co is not distributed in Fe-rich bands (Fig. 12I). The distribution is consistent with enriched patches and layer of Mg, Al, Ti and Mn (Fig. 12 C, D, G, H). The variation diagrams of Cu, Zn vs. Fe contents in a representative transect within analyzed area show that both element contents increase with increasing Fe contents (Fig. 13H, I). However, in the plot of Fe vs. Ni, those increasing trend are not clear (Fig. 13G). Cobalt contents in a representative transect are not positively correlated with Fe contents (Fig. 13F), but increase with Al contents (Fig. 14E). Some points of Ni, Cu and Zn also show increasing trends with Al contents (Fig. 14F, G, H).

6. Discussion

6.1. Redox and hydrothermal contributions associated with the formations of the BIFs and the manganese rocks at the sedimentary environments

6.1.1. Stratigraphies of Fe, Ca and Mn contents in the analyzed strata of the Hotazel Formation

The Kalahari manganese field was suffered from alterations by structurally-controlled hydrothermal fluids through the N-S striking faults or unconformity between the Hotazel Formation and the Olifantshoek Supergroup. Those hydrothermal alterations caused leaching and reprecipitation of Ca- and Mg-carbonate minerals of the BIFs and manganese rocks, resulting in residual Fe- and Mn-enrichment, dolomitization of them and coarse-grained minerals (Kleyenstüber 1985; Gutzemr and Beukes, 1995; Gutzmer and Beukes, 1997; Tsikos et al., 2003; Chetty, 2008; Chetty and Gutzmer, 2012). However, those alterations have been reported mainly in drill cores around Wessels mine and N'chwaning mine of the northern parts of the Kalahari manganese field, which are overlain by unconformity plane of Olifaentshoek Supergroup (Fig. 1B). And, in GL137, above alteration textures are not found macro-

and microscopically (Fig. 3, 4). In addition, stratigraphically increasing trends of Ca and Mn contents, and Ca/Fe and Mn/Fe ratios of GL-137 from the lowermost BIFs to the lowest manganese rocks are in common with them of the least altered BIFs (Tsikos et al., 2003) (Fig. 5 B, C, E, F). Therefore, hydrothermal alterations have less influential on major element compositions of the studied stratum of GL-137. In other words, major-element stratigraphies preserve pre-alteration, or possibly synsedimentary signatures. Increasing trends stratigraphically upwards of Mn/Fe and Ca/Fe ratios from the lowermost BIFs to the lowest manganese-rock layers (Fig. 5E, 5F), suggesting that sedimentary environments transited from dominant depositions of Fe-oxide minerals to dominant depositions of Mn-oxide and Ca-carbonate minerals in analyzed parts.

6.1.2. Relationships between lithofacies and REE + Y contents, and their stratigraphies

Above hydrothermal alterations can also be influential on REE contents even though their influences have been reported only in manganese rocks (Chetty and Gutzmer, 2012; Chetty, 2008). Their previous studies show that the hydrothermal alterations resulted in residual enrichment and much scattering of REE contents

accompanied by leaching of Ca- and Mg-carbonate minerals. However, they also show that their REE + Y are concentrated in diagenetic apatite based on positive correlations between REE + Y and P contents, and their patterns were not altered unless the apatites were decomposed into other REE minerals. In the BIFs of GL-137, all samples show positive correlations between HREE and Fe contents except for JPN6C (Fig. 6C), but some samples (JPN5C-1, JPN5C-2, JPN6C, JPN6D-1, JPN6D-2) have higher LREE and MREE contents relative to other samples with similar Fe contents (Fig. 6A, B). On the other hand, all BIFs show clearly positive correlations between REE + Y and P contents (Fig. 6D, E, F), suggesting that REE + Y in the BIFs is concentrated in apatite. These are also supported by spatial distributions of REE+Y, Ca and P contents of the lowermost BIFs overlying the Ongeluk Formation. The REE + Y in the BIFs are distributed as patch or layer. Their enrichments are often consistent with the distributions of Fe-rich bandings, and are also Mg, Al, P, Ca, Ti and Mn-enriched patches or layer, which are often consistent with each others (Fig. 12A, C, D, E, F, G, H, M, N, O). Especially, the enrichments of REE + Y in the upper right-hand corner of Figure. 12M, N and O are consistent with those of Ca and P in the same area. Those Mg,

Al, P, Ca, Ti and Mn enrichments in Fig. 12 might be reflective of the occurrences of the clastic materials because Al^{3+} and Ti^{4+} are insoluble in aqueous solution (e.g. Martin and Whitfield, 1983; Andrews et al., 2004) and concentrated in clastic materials. Therefore, REE + Y in the BIFs might be concentrated in apatite minerals with the clastic-material origins.

These suggest that REE + Y in the BIFs might be originally derived from adsorbents on Fe oxyhydroxide (precursor minerals of Fe-oxide minerals in the BIFs), and were secondarily moved into the apatite at their diagenesis. The spatial extents of REE + Y diagenetic movements were limited within the spatial extents of analyzed samples as for HREE, but LREE and MREE in above five samples were likely to be secondarily moved above the sample size. However, each anomaly in the REE + Y patterns are not correlated with P contents, which are variable irrespective of the stratigraphy. In addition, above five samples, which have higher LREE and MREE contents with higher P contents than other samples, show similar degrees of positive Eu anomalies and negative Ce anomaly to those at close stratigraphic horizons (Fig. 8A, B). Therefore, it is likely that secondarily movements of REE + Y into apatite at their

diagenesis have a limited effect on each anomaly in the REE + Y patterns of the BIFs. In manganese-rock and FeMn-lutite layer, their P contents are much lower than those of the BIFs, and correlations with REE + Y contents are not clear, suggesting that apatites are not host minerals for REE + Y (Fig. 6D, E, F). In addition, the LREE and MREE contents of the manganese rocks, FeMn lutites and high Mn-content BIFs are positively correlated with Mn contents, suggesting that they were primarily hosted by Mn-oxide minerals in Mn-rich rocks (Fig. 6G, H). These contradict above estimates based on the positive correlations between REE+Y and P contents by Chetty (2008) and Chetty and Gutzmer (2012). These differences are possibly due to lower P contents (0.089-0.013%) in manganese rocks of GL-137 have than those (P contents: 0.0147 - 0.0269 %) analyzed by Chetty (2008), suggesting that they have lower modal abundance in apatite. Therefore, secondary REE + Y concentrations on apatite at diagenesis might be less influential on the manganese rocks of GL-137. Moreover, above hydrothermal alterations could cause the loss or positive Ce anomalies of the manganese rock due to REE + Y redistribution accompanied with decompositions of REE+Y-bearing apatite to other minerals (Chetty, 2008; Chetty and Gutzmer, 2012). However, negative Ce

anomalies are shown consistently in manganese rocks and FeMn lutite of GL-137 (Fig. 7C, D, 8A). Therefore, it might be possible that the manganese rock layers in GL-137 preserve the primary REE + Y patterns.

6.1.3. Implications for redox and hydrothermal influences at the sedimentary environments

Strong positive Eu anomalies as shown in the lowermost BIFs of GL-137 is characteristic of REE+Y compositions in the high-temperature hydrothermal fluids (e.g. Michard et al., 1983). On the fluid-rock interactions of the hydrothermal metamorphisms with high temperature and low Eh/pH, trivalent Eu (III) in rocks is reduced to divalent Eu (II) with large ionic radii, which are prone to be preferentially extracted to fluids relative to neighbor REEs, resulting in positive Eu anomalies of the high-temperature hydrothermal fluids (Sverjensky, 1984). And, modern metalliferous sediments or particles near the hydrothermal vents show positive Eu anomalies (Ruhlin and Owen, 1986; Olivarez and Owen, 1991; German et al., 1990) because those metalliferous minerals adsorb dissolved REE + Y with the hydrothermal signatures.

Similar to them, it is likely that the lowermost BIFs with positive Eu anomalies (Eu/Eu* = 2.0-2.1) were deposited in the ocean under the strong influences of hydrothermal fluids after the eruption of the Ongeluk andesitic basalts (Fig. 7A, 8B). No positive Eu anomaly in the overlying BIFs, the FeMn lutite and manganese rocks after the formation of the lowermost BIFs suggest that they were precipitated from the seawater with no hydrothermal influences (Fig. 7A, B, C, D, 8B). The weak positive Eu anomalies (Eu/Eu* = 1.4-1.5) are shown in carbonate-hematite rocks (JPN19A, 19B), suggesting that their sedimentary environments suffered from intermittent inputs by hydrothermal fluids again (Fig. 7E, 8B).

On the other hand, negative Ce anomalies shown in the manganese rocks are characteristic of the modern oxic seawater (Fig. 7C, D, 8A). In modern oxic aquatic environments, trivalent Ce (III) is oxidized to tetravalent form (IV) by Mn oxide and/or bacteria (Byrne and Sholkovitz, 1996; Tanaka et al., 2010). Tetravalent Ce is insoluble and prone to preferentially removed by Mn oxides relative to neighbor REEs, resulting in negative Ce anomalies of the oxic seawater (Elderfield et al., 1981). Modern metalliferous sediments and particles precipitated under oxic environments also show

negative Ce anomalies, suggesting that those sediments recorded those anomalies of the seawater, from which they were precipitated (Ruhlin and Owen, 1986; Olivarez and Owen, 1991; German et al., 1990). Similarly, negative Ce anomalies of manganese rocks and FeMn lutite in the Hotazel Formation ($Ce/Ce^* = 0.65 – 0.88$) suggest that the seawater had negative Ce anomalies and become evolved to more oxic conditions at their depositions (Fig. 7C, D, 8A).

Above chemostratigraphies of Fe and Mn contents, and Ce and Eu anomalies suggest that their sedimentary settings transited from anoxic environments under influences of the strong high-temperature hydrothermal fluids to oxic environments. The sedimentary environments, at which the stratigraphically lower BIFs in the studied strata of GL-137 deposited, can be thought to have been anoxic due to influences by high-temperature hydrothermal fluid, resulting in preferential depositions of Fe-oxide minerals sometimes with positive Eu anomalies (the depositions of the BIFs with low Mn/Fe ratios). On the other hand, the sedimentary environments correlating to stratigraphically upper BIFs and manganese rocks has been becoming more oxic with hydrothermal influences becoming weak, resulting in precipitation of tetravalent

Mn-oxide minerals (the depositions of the sediments with high Mn/Fe ratios) with negative Ce anomalies, which have higher redox potentials than trivalent Fe. At the depositions of carbonate rocks (JPN19A, JPN19B) after formation of manganese rocks, the sedimentary environments became anoxic and suffered from inputs by hydrothermal fluids as suggested by weak positive Eu anomalies and no Ce negative anomalies, resulting in preferential precipitation of Fe oxyhydroxide relative to manganese-oxide minerals, as indicated by subtle increase of Fe contents and decreased of Mn contents and Mn/Fe ratios (Fig. 5A, B, D).

The all strata of the Hotazel Formation show roughly increasing trends of Ca contents up to the Mooidraai formation composed of carbonate rocks, which were formed at the shallower seawater conditions than the Hotazel Formation (Tsikos et al., 1997; Schneiderhan et al., 2006; Kunzman et al., 2014). Kunzman et al. (2014) interpreted, based on gradual changes of depositional environments from the deep basin to shallower conditions indicated by the lack of a depositional gap at the Hotazel-Mooidraai transition, that the BIFs of the Hotazel Formation were concurrently deposited further offshore in the basin during the formation of the Mooidraai Formation.

If true, the increasing depositions of Ca-carbonate minerals suggested by increasing trend of Ca contents and Ca/Fe ratios of the analyzed strata might be due to shallowing process from the deep offshore to the shallow coast in their sedimentary environments. Summarized above, chemostratigraphy of Ca/Fe ratios, Mn/Fe ratios, Ce anomalies and Eu anomalies in analyzed strata suggest that their sedimentary environments were transited from anoxic deep sea suffered from hydrothermal influences, thorough oxic shallow sea with less hydrothermal influences, finally to anoxic ocean with a hydrothermal influences, again.

Tsikos et al. (2010) showed that the BIFs in the Hotazel Formation with lower Mn/Fe ratios, stratigraphically corresponding to the lowermost BIFs in the analyzed part of GL-137, have isotopically heavier Fe (δ^{57}Fe: 0 ‰ at a maximum); on the other hand, rocks with higher Mn/Fe ratios marked negatively Fe isotope values (as low as -4 ‰). They interpreted that increasing Mn/Fe ratios with decreasing δ^{57}Fe in the Hotazel iron formations are due to that the dissolved marine Fe (II) pool was becoming small progressively by depositions of isotopically heavy Fe-oxide minerals on the assumption of Rayleigh distillation. The marine Fe (II) pool was kept by supply of high-temperature

hydrothermal fluids, as shown by positive Eu anomalies of the BIFs with low Mn/Fe ratios in this study, and was becoming small and enriched in dissolved Mn (II) contents relative to Fe (II) with advancing oxic conditions as suggested by negative Ce anomalies in manganese rock.

6.2. Relationships between lithofacies and transitional elements, and implications for bioavailability of those elements in the Paleoproterozoic ocean

Including the BIFs and manganese rocks in the lower parts of GL-137, their Co, Ni, Zn and U contents increase with Mn contents (Fig. 9B, C, E, F). In addition, their Ni, Zn and U contents are also positively correlated with Ca contents (Fig. 11C, F). Assuming that secondary movements of those elements are insignificant unlike REE + Y, these correlations suggest that those transitional elements are primarily concentrated in Mn- and Ca-bearing minerals such as tetravalent Mn oxide and Ca carbonate minerals. On the other hand, their V contents, except for FeMn lutites, are positively correlated with Fe contents. Within the FeMn lutites, the contents are also posively correlated with Fe contents. They suggest that the element was concentrated in

Fe-bearing minerals such as Fe oxyhydroxide. In addition, their Cu contents show no correlations with Mn, Ca and Fe contents, suggesting that the element occurs without distinction of Mn, Ca or Fe phases. The BIFs composed of magnetite and quartz bandings (JPN6B-2, JPN6C, JPN6D-1, JPN6D-2) are enriched in Zn and Cu relative to samples with similar Mn, Ca or Fe contents (Fig. 9D, E, 10D, E, 11D, E). These are because these samples have abundant sulfide minerals that possibly due to their sulfide minerals that are prone to concentrate those transitional elements (Fig. 4B).

From sequential leaching experiments of modern ferromanganese crusts, Co, Ni and Zn are concentrated in vernadite (δ-MnO_2) relative to amorphous FeOOH because these hydrated and chloro-complexed metal cations are more prone to be adsorbed on the negatively charged δ-MnO_2 phase than slight-positively charged FeOOH phase at modern oceanic condition (Koschinsky and Halbach, 1995). Moreover, in vernadite, Ni is substituted for Mn in the manganese layer and adsorbed at the vacant Mn layer sites in the interlayer; on the other hand, Zn is only adsorbed at the vacant Mn layer sites in the interlayer (Manceau et al., 2007). Unlike Ni and Zn, Co incorporation into the Mn-oxide minerals is associated with its valence modification from divalent to

trivalent. In modern oceans, soluble divalent Co (II) in the seawater sorbs onto the vacant Mn sites in buserite (MnO_2), is oxidized into insoluble trivalent form by the nearest trivalent Mn (III), and finally fixed into them (Manceau et al., 1997). As a result, ferromanganese crusts concentrate Co relative to divalent transitional elements (e.g. Ni, Cu, Zn), and are sinks in oceanic Co cycle, which concentrate Co 10^9 times more than seawater (e.g. Hein et al., 2003). Similar to ferromanganese crusts in modern oxic ocean, positive correlations of Mn contents with Co, Ni and Zn contents in the analyzed strata of GL-137 suggest that Mn-oxide minerals accumulate these elements as sinks in the Paleoproterozoic Ocean (Fig. 9B, C, E).

On the other hand, V dissolves as a pentavalent oxyanion in modern seawater, and is prone to be adsorbed onto slightly-positive charged FeOOH phase (Koschinsky and Halbach, 1995). Therefore, a positive correlation between Fe and V contents of the analyzed samples except for FeMn lutites and the similar correlations within FeMn lutites in this study might be due to the same processes for V adsorptions onto Fe oxyhydroxide in the Paleoproterozoic ocean as in the modern seawater. The differences of the correlations between the BIFs (and the manganese rocks), and the FeMn lutites

might be due to the difference of dissolved V contents in the seawater. In aquatic environments, V varies from +2 to +5 in the valence, and is soluble as various vanadate compounds under oxic conditions. Therefore, the higher V contents in the FeMn lutite might suggest that the seawater V contents were at the FeMn lutite depositions higher than at the BIF depositions because the FeMn lutites are thought to been deposited under more oxic conditions as suggested by their REE + Y compositions.

The micro-scale distributions of Ni, Cu and Zn are seemingly consistent with that of Fe in the lowermost BIFs with low Mn content (Fig. 12A, J, K, L). In one representative transect, Cu and Zn contents are positively correlated with Fe contents (Fig. 13H, I), but Ni contents are not well correlated with Fe contents (Fig. 13G). These characters suggest that much of Zn and Cu are derived from adsorbed elements on Fe oxyhydroxide. However, enriched spots of those transitional elements (especially for Ni) are consistent with that of Mg, Al and Mn (Fig. 12C, D, H), which are consistent with each other. Aluminum is an insoluble element in seawater, and contained abundantly in igneous minerals. Therefore, Mg, Al and Mn are derived from clastic or volcanic materials. And, a part of Ni, Cu and Zn in the BIFs are also derived from those

Al-bearing clastic or volcanic materials. These are also supported by that some of Ni, Cu and Zn contents in one transect are positively correlated with Al contents (Fig. 13D, E, F).

On the other hand, much distribution of Co are not consistent with that of Fe, but consistent with those of Mg-, Al- and Mn-enriched layer or spots (Fig. 10C, D, H, I). In one transect, the Co contents are not positively correlated with Fe contents (Fig. 11E), but with Al contents (Fig. 13C). Therefore, much of Co in the Mn-poor BIFs is not originated from the Paleoproterozoic seawater, but from the clastic or volcanic materials.

The different distributions of Cu, Zn from Co in the Mn-poor BIFs, qualitatively, suggest that dissolved divalent Co (II) were low in Paleoproterozoic ocean; on the other hand, divalent Cu (II) and Zn (II) were significantly dissolved. Under oxic conditions, divalent Co (II) might be oxidized to insoluble trivalent forms and finally fixed within the Mn-oxide deposits. On the other hand, Zn and Cu might exist as soluble divalent forms in the seawater under the oxic conditions.

6.3. Implications for Co bioavailability through the time

In surface environments, cobalt (Co) behaves as divalent and trivalent forms. Under anoxic conditions, Co exists as soluble divalent forms. Therefore, hydrothermal fluids contain Co contents several orders of magnitude above average seawater (Metz and Trefry, 2000). On the other hand, under oxic conditions, they are oxidized to insoluble tetravalent forms and fixed within Mn-oxide minerals, as explained above.

Swanner et al. (2014) compiled whole-rock or mineral-scale Co/Ti ratios (authigenic Co) in the ferruginous sediments including the BIFs throughout the Earth's history, and showed that their ratios increase from 2.8 to 1.8 Ga relative to the ratios of evolving continental crust (Condie, 1993). They suggest that the seawater with corresponding ages were enriched in dissolved cobalt possibly due to the large-volume supply of anoxic hydrothermal fluids with limited cobalt-burial fluxes. However, their estimates are controversial because their Co/Ti ratios are highly variable even in one BIF sequence (from 10^5 to 10^9) and it is not clear whether the chemical compositions are reflective of those of seawater, from which they were precipitated.

The chemical compositions of the BIFs can be controlled by the following

processes, except for some oceanic processes such as seawater chemistry, sedimentation rate (Kato et al., 1998; Kato et al., 2002) and adsorptive interference elements on Fe oxyhydroxide (Konhauser et al., 2009).

Firstly, chemical precipitates other than Fe-oxide minerals and silica minerals in the BIFs could concentrate those minerals, resulting in overestimates of seawater compositions. In fact, increasing Co contents with Mn contents in the BIFs of the Hotazel Formation suggest that tetravalent Mn-oxide minerals concentrated Co, as explained above. For the estimates of Co seawater compositions, Swanner et al. (2014) removed the BIFs with high Mn-content (Mn > 0.5%) for avoiding Co enrichment in Mn-oxide minerals. However, the threshold value is invalid. Even though their mineralogy and chemical contents other than Ti, Al, Mn and Fe are not shown in high whole rock or mineral Co contents (from 10^0-10^2 ppm) in most BIFs from Neoarchean to Paleoproterozoic show positive correlations with Mn contents (Fig. 14). On the other hand, the BIFs with no positive correlations between Mn and Co contents have lower Co contents (from 10^{-2} to 10^0 ppm). Positive correlations in the BIFs xwith high Co contents reflect that much Co in them exists not in Fe oxides but in Mn oxides.

Secondly, clastic materials could be influential on the transitional-element contents in the BIFs because those contaminants usually have higher REE, LILE, HFSE and transitional elements (e.g. Bau, 1993). Especially, igneous minerals present in ultramafic rocks such as olivine, pyroxene and spinel have high abundance of Co (Glassley and Piper, 1978). Swanner et al. (2014) assumed that the potential contaminant sources could be the average continental crust modeled by Condie (1993), but their assumption of single contaminant sources is invalid because the contaminant sources could be variable depending on the constituent rocks of their hinterlands (Viehmann et al., 2015a, b; Aoki et al., 2017). In fact, the 2.94 Ga West Rand Group, South Africa, and the 2.43 Ga Caue Iron Formation, Brazil, compiled by Swanner et al. (2014) show high Co contents up to 10^2 ppm, which are positively correlated with Al contents (Fig. 15). Therefore, a part of BIFs, which have higher Co contents, might be suffered from contaminations by clastic or volcanic materials.

As summarized above, much of cobalt might occur not in the Fe-oxide minerals, but in Mn-oxide minerals and/or clastic or volcanic materials in the Neoarchean to Paleoproterozoic BIFs. On the other hands, the BIFs from the Eoarchean

geologic suites show no positive correlations of Mn or Al, Ti and HFSE contents with Co contents (Aoki et al., 2017). The Neoarchean to Paleoproterozoic BIFs with no positive correlations of Mn, Al, Ti and HFSE with Co contents have lower Co contents than the Eoarchean BIFs. Therefore, it might be possible that dissolved Co contents in the Neoarchean to Paleoproterozoic seawater were decreased. The decrease might be caused by the precipitation of Mn-oxide minerals and their removal of dissolved Co as the surface environments evolved into oxic conditions.

6.4. Implications for Zn bioavailability throughout the time

Zinc (Zn) occurs only as a divalent form in surface environment. Under euxinic (anoxic and sulfidic) conditions, Zn is fixed as sulfide minerals. Aoki et al. (2017) showed that the Eoarchean BIFs in the Isua supracrustal belt have suffered from clastic or volcanic contaminations based on positive correlations between Zn and Zr contents, and estimated that contamination-free BIFs have insignificant Zn contents, suggesting that Zn bioavailability was limited in the Eoarchean oceans.

The micro-scale Zn distribution in the BIFs of the Hotazel Formation show

that much Zn (up to 150 ppm) exists in Fe-rich bands, suggesting that origins of Zn in the BIFs is the Paleoproterozoic seawater rather than clastic or volcanic materials (Fig. 10A, L, 11L). Assuming that Zn contents in the BIFs are correlated with those of seawater, higher abundance in Zn contents suggests that the Paleoproterozoic oceans have higher Zr abundance than the Eoarchean oceans, possibly because of increase in oxic continental weathering and delivery of Zn into the ocean.

6.5. Influence on biological evolutions associated with change of bioavailability in transitional elements

Cobalt is one of the bioessential elements. It is mainly used for cobalamin (vitamin B12), which is concerned with every metabolic activity in cell. For example, methylated cobalamin (Met H) catalyze the synthesis of methionine, which is an amino acid constituting the terminal domain of all proteins. The methods for utilizing vitamin B12 are different between prokaryote and eukaryote. Prokaryotes ingest dissolved cobalt from surrounding environments, and can synthesize vitamin B12 on their own. In contrast, eukaryotes have no ability for synthesis. Half of the eukaryotic algae are

dependent solely on vitamin B12 for methionine synthesis, and they acquire vitamin B12 in symbiosis with vitamin B12-synthesizing bacteria because levels of free vitamin B12 in aquatic environments are too low to support their growth (Croft et al., 2005). On the other hand, half of remaining can substitute zinc-containing enzyme (Met E) for Met H in the case that vitamin B12 is not available in the environments. Moreover, a part of prokaryote (e.g. cyanobacteria and colon bacillus) also possesses Met E, and eukaryotic algae, excavata, and those prokaryotes belong to a monophyletic group as for Met E gene (Helliwell et a., 2011). This phylogenetic study suggests that their eukaryotic organisms acquired the Met E gene on the cyanobacterial endosymbiosis.

Change of bioavailability in Co and Zn suggested by secular variations of the chemical compositions from the Neoarchean to Paleoproterozoic BIFs including the Hotazel Formation might have caused the evolutions from prokaryotes with only Met H gene to them with Met H and Met E, finally resulting in the birth of eukaryotes.

Conclusions

The Paleoproterozoic Hotazel Formation in the Postmasburg Group of the Transvaal Supergroup, South Africa, are composed of the BIFs hosting the manganese rocks at three stratigraphic horizons. Petrographic and geochemical studies from the lowest BIF layer to the BIFs overlying the lowest Manganese-rock layer of the Hotazel Formation have led to the following conclusions:

1. Stratigraphic variations of whole-rock Mn/Fe and Ca/Fe ratios show increasing trends from the lowermost BIFs immediately above the Ongeluk Formation to the lowest Manganese rocks, suggesting that Mn-oxide and Ca-carbonate minerals were more precipitated than Fe-oxide minerals at the sedimentary environments.

2. The lowermost BIFs show strong positive Eu anomalies characteristics of the hydrothermal fluids. The manganse rock and FeMn lutite show negative Ce anomalies characteristics of the modern-like oxic seawater. Positive Eu anomalies are also the BIFs immediately above the FeMn lutite layer.

3. From above stratigraphic varitaions of Mn/Fe, Ca/Fe and REE + Y anomalies from the BIF to the manganese-rock layer, their sedimentary environments were transited

from hydrothermal-dominated deep ocean to oxic shallow ocean. After the precipitation of the manganese rock and FeMn lutite, anoxic hydrothermal fluids were prevailed, resulting in precipitation of the BIFs enriched in Ca-carbonate minerals.

4. Whole-rock transitional-element contents such as Co, Ni and Zn except for pyrite-free samples are positively correlated with Mn contents, suggesting that Mn oxides are sink for these elements in the Proterozoic ocean. Element distribution mappings of the BIFs show that much of Co do occur not in the Fe oxide, but in the Al-rich minerals. On the other hands, Zn occur in the Fe oxide. These contrasting distributions of both elements suggest that much of Co was derived from clastic or volcanic materials, and Zn was derived from the Paleozoic ocean.

5. The BIFs from the Neoarchean to the Paleoproterozoic with high Co contents (10^{1}-10^{2} ppm) show positive correlations between Co and Mn contents, suggesting that dissolved Co in the contemporary seawater were removed by Mn-oxide minerals. On the other hands, with no positive correlations show lower Co contents (10^{-2}-10^{0} ppm) than the Archean BIFs. Therefore, dissolved Co was lower in the Neoarchean to

Paleoproterozoic oceans including the Hotazel Formation than before because much of Co was fixed as insoluble tetravalent forms within the Mn-oxide minerals.

6. On the other hand, Zn contents in the Fe oxide within BIFs of the Hotazel Formation BIFs were higher than the Eoarchean contamination-free BIFs, suggesting that dissolved Zn was increased until the Paleoproterozoic because of increase in oxidative continental weathering and Zn delivery into the ocean.

7. The change in bioavailability of Co and Zn from the Archean to the Proterozoic might cause the evolutions of prokaryotes preferentially using Zn-containing enzyme in the Co-depleted environments and endosymbiosis of them resulting in the evolutions of eukaryotes.

Reference

Albani, A. E., Bengtson, S., Canfield D. E., Bekker, A., Macchiarelli, R, Mazurier, A., Hammarlund, E. U., Boulvais, P., Dupuy J. J., Fontaine, C., F ürisch, F. T., Gaurhier-Lafaye, F., Janvier, P., Javaux, E., Ossa, F. O., Pierson-Wickmann, A. C., Riboulleau, A., Sardini, P., Vachard, D., Whitehouse, M., Meunier, Alain., 2010. Large colonical organism growth in oxygenated environments 2.1 Gyr ago. Nature 466, 100-104.

Anbar, A.D., Duan, Y., Lyons, T.W., Arnold, G.L., Kendall, B., Creaser, R.A., Kaufman, A.J., Gordon, G.W., Scott, C., Garvin, J., Buick, R., 2007. A Whiff of Oxygen Before the Great Oxidation Event? Science 317, 1903-1906.

Anbar, A.D. 2008, Elements and Evolution. Science 322, 1481-1483.

Awaji, S., Nakamura, K., Nozaki, T., Kato, Y., 2006. A simple method for precise determination of 23 trace elements in granitic rocks by ICP-MS after lithium tetraborate fusion. Resource Geology 56, 471-478.

Bau, M., 1993. Effects of syn- and post-depositional processes on the rare-earth element distribution in Precambrian iron-formations. European Journal of Mineralogy 5, 257-267.

Bau, M., Dulski, P., 1996. Distribution of yttrium and rare-earth elements in the Penge and Kuruman iron-formations, Transvaal Supergroup, South Africa. Precambrian Research 79, 37-55.

Bau, M., Romer, R., Luders, V., Beukes, N.J., 1999. Pb, O, and C isotopes in silicified Mooidraai dolomite (Transvaal Supergroup, South Africa): implications for the composition of Palaeoproterozoic seawater and ‘dating’ the increase of oxygen in the Precambrian atmosphere. Earth Planetary Science Letters 174, 43–57.

Bekker, A., Holland, H.D., Wang, P.–L., Rumble, D., Stein, H.J., Hannah, J.L., Coetzee, L.L., Neukes, N.J. 2004. Dating the rise of atmospheric oxygen. Nature 427, 117-120.

Beukes, N. J., 1983. Paleoenvironmental setting of iron-formation in the depositonal basin of the Transvaal Supergroup, South Africa. In:Trendall, A. F., Morris, R. C. (Eds.), Iron-formation: Facts and Problems, Elsevier, Amsterdam, pp. 131-209.

Beukes, N. J., Smit, C . A., 1987. New evidence for thrust faulting in Griqualand West, South Africa: Implications for stratigraphy and the age of red beds. South African Journal of Geology 90, 378-394.

Bjerrum, C.J., Canfield, D.E., 2002. Ocean productivity before about 1.9 Gyr ago limited by phosphorus adsorption onto iron oxides. Nature 417, 159–162.

Bolhar, R., Kamber, B.S., Moorbarth, S., Fedo, C.M., Whitehouse, M.J., 2004. Characterisation of early Archaean chemical sediments by trace element signatures. Earth and Planetary Science Letters 222,43-60.

Brand, U., Veizer, J., 1980. Chemical diagenesis of a multicomponent carbonate system. 1. Stable isotopes. Jounral of Sedimentary Petrology 51, 987-997.

Brand, U., Veizer, J., 1981. Chemical diagenesis of a multicomponent carbonate system. 1. Trace elements. Jounral of Sedimentary Petrology 50, 1219-1236.

Byrne, R.H., Sholkovitz, E.R., 1996. Marine chemistry and geochemistry of the lanthanides. In: Gschneider Jr., K.A., Eyring, L. (Eds.) Handbook on the Physics and Chemistry of Rare Earths 23, Elsevier, Amsterdam, pp. 497-593.

Canfield, D.E., 1998. A new model for Proterozoic ocean chemistry. Nature 396, 450-453.

Chetty, D., 2008. A geometallurgical evaluation of the ores of the northern Kalahari Manganese Deposit, South Africa [PhD thesis]. University of Johannesburg, Johannesburg, 271 pp.

Chetty, D., Gutzmer, J., 2012. REE redistribution during hydrothermal alteration of ores of the Kalahari Manganese Deposit. Ore Geology Reviews 47, 126-135.

Cloud, P. E., 1968. Atmospheric and hydrospheric evolution on the priimitive Earth. Science. Science 160, 729-736.

Fairey, B., Tsikos, H., Corfu, F., Polteau, S., 2013. U-Pb systematics in carbonates of the Postmasburg Group, Transvaal Supergroup, South Africa: Primary versus metasomatic fluids. Precambrian Research 231, 194-205.

Guo, Q., Strauss, H., Kaufman, A.J., Schröder, S., Gutzmer, J., Wing, B., Baker, M.A., Bekker, A., Jin Q., Kim, S.-T., Farquhar, J., 2009. Reconstructing Earth's surface oxidation across the Archean-Proterozoic transition. Geology 37, 399-402.

Walker, J.C.G., 1977. Evolution of the Atmosphere. Macmillan.

Walker, J.C.G., 1982. Climatic factors on the Archean earth. Palaeogeography,

Palaeoclimatology, Palaeoecology 40, 1-11.

Cairncross, B., Beukes, N. J. & Gutzmer, J. (1997) The Manganese Adventure: The South African Manganese Fields. Associated Ore & Metal Corporation, Johannesburg, South Africa.

Condie, K.C., 1993. Chemical composition and evolution of the upper continental crust: Contrasting results from surface samples and shales. Chemical Geology 104, 1-37.

Cornell, L.R., Schitte, S.S., Eglington, B.L., 1996. The Ongeluk basaltic andesite formation in Griqualand West, South Africa: submarine alteration in a 2222 Ma Proterozoic sea. Precambrian Research 79, 101–123.

Croft, M.T., Lawrence, A.D., Raux-Deery, E., Warren, M.J., Smith, A.G., 2005. Algae acquire vitamin B12 through a symbiotic relationship with bacteria. Nature 438, 90-93.

Dulski, P., 2001. Reference materials for geochemical studies: new analytical data by ICP-MS and critical discussion of reference values. Geostandard Newsletter 25, 87-125.

Dupont, C.L., Yang. S., Palenik, B., Bourne, P.E., 2006. Modern proteomes contain putative imprints of ancient shifts in trace metal geochemistry. PNAS 47, 17822-17827.

Eggins, S.M., Woodhead, J.D., Kinsley, L.P.J., Mortimer, G.E., Sylvester, P., McCulloch, M.T., Hegt, J.M., Handler, M.R., 1997. Chemical Geology 134, 311-326.

Elderfield, H., Hawkesworth, C.J., Greaves, M.J., Calvert, S.E., 1981. Rare earth element geochemistry of oceanic ferromanganese nodules and associated sediments. Geochimica et Cosmochimica Acta 45, 513-528.

Evans, D.A., Beukes, N.J., Kirschvink, J.L., 1997. Low-latitude glaciation in the Palaeoproterozoic era. Nature 386, 262-266.

Faquhar, J., Bao, H., Thiemens, M., 2000. Atmospheric influence of Earth's earliest sulfur cycle. Science 289, 756-758.

German, C.R., Klinkhammer, G.P., Edmond, J.M., Mitra, A., Elderfield, H. 1990. Hydrothermal scavenging of rare earth elements in the ocean. Nature 345, 516-518.

Glassley, W.E., Piper, D.Z., 1978. Cobalt and scandium partitioning versus iron content

for crystalline phases in ultramafic nodules. Earth and Planetary Science Letters 39, 173-178.

Gutzmer, J., Beukes, N.J., 1995. Fault controlled metasomatic alteration of Early Proterozoic sedimentary manganese ores in the Kalahari manganese field. Economic Geology 90, 823-844.

Gutzmer, J., Beukes, N.J., 1997. Effects of mass transfer, compaction and secondary porosity on hydrothermal upgrading of Paleoproterozoic sedimentary manganese ore in the Kalahari manganese field, South Africa. Mineralium Deposita 32, 250-256.

Han, T. M., Runnegar, B., 1992. Megascopic eukaryotic algae from the 2.1-billion-year-old Negaunee iron-formation, Michigan. Science 257, 232-235.

Hein, J.R., Koschinsky, A., Halliday, A.N., 2003. Global occurrence of tellurium-rich ferromanganese crusts and a model for the enrichment of tellurium. Geochimica et Cosmochimica Acta 67, 1117-1127.

Helliwell, K.E., Wheeler, G.L., Leptos, K.C., Goldstein, R.E., Smith, A.G., 2011. Insights into the evolution of vitamin B12 auxotrophy from sequenced algal genomes. Molecular Biology and Evolution 28, 2921-2933.

Isley, A.E., Abbott, D.H., 1999. Plume-related mafic volcanism and the deposition of banded iron formations. Journal of Geophysical Research 104, 15461-15477.

Kasting, J.F., 1987. Theoretical constraints on oxygen and carbon dioxide concentrations in the Precambrian atmosphere. Precambrian Research 34, 205-229.

Kato, Y., Ohta, I., Tsunematsu, T., Watanabe, Y., Isozaki, Y., Maruyama, S., Imai, N., 1998. Rare earth element variations in mid-Archean banded iron formations: implications for the chemistry of ocean and continent and plate tectonics. Geochimica et Cosmochimica Acta 62, 3475-3497.

Kato, Y., Kano, T., Kunugiza, K., 2002. Negative Ce Anomaly in the Indian Banded Iron Formations: Evidence for the Emergence of Oxygenated Deep-Sea at 2.9-2.7 Ga. Resource Geology 52, 101-110.

Kato, Y., Yamaguchi, K.E., Ohmoto, H., 2006. Rare earth elements in Precambrian banded iron formations: Secular changes of Ce and Eu anomalies and evolution of atmospheric oxygen. In:Kesler, S.E., Ohmoto, H. (Eds.), Evolution of Early Earth's Atmosphere, Hydrosphere and Biosphere Constraints from Ore Deposits.

Geological Society of America Memoir 198, Geological Society of America. 269-289.

Konhauser, K.O., Pecoits, E., lalonde, S.V., Papineau, D., Nisbet, E.G., Barley, M.E., Arndt, N.T., Zahnle, K., Kamber, B.S., 2009. Oceanic nickel depletion and a methanogen famine before the Great Oxidation Event. Nature 458, 750-754.

Konhauser, K.O., Lalonde, S.V., Planavsky, N.J., Pecoits, E., Lyons, T.W., Mojzsis, S.J., Rouxel, O.J., Barley, M.E., Rosière, C., Fralick, P.W., Kump, L.R., Bekker, A., 2011. Aerobic bacterial pyrite oxidation and acid rock drainage during the Great Oxidation Event. Nature 478, 369-374.

Koschinsky, A., Halbach, P., 1995. Sequential leaching of marine ferromanganese precipitates: Genetic implications. Geochimica et Cosmochimica Acta 59, 5113-5132.

Kunzmann, M., Gutzmer, J., Beukes, N.J., Halverson, G.P., 2014. Depositional environment and lithostratigraphy of the Paleoproterozoic Mooidraai Formation, Kalahari Manganese Field, South Africa. South African Journal of Geology 117, 173-192.

Kirschvink, J.L., Gaidos, E.J., Bertani L.E., Beukes, N.J., Gutzmer, J., Maepa, L.N., Steinberger, R.E., 2000. Paleoproterozoic snowball Earth: Earth climatic and geochemical global change and its biological consequences. PNAS 97, 1400-1405.

Klein, C., Beukes, N.J., 1992. Time distribution, stratigraphy, and sedimentologic setting, and geochemistry of Precambrian iron-formations. In:Schopf, J.W., Klein, C. (Eds), The Proterozoic Biosphere: A multidisciplinary Approach. Cambridge University Press, New York, 139-147.

Klein, C., 2005. Some Precambrian banded iron-formations (BIFs) from around the world: their age, geologic setting, mineralogy, metamorphism, geochemistry, and origins. American Mineralogists 90, 1473–1499.

Kleyenstüber, A.S.E., 1984. The mineralogy of the manganese-bearing Hotazel Formation, of the Proterozoic Transvaal Sequence in Griqualand West, South Africa. Transactions of the Geological Society of South Africa 87, 257-272.

Kleyenstüber, A.S.E., 1985. A regional mineralogical study of the manganese-bearring Voëlwater Subgroup in the Northern Cape Province. [PhD thesis]. Rand Afrikaans University, Johannesburg, 328 pp.

Komiya, T., Yamamoto, S., Aoki, S., Sawaki, Y., Ishikawa, A., Tashiro, T., Koshida, K., Shimojo, M., Aoki, K., Collerson, K.D., 2015. Geology of the Eoarcehan, >3.95 Ga, Nulliak supracrustal rocks in the Saglek Block, northern Labrador, Canada: The oldest geological evidence for plate techtonics. Tectonophysics 662, 40-66.

Manceau, A., Drits, V.A., Silvester, E., Bartoli, C., Lanson, B., 1997. Structural mechanism of Co^{2+} oxidation by the phyllomanganate buserite. American Mineralogist, Volume 82, 1150-1175.

Manceau, A., Lanson, M., Geoffroy, N., 2007. Natural speciation of Ni, Zn, Ba, and As in ferromanganese coatings on quartz using X-ray fluorescence, absorption, and diffraction. Geochimical et Cosmochimica Acta 71, 95-128.

Metz, S., Trefry, J.H., 2000. Chemical and mineralogical influence on concentrations of trace metals in hydrothermal fluids. Geochimica et Cosmochimica Acta 64, 2267-2279.

Michard, A., Albarède, F., Michard, G., Minster, J.F., Charlou, J.L., 1983. Rare earth elements and uranium in high-temperature solutions from East Pacific Rise hydrothermal vent field (13◦ N). Nature 303, 795–797.

Nishizawa, M., Miyazaki, J., Makabe, A., Koba, K., Takai, K. 2014. Physiological and isotopic characteristics of nitrogen fixation by hyperthermophilic methanogens: Key insights into nitrogen anabolism of the microbial communities in Archean hydrothermal systems. Geochimica et Cosmochimica Acta 138, 117-135.

Olivarez, A.M., Owen, R.M., 1991. The europium anomaly of seawater: implications for fluvial versus hydrothermal REE inputs to the oceans. Chemical Geology 92, 317-328.

Partin, C.A., Lalonde, S.V., Planavsky, N.J., Bekker, A., Rouxel, O.J., Lyons, T.W., Konhauser, K.O., 2013. Uranium in iron formations and the rise of atmospheric oxygen. Chemical Geology 362, 82-90.

Pavlov, A.A., Kasting, J.F., 2002. Mass-independent fractionation of sulfur isotopes in Archean sediments: Strong evidence for anoxic Archean atmosphere. Astrobiology 2, 27-41.

Pearce, N.J.G., Perkins, W.T., Westgate, J.A., Gorton, M.P., Jackson, S.E., Neal, C.R., Chenery, S.P., 1997. A compilation of new and published major and trace element data for NIST SRM 610 and NIST SRM 612 Glass Reference Materials. Geostandards Newsletter 21, 115-144.

Planavsky, N.J., Asael, D., Hofmann, A., Reinhard, C.T., Lalonde, S.V., Knudsen, A., Wang, X., Ossa, F.O., Pecoits, E., Smith, A.J.B., Beukes, N.J., Bekker, A., Johnson, T.M., Konhauser, K.O., Lyons, T.W., Rouxel. O.J., 2014. Evidence for oxygenic photosynthesis half a billion years before the Great Oxidation Event. Nature Geoscience 7, 283-286.

Robbins, L.J., Lalonde, S.V., Saito, M.A., Planavsky, N.J., Mloszewska, A.M., Pecoits, E., Scott, C., Dupont, C.L., Kappler, A., Konhauser, K.O., Authigenic iron oxide proxies for marine zinc over geological time and implications for eukaryotic metallome evolution. Geobiology 2013, 295-306.

Roy, S., 1981. Manganese deposits: London, Academic Press.

Ruhlin, D.E., Owen, R.M., 1986. The rare earth element geochemistry of hydrothermal sediments from the East Pacific Rise: Examination of a seawater scavenging mechanism. Geochimica et Cosmochimica Acta 50, 393-400.

Saito, M.A, Sigman, D.M., Morel, F. M. M., 2003, The bioinorganic chemistry of the ancient ocean: the co-evolution of cyanobacterial metal requirements and biogeochemical cycles at the Archean-Proterozoic boundary?. Inorganica Chimica Acta 356, 308-318.

Schneiderhan, E.A., Gutzmer, J., Strauss, H., Mezger, K., Beukes, N.J., 2006. The chemostratigraphy of a Paleoproterozoic MnF-BIF succession – the Voëlwater Subgroup of the Transvaal Supergroup in Griqualand West, South Africa. South African Journal of Geology 109, 63-80.

Schopf, J.W., 1992. Palaeobiology in the Archean. In:Schopf, J.W., Klein, C. (Eds.), The Proterozoic Biosphere: A Multidisciplinary Study, Cambridge University Press, pp. 25–39.

Schröder, S., Bedorf, D., Beukes, N. J., Gutzmer, J., 2011. From BIF to red beds: sedimentology and sequence stratigraphy of the Paleoproterozoic Koegas Subgroup (South Africa). Sedimentary Geology 236, 25–44.

Shen, Y., Buick, R., Canfield, D.E., 2001. Isotopic evidence for microbial sulphate reduction in the early Archean era. Nature410, 77-81.

Sumner, D. Y., 1997. Carbonate precipitation and oxygen stratification in Late Archean seawater as deduced from facies and stratigraphy of the Gamohaan and Frisco Formations, Transvaal Supergroup, South Africa. American Journal of Science 297, 455-487.

Sumner, D. Y., Beukes, N. J., 2006. Sequence stratigraphic development of the Neoarchean Transvaal carbonate platform, Kaapvaal Craton, South Africa. South African Journal of Geology 109, 11-22.

Sumner, D.Y., Bowring, S.A., 1996. U–Pb geochronologic constraints on deposition of the Campbellrand Subgroup, Transvaal Supergroup, South Africa. Precambrian Research 79, 25–35.

Sverjensky, 1984. Europium redox equilibria in aqueous solution. Earth and Planetary Science Letters 67, 70-78.

Swanner, E.D., Planavsky, N.J., Lalonde, S.V., Robbins, L.J., Bekker, A., Rouxel, O.J., Saito, M. A., Kappler, A., Mojzsis, S.J., Konhauser, K.O., 2014. Cobalt and marine redox evolution. Earth and Planetary Science Letters 290, 253-263.

Tanaka, K., Tani, Y., Takahashi, Y., Tanimizu, M., Suzuki, Y., Kozai, N., Ohnuki, T., 2010. A specific Ce oxidation process during sorption of rare earth elements on biogenic Mn oxide produced by Acremonium sp strain KR21-2. Geochimica et Cosmochimica Acta 74, 5463–5477.

Taylor, S.R., McLennan, S.M., 1985. The continental crust: Its composition and evolution. Blackwell, Oxford, 312 pp.

Tsikos, H., Moore, J.M., 1997. Petrography and Geochemistry of the Paleoproterozoic Hotazel Iron-Formation, Kalahari Manganese Field, South Africa: Implications for Precambrian Manganese Metallogenesis. Economic Geology 92, 87-97.

Tsikos, H., Beukes, N.J., 2003. Deposition, Diagenesis, and Secondary Enrichment of Metals in the Paleoproterozoic Hotazel Iron Formation, Kalahari Manganese Field, South Africa. Economic Geology 98, 1449-1462.

Tsikos, H., Matthews, A., Erel, Y., Moore, J.M., 2010. Iron isotopes constrain biogeochemical redox cycling of iron and manganese in a Palaeoproterozoic stratified basin. Earth and Planetary Science Letters 298, 125-134.

Ueno Y., Yamada K., Yoshida N., Maruyama S., and Isozaki Y. 2006. Evidence from fluid inclusions for microbial methanogenesis in the early Archaean era. Nature 440, 516-519.

van der Westhuizen, W.A. and de Bruiyn, H. 2000. High temperature ash flow - wet sediment interaction in the Makwassie Formation, Ventersdorp Supergroup, South Africa. Precambrian Research 101, 341–351.

Yoshiya, K., Nishizawa, M., Sawaki, Y., Ueno, Y., Komiya, T., Yamada, K., Yoshida,

N., Hirata, T., Wada, H., Maruyama, S., 2012. *In situ* iron isotope analyses of pyrite and organic carbon isotope ratios in the Fortescue Group: Metabolic variations of a Late Archean ecosystem. Precambrian Research 212-213, 169-193.

Yoshiya, K., Sawaki, Y., Hirata, T., Maruyama, S., Komiya, T., 2015. In-situ iron isotope analysis of pyrites in ~ 3.7 Ga sedimentary protoliths from the Isua supracrustal belt, southern West Greenland. Chemical Geology 401, 126-139.

Viehmann, S., Bau, M., Smith, A.J.B., Beukes, N.J., Dantas, E.L., Bühn, B., 2015a. The reliability of ~2.9 Ga old Witwatersrand banded iron formations (South Africa) as archives for Mesoarchean seawter: Evidence from REE and Nd isotope systematics. Journal of African Earth Sciences 111, 322-334.

Viehmann, S., Bau, M., Hoffmann, J.E., Münker, C., 2015b. Geochemistry of the Krivoy Rog Banded Iron Fomration, Ukline, and the impact of peak episodes of increased global magmatic activity on the trace element composition of Precambrian seawater. Precambrian Research 270, 165-180.

Walker, J.C.G., Evolution of the Atmosphere.

Zerkle, A.L., House, C.H., Brantley, S.L., 2005. Biogeochemical signatures through time as inferred from whole microbial genomes. American Journal of Science 305, 467–502.

Figure captions

Figure 1. (A) Geographical distribution of the Transvaal Supergroup in South Africa (inset) and the geological map of the Transvaal Supergroup in the Griqualand West Basin including the locality of the Kalahari manganese field (KMF) (modified from Tsikos et al., 2010). (B) The detailed map of the Kalahari manganese field (KMF) showing the distributions of important structural features, localities of presently operating mine localities, and locality of the core sample GL-137 used in this study.

Figure 2. Simplified lithostratigraphic column of the core sample GL-137 recovered around the Gloria mine in the Kalahari manganese field (KMF). It covers from the Ongeluk Formation through the Hotazel Formation to the Mooidraai Formation, and shows that the BIFs are interlayered with manganese-rock layers at three stratigraphic horizons in the Hotazel Formation.

Figure 3. (A) The detailed lithostratigraphy of the lower part in the GL-137 analyzed in this study, and (B-G) photographs of representative lithofacies in Fig. 3A. (B) hematite-jasper BIF immediately above the Ongeluk Formation, (C) magnetite-quartz BIF, (D) hematite-jasper BIF bearing abundant carbonate minerals, (E) FeMn lutite, (F) manganese rock and (G) carbonate-rich rock.

Figure 4. Back scattered electron (BSE) images and X-ray distribution maps for Fe, Si, Mn, Ca, Mg and P of the analyzed samples. (A) The lowest parts of the BIF layer above the Ongeluk Formation corresponding to JPN5A-1, JPN5A-2 and JPN5A-3, showing the alterations of hematite- and quartz-rich bands scattered with apatite grains (scale: 500 μm). (B) The middle parts of the BIF layer corresponding to JPN6C, composed of alterations of magnetite and quartz with fibrous or layered minnesotite. Apatite grains are scattered about (scale: 500 μm). (C) The upper parts of the BIF layer, corresponding to JPN8C-1, composed of bands with hematite and carbonate minerals and bands with quartz (scale: 500 μm). (D) The FeMn lutite layer, corresponding to JPN10.5D-2, composed mainly of kutnohorite surrounded by hematite. Lizardite grains are scattered in

patches (scale: 50 μm). (E) The manganese-rock layer, corresponding to JPN13.5C-3, showing alterations of kutnohorite, braunite and calcite scattered with oval structures of ankerite and lizardite (scale: 500 μm) and (F) The BIF layer immediately above the upper FeMn lutite layer, corresponding to JPN19A, showing the alterations of bands of kutnorite and lizardite and bands of hematite (scale: 100 μm).

Abbreviations: Hem - hematite; Mag - magnetite; Qz - quartz; Ap - apatite; Py - pyrite; Mns - minnesotaite; Ank - ankerite; Kut - kutnohorite; Cal - calcite; Lz – lizardite.

Figure 5. Chemostratigraphic variations in whole-rock (A) Fe, (B) Mn, (C) Ca, (D) P contents, (E) Mn/Fe and (F) Ca/Fe ratios of the lower parts of the Hotazel Formation in the core GL-137.

Figure 6. Covariance diagrams of whole-rock REE+Y contents with (A)-(C) Fe contents, (D)-(F) P and (G)-(I) Mn contents.

Figure 7. PAAS-normalized REE + Y contents of (A) the hematite-jasper BIFs, (B) the magnetite-quartz BIFs, (C) the FeMn lutites, (D) the manganese rocks and (E) the carbonate rocks of the lower parts of the Hotazel Formation in the core GL-137. PAAS values were adopted from Taylor and Mclennan (1985).

Figure 8. Chemostratigraphic variations of (A) Negative Ce anomalies and (B) Positive Eu anomalies of the lower parts of the Hotazel Formation in drill core GL-137. Negative Ce anomaly and positive Eu anomaly are respectively defined as $Ce/Ce^* = Ce_{SN}/(2Pr_{SN}-Nd_{SN})$ and $Eu/Eu^* = Eu_{SN}/(0.67Sm_{SN}+0.33Tb_{SN})$.

Figure 9. Covariance diagrams of (A) V, (B) Co, (C) Ni, (D) Cu, (E) Zn and (F) U with Mn contents of the lower parts of the Hotazel Formation in the core GL-137.

Figure 10. Covariance diagrams of (A) V, (B) Co, (C) Ni, (D) Cu, (E) Zn and (F) U with Fe contents of the lower parts of the Hotazel Formation in the core GL-137.

Figure 11. Covariance diagrams of (A) V, (B) Co, (C) Ni, (D) Cu, (E) Zn and (F) U with Ca contents of the lower parts of the Hotazel Formation in the core GL-137.

Figure 12. Micro-scale distribution maps of (A) Fe, (B) Si, (C) Mg, (D) Al, (E) P, (F) Ca, (G) Ti, (H) Mn, (I) Co, (J) Ni, (K) Cu, (L) Zn, (M) Y, (N) Pr and (O) Yb in the lowermost BIFs immediately above the Ongeluk Formation, which correspond to JPN5A-1, JPN5A-2 and JPN5A-3.

Figure 13. Covariance diagrams of element contents of Fe contents with (A) Mg, (B) Al, (C) P, (D) Ca, (E) Mn, (F) Co, (G) Ni, (H) Cu, (I) Zn, (J) Y, (K) Pr and (L) Yb contents in a representative one of 50 continual transects constituting the distribution maps of Figure. 12.

Figure 14. Covariance diagrams of element contents of Al contents with (A) Mg, (B) P, (C) Ca, (D) Mn, (E) Co, (F) Ni, (G) Cu, (H) Zn, (I) Y, (J) Pr and (K) Yb contents in a representative one of 50 continual transects constituting the distribution maps of Figure. 12.

Figure 15. Covariance diagrams of element contents of Ca contents with (A) P, (B) Y, (C) Pr and (C) Yb contents in a representative one of 50 continual transects constituting the distribution maps of Figure. 12.

Figure 14. Covariance diagrams of element contents of Mn vs. Co in the BIFs of (A) the 2.74 Ga Carajas Iron Formation, (B) the 2.72 Ga Upper Deloro Formation, (C) the 2.32 Timeball Hill Formation, and (D) the 1.65 Ga Bushmanland Group compiled by Swanner et al. (2014).

Figure 15. Covariance diagrams of element contents of Mn vs. Co in the BIFs of (A) the 2.94 Ga West Rand Group, (B) the 2.43 Ga Caue Iron Formation compiled by Swanner et al. (2014).

Supplementary Table 1. Analytical data of a standard, BIR-1

	BIR-1 (n = 12)	RSD (%, 2sd)	Reference values*
%			
Al	8.1	0.1	8.2
Ti	0.572	0.4	0.575
Fe	7.88	0.3	7.90
Mg	5.79	0.4	5.85
Mn	0.135	0.2	0.136
Ca	9.51	0.2	9.51
Na	1.32	0.5	1.35
K	0.251	1.2	0.0249
P	0.0048	0.6	0.0046
ppm			
Li	3.35	12	3.32
Be	0.123	15	0.116
Sc	43.7	2.1	43.8
V	320	3.2	322
Co	52	2.4	53
Ni	170	4.1	175
Cu	115	2.3	113
Zn	68	1.9	65
Rb	0.198	3.7	0.195
Sr	107.0	1.2	106.4
Y	16.21	1.6	16.20
Zr	14.42	3.2	14.47
Nb	0.553	2.3	0.558
Ba	6.58	1.2	6.52
La	0.61	0.2	0.604
Ce	1.90	0.4	1.897
Pr	0.376	0.8	0.378
Nd	2.37	1.2	2.38
Sm	1.116	2.2	1.117
Eu	0.523	1.3	0.524
Gd	1.850	1.2	1.850
Tb	0.378	1.5	0.379
Dy	2.52	1.1	2.53
Ho	0.584	1.9	0.585
Er	1.734	0.6	1.734
Tm	0.25	0.5	0.25
Yb	1.648	0.4	1.649
Lu	0.245	1.9	0.247
Hf	0.563	3.2	0.562
Ta	0.004	4.3	0.0041
Th	0.00307	5.6	0.00302
U	0.0009	2.6	0.0010

*Reference values for Tm (Dulski, 2001) and others (Eggins et al., 1997)

Table.1 Whole-rock compositions for the BIFs, the Manganese rocks and the FeMn lutites in the lower parts of the GL-137

Sample No.	JPN5A-1	JPN5A-2	JPN5A-3	JPN5C-1	JPN5C-2	JPN6B-2	JPN6C	JPN6D-1	JPN6D-2	JPN8B-1	JPN8B-2	JPN8C-1	JPN9A-2	JPN9A-3	JPN9B-2	JPN10A-1	JPN10A-2	JPN10D-1	JPN10E-1	JPN10E-2
Rock Type	BIF	BIF	BIF	BIF	BIF	BIF	BIF	BIF	BIF	BIF	BIF	BIF	BIF	BIF	BIF	BIF	BIF	BIF	BIF	BIF
Distance (m)*	0.161	0.161	0.161	0.157	0.157	1.568	1.567	1.566	1.566	4.864	4.864	4.863	7.990	7.990	7.989	9.189	9.189	9.186	9.185	9.185
%																				
Al	0.0551	0.0499	0.0555	0.0715	0.0689	0.0761	0.151	0.104	0.0919	0.121	0.0951	0.0769	0.0532	0.0469	0.0526	0.00665	0.0585	0.0628	0.0716	0.0672
Ti	0.00245	0.00224	0.00221	0.00774	0.00768	0.00551	0.00565	0.00648	0.00593	0.00595	0.00497	0.00578	0.00290	0.00283	0.00404	0.00459	0.00532	0.00297	0.0038	0.00413
Fe	21.6	19.0	19.8	32.6	30.7	43.4	30.7	41.6	42.0	45.1	42.5	34.2	35.1	31.3	31.6	32.7	24.6	20.3	26.0	29.5
Mg	0.0422	0.0368	0.0417	0.0475	0.0478	1.35	2.31	1.76	1.67	0.622	0.482	0.427	4.47	4.99	6.37	3.79	3.47	4.36	3.95	3.44
Mn	0.00931	0.00696	0.0118	0.0118	0.0128	0.0816	0.0604	0.0728	0.0745	1.65	1.53	0.617	9.28	9.70	11.0	12.1	12.7	8.65	12.9	15.0
Ca	0.190	0.119	0.227	0.228	0.234	0.293	0.821	0.541	0.389	2.42	1.75	1.38	1.17	1.17	0.762	2.04	2.73	1.58	1.98	2.37
Na	0.00775	0.00764	0.00765	0.00799	0.00919	0.00410	0.00840	0.00639	0.00470	0.00450	0.00360	0.00459	0.00848	0.00865	0.0120	0.0106	0.0114	0.0109	0.0137	0.0101
K	0.0038	0.0042	0.0040	0.0037	0.0044	0.00185	0.00362	0.00235	0.00191	0.00442	0.00360	0.00267	0.00270	0.00231	0.00383	0.00384	0.00336	0.00348	0.00406	0.0031
P	0.019	0.018	0.018	0.051	0.049	0.055	0.220	0.12	0.082	0.032	0.025	0.048	0.020	0.019	0.023	0.0095	0.012	0.0068	0.014	0.015
ppm																				
Li	4.67	4.55	4.95	1.25	1.24	0.841	1.12	1	0.803	0.782	0.593	0.59	1.58	1.6	1.91	4.65	4.16	3.48	3.56	3.74
Be	1.1	0.97	1.1	1.4	1.5	5.1	2.3	2.4	3.2	1.4	1.1	1.8	1.4	1.4	1.3	1.6	1	0.78	1.1	1.1
Sc	0.539	0.435	0.47	0.912	0.808	1.21	1.91	1.62	1.39	1.44	1.03	0.93	0.972	0.877	1.11	1.16	1.16	0.98	1.26	0.988
V	2.63	2.53	2.40	6.33	5.98	7.05	7.75	7.44	7.46	7.06	5.36	5.39	4.47	3.84	4.35	2.18	1.93	1.32	1.93	1.73
Co	0.043	0.04	0.053	0.041	0.053	2.2	0.16	0.11	0.13	1.46	1.12	1.75	37	40	47.0	56	49	61	56.0	49.0
Ni	0.28	0.32	0.45	0.35	0.36	2.8	1.1	0.93	0.96	1.6	1.2	2.2	2.9	3.3	4.1	4.4	3.8	5.4	4.8	4.2
Cu	0.903	1.06	1.01	0.731	0.737	5.85	5.52	4.17	3.84	0.633	0.46	1.06	0.406	0.52	0.63	0.13	0.103	0.0677	0.0882	0.121
Zn	1.5	1.0	1.2	3.0	2.3	13	24	20	16	3.0	2.4	3.8	15	17	22	15	13	17	15	13
Rb	0.32	0.296	0.234	0.337	0.407	0.127	0.18	0.171	0.128	0.379	0.327	0.284	0.29	0.267	0.33	0.502	0.408	0.409	0.459	0.419
Sr	3.781	3.53	3.81	6.614	6.363	3.9	12.13	6.656	5.066	6.532	5.0	5.959	9.694	8.747	10.05	13.74	13.75	9.8	12.95	13.38
Y	6.14	5.79	6.07	12.9	12.1	11.3	27.7	18.3	14.4	12.5	9.56	12.8	9.76	9.26	10.5	8.97	7.72	6.21	8.65	8.38
Zr	2.01	2.02	1.95	4.44	3.9	5.35	5.19	5.55	5.64	6.08	4.69	5.42	2.4	2.55	3.1	3.97	4.97	2.5	4.19	3.97
Nb	0.137	0.147	0.131	0.583	0.538	0.336	0.378	0.415	0.38	0.497	0.373	0.38	0.279	0.261	0.306	0.36	0.416	0.252	0.34	0.357
Ba	4.014	4.002	3.911	5.074	5.503	3.032	6.785	6.61	5.698	18.89	15.12	14.31	13.42	12.48	14.15	43.69	38.35	29.04	36.08	35.21
La	3.54	3.209	3.29	7.78	7.33	3.01	9.34	6.15	4.79	3.919	3.13	4.05	2.85	2.624	3.04	3.32	2.81	2.17	3.06	3.02
Ce	4.37	4.006	4.06	9.48	8.98	5.10	15.23	10.70	8.40	5.15	4.04	5.39	3.12	2.878	3.30	3.72	3.08	2.45	3.55	3.410
Pr	0.528	0.4687	0.483	1.111	1.033	0.679	1.96	1.398	1.109	0.6684	0.545	0.684	0.417	0.375	0.436	0.499	0.417	0.311	0.471	0.455
Nd	2.03	1.699	1.79	4.40	4.11	3.01	8.60	6.23	4.97	2.699	2.16	2.89	1.67	1.637	1.80	2.02	1.52	1.29	1.80	1.81
Sm	0.390	0.333	0.341	0.771	0.701	0.679	1.825	1.334	1.043	0.512	0.396	0.556	0.343	0.339	0.342	0.376	0.293	0.261	0.381	0.342
Eu	0.188	0.161	0.174	0.362	0.347	0.188	0.532	0.362	0.283	0.13	0.102	0.140	0.105	0.100	0.104	0.093	0.083	0.058	0.090	0.089
Gd	0.530	0.448	0.484	1.090	0.994	0.966	2.550	1.790	1.410	0.735	0.590	0.752	0.496	0.464	0.522	0.495	0.446	0.343	0.495	0.471
Tb	0.0849	0.074	0.0743	0.168	0.155	0.158	0.402	0.308	0.229	0.114	0.0943	0.125	0.0841	0.0791	0.0903	0.0889	0.0701	0.0626	0.0853	0.0869
Dy	0.508	0.517	0.497	1.130	0.979	1.110	2.650	1.880	1.590	0.848	0.699	0.893	0.628	0.588	0.677	0.674	0.567	0.469	0.633	0.565
Ho	0.138	0.118	0.123	0.267	0.251	0.260	0.646	0.454	0.355	0.230	0.188	0.242	0.179	0.167	0.190	0.188	0.153	0.127	0.178	0.155
Er	0.386	0.363	0.382	0.765	0.747	0.879	1.850	1.340	1.070	0.813	0.616	0.745	0.630	0.591	0.648	0.624	0.494	0.418	0.582	0.555
Tm	0.0517	0.0476	0.0488	0.111	0.102	0.133	0.239	0.187	0.152	0.120	0.0915	0.110	0.100	0.0871	0.105	0.0967	0.0872	0.0691	0.0899	0.0818
Yb	0.318	0.307	0.291	0.671	0.665	0.885	1.390	1.190	0.983	0.831	0.640	0.680	0.656	0.610	0.755	0.676	0.580	0.466	0.615	0.570
Lu	0.0507	0.0531	0.0436	0.0989	0.1040	0.1420	0.2090	0.1690	0.1590	0.1320	0.0990	0.1170	0.1050	0.1050	0.1280	0.1130	0.0989	0.0758	0.1080	0.0897
Hf	0.0277	0.02	0.0279	0.0743	0.0607	0.0803	0.0709	0.0761	0.0694	0.0616	0.0546	0.0658	0.0283	0.0317	0.0384	0.0498	0.0658	0.0324	0.0458	0.0495
Ta	0.0106	0.0081	0.0079	0.0151	0.0029	0.0074	0.0141	0.0166	0.0182	0.0228	0.0098	0.0140	0.0137	0.0100	0.0142	0.0263	0.0285	0.0160	0.0154	0.0249
Th	0.146	0.144	0.143	0.409	0.397	0.243	0.246	0.292	0.296	0.428	0.343	0.348	0.241	0.254	0.324	0.428	0.407	0.228	0.315	0.335
U	0.0368	0.0337	0.0329	0.0854	0.0774	0.0503	0.0572	0.0651	0.0642	0.0905	0.0708	0.0605	0.0623	0.0513	0.0611	0.0876	0.0604	0.0549	0.0793	0.0630
Y/Ho	44.5	49.1	49.3	48.3	48.2	43.5	42.9	40.3	40.6	54.3	50.9	52.9	54.5	55.4	55.3	47.7	50.5	48.9	48.6	54.1
La/La*	1.82	1.63	1.69	2.06	2.12	1.93	2.01	1.98	2.00	1.82	1.69	2.15	2.08	2.86	2.32	2.09	1.62	2.33	1.74	1.98
Ce/Ce*	0.99	0.96	0.96	1.06	1.08	1.09	1.11	1.12	1.12	0.98	0.92	1.06	0.94	1.09	0.99	0.95	0.83	1.03	0.89	0.93
Eu/Eu*	2.06	2.04	2.17	2.00	2.10	1.15	1.24	1.13	1.16	1.07	1.06	1.06	1.24	1.22	1.19	1.02	1.17	0.90	0.99	1.04

*Distance from the Ongeluk Formation

La/La*, Ce/Ce* and Eu/Eu*are defined by $[La/(3Pr\text{-}2/Nd)]_{PAAS}$, $[Ce/(2Pr\text{-}Nd)]_{PAAS}$ and $[Eu/(0.67Sm+0.33Tb)]_{PAAS}$, respectively.

Table.1 continued

Sample No.	JPN10.5A-1	JPN10.5A-2	JPN10.5B-1	JPN10.5B-2	JPN10.5C	JPN10.5D-2	JPN11.5A	JPN13.5A-2	JPN13.5B-1	JPN13.5B-2	JPN13.5C-3	JPN16A	JPN19A
Rock Type	FeMn lutite	FeMn lutite	FeMn lutite	FeMn lutite	FeMn lutite	FeMn lutite	Mn rock	Mn rock	Mn rock	Mn rock	Mn rock	FeMn lutite	BIF
Distance (m)*	9.927	9.927	9.926	9.926	9.925	9.924	15.758	19.019	19.018	19.018	19.017	22.215	23.834
%													
Al	0.0824	0.0805	0.0775	0.0796	0.0786	0.0754	0.151	0.152	0.132	0.135	0.126	0.1010	0.111
Ti	0.00424	0.00418	0.00414	0.00410	0.00488	0.00401	0.00555	0.00624	0.00653	0.00639	0.0122	0.00437	0.0037
Fe	11.6	11.3	12.8	13.5	17.4	12.1	3.66	5.31	5.81	5.56	4.95	8.82	11.6
Mg	3.49	3.46	4.09	4.32	3.04	3.64	2.62	1.58	1.44	1.39	1.47	3.22	3.03
Mn	18.7	18.5	20.2	20.6	15.9	18.0	40.3	34.6	34.0	33.1	32.2	13.8	11.3
Ca	8.68	8.00	8.35	8.39	6.10	7.65	8.05	10.7	11.2	10.6	12.0	9.4	11.1
Na	0.0218	0.0213	0.0201	0.0220	0.0182	0.0207	0.0133	0.0142	0.0135	0.0127	0.0134	0.0187	0.0099
K	0.00499	0.00489	0.00498	0.00528	0.00446	0.00476	0.0106	0.0176	0.0151	0.0148	0.0122	0.0096	0.00277
P	0.016	0.015	0.015	0.016	0.014	0.015	0.0073	0.012	0.012	0.012	0.011	0.012	0.0093
ppm													
Li	10.3	10.2	10.6	11.6	10.40	10.60	9.26	9.49	8.84	8.97	9.23	3.04	1.91
Be	0.65	0.64	0.82	0.92	0.97	0.97	0.48	0.67	0.69	0.7	0.71	0.81	0.79
Sc	0.963	0.913	1.01	1.00	1.06	0.91	0.927	1.07	1.15	1.09	0.966	1.09	1.12
V	8.89	8.77	8.15	8.31	35.0	14.4	1.76	1.92	2.02	2.06	2.11	4.58	2.89
Co	56	57	60	64	44.00	53.00	41	61	56	59	53	76	36
Ni	6.6	6.6	6.6	6.8	6.1	6	11	11	11	11	11	9.6	9.8
Cu	0.118	0.0723	0.0709	0.0234	0.04	0.04	1.17	1.02	1.15	1.37	1.8	0.244	0.107
Zn	15	15	16	17	13	15	33	27	30	28	30	12	10
Rb	0.50	0.485	0.485	0.524	0.50	0.44	1.09	1.43	1.16	1.2	1.02	2.11	0.168
Sr	57.3	56.2	61.86	64.24	50.43	58.63	82.57	174.9	175.6	168.8	184.5	229.6	72.46
Y	8.36	8.15	9.41	9.92	7.37	8.66	6.78	8.75	9.01	8.97	8.76	8.61	8.63
Zr	4.16	3.92	4.3	4.14	4.61	3.89	4.07	4.88	5.34	5.28	4.64	4.66	4.13
Nb	0.363	0.403	0.289	0.3	0.34	0.28	0.369	0.496	0.494	0.495	0.448	0.322	0.267
Ba	55.89	54.03	62.67	65.23	61.12	59.45	399.1	84.36	85.69	82.49	88.68	132.5	51.88
La	4.33	4.11	4.73	4.86	3.85	4.34	3.109	5.04	5.015	4.948	4.822	3.05	4.503
Ce	4.84	4.62	5.32	5.54	4.35	4.89	3.839	4.793	4.752	4.671	4.334	2.221	4.697
Pr	0.610	0.576	0.645	0.676	0.56	0.60	0.6225	0.8443	0.8167	0.8143	0.7898	0.4375	0.6242
Nd	2.45	2.37	2.63	2.67	2.25	2.42	2.625	3.385	3.286	3.281	3.24	1.781	2.546
Sm	0.439	0.419	0.500	0.512	0.395	0.447	0.511	0.617	0.573	0.581	0.554	0.344	0.458
Eu	0.125	0.118	0.135	0.145	0.111	0.130	0.1585	0.1641	0.1585	0.1619	0.1558	0.0871	0.1574
Gd	0.597	0.563	0.671	0.715	0.555	0.587	0.664	0.794	0.747	0.735	0.712	0.502	0.6261
Tb	0.0930	0.0928	0.106	0.112	0.0876	0.100	0.109	0.121	0.126	0.124	0.111	0.0922	0.096
Dy	0.646	0.616	0.716	0.727	0.574	0.658	0.692	0.8	0.795	0.816	0.76	0.653	0.689
Ho	0.165	0.161	0.184	0.192	0.148	0.172	0.172	0.193	0.198	0.198	0.187	0.181	0.176
Er	0.515	0.522	0.562	0.602	0.453	0.534	0.543	0.586	0.606	0.613	0.579	0.583	0.563
Tm	0.0823	0.0751	0.0853	0.0903	0.0667	0.0802	0.0799	0.087	0.0934	0.0903	0.0851	0.0847	0.0821
Yb	0.517	0.474	0.555	0.577	0.440	0.537	0.501	0.543	0.589	0.582	0.538	0.561	0.521
Lu	0.0825	0.0821	0.0928	0.0934	0.0704	0.0853	0.0784	0.0846	0.0927	0.0914	0.0805	0.092	0.084
Hf	0.0596	0.0554	0.0537	0.0574	0.0647	0.0565	0.0845	0.0809	0.0746	0.0768	0.0753	0.058	0.0658
Ta	0.0241	0.0241	0.0234	0.0213	0.0233	0.0214	0.0298	0.0405	0.0387	0.0406	0.034	0.024	0.0229
Th	0.335	0.321	0.339	0.347	0.370	0.327	0.331	0.565	0.581	0.56	0.478	0.341	0.338
U	0.0861	0.0850	0.0718	0.0704	0.260	0.113	0.116	0.157	0.156	0.158	0.142	0.144	0.183
Y/Ho	50.7	50.6	51.1	51.7	49.8	50.3	39.4	45.3	45.5	45.3	46.8	47.6	49.0
La/La*	2.16	2.34	2.36	2.09	2.05	2.31	1.79	1.82	1.89	1.88	1.99	2.22	2.31
Ce/Ce*	1.00	1.04	1.06	1.01	0.96	1.05	0.83	0.71	0.73	0.73	0.71	0.65	0.97
Eu/Eu*	1.23	1.19	1.16	1.20	1.19	1.23	1.34	1.19	1.18	1.20	1.24	0.98	1.49

*Distance from the Ongeluk Formation

La/La*, Ce/Ce* and Eu/Eu*are defined by $[La/(3Pr-2/Nd)]_{PAAS}$, $[Ce/(2Pr-Nd)]_{PAAS}$ and $[Eu/(0.67Sm+0.33Tb)]_{PAAS}$, respectively.

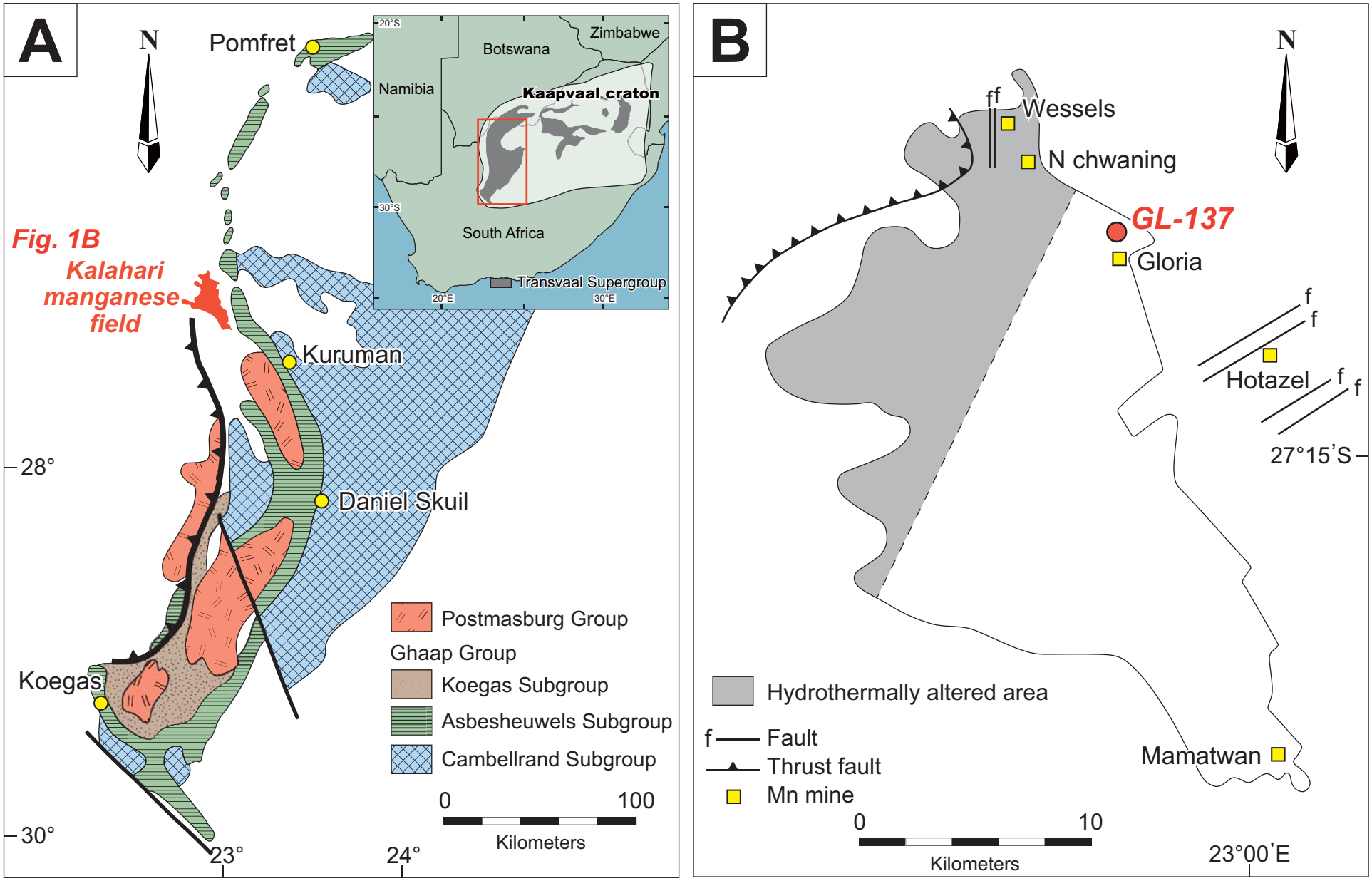
A
N
Pomfret
20°S
Botswana
Zimbabwe
Namibia
Kaapvaal craton
30°S
South Africa
Transvaal Supergroup
20°E
30°E
Fig. 1B
Kalahari manganese field
Kuruman
Daniel Skuil
28°
Koegas
30°
23°
24°
Postmasburg Group
Ghaap Group
Koegas Subgroup
Asbesheuwels Subgroup
Cambellrand Subgroup
0
100
Kilometers
B
N
ff
Wessels
N chwaning
GL-137
Gloria
f
f
Hotazel
f
f
27°15'S
Hydrothermally altered area
f
Fault
Thrust fault
Mn mine
0
10
Kilometers
Mamatwan
23°00'E

Figure.1

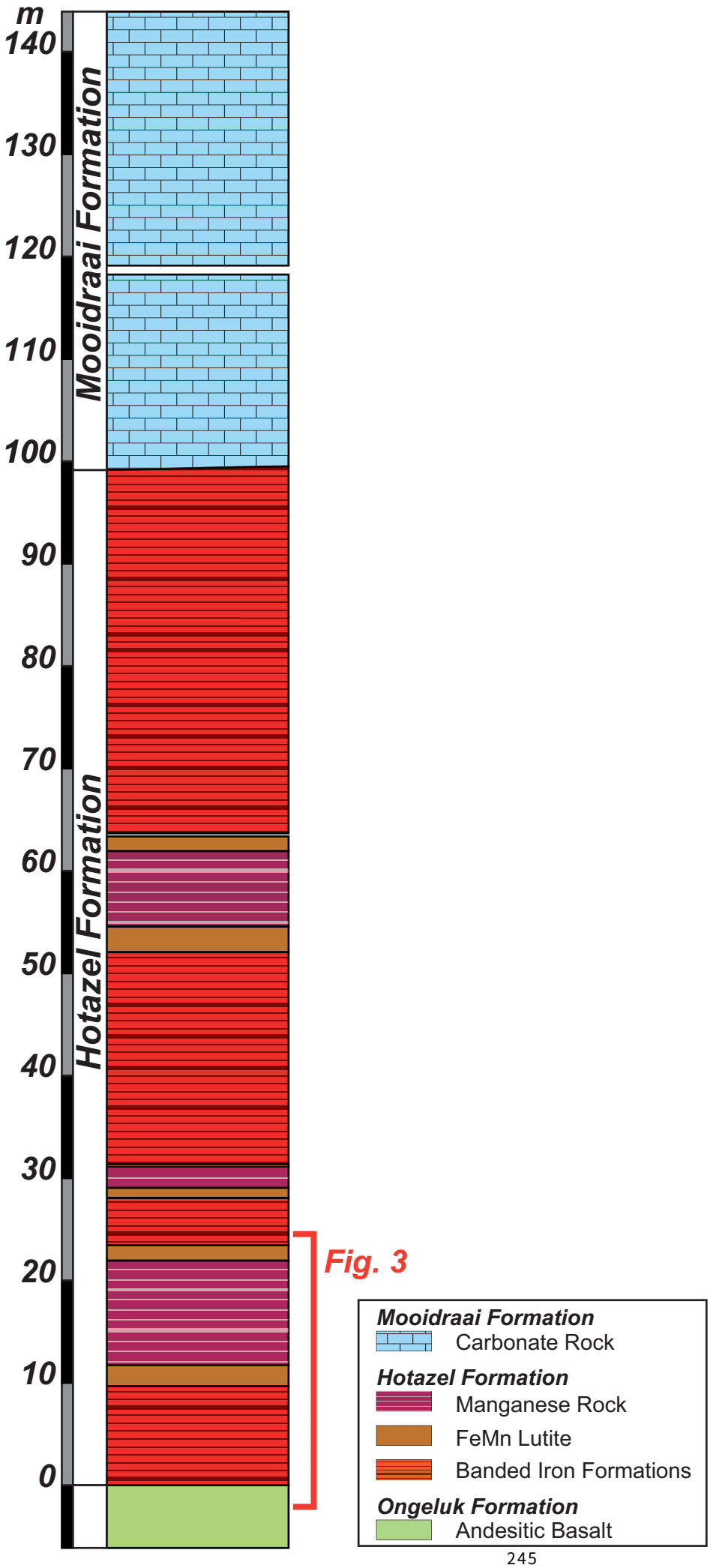
m
140
130
120
110
100
90
80
70
60
50
40
30
20
10
0
Mooidraai Formation
Hotazel Formation
Fig. 3
Mooidraai Formation
Carbonate Rock
Hotazel Formation
Manganese Rock
FeMn Lutite
Banded Iron Formations
Ongeluk Formation
Andesitic Basalt

Figure. 2

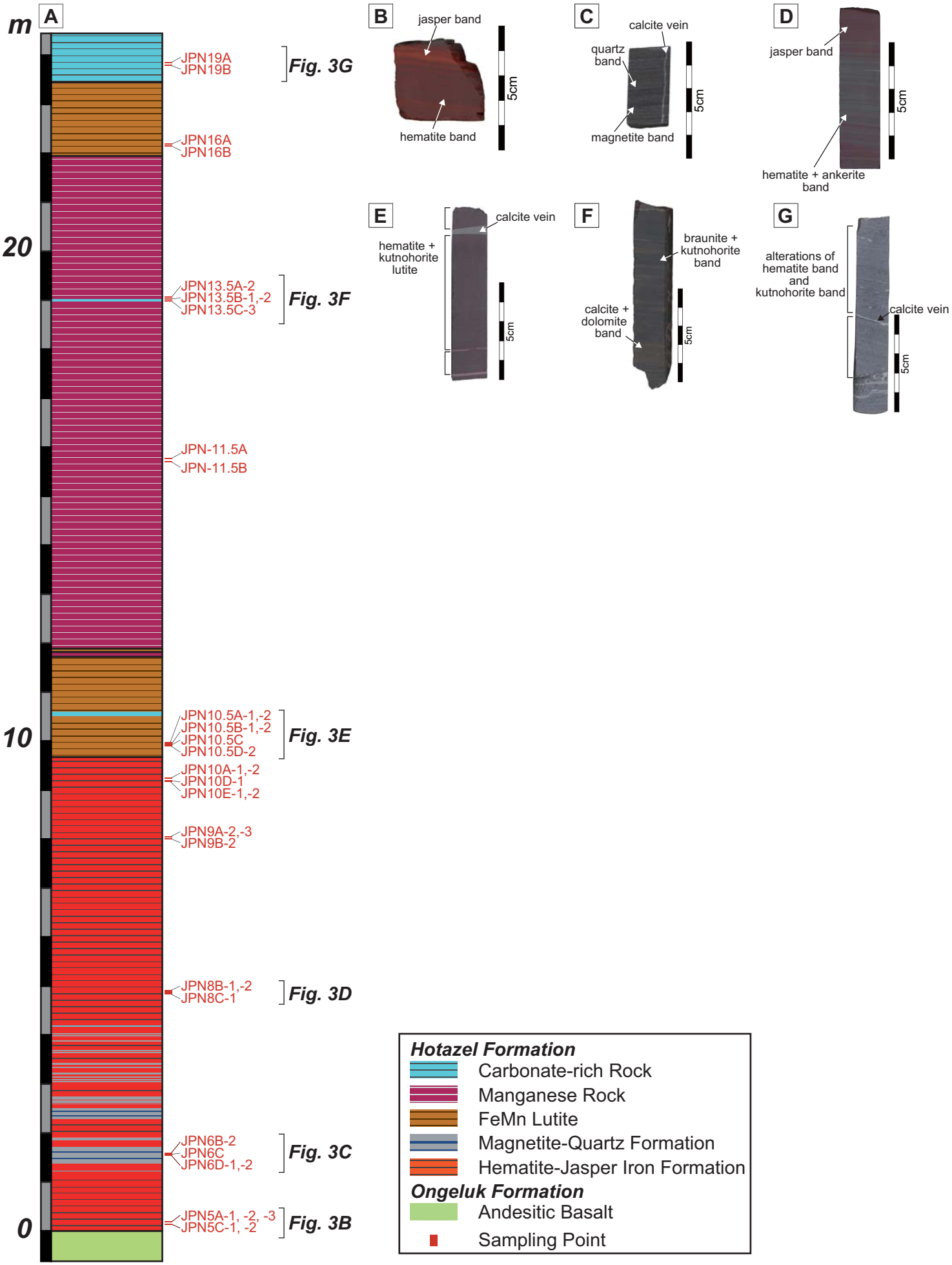
m
A
20
10
0
JPN19A
JPN19B
JPN16A
JPN16B
JPN13.5A-2
JPN13.5B-1,-2
JPN13.5C-3
JPN-11.5A
JPN-11.5B
JPN10.5A-1,-2
JPN10.5B-1,-2
JPN10.5C
JPN10.5D-2
JPN10A-1,-2
JPN10D-1
JPN10E-1,-2
JPN9A-2,-3
JPN9B-2
JPN8B-1,-2
JPN8C-1
JPN6B-2
JPN6C
JPN6D-1,-2
JPN5A-1, -2, -3
JPN5C-1, -2
Fig. 3G
Fig. 3F
Fig. 3E
Fig. 3D
Fig. 3C
Fig. 3B
B
jasper band
hematite band
5cm
C
calcite vein
quartz band
magnetite band
5cm
D
jasper band
hematite + ankerite band
5cm
E
calcite vein
hematite + kutnohorite lutite
5cm
F
braunite + kutnohorite band
calcite + dolomite band
5cm
G
alterations of hematite band and kutnohorite band
calcite vein
5cm
Hotazel Formation
Carbonate-rich Rock
Manganese Rock
FeMn Lutite
Magnetite-Quartz Formation
Hematite-Jasper Iron Formation
Ongeluk Formation
Andesitic Basalt
Sampling Point

Figure. 3

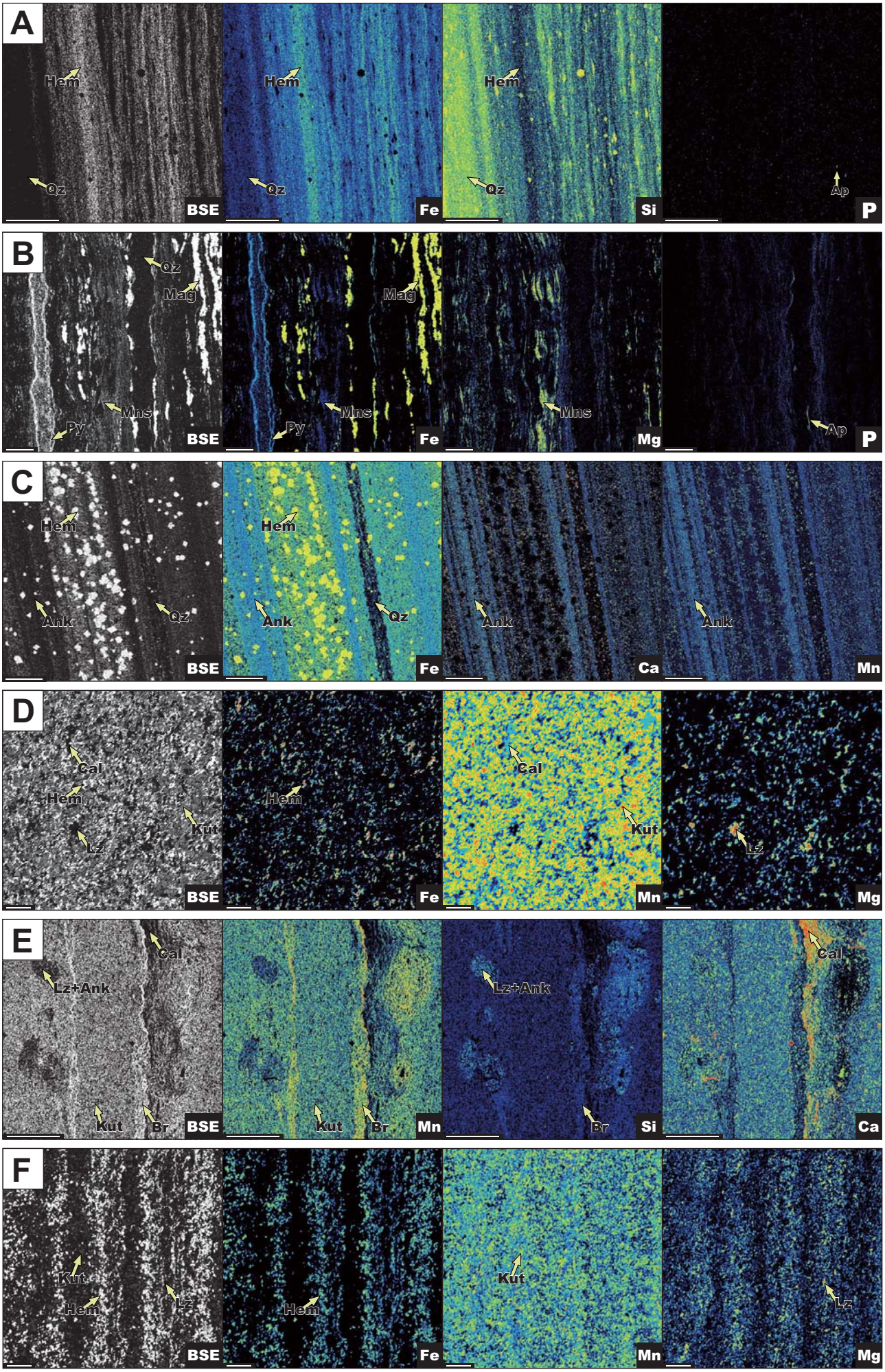
A
Hem
Qz
BSE
Hem
Qz
Fe
Hem
Qz
Si
Ap
P
B
Qz
Mag
Mns
Py
BSE
Mag
Mns
Py
Fe
Mns
Mg
Ap
P
C
Hem
Ank
Qz
BSE
Hem
Ank
Qz
Fe
Ank
Ca
Ank
Mn
D
Cal
Hem
Kut
Lz
BSE
Hem
Fe
Cal
Kut
Mn
Lz
Mg
E
Cal
Lz+Ank
Kut
Br
BSE
Kut
Br
Mn
Lz+Ank
Br
Si
Cal
Ca
F
Kut
Hem
Lz
BSE
Hem
Fe
Kut
Mn
Lz
Mg

Figure. 4

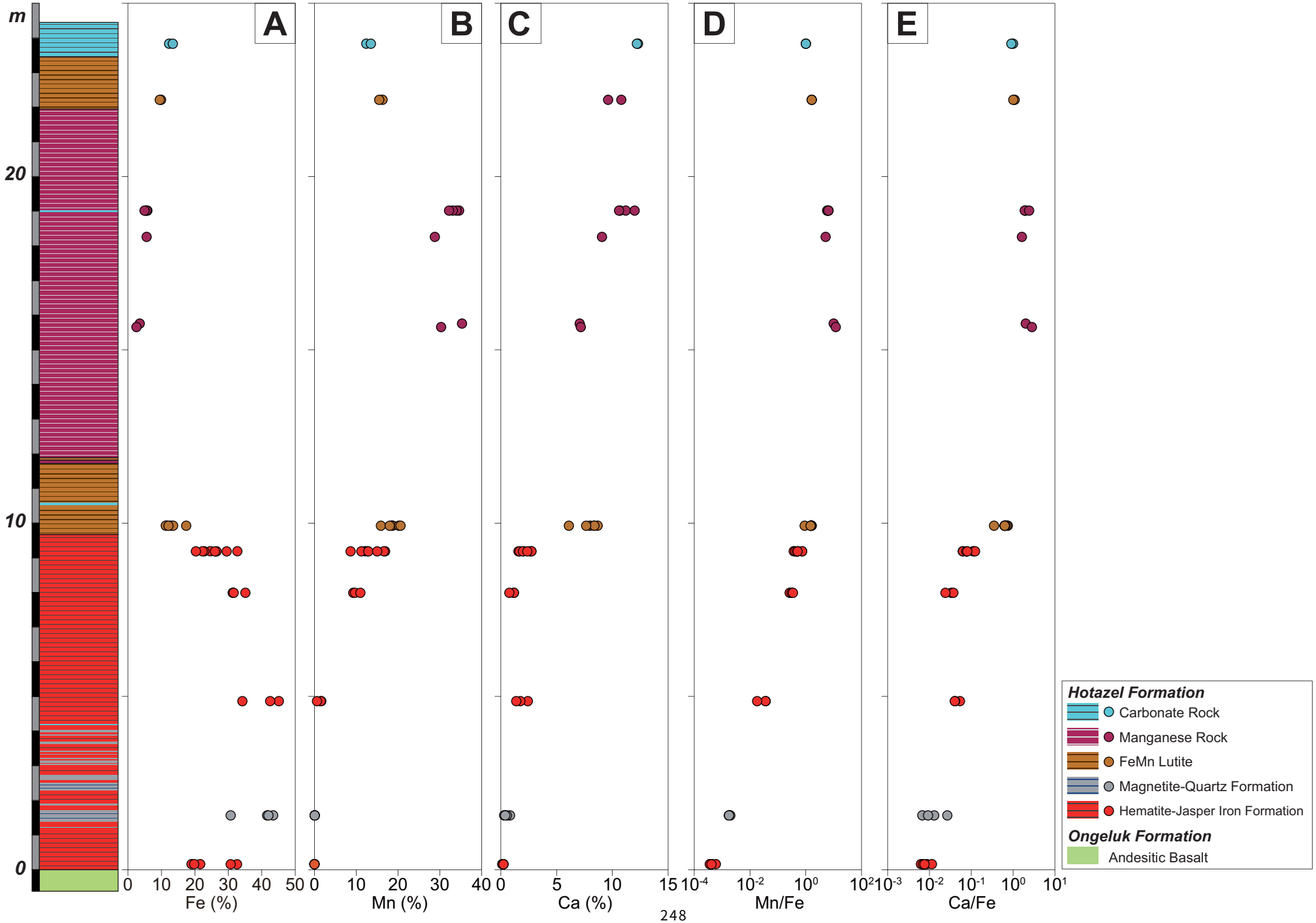
m
20
10
0
A
B
C
D
E
0 10 20 30 40 50
Fe (%)
0 10 20 30 40
Mn (%)
0 5 10 15
Ca (%)
10-4 10-2 100 102
Mn/Fe
10-3 10-2 10-1 100 101
Ca/Fe
Hotazel Formation
Carbonate Rock
Manganese Rock
FeMn Lutite
Magnetite-Quartz Formation
Hematite-Jasper Iron Formation
Ongeluk Formation
Andesitic Basalt

Figure.5

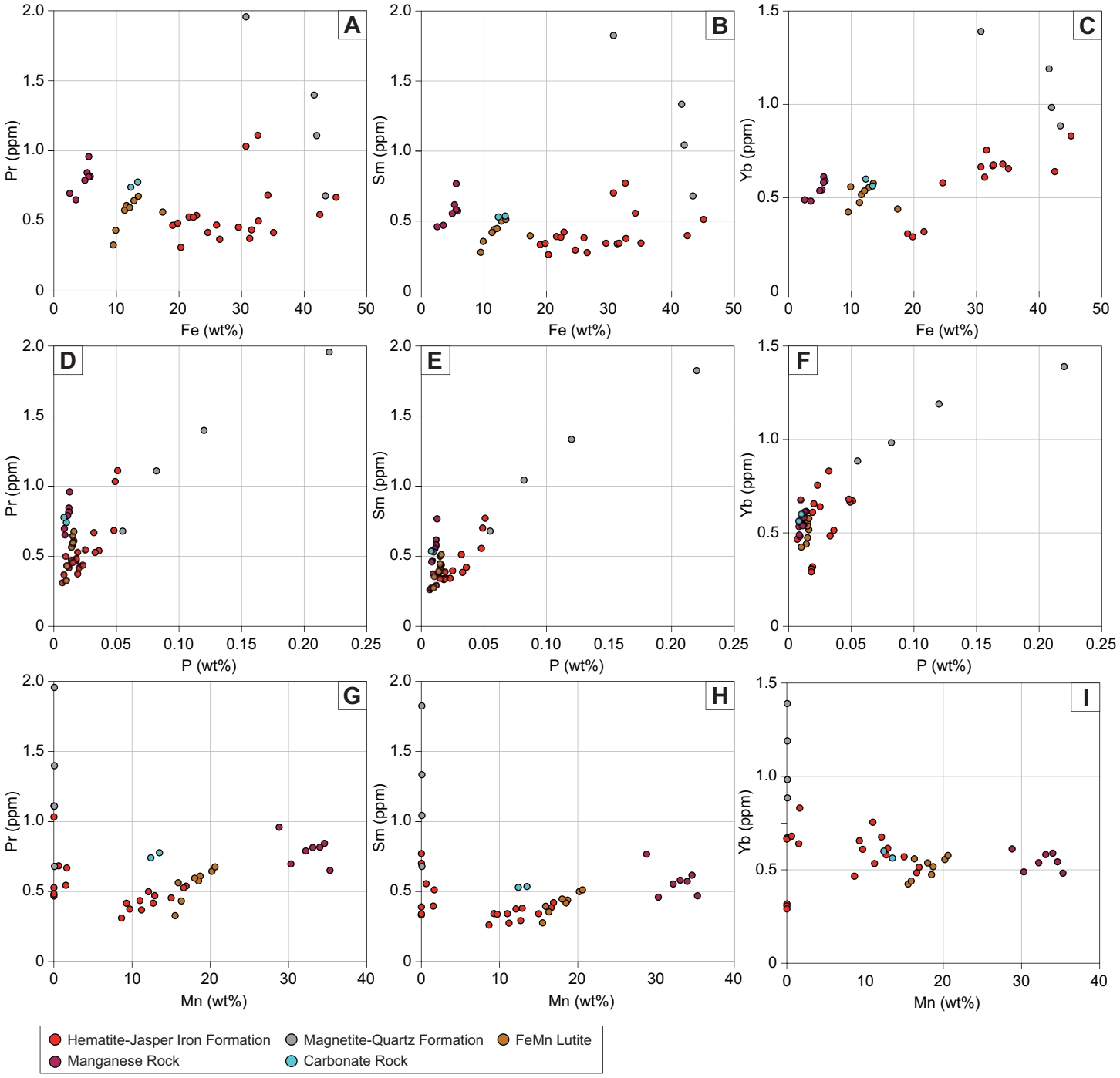
A
B
C
D
E
F
G
H
I
Pr (ppm)
Sm (ppm)
Yb (ppm)
Fe (wt%)
P (wt%)
Mn (wt%)
Hematite-Jasper Iron Formation
Magnetite-Quartz Formation
FeMn Lutite
Manganese Rock
Carbonate Rock

Figure. 6

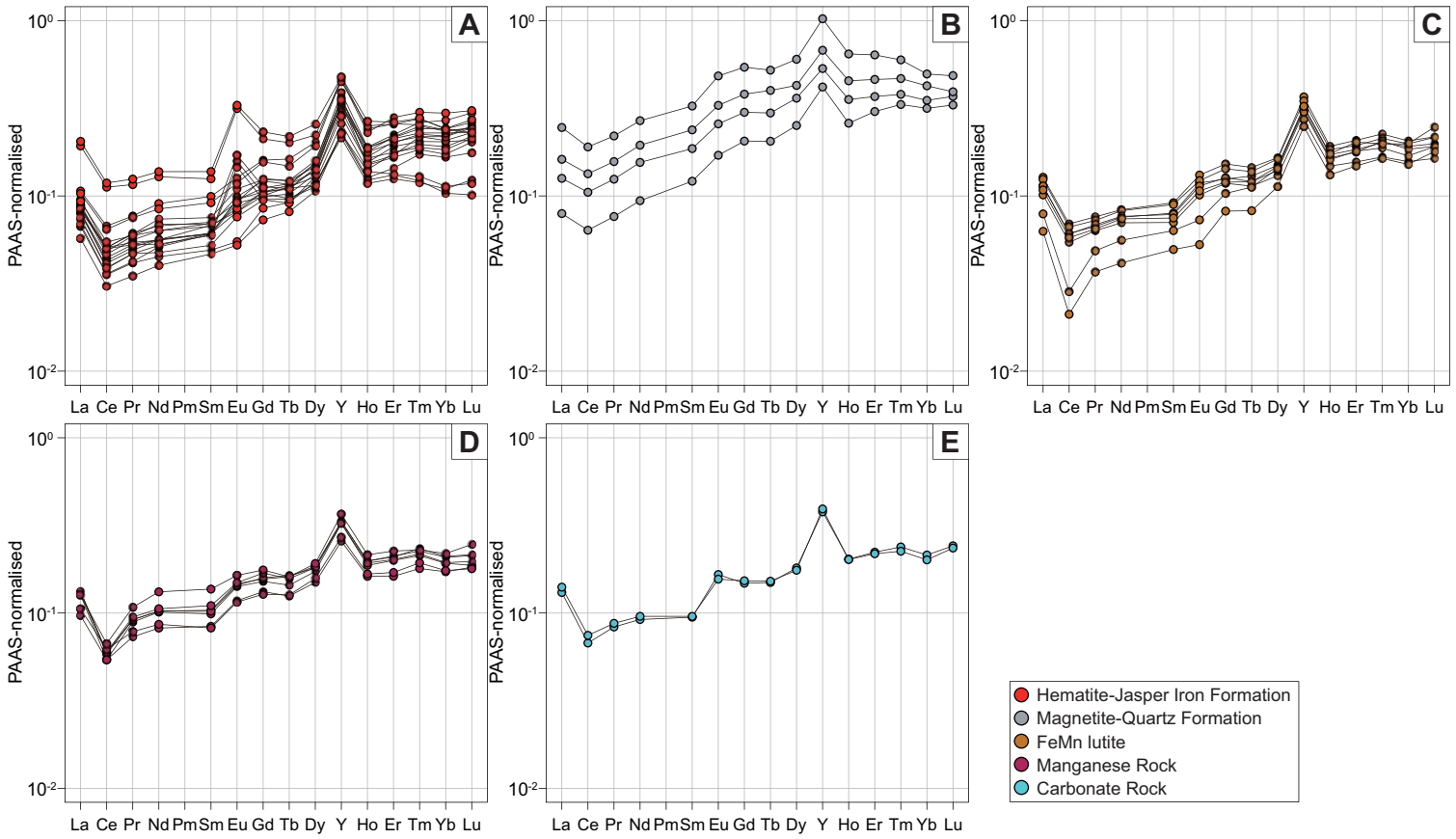
A
B
C
D
E
PAAS-normalised
10^0
10^{-1}
10^{-2}
La Ce Pr Nd Pm Sm Eu Gd Tb Dy Y Ho Er Tm Yb Lu
Hematite-Jasper Iron Formation
Magnetite-Quartz Formation
FeMn lutite
Manganese Rock
Carbonate Rock

Figure. 7

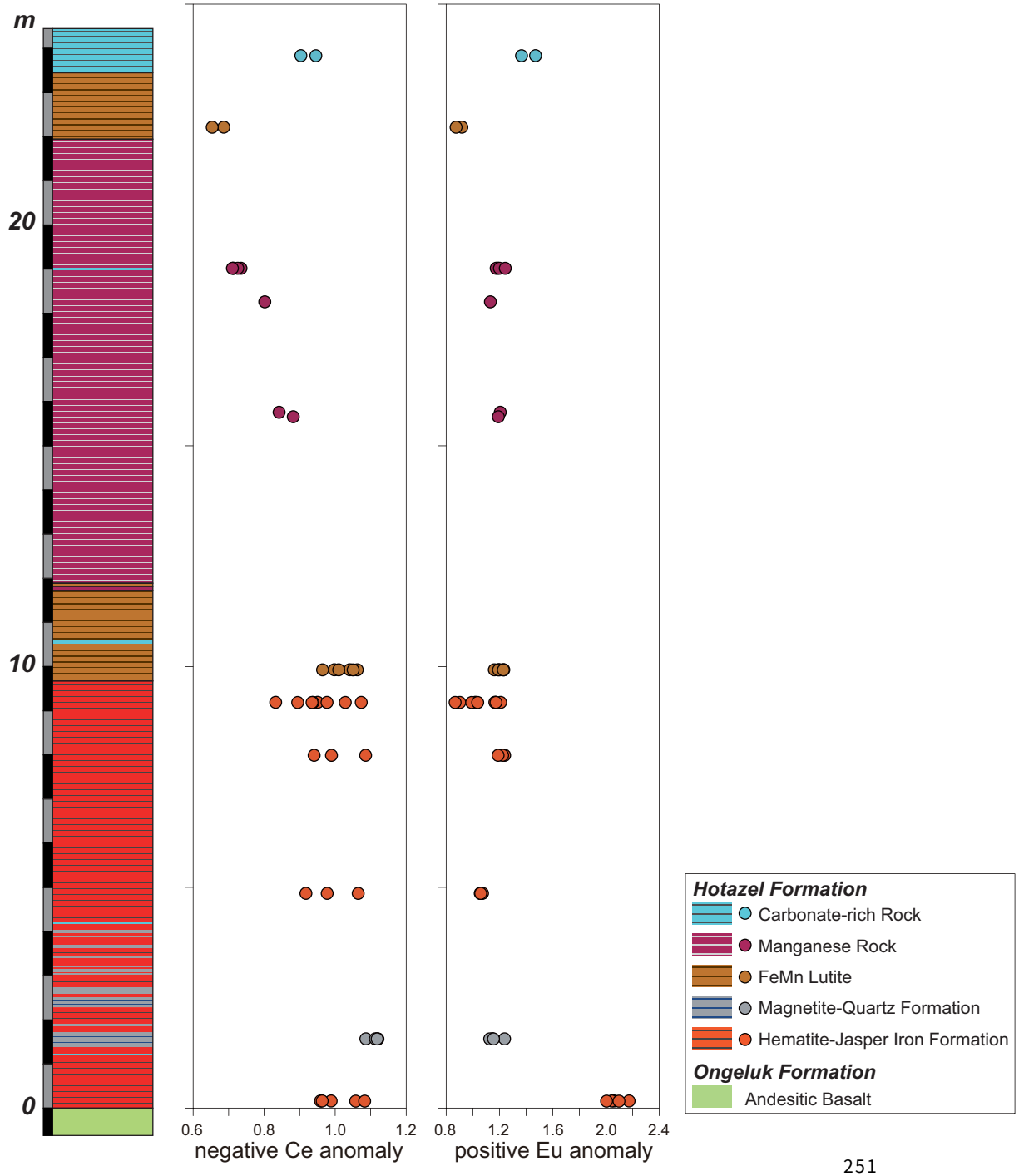
m
20
10
0
0.6
0.8
1.0
1.2
negative Ce anomaly
0.8
1.2
1.6
2.0
2.4
positive Eu anomaly
Hotazel Formation
Carbonate-rich Rock
Manganese Rock
FeMn Lutite
Magnetite-Quartz Formation
Hematite-Jasper Iron Formation
Ongeluk Formation
Andesitic Basalt

Figure.8

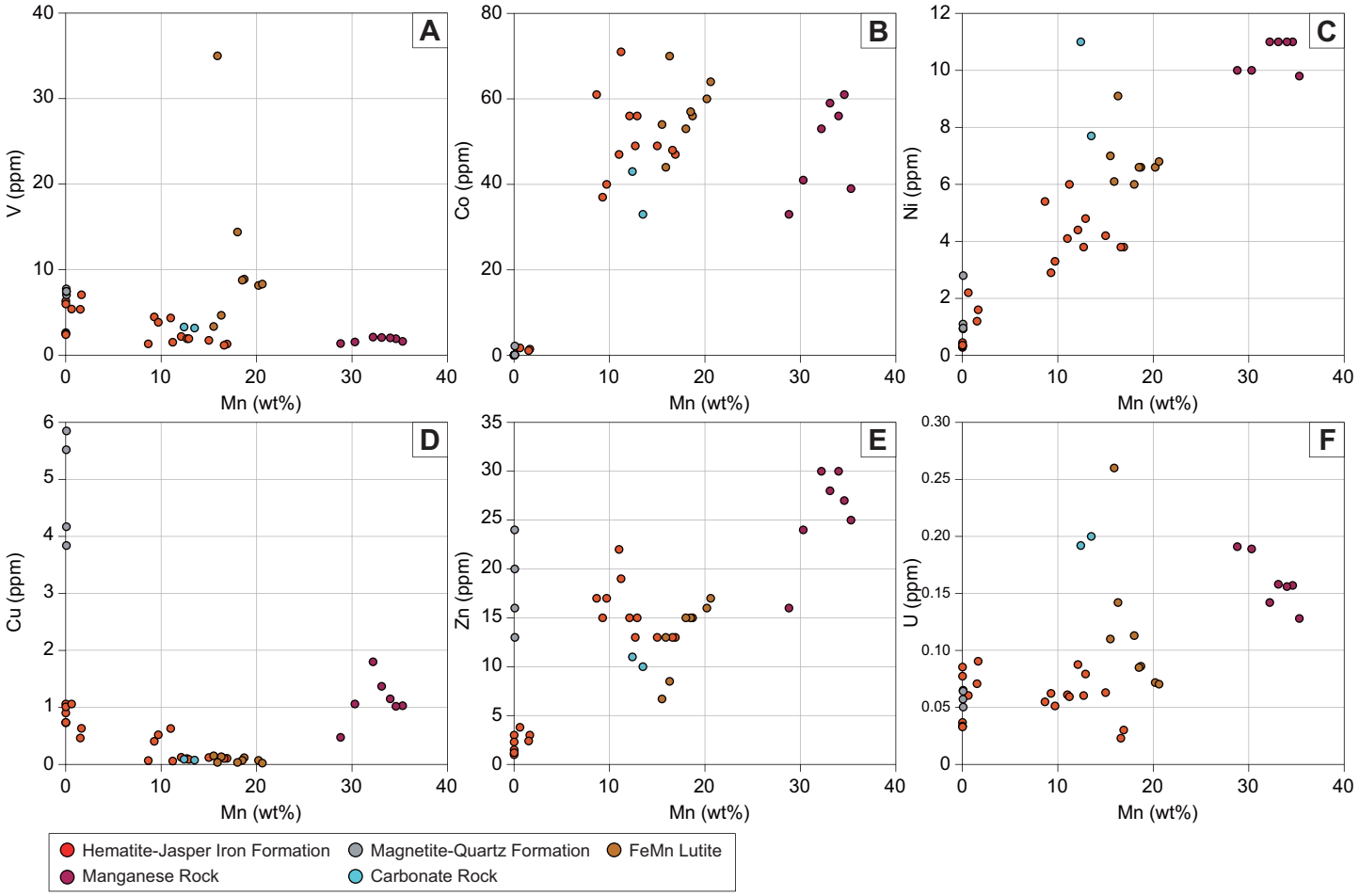
A
V (ppm)
Mn (wt%)
B
Co (ppm)
Mn (wt%)
C
Ni (ppm)
Mn (wt%)
D
Cu (ppm)
Mn (wt%)
E
Zn (ppm)
Mn (wt%)
F
U (ppm)
Mn (wt%)
Hematite-Jasper Iron Formation
Magnetite-Quartz Formation
FeMn Lutite
Manganese Rock
Carbonate Rock

Figure. 9

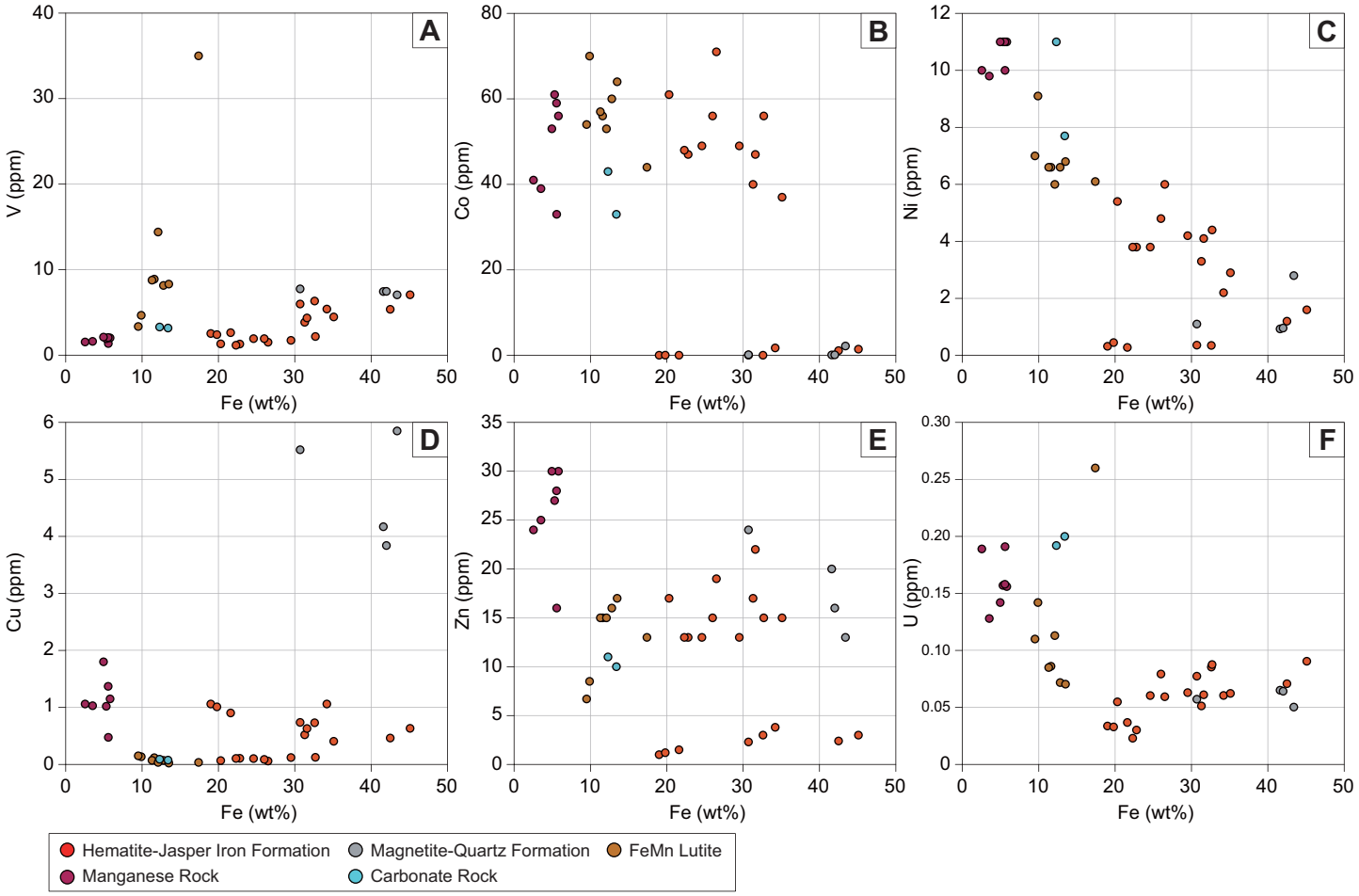
A
B
C
D
E
F
V (ppm)
Co (ppm)
Ni (ppm)
Cu (ppm)
Zn (ppm)
U (ppm)
Fe (wt%)
Hematite-Jasper Iron Formation
Magnetite-Quartz Formation
FeMn Lutite
Manganese Rock
Carbonate Rock

Figure. 10

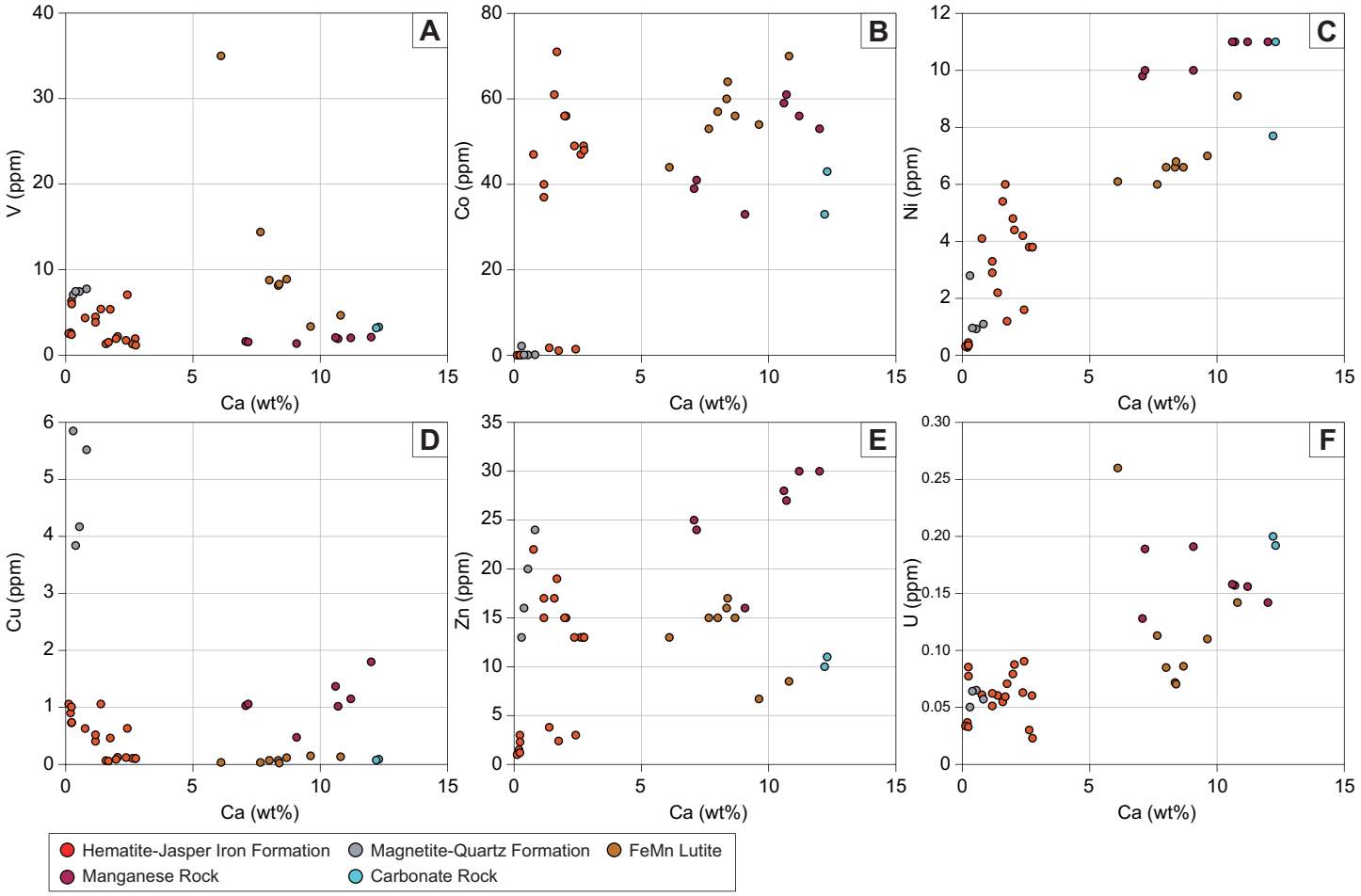
A
V (ppm)
Ca (wt%)
B
Co (ppm)
Ca (wt%)
C
Ni (ppm)
Ca (wt%)
D
Cu (ppm)
Ca (wt%)
E
Zn (ppm)
Ca (wt%)
F
U (ppm)
Ca (wt%)
Hematite-Jasper Iron Formation
Magnetite-Quartz Formation
FeMn Lutite
Manganese Rock
Carbonate Rock

Figure. 11

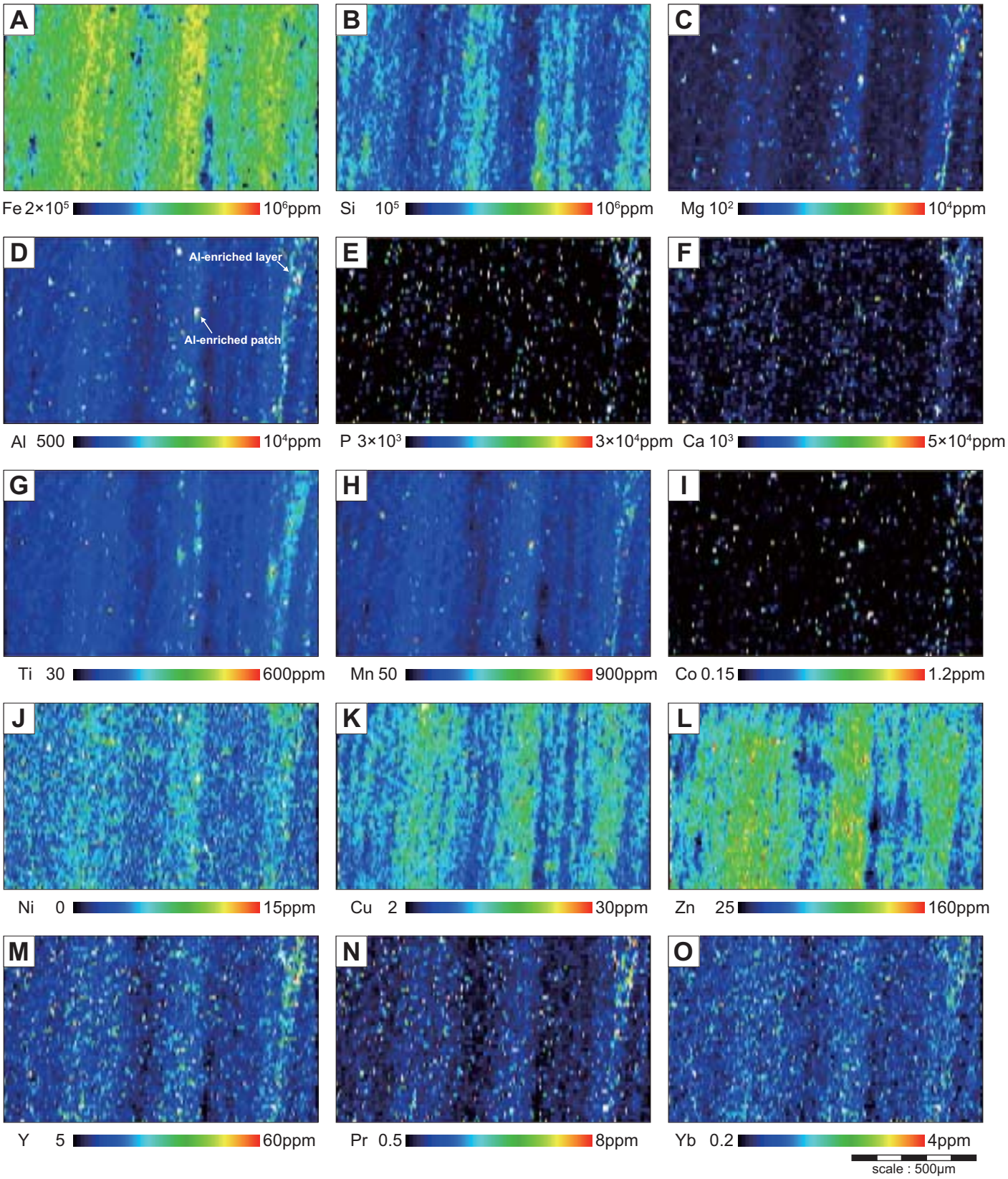
A
B
C
Fe 2×10⁵ 10⁶ppm
Si 10⁵ 10⁶ppm
Mg 10² 10⁴ppm
D
Al-enriched layer
Al-enriched patch
E
F
Al 500 10⁴ppm
P 3×10³ 3×10⁴ppm
Ca 10³ 5×10⁴ppm
G
H
I
Ti 30 600ppm
Mn 50 900ppm
Co 0.15 1.2ppm
J
K
L
Ni 0 15ppm
Cu 2 30ppm
Zn 25 160ppm
M
N
O
Y 5 60ppm
Pr 0.5 8ppm
Yb 0.2 4ppm
scale : 500μm

Figure. 12

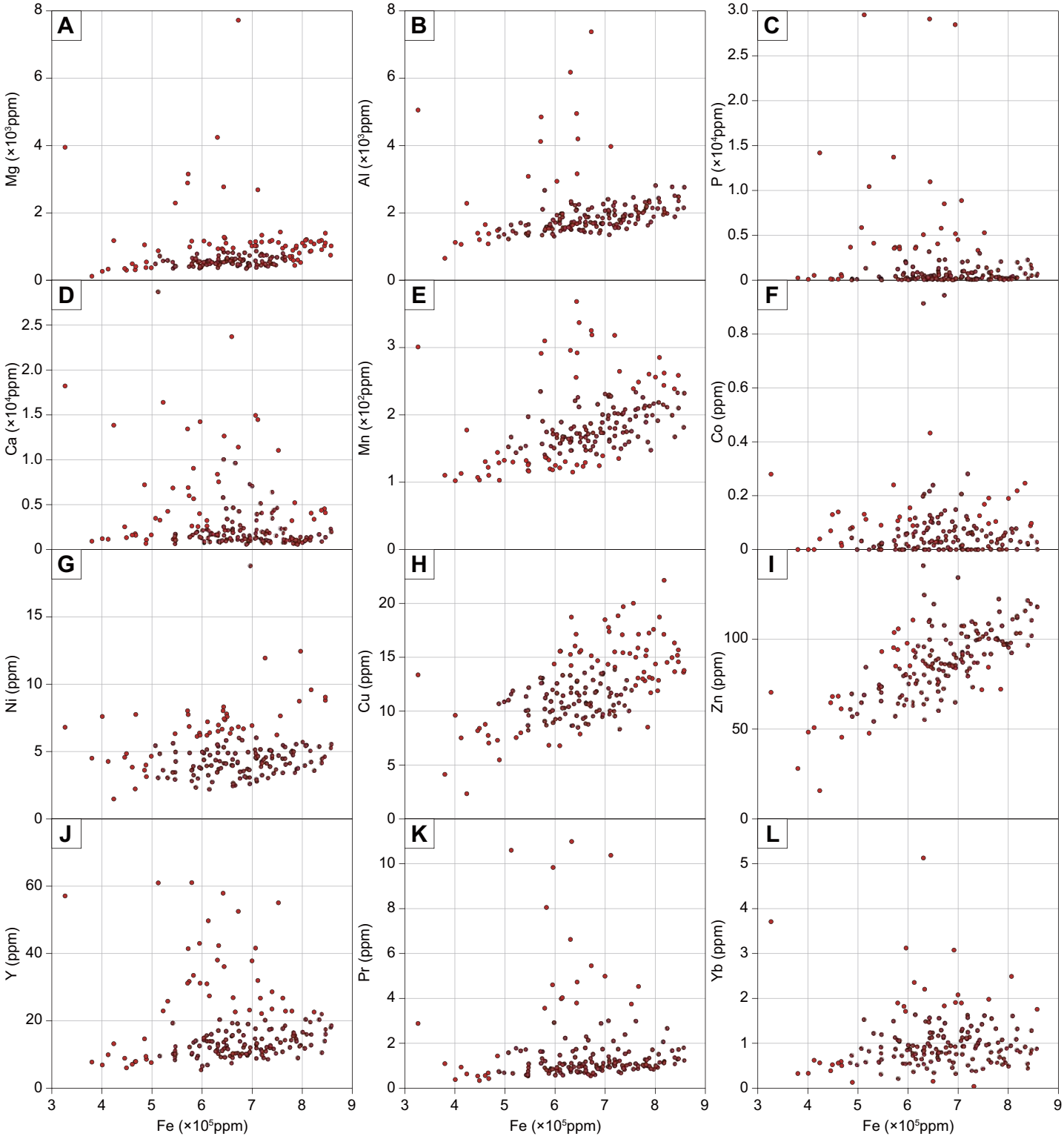
A
Mg (×10³ppm)
B
Al (×10³ppm)
C
P (×10⁴ppm)
D
Ca (×10⁴ppm)
E
Mn (×10²ppm)
F
Co (ppm)
G
Ni (ppm)
H
Cu (ppm)
I
Zn (ppm)
J
Y (ppm)
K
Pr (ppm)
L
Yb (ppm)
Fe (×10⁵ppm)
Fe (×10⁵ppm)
Fe (×10⁵ppm)

Figure. 13

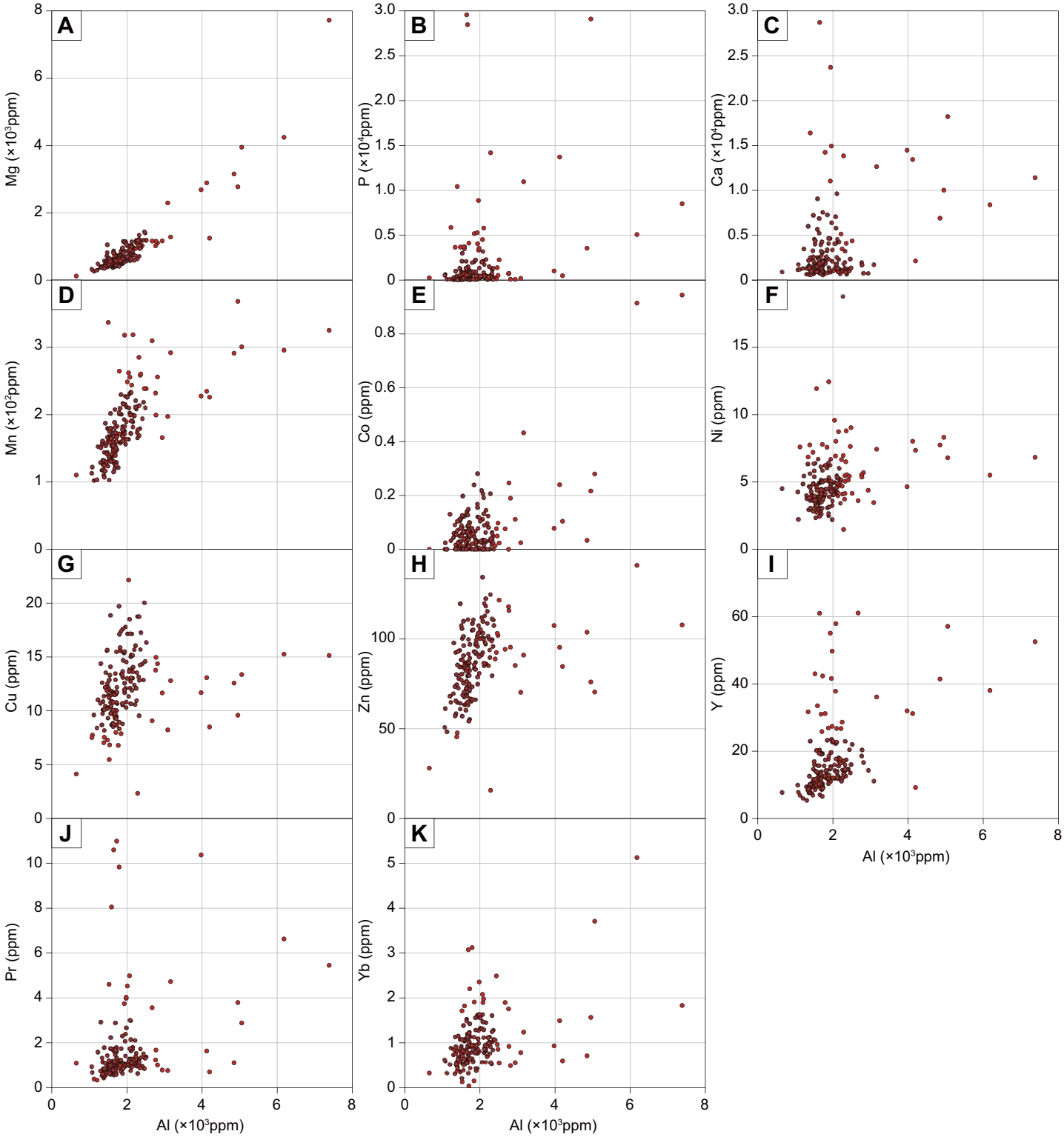
A
Mg (×10³ppm)
B
P (×10⁴ppm)
C
Ca (×10⁴ppm)
D
Mn (×10²ppm)
E
Co (ppm)
F
Ni (ppm)
G
Cu (ppm)
H
Zn (ppm)
I
Y (ppm)
J
Pr (ppm)
K
Yb (ppm)
Al (×10³ppm)
Al (×10³ppm)
Al (×10³ppm)

Figure. 14

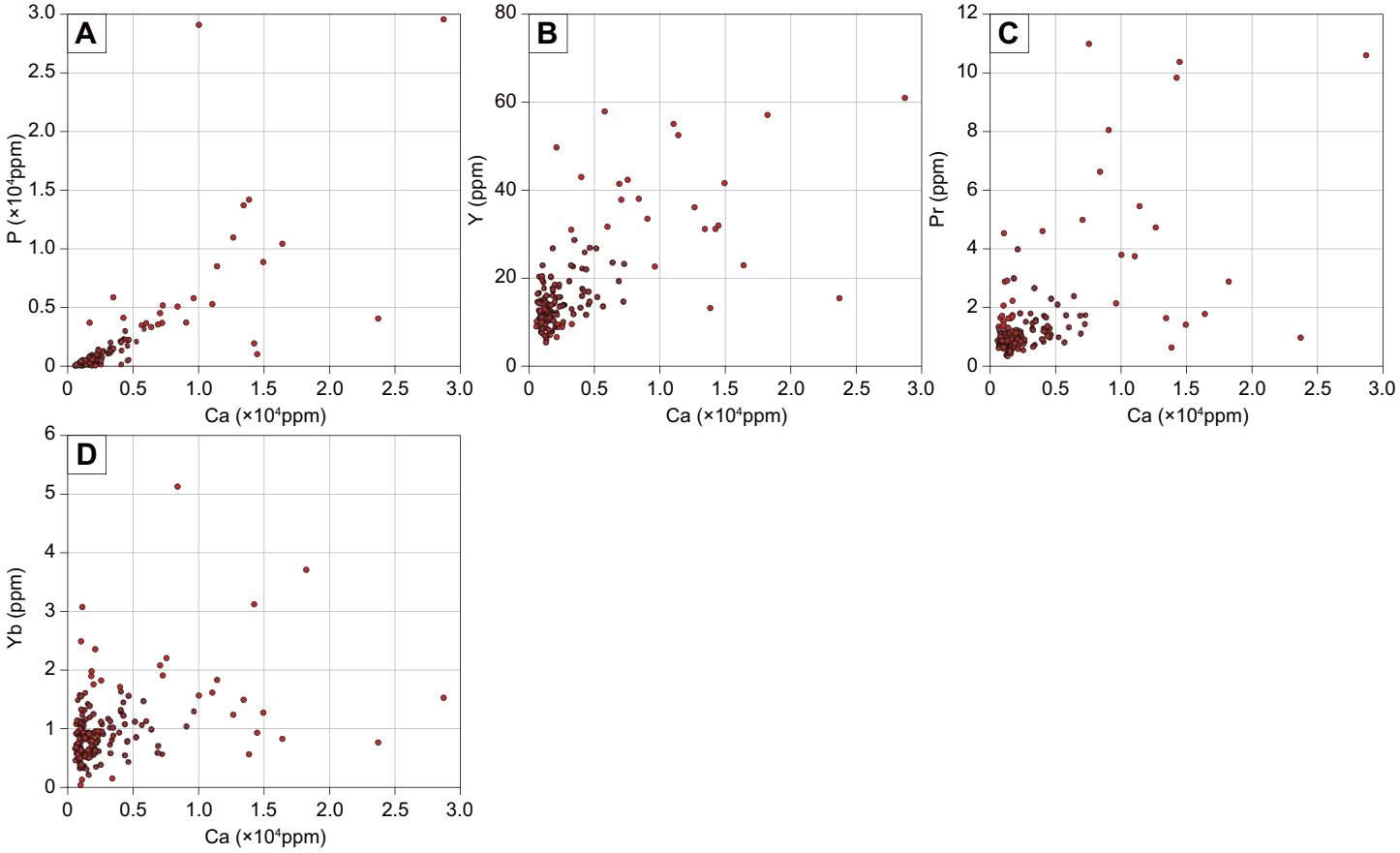
A
P (×10⁴ppm)
Ca (×10⁴ppm)
B
Y (ppm)
Ca (×10⁴ppm)
C
Pr (ppm)
Ca (×10⁴ppm)
D
Yb (ppm)
Ca (×10⁴ppm)

Figure. 15

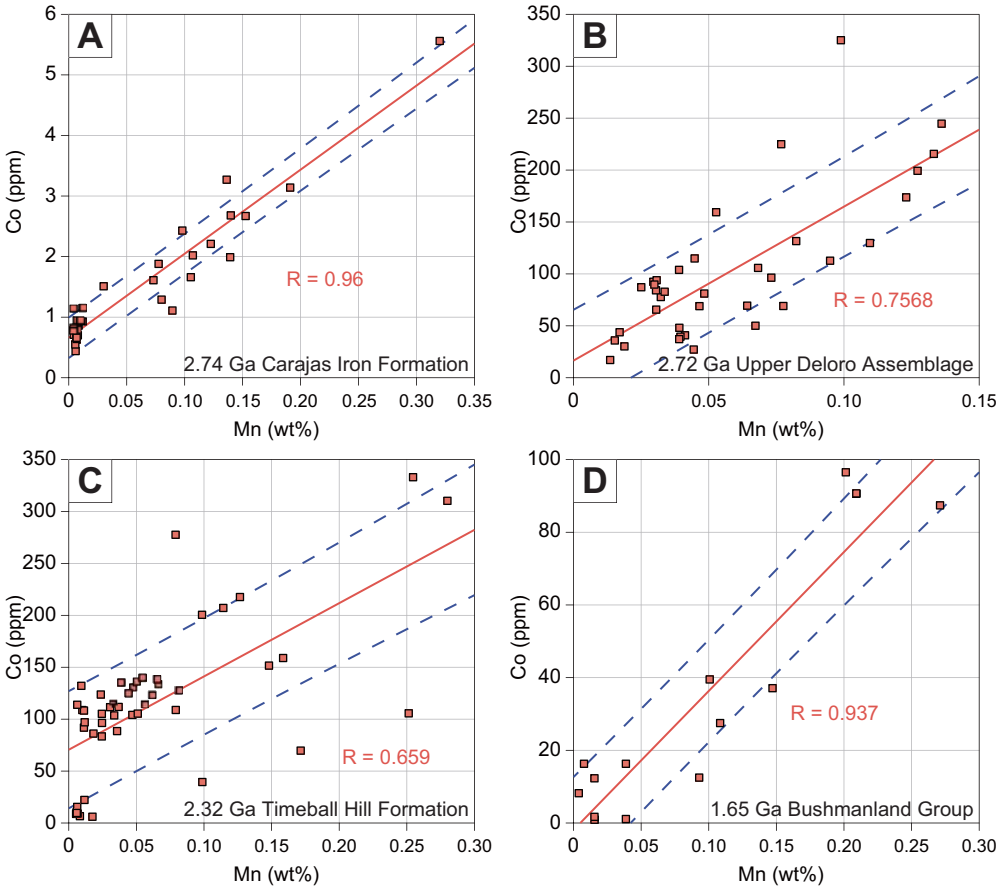
A
R = 0.96
2.74 Ga Carajas Iron Formation
Co (ppm)
Mn (wt%)
B
R = 0.7568
2.72 Ga Upper Deloro Assemblage
Co (ppm)
Mn (wt%)
C
R = 0.659
2.32 Ga Timeball Hill Formation
Co (ppm)
Mn (wt%)
D
R = 0.937
1.65 Ga Bushmanland Group
Co (ppm)
Mn (wt%)

Figure. 16

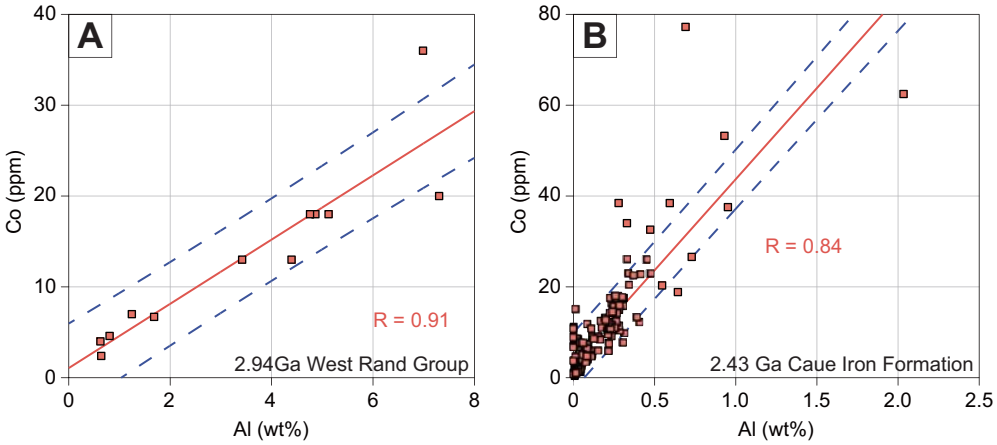
A
Co (ppm)
Al (wt%)
R = 0.91
2.94Ga West Rand Group
B
Co (ppm)
Al (wt%)
R = 0.84
2.43 Ga Caue Iron Formation

Figure. 17

Chapter V.

General Conclusions

All lives on the earth are dependent on a number of chemical elements. First of all, they are dependent on oxygen for their physiological characters such as metabolisms and body sizes, more or less. Therefore, the evolutions of the redox potentials and partial pressures of oxygen in the surface environments have had effects on the biological evolutions throughout the time in the Earth history (e.g. Kasting, 1987). However, all of organisms on the earth are also dependent on variable bioessential elements such as transitional elements other than oxygen. Those transitional elements are used for critical components of DNA, RNA, enzymes and other biomolecules. And, the degrees of dependence on those elements are different depending on their metabolic types and/or phylogenies (Zerkle et al., 2005; Dupont et al., 2006). Therefore, it might be reasonable to think that the compositions of those bioessential elements in the surface environments have influenced on the evolutions of organisms with specific metabolisms and/or belonging to specific phylogenies throughout the time.

For examining the influences of bioavailability of transitional elements on biological evolutions in the Earth history, it is important to estimate the compositions of

those elements in the past oceans. However, the distributions of bioessential elements in ancient oceans cannot be studied directly, because we cannot sample the past seawater. Therefore, the compositions of chemical sedimentary rocks, which were precipitated from the past seawater, have been used as proxies for the seawater chemical compositions. Especially, the banded iron formations (BIFs) could be useful for discussing the secular variations of the seawater compositions, because they were seen in the Precambrian geologic suites except for the Mesoproterozoic (Isley and Abbott, 1999; Klein and Beukes, 1992; Komiya et al., 2015) (see Fig. 2 in Chapter I). Since Bjerrum and Canfield (2002), the geochemical studies of the BIFs have been performed for reconstructing the secular variations of bioavailability of bioessential elements including transitional elements in the seawater, based on the assumption that ferrihydrite adsorbed dissolved elements in the past seawater (e.g. Konhauser et al., 2009; Konhauser et al., 2011; Swanner et al., 2014). However, those analyzed values of the BIFs, within one geologic suite, are too variable to discuss the secular variations of the chemical evolutions in the seawater, quantitatively and/or qualitatively. Therefore, we have to discuss some components controlling their chemical compositions firstly.

Especially, their mineralogy of the BIFs could control their chemical compositions because they do not contain Fe-oxide and silica minerals, but also carbonate, silicate, sulfide minerals and others (e.g. Klein, 2005). Those minerals are precipitates from seawater, igneous, clastic or metamorphic minerals. In previous studies, many researchers adopt samples under threshold values of the compositions of the elements derived from the above effects for discussing the seawater chemistry (e.g. Konhauser et al., 2009; Swanner et al., 2014). However, their threshold values have no foundation.

In this Ph.D. thesis, I tried to estimate the secular variations of some transitional-element compositions in the seawater based on the chemical compositions of the BIFs focusing on above components. And, finally, I discussed whether the biological evolutions have been controlled by the bioavailability of the transitional elements in the surface environments throughout the Earth history, based on the estimated secular variations of the transitional-element compositions in the seawater.

In the Chapter II, I studied the BIFs of the Eoarchean Isua supracrustal belts (ISB) in the geological, petrological and geochemical perspectives. The ISB BIFs,

based on their macro- and microscopic lithofacies, are classified into four types: Black-, Gray-, Green- and White-types, respectively. Amphibole-bearing IFs such as Green-, Gray- and White-type BIFs have higher REE + Y and transitional element contents than other samples with similar Fe contents. Even though the origins of amphibole minerals are unclear, those elements are not derived from adsorbents on the ferrihydrite. In magnetite-rich Black-type BIFs, their REE and transitional-element contents are positively correlated with Zr contents, suggesting that those elements were derived not from the contemporary seawater, but from the clastic or volcanic materials. Similar positive correlations are seen in the younger BIFs. Contamination-free BIFs show that Ni contents of the Eoarchean BIFs have higher than the Neoarchean ones, suggesting that dissolved Ni were higher in the Eoarchean oceans possibly because of hydrothermal activities associated with eruption of Ni-rich komatiite, which are consistent with the previous study by Konhauser et al. (2009). However, Ni availability has already been limited since *ca*. 2.9 Ga earlier than estimate by the previous study (*ca.* 2.7 Ga).

Nickel is one of the bioessential elements, which are used as a key metal

cofactor for methanogenesis. If the Ni content of seawater controlled the activity of methanogens, the activity declined from *ca.* 2.9 Ga. Recently, some geochemical evidence suggested that the emergence and prosperity of oxygen-producing bacteria have already occurred around 2.7-3.0 Ga based on REE contents and Ce anomalies of carbonate minerals (Komiya et al., 2008), Fe isotopes of sulfides in carbonate rocks (Nishizawa et al., 2010) and Mo isotopes of the BIFs (Planavsky et al., 2014). The decline of dissolved Ni contents in seawater before 2.7 Ga is possibly related with the emergence of oxygen-producing bacteria.

In the Chapter III, I studied the geology and geochemistry of the BIFs in two geological sections within the > 3.9 Ga Nulliak supracrustal rocks in the Saglek Block. I found that the BIFs in both areas have magnetite, quartz and pyroxene, suggesting that they have suffered from high-grade metamorphism. And, the bulk compositions of them suggest that pyroxene minerals were derived from dolomitic carbonate minerals. The BIFs with low modal abundances of pyroxene (primarily thought to be dolomite) show positive correlations of rare earth element (REE) and transitional element (V, Cr, Ni, Cu,

U) contents with Zr contents, suggesting that involvement of clastic and volcanic materials influenced on their contents, similar to the ISB BIFs in the Chapter II. The contamination-free BIFs have low V, Cr and U contents, suggesting that the Eoarchean seawater had quite low V, Cr and U contents possibly because of the anoxic conditions of ocean and terrestrial environments. On the other hand, Ni contents in contamination-free BIFs are higher than those of the Late Archean BIFs, suggesting that the Eoarchean seawater was enriched in dissolved Ni, as suggested by Chapter I.

In the Chapter IV, I performed the petrological and geochemical analysis of the BIFs and manganese rocks from the Hotazel Formation for the estimate of their sedimentary environments and the bioavailability of transitional elements in the Paleoproterozoic ocean. The Hotazel BIFs are interlayered with the manganese rocks at three stratigraphic horizons. In this study, I analyzed the chemostratigraphic variations from the lowermost BIFs to the BIFs overlying the lowest manganese rocks.

Within all analyzed samples, the whole-rock contents of transitional elements such as Ni, Zn and Co are positively correlated with Mn contents, suggesting that

Mn-oxide minerals might have been sink for those elements in the Paleoproterozoic ocean. The distribution maps of the Mn-poor BIFs, which are composed of alternation of hematite and quartz bands, show that Ni, Cu and Zn exist significantly in the hematite bands; on the other hand, much of Co exist not in hematite bands, but in Al-rich bands or spots derived from the clastic materials. Moreover, their whole-rock Co contents are much lower than those of the Eo- to Mesoarchean BIFs. Cobalt contents and its spatial distributions in the BIFs of the Hotazel Formation suggest that dissolved Co was limited in the Paleoproterozoic ocean possibly because Co was fixed as insoluble trivalent forms within Mn-oxide minerals. Moreover, similar positive correlations of Co with Mn contents are also seen in other BIFs from the Neoarchean to Paleoproterozoic. Therefore, it might be possible that significant Co fixation within the Mn oxide occurred from the Neoarchean, suggesting that bioavailable Co in the ocean was limited since the Neoarchean. These suggestions are inconsistent with previous studies by Swanner et al. (2014), which did not take account of the influences of Mn oxide in the BIFs.

Cobalt is mainly used for cobalamin (vitamin B12), which is concerned with

every metabolic activity in cell. For example, methylated cobalamin (Met H) catalyze the synthesis of methionine, which is an amino acid constituting the terminal domain of all proteins. Many prokaryotes can synthesize Met H, and their dependencies on Co are higher than eukaryotes. On the other hand, prokaryotes cannot synthesize Met H, and they acquire it from symbiotic eukaryotes or use Zn-bearing enzymes (Met E) in place of Co. Therefore, dependencies on Co in all metalloproteins in prokaryotes are higher than eukaryotes (Dupont et al., 2006). Recent studies show that a part of prokaryotes such as cyanobacteria can also use Zn-bearing Met E, and Met E-containing cyanobacteria and eukaryotic algae belong to a monophyletic group as for Met E gene (Helliwell et al., 2011). Decrease in Co bioavailability of the oceans from Neoarchean to Paleoproterozoic might provoke the birth of cyanobacteria using Met E. It might be possible that, subsequently, Co-independent eukaryotes evolved from symbiosis of cyanobacteria using Met E.

The previous modeling studies for reconstructing the secular variations of the bioessential transitional elements in the past ocean have been often performed based on

the dependencies on those elements by the modern organism (Zerkle et al., 2005; Dupont et al., 2006) or simple redox-secular-variation model (Saito et al., 2003). Therefore, they had low temporal resolutions for discussing the relationships between the timing of the occurrences of the organisms and secular variations of bioessential-element compositions in the environments.

In this Ph.D. study, the compositions of the BIFs clarified that the secular variations of seawater transitional-element compositions might have been fluctuated through geological time accompanied by fluctuation of the redox potentials and the chemical compositions of supply-source rocks of their elements. And, this study suggests that those secular variations of the bioavailabilities of those transitional evolutions in the ocean might have influenced on the metallomes of the organism. In other words, oceanic seawater chemistry and biological chemistry have co-evolved as for transitional elements, and those co-evolutions are preserved in metallomes of modern organisms.

References

Albani, A. E., Bengtson, S., Canfield D. E., Bekker, A., Macchiarelli, R, Mazurier, A., Hammarlund, E. U., Boulvais, P., Dupuy J. J., Fontaine, C., F ürisch, F. T., Gaurhier-Lafaye, F., Janvier, P., Javaux, E., Ossa, F. O., Pierson-Wickmann, A. C., Riboulleau, A., Sardini, P., Vachard, D., Whitehouse, M., Meunier, Alain., 2010. Large colonical organism growth in oxygenated environments 2.1 Gyr ago. Nature 466, 100-104.

Bjerrum, C.J., Canfield, D.E., 2002. Ocean productivity before about 1.9 Gyr ago limited by phosphorus adsorption onto iron oxides. Nature 417, 159-162.

Han, T. M., Runnegar, B., 1992. Megascopic eukaryotic algae from the 2.1-billion-year-old Negaunee iron-formation, Michigan. Science 257, 232-235.

Isley, A.E., Abbott, D., 1999. Plume-related mafic volcanism and the deposition of banded iron formation. Journal of Geophysical Research 104, 15461-15477.

Dupont, C.L., Yang, S., Palenik, B., Bourne, P.E., 2006. Modern proteomes contain putative imprints of ancient shifts in trace metal geochemistry. PNAS 47, 17822-17827.

Kasting, J.F., 1987. Theoretical constraints on oxygen and carbon dioxide concentrations in the Precambrian atmosphere. Precambrian Research 34, 205-229.

Klein, C., Beukes, N.J., 1992. 4.2. Time distribution, stratigraphy, and sedimentologic setting, and geochemistry of Precambrian iron-formation. In: Schopf, J.W., Klein, C. (Eds.), The Proterozoic Biosphere: A Multidisciplinary Study. Cambridge University Press, New York, pp. 139-146.

Klein, C., 2005. Some Precambrian banded iron-formations (BIFs) from around the world: Their age, geologic setting, mineralogy, metamorphism, geochemistry, and origins. American Mineralogist 90, 1473-1499.

Komiya, T., Yamamoto, S., Aoki, S., Sawaki, Y., Ishikawa, A., Tashiro, T., Koshida, K., Shimojo, M., Aoki, K., Collerson, K.D., 2015. Geology of the Eoarcehan, >3.95 Ga, Nulliak supracrustal rocks in the Saglek Block, northern Labrador, Canada: The oldest geological evidence for plate techtonics. Tectonophysics 662, 40-66.

Konhauser, K.O., Pecoits, E., Lalonde, S.V., Papineau, D., Nisbet, E.G., Barley, M.E., Arndt, N.T., Zahnle, K., Kamber, B.S., 2009. Oceanic nickel depletion and a methanogen famine before the Great Oxidation Event. Nature 458, 750-753.

Konhauser, K.O., Lalonde, S.V., Planavsky, N.J., Pecoits, E., Lyons, T.W., Mojzsis, S.J., Rouxel, O.J., Barley, M.E., Rosiere, C., Fralick, P.W., Kump, L.R., Bekker, A., 2011. Aerobic bacterial pyrite oxidation and acid rock drainage during the Great Oxidation Event. Nature 478, 369-373.

Swanner, E.D., Planavsky, N.J., Lalonde, S.V., Robbins, L.J., Bekker, A., Rouxel, O.J., Saito, M.A., Kappler, A., Mojzsis, S.J., Konhauser, K.O., 2014. Cobalt and marine redox evolution. Earth and Planetary Science Letters 390, 253-263.

Zerkle, A.L., House, C.H., Brantley, S.L., 2005. Biogeochemical signatures through time as inferred from whole microbial genomes. American Journal of Science 305, 467–502.

Zhang, Y., Rodionov, D.A., Gelfand, M.S., Gladyshev, V.N. 2009. Comparative genomic analyses of nickel, cobalt and vitamin B12 utilization. BMC Genomics 10, 78.

Acknowledgements

I would like to thank Dr. Tsuyoshi Komiya for supervising my research activities for five years. I also thank Dr. Takafumi Hirata, Dr. Takeshi Ohno, Dr. Shuhei Sakata and Kentaro Hattori for technical assistance with the experiments by ICP-MS. And, I thank Dr. Yoshio Takahashi, Dr. Yasuhiro Kato and Dr. Harilaos Tsikos for providing the samples. Finally, I am grateful to Dr. Akira Ishikawa, Dr. Shinji Yamamoto, Masanori Shimojo, Keiko Koshida and Takayuki Tashiro for useful discussions and other supports in my research activities.